

**Self-assembly and Gelation Kinetics in Nucleic  
acid-Polyelectrolyte complexes and Gels**

**Thesis submitted to the Jawaharlal Nehru University  
for the award of the degree of**

**DOCTOR OF PHILOSOPHY**

**PANKAJ KUMAR PANDEY**




**SCHOOL OF PHYSICAL SCIENCES  
JAWAHARLAL NEHRU UNIVERSITY  
NEW DELHI-110067**

**2018**

## DECLARATION

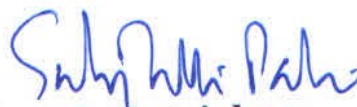
I hereby declare that the work carried out in this thesis entitled "Self-assembly and Gelation Kinetics in Nucleic acid-Polyelectrolyte complexes and Gels" is entirely original. It was carried out by me in School of Physical Sciences, Jawaharlal Nehru University, New Delhi, India under the supervision of Prof. H. B. Bohidar. I further declare that it was not formed the basis for the award of any diploma, membership or similar title of any university or institution.



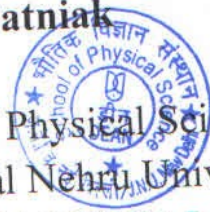
**Pankaj Kumar Pandey**  
School of Physical Sciences  
Jawaharlal Nehru University  
New Delhi-110067, India



**Prof. H. B. Bohidar**  
Thesis Supervisor  
School of Physical Science  
Jawaharlal Nehru University  
New Delhi-110067, India



**Prof. S. Patniak**  
Dean  
School of Physical Science  
Jawaharlal Nehru University  
New Delhi-110067, India



*Dedicated*

*To*

*My beloved*

*Late Grand Mother*

# TABLE OF CONTENTS

---

## CHAPTER-1

### Introduction

<b>1.1</b>	<b>Soft matter</b>	<b>1</b>
<b>1.2</b>	<b>Biopolymers</b>	<b>1</b>
	<b>1.2.1</b> Types of biopolymers	<b>2</b>
	<b>1.2.2</b> Polyelectrolytes and Polyampholytes	<b>8</b>
<b>1.3</b>	<b>Interactions</b>	<b>9</b>
	<b>1.3.1</b> Covalent Bonding	<b>9</b>
	<b>1.3.2</b> Electrostatic Interaction	<b>9</b>
	<b>1.3.3</b> Hydrophobic Interaction	<b>13</b>
	<b>1.3.4</b> van der Waals Interaction	<b>15</b>
	<b>1.3.5</b> Hydrogen Bonding	<b>17</b>
	<b>1.3.6</b> Surface Patch Binding	<b>17</b>
<b>1.4</b>	<b>Polymeric Phases</b>	<b>19</b>
	<b>1.4.1</b> Sol	<b>19</b>
	<b>1.4.2</b> Gel	<b>19</b>
	<b>1.4.3</b> Coacervation	<b>21</b>
<b>1.5</b>	<b>Biosensors</b>	<b>22</b>
<b>1.6</b>	<b>Quantum dot</b>	<b>23</b>
<b>1.7</b>	<b>Motivation of thesis</b>	<b>27</b>
<b>1.8</b>	<b>References</b>	<b>28</b>

## CHAPTER-2

### Materials and Characterization Techniques

<b>2.1</b>	<b>Materials</b>	<b>32</b>
	<b>2.1.1</b> DNA	<b>32</b>
	<b>2.1.2</b> Ionic Liquid	<b>33</b>



2.1.3 Protein- Zein	35
2.2 Characterization Techniques	35
2.2.1 Light Scattering	35
2.2.2 Small Angle Neutron Scattering	41
2.2.3 Rheology	45
2.2.4 Viscometer	50
2.2.5 Electrophoresis	51
2.2.6 FTIR	52
2.2.7 Scanning Electron Microscope	54
2.2.8 Transmission Electron Microscope	55
2.2.9 UV-vis Spectroscopy	57
2.2.10 Fluorescence Spectroscopy	59
2.2.11 XRD	61
2.2.12 Cyclic –Voltammetry	63
2.2.13 Atomic Force Microscopy	64
2.2.14 Confocal Microscopy	66
2.2.15 Gamma Irradiation	66
2.3 References	66

## **CHAPTER-3**

### **DNA hydrogel and ionogel and low concentration ionogel and Gamma irradiated ionogel**

3.1 Introduction	70
3.2 Part [A]: DNA Hydrogel	
3.2.1 Sample preparation	75
3.2.2 Result and Discussion	75
3.2.2.1 Sol-gel Transition	75
3.2.2.2 Static Structure Factor	78
3.3 Part [B]: [C2mim][Cl] based Ionogel	
3.3.1 Sample preparation	84

3.3.2 Result and Discussion	84
3.3.2.1 Scaling and Gelation time	84
3.3.2.2 Dynamic Arrest and Ergodicity Breaking	86
3.3.2.3 Static Structure Factor	89
3.3.2.4 Rheology	92
3.4 Part [C] [C8mim][Cl] based Low concentration DNA gel discussion	
3.4.1 Sample preparation	95
3.4.2 Result of Discussion	96
3.4.2.1 Universality of sol-gel transition	96
3.4.2.2 Viscoelastic Behavior	100
3.4.2.3 Relaxation Dynamics	103
3.4.2.4 Small Angle neutron Scattering	107
3.4.2.5 Phenomenology of Gelation	109
3.5 Part [D]: Effect of $\gamma$ -radiation on DNA ionogel: Structure-property evaluation	
3.5.1 Sample preparation	111
3.5.2 Results and Discussion	112
3.5.2.1 Secondary Structure	
3.5.2.2 Agarose gel electrophoresis	113
3.5.2.3 Viscosity Measurement	114
3.5.2.4 Dynamic Arrest	116
3.5.2.5 Viscoelastic properties	118
3.6 Conclusion	120
3.7 References	124

## CHAPTER-4

### Complex Coacervation of dsDNA and in situ formed Zein nanoparticles

4.1 Introduction	131
4.2 Sample preparation	134
4.3 Result and Discussion	135
4.3.1 DNA-Zein binding	135

4.3.2 Condensation of DNA ( $C_{Zein} < 0.2\%$ (w/v))	137
4.3.3 Complex coacervation ( $0.2 < C_{Zein} < 0.5\%$ (w/v))	139
4.3.4 Microstructure of coacervates	141
4.3.5 Structure Factor	144
4.3.6 Salt dependent Coacervation	147
4.3.7 Fourier-transform infrared spectroscopy (FTIR)	150
4.3.8 Viscoelastic properties of coacervates	151
4.4 Conclusion	157
4.5 References	159

## **CHAPTER-5**

### **Green and Enzyme-free DNA ionogel based platform for Urea detection**

5.1 Introduction	164
5.2 Sample preparation	165
5.2.1 Preparation of DNA ionogel/ITO electrodes	165
5.3 Result and Discussion	166
5.3.1 Optimization of electrode parameters	166
5.3.2 Detection of analytes	168
5.3.3 FTIR	171
5.3.4 Surface Morphology characterization	172
5.4 Conclusion	173
5.5 References	173

## **CHAPTER-6**

### **Concentration Dependent 1-Octyl-3 Methylimidazolium Chloride based DNA ionogel : Application as Citric Acid Sensor**

6.1 Introduction	176
6.2 Sample preparation	177
6.3 Result and Discussion	178
6.3.1 Viscoelastic Behavior of ionogels	178

6.3.2	Microscopic Information	180
6.3.3	Preparation of DNA ionogel-ITO electrodes	182
6.3.4	Fourier transform Infrared spectroscopy (FTIR)	183
6.3.5	Optimization of parameters	184
6.3.6	Detection of analytes	187
6.4	Conclusion	190
6.5	References	191

## CHAPTER-7

### Synthesis of water soluble MoS<sub>2</sub> Quantum Dot and Crosslinked DNA Nanocomposite Hydrogels

7.1	Introduction	195
7.2	Sample preparation	197
7.2.1	Synthesis of MoS <sub>2</sub> quantum dots	197
7.2.2	Synthesis of fluorescent DNA nanocomposite hydrogel	197
7.3	Result and Discussion	197
7.3.1	Morphology and structure of MoS <sub>2</sub> QDs	197
7.3.2	Bandgap	199
7.3.3	Viscoelasticity of nanocomposite hydrogels	199
7.3.4	Dynamics and ergodicity	202
7.3.5	Small Angle X-Ray Scattering	205
7.3.6	Phenomenology of pseudo-crosslinking	207
7.4	Conclusion	209
7.5	References	210

## CHAPTER-8

### Fluorescent multipurpose DNA- Dots: Luminescent DNA gels, Cell Imaging and Dopamine Detection

8.1	Introduction	213
8.2	Sample preparation	215
8.2.1	Synthesis of DNA Dots (DD)	215
8.2.2	Synthesis of Fluorescent DNA-DNA Dot hydrogel	215
8.2.3	Microbial Strains and Growth media	216
8.2.4	Assessment of microbial toxicity of DNA Dots (DDs)	216
8.2.5	Intracellular Reactive Oxygen Species (ROS)	217
8.2.6	Cellular uptake of DDs by the fungal cells	218
8.2.7	Fluorescence Microscopy	218
8.2.8	Electrochemical sensing	219
8.3	Result and Discussion	219
8.3.1	Viscoelastic Properties of DNA-DD hydrogel	221
8.3.2	Morphology of DNA-DD hydrogel	224
8.3.3	Microbial toxicity of DDs	227
8.3.4	DD induced intracellular ROS	228
8.3.5	Cellular uptake of DDs	230
8.3.6	Dopamine detection	233
8.4	Conclusion	236
8.5	References	238

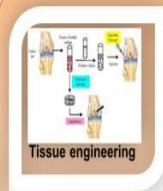
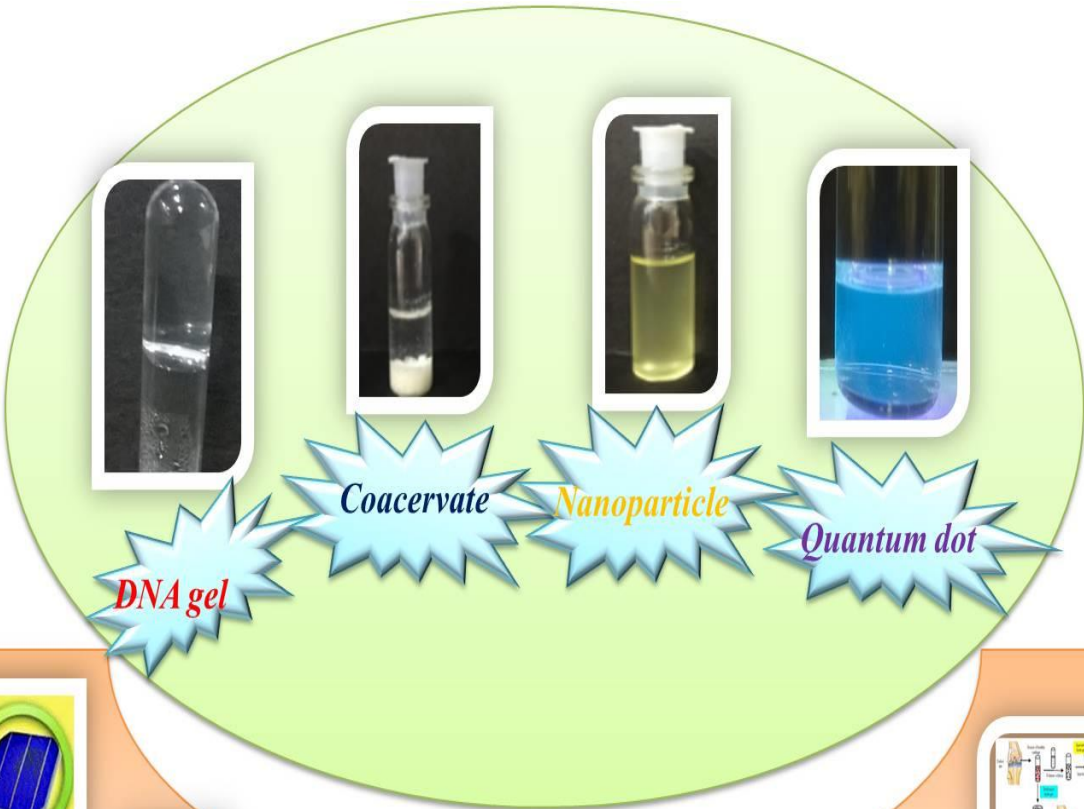
## CHAPTER-9

### Summary

9.1	Main Summary of the thesis	242
9.2	Ongoing Work	244
9.3	Open problems for future	244

Publications

Conferences, Seminars and Workshops



# CHAPTER-1

---

## Introduction

**Abstract:** This chapter will explain the basics of soft matter physics, biopolymers, binding interactions, different polymeric phases of biopolymers, quantum dots and electrochemical sensors. It describes the motivation of present research work and outline of this thesis.

### 1.1 Soft matter

Soft matters are those materials which can be deformed by external forces such as electromagnetic field, external stress, and thermal fluctuations. These materials are bound by weak forces so that they can be easily deformed under external stress. The energy of the statistical number of constituent particles of soft matter system is defined by thermal energy. The expression for thermal energy is  $k_B T$  where  $k_B$  is Boltzmann constant and  $T$  is absolute temperature. Examples of soft materials are biopolymers, gel, coacervates, foams, liquid crystals etc.

### 1.2 Biopolymers

Polymers obtained from living beings are known as biopolymers. These are biodegradable in nature. A large number of covalently bonded monomeric units from biopolymers such as carbohydrates, amino acid, and nucleotides.

### Applications of Biopolymers

- Coatings packaging
- Fibers and textiles
- Bioplastics

- Cosmetics and personal care products
- Paper and pip
- Pharmaceutical formulation
- Biomedical implements
- Food and beverage products

**Generally, biopolymer can be divided into three types:**

### **1.2.1 Types of biopolymers**

The first kind of biopolymers use amino acids as a monomer unit. Proteins such as zein, beta-lactoglobulin, elastin, gelatin, insulin, hemoglobin, bovine serum albumin, keratin are the examples etc. The second kind of biopolymers contain nucleotide as monomer unit. DNA (deoxyribonucleic acid) and RNA (ribonucleic acid) are example of this category. In the third kind of biopolymers saccharides act as monomer unit, that give rise to carbohydrates such as pectin, agar, cellulose, and chitin.

#### **Amino Acid**

The monomer unit of protein is an amino acid. Amino acid consists of  $-\text{NH}_2$  (amine) and  $-\text{COOH}$  (Carboxyl) functional group with side chain R. The total amino acid found in all biological entities is limited to 20. Based on their nature these are generally divided on the basis of their polarity:

1. Non polar amino acid
2. Polar amino acid



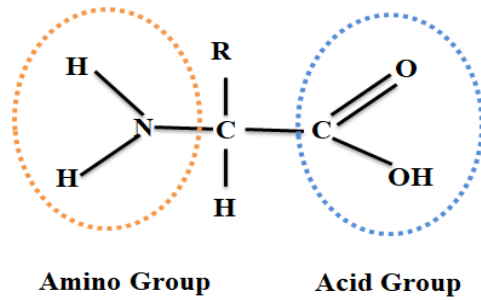
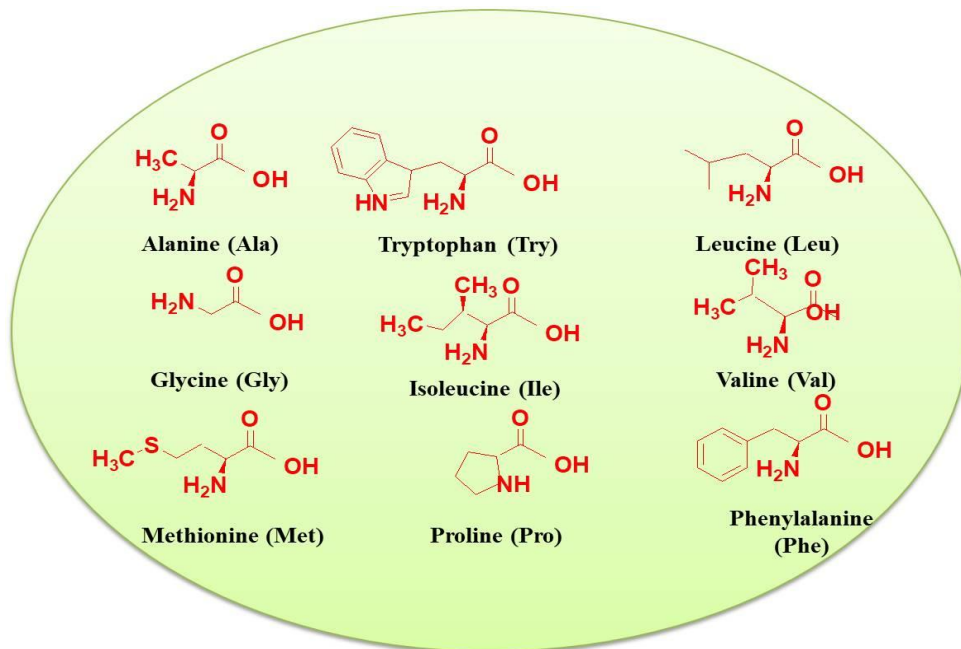


**Figure 1.1.** Chemical formula of amino acid

There are nine numbers of non-polar amino acids among the available 20. Nonpolar amino acids are hydrophobic in nature. The presences of polar groups like  $\text{-NH}_2$ ,  $\text{-OH}$  and  $\text{-COOH}$  in the side chain of amino acid make polar proteins. These are acidic and basic in nature. Some amino acids do not show acidic or basic behaviors so are called neutral amino acids.

### Polar amino acids



## Non-polar amino acids

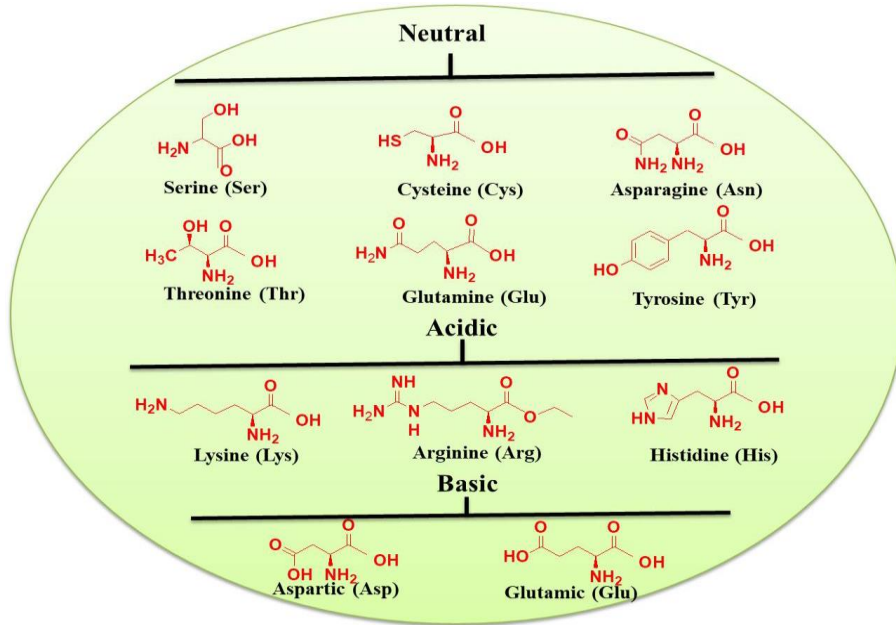


**Figure 1.2.** Classification of amino acids as per polarity

## Nucleotides

Nucleotides are those molecules that fill in as the monomer units for forming the nucleic acid polymers deoxyribonucleic acid (DNA) and ribonucleic acid (RNA), the two of which are crucial biomolecules in all living things. Nucleotides are the basic building unit of nucleic acids; they are made of three subunits: a nitrogenous base, a five-carbon sugar (ribose or deoxyribose), and minimum one phosphate bunch. DNA carries genetic information.

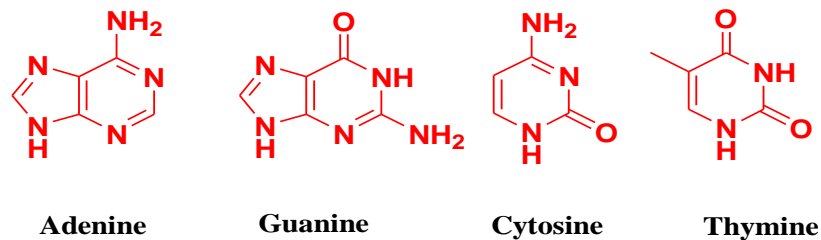


**Figure 1.3.** Bases of DNA

DNA molecule has four bases which are Adenine (A), Thymine (T), Guanine (G) and Cytosine (C) which appears in the Fig. 1.3 while RNA has also four bases but it contains Uracil (U) rather than Thymine (T) (Fig. 1.4)

The sugar-phosphate backbone of DNA is deoxyribose whereas in RNA has ribose as a backbone.

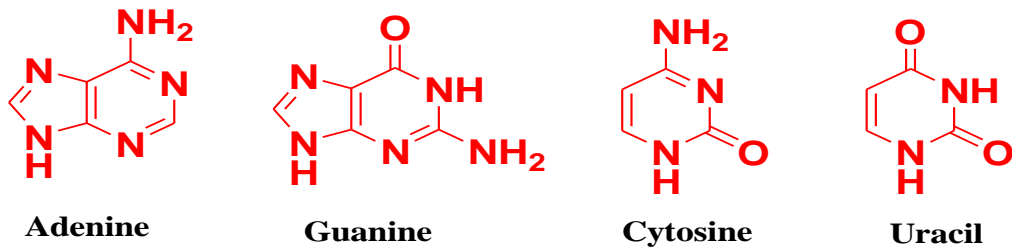


**Figure 1.4.** Bases of RNA

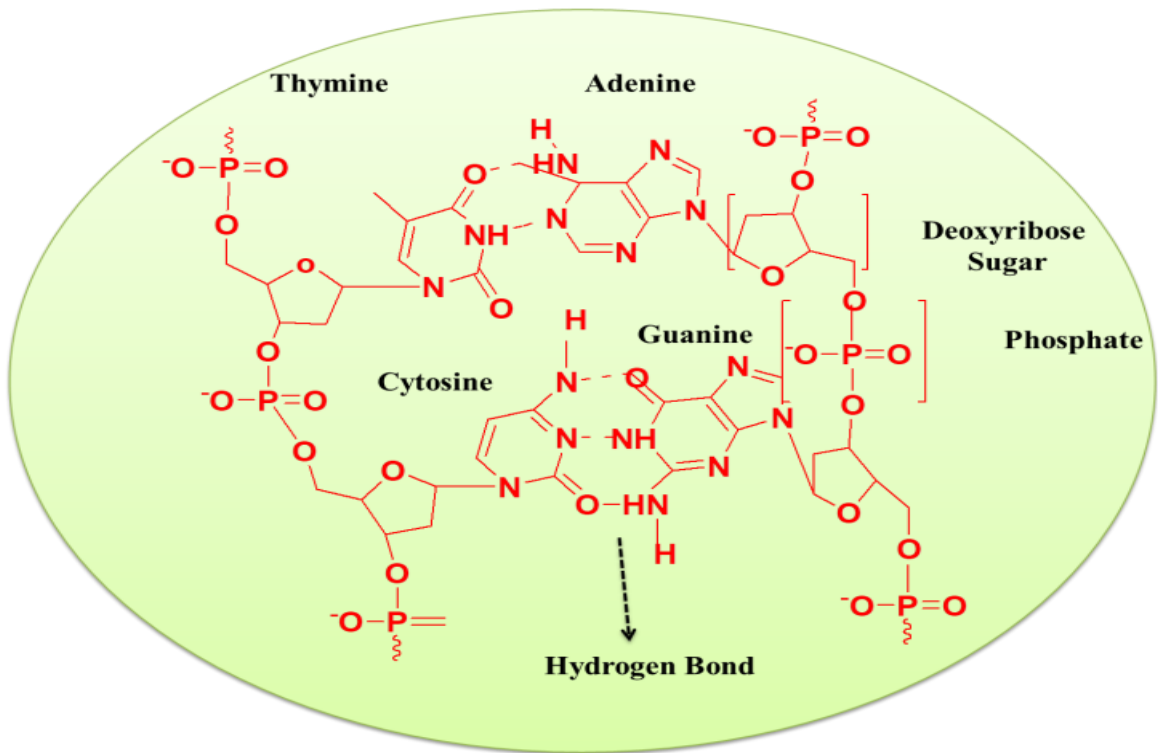


**Figure 1.5.** Chemical structure of DNA

Both nucleic acids either DNA or RNA are formed by a condensation reaction between phosphate and hydroxyl group. H-bonding occurs between distinctive bases of DNA. A and T bases have two hydrogen bonds, and G and C have three hydrogen bonds which is shown in Fig.1.5 DNA is composed of twofold helix whereas RNA is made of single helix structure. In RNA hydroxyl group is joined to pentose ring structure. RNA takes part in different forms like coding, decoding, gene regulation etc.

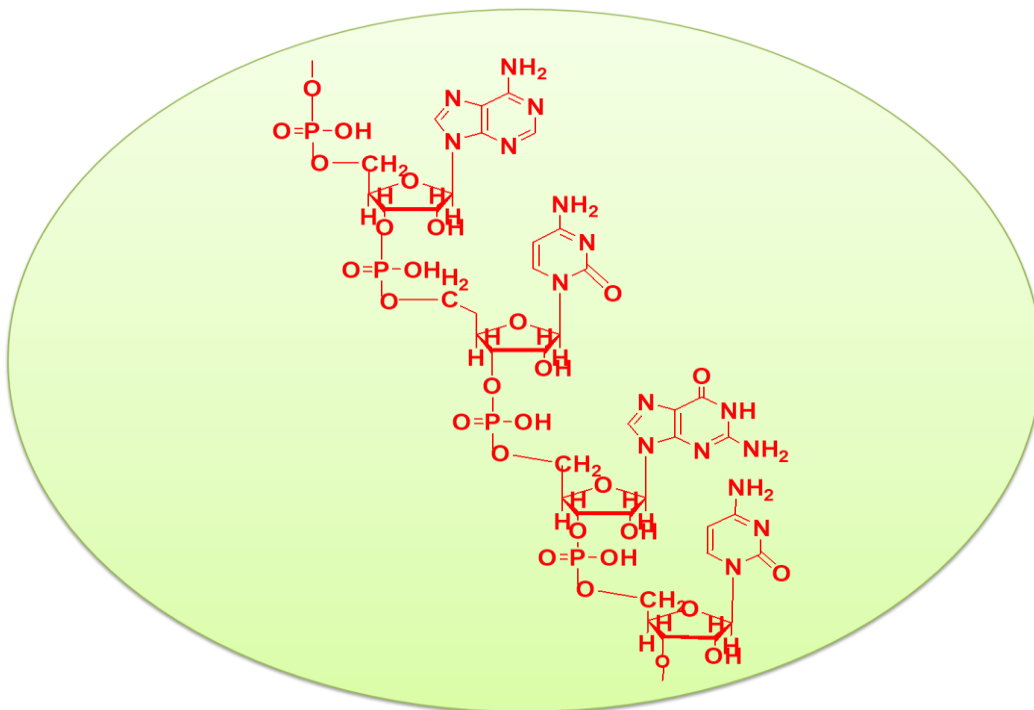


**Figure 1.6.** Chemical structure of RNA

## Carbohydrate

The third type of biopolymer is carbohydrate. It is a naturally occurring organic compound composed of oxygen, carbon, and hydrogen. The general formula for carbohydrate is  $C_x(H_2O)_y$ . It is generally formed by plants during photosynthesis process. Carbohydrates can be distinguished from each other by the hydroxyl group and carbohydrates joined together.

Commonly used carbohydrates are agar, pectin, cellulose, and chitosan. Further carbohydrates are divided into three types,

- (i) Monosaccharides
- (ii) Disaccharides
- (iii) Polysaccharides

Monosaccharides have a cyclic structure. The basic unit of such carbohydrates is a ketone or polyhydroxy aldehyde. eg. D-glucose, Fructose and Galactose.

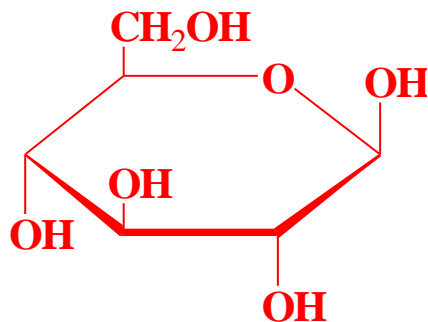


**Figure 1.7** Structure of D-Glucose

Two monosaccharide units are joined by glycosidic linkage form Disaccharides such as sucrose, lactose, and maltose.

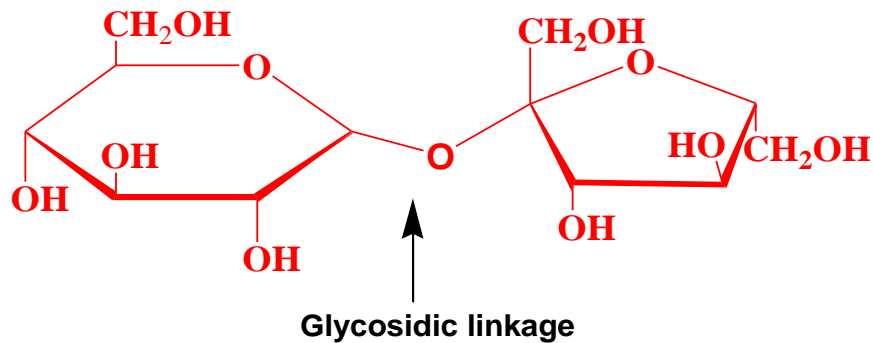


**Figure 1.8** Structure of sucrose

Finally, 20 to 107 monosaccharide units join together to form polysaccharides such as agar, pectin, chitosan, and cellulose etc.

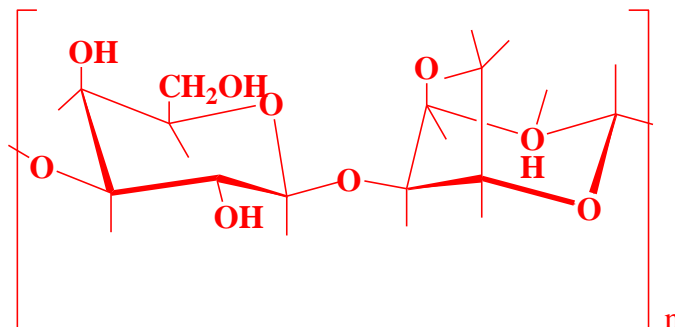


**Figure 1.9** Structure of agar

### 1.2.2 Polyelectrolytes and Polyampholytes

Polymers composed of polycation or polyanion are called polyelectrolyte. Nucleic acids such as DNA, RNA are examples of polyelectrolyte. The charge on the polyelectrolyte is due to the ionizable group attached to them [1-3]. Polyampholyte is a kind of polyelectrolyte which have both cationic and anionic functional groups. These are of two types

- (i) Annealed polyampholyte
- (ii) Quenched polyampholyte

In annealed polyampholyte monomer unit are pH sensitive that is with pH the charge of polymer changes. In comparison quenched polyampholyte charge is independent of pH.

With the pH variation net charge on polymer becomes zero at isoelectric point (pI). Examples of some polyelectrolytes are DNA, RNA, agar, chitosan etc.

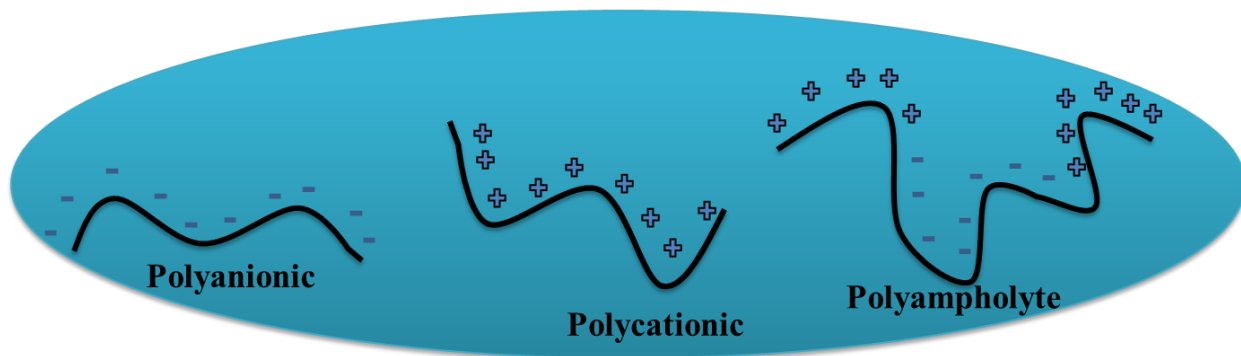


**Figure 1.10.** Schematic diagram for Polyelectrolyte and polyampholyte

### 1.3 Interactions

#### 1.3.1 Covalent Bonding

Here two atoms share electrons to form a chemical bond through covalent bonding. The basic backbones of bonding in proteins are covalent in nature [4]. The typical bond strength of the covalent bond is 80-100 kcal/mole. The bond between the polymer and ionic liquid salt is a covalent bond [5].

#### 1.3.2 Electrostatic Interaction

The interaction between two oppositely charged biopolymers is known as electrostatic interaction. This interaction leads to the minimization of free energy when binding is taken into account. The examples of electrostatic interactions are protein-protein interaction [6] and protein-polyelectrolyte interaction [7]. These interactions are also called coulombic interaction. It depends on pH, ionic strength and temperature. When only van der Waals forces exist then all dispersed molecules may aggregate but this does not occur always because of long-range repulsive force.

The colloidal particles have charge and they remain in an equilibrium state in the solvent due to Brownian and electrostatic forces. Consider a microion with negative charge in a medium of 1:1 electrolyte solution. The mobile ion will organize themselves in the distinct regions given below,

1. Stern layer where immobile ions are at the surrounding of this particle.
2. A region between Shear and Stern plane where ions are movable and spread away from these particles.

This can be easily understood from the following Fig. 1.11.

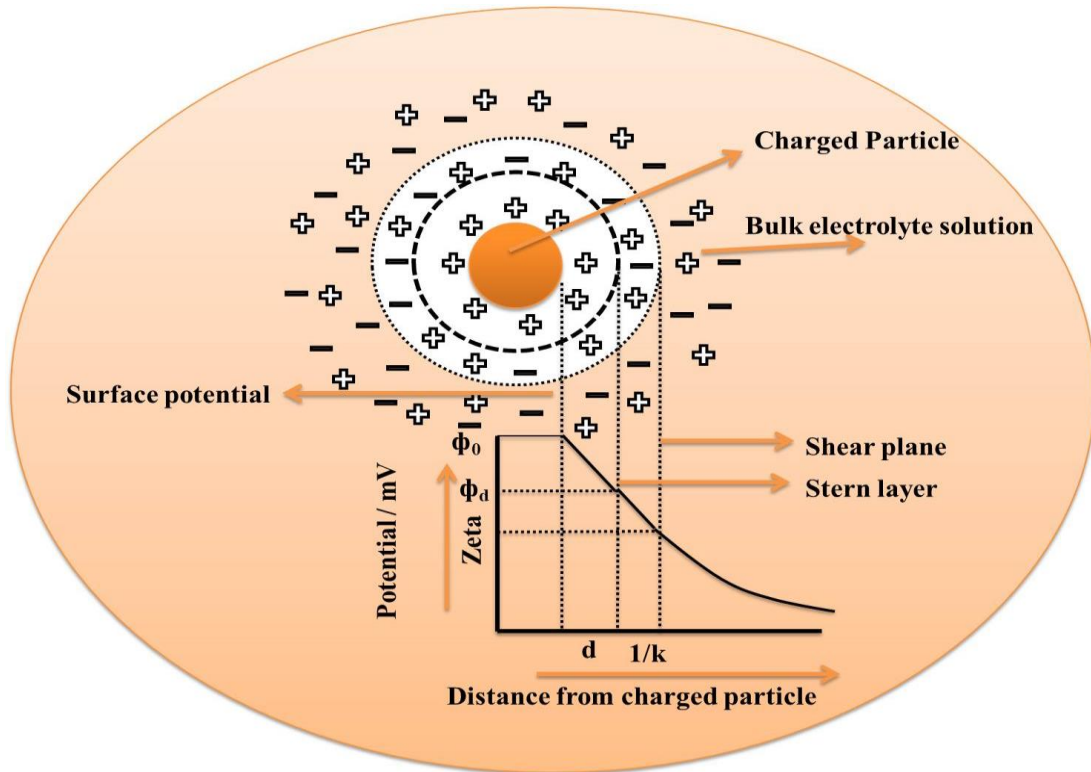


**Figure 1.11.** The electric double layer with the variation in potential.  $k$  is the Debye parameter and the reciprocal of this defines the screening length.

The width of the Stern region is known as Bjerrum length which is given by

$$l_B = \frac{q^2}{4\pi\epsilon k_B T} \quad (1.1)$$



Where  $q$  is a charge on ionized macromolecule, and  $\epsilon$  is the dielectric constant of the medium. In Fig.1.11 the twofold layer is appears at a specific distance from the charged particle. It is to see that potential on Stern layer varies as  $1/r$  then it exponentially decreases.  $\phi_c$  denotes the surface potential of a charged particle,  $\phi_s$  shows potential on a stern plane and third potential is corresponding to zeta potential.

Mathematically electrostatic double layer on the Fig.1.11 can be explained by the potential (diffusion part) at distance  $d$

$$\nabla^2\phi = -\frac{\rho}{\epsilon\epsilon_0} \quad (1.2)$$

Where  $\rho$  is surface charge density,  $\epsilon$  is dielectric constant and  $\epsilon_0$  is known is permittivity of free space.

As the value of dielectric constant remains invariant in diffusive part but it varies inside the Stern layer.

Considering the problem for one dimension normal to solid and solution interface, the eqn (1.2) can be written as

$$\frac{d^2\phi}{dx^2} = -\frac{\rho}{\epsilon\epsilon_0} \quad (1.3)$$

The work done to bring the ion from infinite to the point where potential is finite will be  $z_i e \phi$ , where  $z_i$  is valence of  $i^{\text{th}}$  ion

Therefore, distribution of ions in this region is given by Boltzmann distribution function,

$$n_i = n_i^\infty e^{-\left(\frac{z_i e \phi}{k_B T}\right)} \quad (1.4)$$

The total charge density is given by,

$$\rho = \sum_i z_i e n_i \quad (1.5)$$

From eqn (1.4) and (1.5),

$$\rho = \sum_i z_i e n_i^\infty e^{-\left(\frac{z_i e \phi}{k_B T}\right)} \quad (1.6)$$

Therefore from eqn (1.3)

$$\frac{d^2 \phi}{dx^2} = -\frac{e}{\epsilon \epsilon_0} \sum_i z_i n_i^\infty e^{-\left(\frac{z_i e \phi}{k_B T}\right)} \quad (1.7)$$

This equation is known as Poisson-Boltzmann relation.

The solution of the above equation yields the value of the potential at distance x

The exponential term  $e^{-\left(\frac{z_i e \phi}{k_B T}\right)}$  can be expanded as

$$e^{-\left(\frac{z_i e \phi}{k_B T}\right)} = 1 - \left(\frac{z_i e \phi}{k_B T}\right) + \frac{1}{2!} \left(\frac{z_i e \phi}{k_B T}\right)^2 - \dots \quad (1.8)$$

If the potential is low, i.e.  $\left|\frac{z_i e \phi}{k_B T}\right| < 1$ , this is known as Debye-Huckel approximation, eqn (1.8)

becomes,

$$e^{-\left(\frac{z_i e \phi}{k_B T}\right)} \approx 1 - \left(\frac{z_i e \phi}{k_B T}\right) \quad (1.9)$$

Therefore the total charge density is given by,

$$\rho = \sum_i z_i e n_i^\infty \left[ 1 - \left(\frac{z_i e \phi}{k_B T}\right) \right] \quad (1.10)$$

In the bulk solution

$$\rho = \sum_i z_i e n_i^\infty = 0 \quad (\text{for electro neutrality}) \quad (1.11)$$

$$\text{Therefore, } \rho = -\frac{1}{k_B T} \sum_i z_i^2 e^2 n_i^\infty \phi \quad (1.12)$$

From eqn (1.7) becomes the linearized Poisson Boltzmann equation,

$$\frac{d^2 \phi}{dx^2} = \frac{1}{\epsilon \epsilon_0 k_B T} \sum_i z_i^2 e^2 n_i^\infty \phi \quad (1.13)$$

The Debye - Huckel parameter is given by k (unit in  $m^{-1}$ ) and

$$k^2 = \frac{e^2}{\epsilon \epsilon_0 k_B T} \sum_i z_i^2 n_i^\infty \quad (1.14)$$

Therefore eqn (1.13) becomes

$$\frac{d^2\varphi}{dx^2} = k^2 \varphi \quad (1.15)$$

On applying following boundary condition for above expression,

$$x \rightarrow d, \varphi \rightarrow \varphi_d \quad \text{and} \quad x \rightarrow \infty, \varphi \rightarrow 0$$

The solution of the eqn 1.15 is obtained as

$$\varphi = \varphi_d e^{[-k(x-d)]} \quad (1.16)$$

This is corresponding to exponentially decaying profile of potential with distance which is shown in Fig.1.11.

From the Debye-Huckel parameter Debye length also called double layer thickness for  $i^{\text{th}}$  ion is estimated which is denoted by  $k^{-1}$ , and is given by,

$$k^{-1} = \left( \frac{N_A e^2}{\epsilon \epsilon_0 k_B T} \sum_i z_i^2 c_i^\infty \right)^{-\frac{1}{2}} \quad (1.17)$$

Typically, for 0.1 M NaCl solution  $k^{-1} = 0.96$  nm while for 0.01 M NaCl it is = 3.04 nm. Thus, the double layer gets compressed in high ionic strength solution.

### 1.3.3 Hydrophobic Interaction

Biopolymers which have a hydrophobic group (the group does not interact with water molecule) when dissolved in aqueous medium form hydrophobic bond and such interaction are called hydrophobic interaction. These are long-range forces with the typical energy of 5-10 kJ/mol. Protein folding takes place in water when hydrophobes arrange to minimize water content. Hydrophobic molecules are non-polar and interact with non-polar solvents [8].

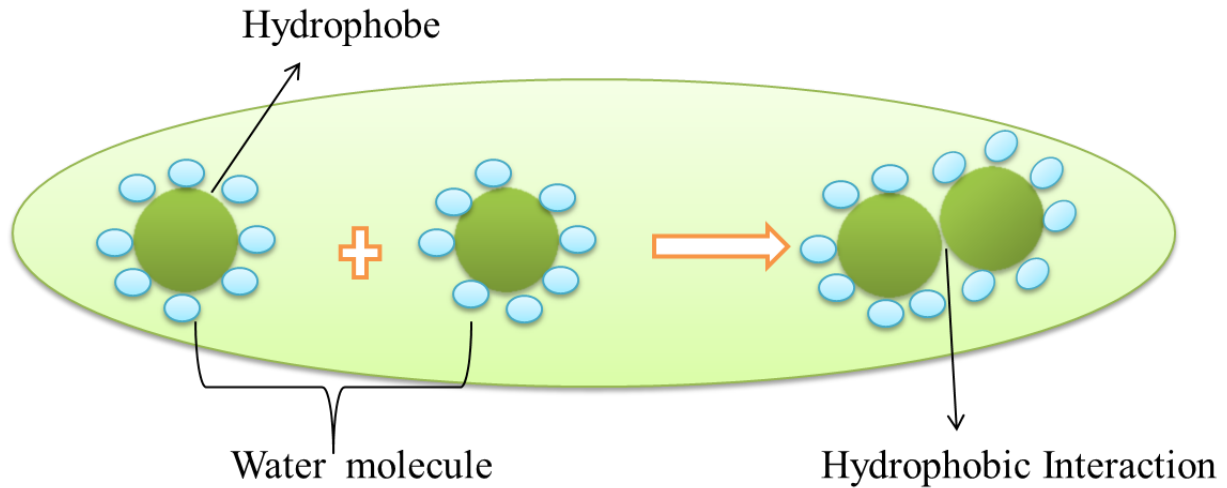


**Figure 1.12.** Hydrophobic interaction between two molecules

It is known that the water molecule is polar in nature and it forms a strong hydrogen bond with another water molecule. These interactions depend on temperature and the polarity of the medium. If temperature increases upto 60 °C its strength increases linearly. If the dielectric constant of the aqueous medium is low for example with mixing ethanol the hydrophobic interaction increases [9].

The potential defined for two interacting surfaces is given by the potential,

$$W(D) = -2\gamma H_y e^{\frac{-r}{D_H}} \quad (1.18)$$

Where  $\gamma$  interfacial surface tension,  $D_H$  is decay length for hydrophobic or hydrophilic interaction and  $H_y$  is known as hydration parameter (dimensionless).

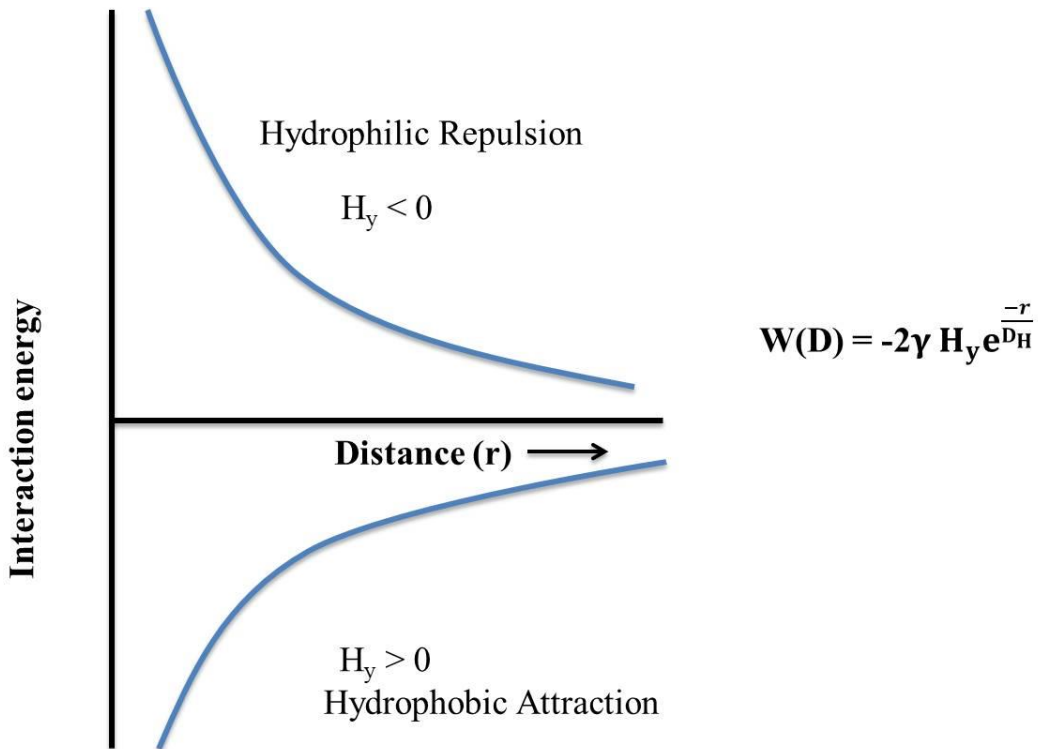


**Figure 1.13.** Interaction potential for hydrophobic interaction.

If  $H_y > 0$  is corresponding to interaction in between partially hydrophobic surfaces. The interaction between hydrophobic surface would be maximum when  $H_y = 1$  i.e. fully hydrophobic surfaces are interacting with each other. The interaction potential becomes positive when  $H_y < 0$  i.e. system is hydrophilic in nature which indicates hydrated interfacial surface [10].

### 1.3.4 van der Waals Interaction

van der Waals force arises between macromolecule with

- (i) two permanent dipoles
- (ii) induced and permanent dipole
- (iii) two induced dipoles

This force of dipole–dipole interaction is van der Waals interaction. This instantaneous potential dipole-induced dipole is called London dispersion forces [11, 12] which are very weak forces.

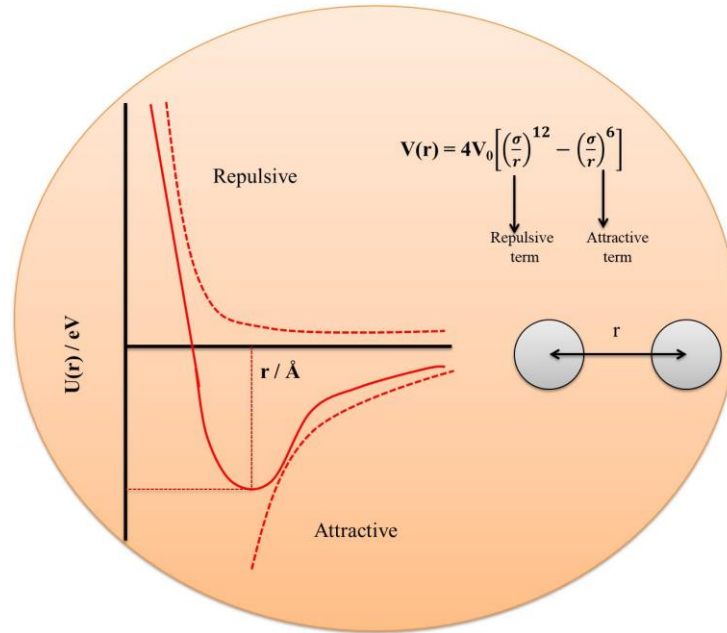


**Figure 1.14.** Lennard –Jones potentials between two particles

These interactions are attractive at longer the distances and repulsion takes place when distance becomes shorter which can be understood from the Pauli exclusion principle. The interaction potential is written as

$$V(r) = 4V_0 \left[ \left( \frac{\sigma}{r} \right)^{12} - \left( \frac{\sigma}{r} \right)^6 \right] \quad (1.19)$$

The Lennard –Jones potentials explains the interaction between two particles at distance  $r$ , where  $V_0$  is potential well depth,  $r$  is distance between two spheres (particles) and  $\sigma$  is radius of hard spheres (see Fig. 1.14).

### 1.3.5 Hydrogen Bonding

The interaction between H atom and the electronegative atom is called H-bonding. These are stronger in non-polar medium because of ionic nature of these electronegative atoms and H-atom. There are of two types intermolecular (H-bonding between same or different molecules) and intramolecular (H-bonding within same molecules). Examples are: Water molecule, O-nitrophenol

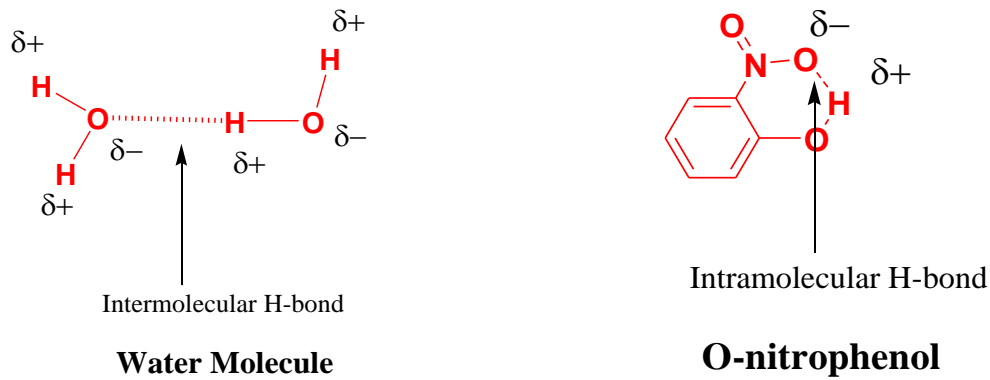


**Figure 1.15.** Intermolecular and Intramolecular H-bonding.

The potential term for H- bonding is given by,

$$U_{HB}(r) = \frac{A}{r^{12}} - \frac{C}{r^{10}} \quad (1.20)$$

Where r is the distance between donor and acceptor atoms in which H-bonding is taking place [13].

### 1.3.6 Surface Patch Binding

Surface patch binding is a specific kind of binding obtained between similarly charged biopolymers (negative-negative or positive-positive). In recent past years, polyelectrolyte and

protein interaction has been studied. It was observed that despite having the same surface charges under a specific pH condition protein and polyelectrolyte bind together. Therefore, it was found that there are positive patches on the protein surface which interact with a polyelectrolyte to form complexes [14-16]. For example surface patch binding occurs between two proteins Gelatin –BSA which have nearly same pI and zeta potential profile [17].

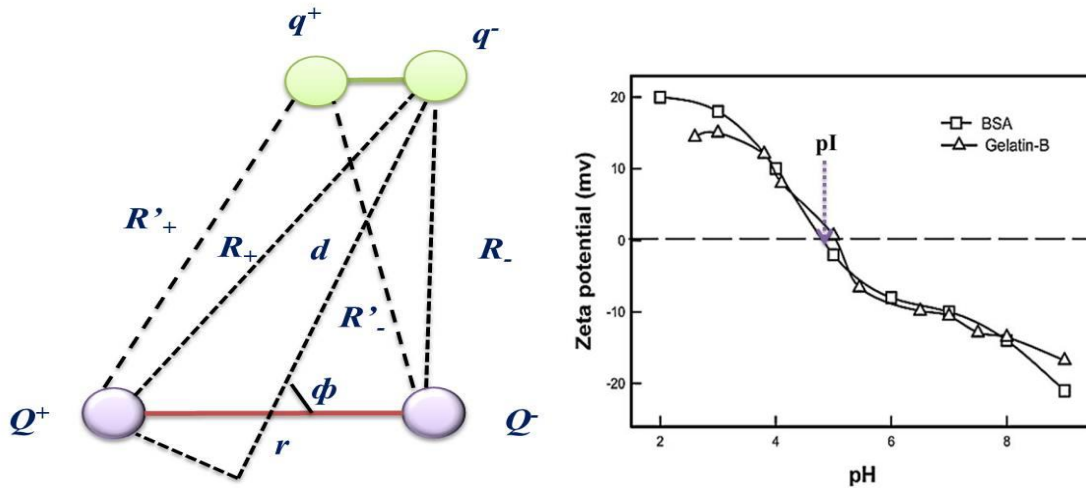


**Figure 1.16.** Interaction potential for protein polyelectrolyte system under surface patch binding, zeta potential profile for Gelatin and BSA protein taken from ref. [18].

The interaction potential for protein and polyelectrolyte is given as

$$U = \frac{q_-}{2\epsilon} \left[ \left\{ \frac{Q_- e^{-kR_+}}{R_+} \right\} e^{-kR_+} - \left\{ \frac{Q_+ e^{-kR_-}}{R_-} \right\} e^{-kR_-} \right] \quad (1.21)$$

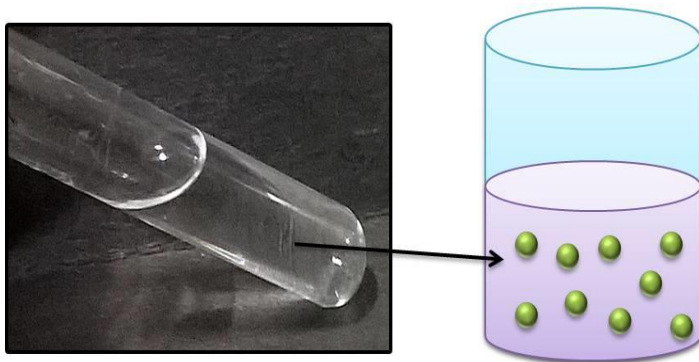
Where  $R_+ \approx R'_+ = d_+ (r/2) \cos\phi$ ,  $R_- \approx R'_- = d_- (r/2) \cos\phi$  and  $k^{-1}$  is Debye screening length.



## 1.4 Polymeric Phases

### 1.4.1 Sol

Solution in which the dispersed phase consists of particles having a polymeric structure are called sol phase.



**Sol Phase : Colloids are dispersed in the solution**

**Figure 1.17.** Physical and schematic image of sol phase.

### 1.4.2 Gel

Linking the polymer chain together leads to large branched structures. When this linking becomes so large that the branched polymer spans whole volume with high elastic modulus, an infinite polymer network grows which is called gel [19, 20].

It can be divided into two categories:

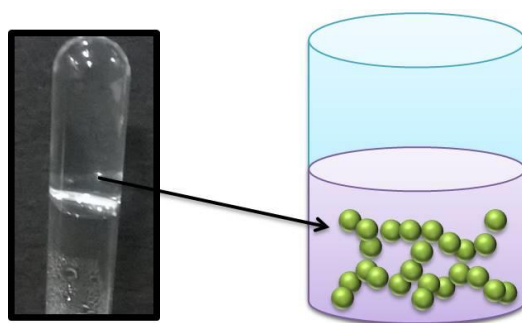
1. Physical gel:

Physical gels those are formed and stabilized via different non-covalent interactions like hydrogen bond, van der Waals force, hydrophobic and electrostatic interactions [21, 22]. These

give rise to are soft and fragile physical gels. Further, formation of colloidal gels cross-linked through secondary forces has been reported [23].

## 2. Chemical gel:

Gels formed by reaction (copolymerization, polycondensation etc) leads to the formation of branched or cross-linked networks made up of linear flexible chains attached by covalent bonds [24]. These gels are more rigid and stronger. e.g. silica, epoxy resin, rubber (vulcanized) based gels.



**Gel Phase : Colloidal gel formation**

**Figure 1.18.** Physical and schematic image of gel phase.

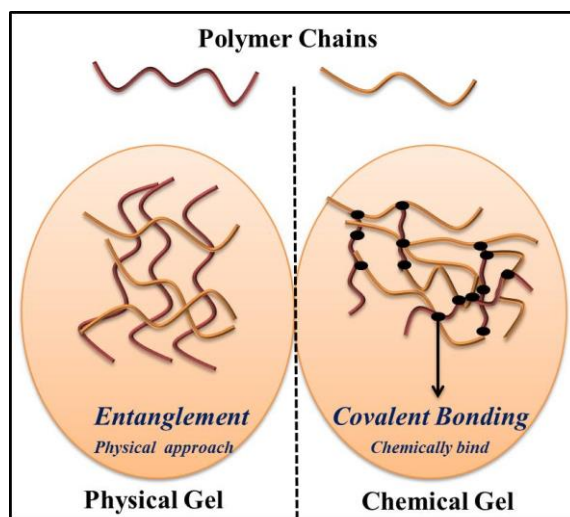


**Figure 1.19.** Schematic of chemical and physical gel.

### 1.4.3 Coacervation

Coacervation is defined as electrostatically-driven liquid-liquid phase partition, coming about from the arrangement of oppositely charged macro-ions mostly by electrostatic forces. It is assisted by intermolecular interaction between oppositely charged macromolecules. Phase separation is a unconstrained arrangement of two fluid phases, dense and rich within the polymer (called coacervate) and the other fluid with low polymer content (supernatant) [25, 26]. This whole process is known as coacervation. This phase separation takes place due to the interaction between complementary net charged molecules. This can be seen between various polyelectrolytes [27]. It can also be observed in polyelectrolytes-colloidal particles of opposite polarity. Some examples of complex coacervation are: Poly(dimethyldiallylammonium chloride)-BSA [28], gelatin-chitosan [29], gelatin-gelatin [30, 31], gelatin-agar [32, 33], gelatin – DNA [34-36], zein –DNA [37] etc.

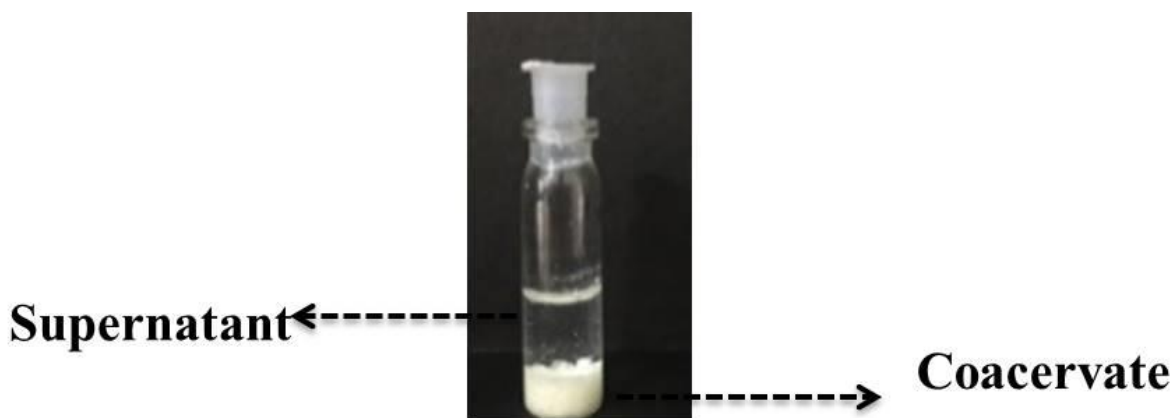


**Figure 1.20.** Physical image of phase separation during coacervation.

## 1.5. Biosensors

The biosensor is an analytical device which is used for analyte detection. In design, protein, antibody, enzyme, DNA and various nanomaterials etc. are used as the active materials which perform the signal detection. Then the signal conditioning circuit transmits these signals (by amplification) to the display device [38]. The signal transduction and processing unit can be a potentiometer, photometer, piezoelectric, thermometric or semiconductor devices etc. Signal conditioning circuit consists of amplifiers, filters, multiplexers, compressors and analog-to-digital converter etc.

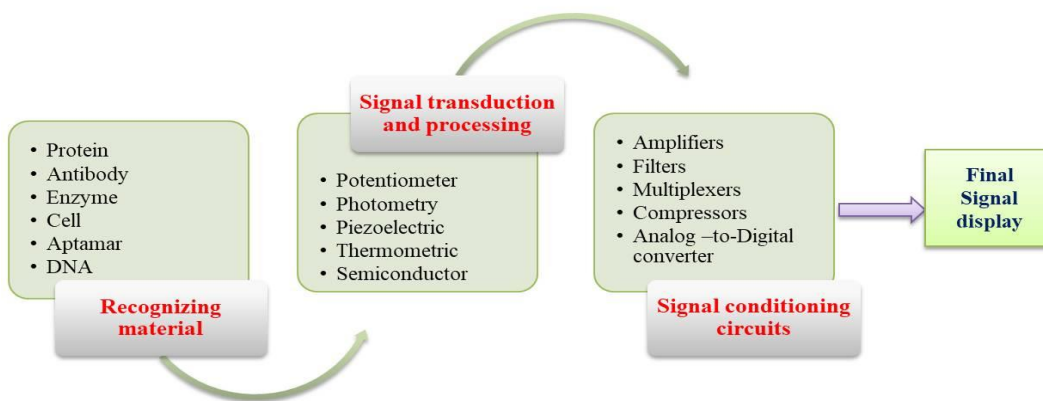


**Figure 1.21.** Working of Biosensor

Biosensors are also used as diagnostic medical devices. Affinity (antibody, DNA, aptamer, cell), catalytic (enzyme, microorganism, plant and animal tissue, cells) and biomimetic (synthetic binding and catalytic system) sensors are three categories of biosensors.

A good biosensor must depend on some of the following parameters such as:

1. **Linear range:** It works on a linear range of calibration curve which is corresponding to steady-state response versus the concentration of an analyte.

2. **Sensitivity:** It is decided from the slant of the calibration bend within the linear range.
3. **Limit of Detection:** The lowest detectable value of analyte which is known as a Limit of Detection (LOD).
4. **Precision and accuracy:** This is defined as the error and standard deviation of measurement from real value.
5. **Response time:** Response time is the time required to come to an equilibrium for 95% of the response
6. **Selectivity:** This is an ability to differentiate specific analyte from others.
7. **Stability:** Atmosphere humidity and temperature change
8. **Working lifetime:** Duty cycle must be large
9. **Reproducibility:** Data reliability must be large

## 1.6. Quantum dot

The variation in the dimension of the bulk material to lower dimension brings the adequate change in the characteristic properties of the material. In the low dimension material, there is confinement of electrons and holes generate the effective change in electrical, mechanical, magnetic and optical properties of the material.

**The low dimensional structure can be characterized by following:**

**Three dimensional (3-D) structure:** In 3-D structure there is no quantization in the motion of the particle i.e. particle can move freely in the three dimensions. Therefore electron and holes can move freely in the three dimensional space. i.e. nanoballs, nanoflowers and nanocone structures etc

**Two dimensional (2-D) structure:** In 2-D structure the quantization of the motion of the particle in 1-dimension and it can move freely in other 2- dimensions. Therefore electron and holes can move freely in the 2-dimension in conduction and. i.e. nanosheet, nanodisk and nanowall structures etc.

**One dimensional (1-D) structure:** In 1-D structure the quantization of the motion of the particle in 2-dimension and it can only move freely in other 1- dimension, i.e. nanotube, nanowire and nanoribbon structures etc.

**Zero dimensional (0-D) structure:** In 0-D structure the quantization of the motion of the particle in all 3-dimension and it cannot move freely. The motion of electron and holes are confined in all three directions with discrete energy levels. The typical size is 1-10 nm, i.e. quantum dot and nanodots etc.

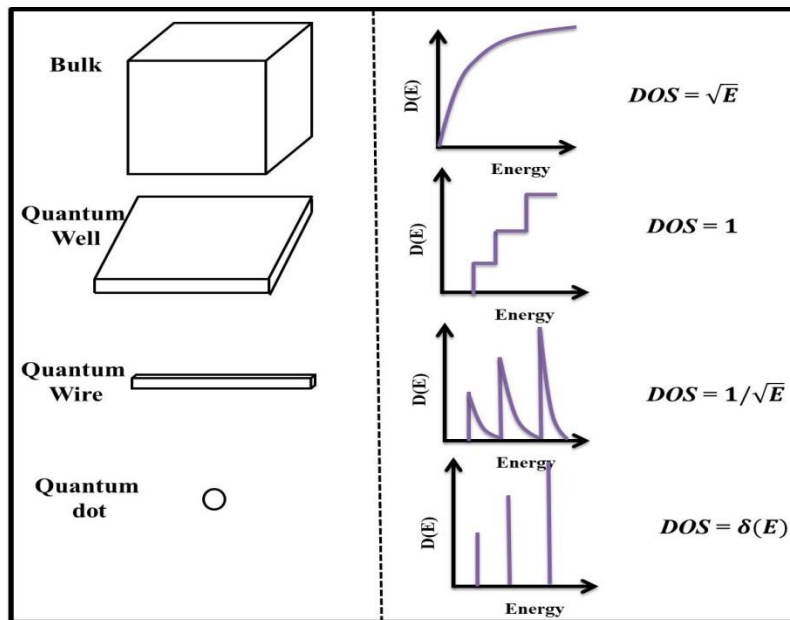


**Figure 1.22.** Dimension dependent structures and variation of there (DOS) density of state  $D(E)$  with energy  $E$ .

The density of state (DOS) is defined by the number of energy states available at any energy level that electrons are permitted to involve. As moving from bulk to 0-D there's a alter in the density of states, which is given by

$$DOS = \frac{dN}{dE} = \left(\frac{dN}{dk}\right) \left(\frac{dk}{dE}\right) \quad (1.22)$$

where  $k$  is wave vector,  $N$  is no of permitted electrons and  $E$  is energy of electrons.

To understand quantum dot or zero dimension shape it is required to solve Schrödinger equation for box potential. In a quantum dot, all 3-D are confined or quantum dot is localized in 3-D, and therefore degree of freedom are restricted.

Let us consider the potential in the quantum box is zero and infinite elsewhere,

$$V(x, y, z) = \begin{cases} 0, & \{0 < x < L_x\} \cap \{0 < y < L_y\} \cap \{0 < z < L_z\} \\ \infty, & \text{elsewhere} \end{cases} \quad (1.23)$$

Where  $L_x$ ,  $L_y$  and  $L_z$  is width, length and height of box potential

Therefore 3D Schrödinger equation for the box potential is given by,

$$-\frac{\hbar^2}{2m} \left( \frac{\partial^2}{\partial x^2} + \frac{\partial^2}{\partial y^2} + \frac{\partial^2}{\partial z^2} \right) \varphi(x, y, z) = E\varphi(x, y, z) \quad (1.24)$$

By solving this variable separation method, obtained eigen function is given as,

$$\varphi_{n_x, n_y, n_z}(x, y, z) = \sqrt{\frac{8}{L_x L_y L_z}} \sin\left(\frac{n_x \pi x}{L_x}\right) \sin\left(\frac{n_y \pi y}{L_y}\right) \sin\left(\frac{n_z \pi z}{L_z}\right) \quad (1.25)$$

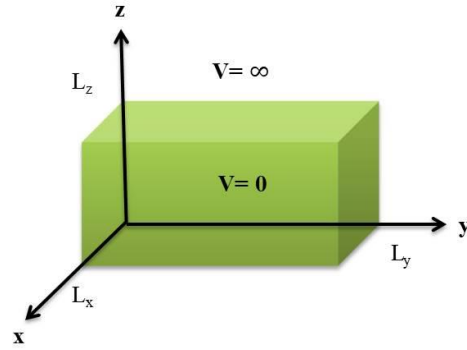


**Figure 1.23.** Quantum dot as a box potential

Where  $n_x$ ,  $n_y$  are  $n_z$  are the principal quantum number and have values 1,2,3,.....

Corresponding to above eigen function, energy is given by,

$$E_{n_x, n_y, n_z} = \frac{\hbar^2 \pi^2}{2m} \left[ \frac{n_x^2}{L_x^2} + \frac{n_y^2}{L_y^2} + \frac{n_z^2}{L_z^2} \right] \quad (1.26)$$

$$E_n = \frac{\hbar^2 \pi^2 n^2}{2mL^2} \quad (1.27)$$

Therefore this is total energy of the particle when it is localized in 3D which is corresponding to discrete energy levels for quantum dots.

These are semiconductor materials. The gap between valence band and a conduction band of the semiconductor is called band gap. The band gap of a quantum dot can be tunable by size which makes them useful for many electrical applications. Quantum confinement of quantum dot corresponding to 3D confinement of excitons (electron-hole pair). The quantum confinement takes place when the diameter of the particle approaches to de Broglie wavelength of electron in the conduction band. The band gap of quantum dot increases with the decrease in the size of a quantum dot. Therefore an optical property of quantum dot varies with size. The bigger quantum dot shows red shift and as the size of the quantum dot decreases it shows a blue



shift. Some examples of the quantum dot are MoS<sub>2</sub>, CdSe, CdTe and CdS etc. Quantum dots can be used in the Solar cell, a Light emitting diode (LED), Transistor, Sensor, bioimaging etc. (Table.1.1) [39].

**Table.1.1** different quantum dots size and application

Quantum dot	Size(nm)	Application	Reference
MoS <sub>2</sub>	3.3	Solar cell	[40]
Graphene	5.5	Neurotransmitter sensing	[41]
CdSe	4.8	LED	[42]
PbS	6.5	FET	[43]
CdTe	4.0	Bioimaging	[44]
ZnSe	2.5	Biomedical	[45]
Carbon dot	5.0	Bioimaging	[46]

### 1.7. Motivation of thesis

The main motivation of thesis is to study phase transition in biopolymer such as DNA based gels and to study the interaction of DNA to other protein like zein and quantum dots. The outline of the thesis is as follows

1. In chapter 2, we have discussed the materials and characterization techniques used in the thesis.

2. In chapter 3, we have studied the relaxation dynamics, viscoelastic and microscopic properties of DNA hydrogels, ionogels and gamma irradiated ionogels.
3. In chapter 4, we have studied the DNA-protein (zein) complex coacervation without and with salt medium.
4. In chapter 5, we have studied the electrochemical properties of DNA ionogel based urea sensor.
5. In chapter 6, concentration dependence of 1-octyl-3 methyl imidazolium ionic liquid based DNA gels are studied and used it to fabricate citric acid sensor.
6. In chapter 7, we have synthesized water soluble MoS<sub>2</sub> quantum dots and further MoS<sub>2</sub> crosslinked DNA hydrogels were studied by different techniques.
7. In chapter 8, we have synthesized water soluble DNA dots and studied their multifunctional properties.
8. In chapter 8, we have given the summary of whole work described in this thesis.

## 1.8 References

- [1] A.V. Dobrynin, R.H. Colby and M. Rubinstein, *J. Polymer Sci., Part B: Polymer Physics*, **42**, 3513 (2004).
- [2] J.L. Barrat and J.F. Joanny, *Theory of Polyelectrolyte solutions*, *Advances in Chemical Physics* (John Wiley & Sons, New York, 1995).
- [3] A. Harper and M. R. Anderson, *Sensors* **10**, 8248 (2010).
- [4] C. Barndon and J. Tooze, *Introduction to Protein Structure* (Garland Publishing, New York, London, 1991).
- [5] J. Guan, Y. Wang, S. Wu, Y. Li and J. Li, *Biomacromolecules* **18**, 4364 (2017).

- [6] R. Norel, F. Sheinerman, D. Petrey and B. Honig, *Protein Science* **10**, 2147 (2001).
- [7] Y. Cao, Y. Fang, K. Nishinari and G. O. Phillips, *Scientific Reports* **6**, 23739 (2016).
- [8] E. Dickinson, *Trends in Food Science & Technology* **9**, 347 (1998).
- [9] D. J. McClements, E. A. Decker, Y. Park, and J. Weiss, *Critical Reviews in Food Science and Nutrition* **49**, 577 (2009).
- [10] H. Stephen, Jr. Donaldson, A. Røyne, K. Kristiansen, M. V. Rapp, S. Das, M. A. Gebbie, D. W. Lee, P. Stock, M. Valtiner and J. Israelachvili, *Langmuir* **31**, 2051 (2015).
- [11] E.M. Lifshitz, *Soviet Phys. JETP*. **2**, 73 (1956).
- [12] I.D. Dzyaloshinskii, E.M. Lifshitz and L.P. Pitaevskii. *Soviet Phys. Usp.* **4**, 153 (1961).
- [13] B. R. Gelin, M. Karplus, *Biochemistry* **18**, 1256 (1979).
- [14] A. N. Gupta and H. B. Bohidar, *J. Phys. Chem. B* **111**, 10137 (2007).
- [15] Y. Xu, M. Mazzawi, K. Chen, L. Sun and P.L. Dubin, *Biomacromolecules* **12**, 1512 (2011).
- [16] K. Chen, Y. Xu, S. Rana, O.R. Miranda, P.L. Dubin, V.M. Rotello, L. Sun and X. Guo, *Biomacromolecules* **12**, 2552 (2011).
- [17] J. Pathak, K. Rawat and H. B. Bohidar, *RSC Adv.* **4**, 24710 (2014).
- [18] J. Pathak, K. Rawat and H. B. Bohidar, *RSC Adv.* **6**, 40123 (2016).
- [19] J. D. Ferry, *Viscoelastic Properties of Polymers* (New York: Wiley, 1980).
- [20] M. Rubinstein and R.H. Colby, *Polymer Physics* (Oxford University Press Inc., New York, 2003).
- [21] H. B. Bohidar and S. S. Jena, *J. Chem. Phys.* **98**, 8970 (1998).
- [22] F. Ikkai and M. Shibayama, *Phys. Rev. Lett.* **82**(24), 4946 (1999).
- [23] B. J. Park, J. P. Pantina and E. M. Furst, *Langmuir* **24**, 1686 (2008).

- [24] G. Deng, C. Tang, F. Li, H. Jiang and Y. Chen, *Macromolecules* **43**, 1191 (2010).
- [25] H. G. Bungenberg de Jong and H. R. Kruyt, *Colloid Science* (Elsevier Academic Press, New York, 1949).
- [26] E. Tsuchida and K. Abe, *Intermacromolecular Complexes* (Springer, Heidelberg, 1982).
- [27] J. M. Park, B. B. Muhoberac, P. L. Dubin and J. Xia, *Macromolecules* **25**, 290 (1992).
- [28] K. Kaibara, T. Okazaki, H. B. Bohidar and P. L. Dubin, *Biomacromolecules* **1**, 100 (2000).
- [29] A. Gupta and H. B. Bohidar, *J. Phys. Chem. B* **111**, 10137 (2007).
- [30] A. Tiwari, S. Bindal and H. B. Bohidar, *Biomacromols* **10**, 184 (2009).
- [31] D. J. Burgess, *J. Colloid Interface Sci.* **140**, 227 (1990).
- [32] S. S. Singh, V. K. Aswal and H. B. Bohidar, *Int. J. Biomacromols.* **41**, 301 (2007).
- [33] S. Boral and H. B. Bohidar, *J. Phys. Chem. B* **114**, 12027 (2010).
- [34] N. Arfin and H. B. Bohidar, *J. Phys. Chem. B* **116**(44), 13192 (2012).
- [35] N. Arfin, V. K. Aswal and H. B. Bohidar, *RSC Adv.* **4**(23), 11705 (2014).
- [36] K. Rawat, V. K. Aswal and H. B. Bohidar, *J. Phys. Chem. B* **116**(51), 14805 (2012).
- [37] P. K. Pandey, P. Kaushik, K. Rawat, V. K. Aswal and H. B. Bohidar, *Soft Matter* **13**, 6784 (2017).
- [38] P.R. Solanki, A. Kaushik, V.V. Agrawal and B.D. Malhotra, *NPG Asia Mater.* **3**(1), 17 (2011).
- [39] H. Y. Ramírez, J. Flórez and A. S. Camacho, *Phys. Chem. Chem. Phys.* **37**, 23938 (2015).
- [40] W. Xing, Y. Chen, X. Wang, L. Lv, X. Ouyang, Z. Ge and H. Huang, *ACS Appl. Mater. Interfaces* **8**, 26916 (2016).

- [41] S. Baluta, A. Lesiak and J. Cabaj, *Electroanalysis* **30**, 1781(2018).
- [42] H. S. Jang, H. Yang, S. W. Kim, J. Y. Han, S. G. Lee and D. Y. Jeon, *Adv. Mater* **20**, 2696 (2008).
- [43] V. Adinolfi, I. J. Kramer, A. J. Labelle, B. R. Sutherland, S. Hoogland and E. H. Sargent, *ACS Nano* **9**, 356 (2015).
- [44] Y. Zheng, S. Gao and J. Y. Ying, *Adv. Mater.* **19**, 376 (2007).
- [45] I. M. R. Moura, P. E. C. Filho, M. A. B. L. Seabra, G. Pereira, G. A.L. Pereira, A. Fontes and B. S. Santos, *Journal of Luminescence* **201**, 284 (2018).
- [46] L. Cao, X. Wang, M. J. Meziani, F. Lu, H. Wang, P. G. Luo, Y. Lin, B. A. Harruff, L. M. Veca, D. Murray, S.-Y. Xie and Y.-P. Sun, *J. Am. Chem. Soc.* **129**, 11318 (2007).

## CHAPTER-2

---

### Materials and Characterization Techniques

**Abstract:** In this chapter the materials and characterization techniques have been discussed for the achievement of present research. Scattering techniques such as light and neutron scattering was used to detect structural changes within the system. Viscoelastic properties of the system were probed by rheology and viscometry measurement. SEM, TEM, AFM and confocal were used for imaging purposes. Zeta potential, UV-vis, Fluorescence, FTIR and electrochemical analyzer were used for surface potential, absorbance, emission, functional group identification and electrochemical properties of the system.

#### 2.1 Materials

##### 2.1.1 DNA

Sodium salt, Deoxyribonucleic acid (DNA) from Salmon Testes (Cat. No. D1626) was purchased from Sigma Aldrich USA. It has ~2000 base pair and its molecular weight (MW) is 1300 kD [1]. The storage temperature is 2-8 °C. It is double strand DNA (ds DNA). DNA is a double helical structure which carries the genetic code.

In DNA single strand is made up of purine base (Adenine (A), Thymine (T), Guanine (G), and Cytosine (C) which is linked with deoxyribose sugar and phosphate group. Sperm cell obtained from salmon testes is a huge source of non-mammalian DNA. The isolation process is described in ref. [2]. The % G-C content in salmon testes DNA is 41.2 % with melting temperature of  $T_{\text{melt}} = 87.5$  °C in 0.15 M sodium chloride and 0.015 M sodium citrate [3].

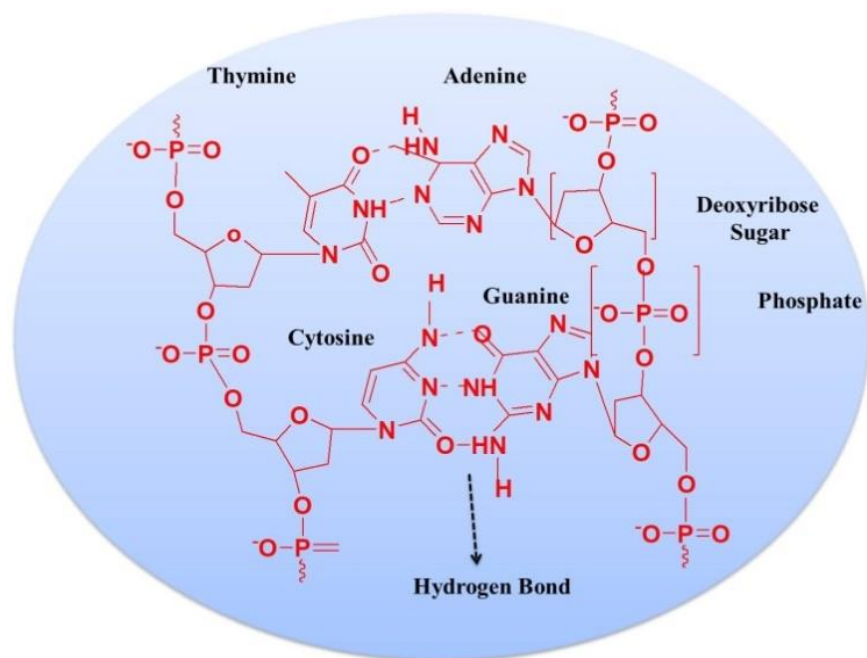


**Figure 2.1.** Chemical structure of DNA

### 2.1.2 Ionic Liquid

Ionic liquids (IL) are organic solvents which have melting point less than 100 °C. These are also known as organic salts. Ionic liquids are thermally stable. They have low vapor pressure, high electrical conductivity, non-flammable, non-volatile and thermally stable. These are also known as green solvents. They have organic cation (imidazolium, pyrrolidinium and/or quaternary ammonium head group) and anions (halides, nitrates, imides etc.). These are used in fuel cells, solar cells, sensors, batteries, coating etc. [4–8]. The alkene tail is predominantly hydrophobic and the length for water soluble ILs can vary between C<sub>2</sub> to C<sub>16</sub>.

Ionic liquid used in research are salts {1-ethyl-3-methylimidazolium chloride [C<sub>2</sub>mim][Cl]} and {1-octyl-3-methyl imidazolium chloride [C<sub>8</sub>mim][Cl]}. These both were brought from Sigma Aldrich, USA.

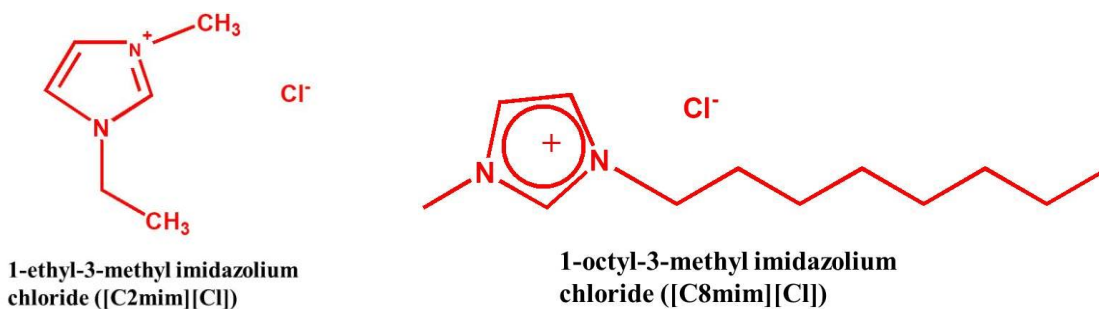


**Figure 2.2.** Chemical structure of Ionic liquid salts {1-ethyl-3-methylimidazolium chloride [C2mim][Cl]} and {1-octyl-3-methylimidazolium chloride [C8mim][Cl]}

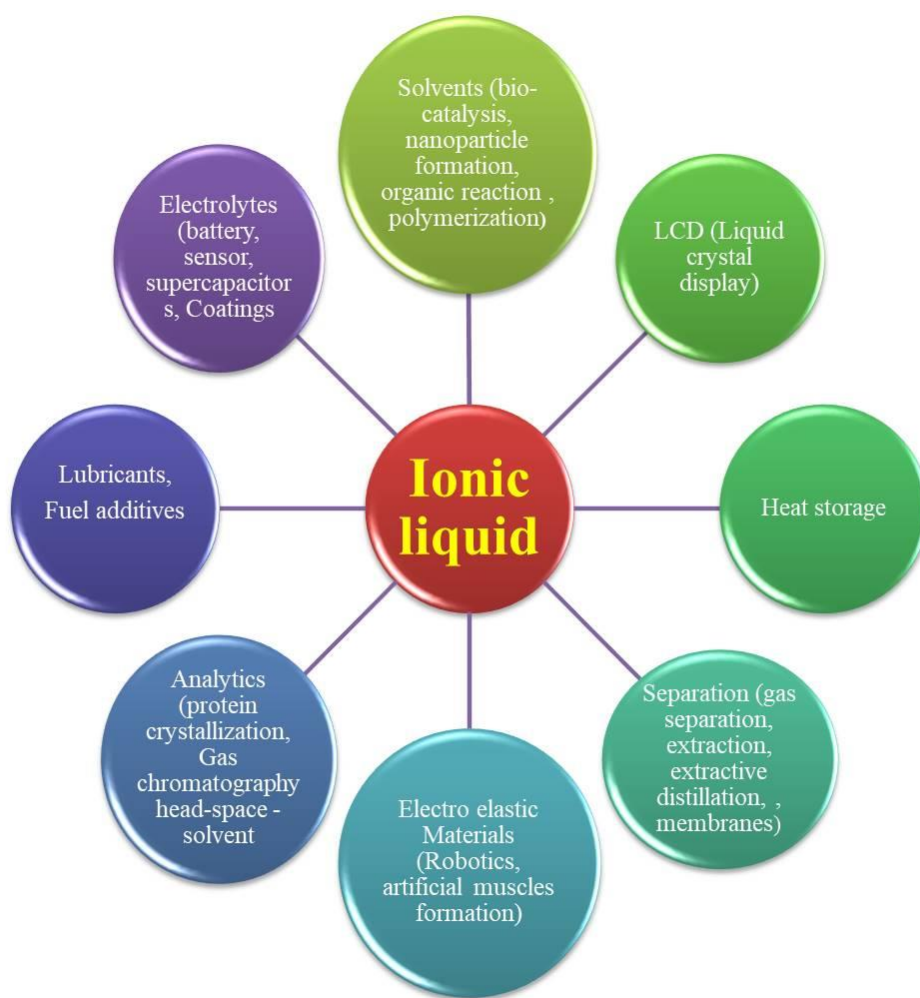


**Figure 2.3.** Ionic liquid uses in different areas of research



### 2.1.3 Protein- Zein

Zein is a prolamine protein which is extracted from maize. It is composed of three fractions,

1.  $\alpha$ - Zein: MW = 19 – 24kDa and 75-80 % of total protein content
2.  $\beta$ -Zein: MW = 17 – 18kDa and it contributes 10-15 % of total protein content
3.  $\gamma$ -Zein: MW = 27kDa and it contributes only 5-10 % of total protein content

It has large number of nonpolar groups such as leucine, alanine, phenylalanine and proline which are responsible for its insolubility in water i.e. hydrophobicity. Its tertiary structure facilitates it to form nanoparticle (80-200 nm) via liquid –liquid dispersion process [9–13]. In this work zein ( $\alpha$ ) was purchased from Sigma Aldrich, USA with MW=19kDa.

## 2.2 Characterization Techniques

### 2.2.1 Light Scattering

Light scattering is used to probe the random motion of the colloidal macromolecules such as polymers, protein, nanoparticle, micelles etc. Changes in the structure and dynamics occur during the phase transition from sol to gel phase. In this thesis, Photocor (USA) dynamic light scattering instrument was used. This instrument uses a He-Ne laser source emitting on 35 mW of power at 632.5 nm wavelength. Experiments were performed on multi tau mode with time scale of 8 decades spanning from 0.5  $\mu$ s to 10 s. The sample was loaded in optical quality cylindrical glass cell and inserted in scattering geometry. A PID temperature controller bath is attached to this geometry to regulate sample temperature from room temperature to 100  $^{\circ}$ C.

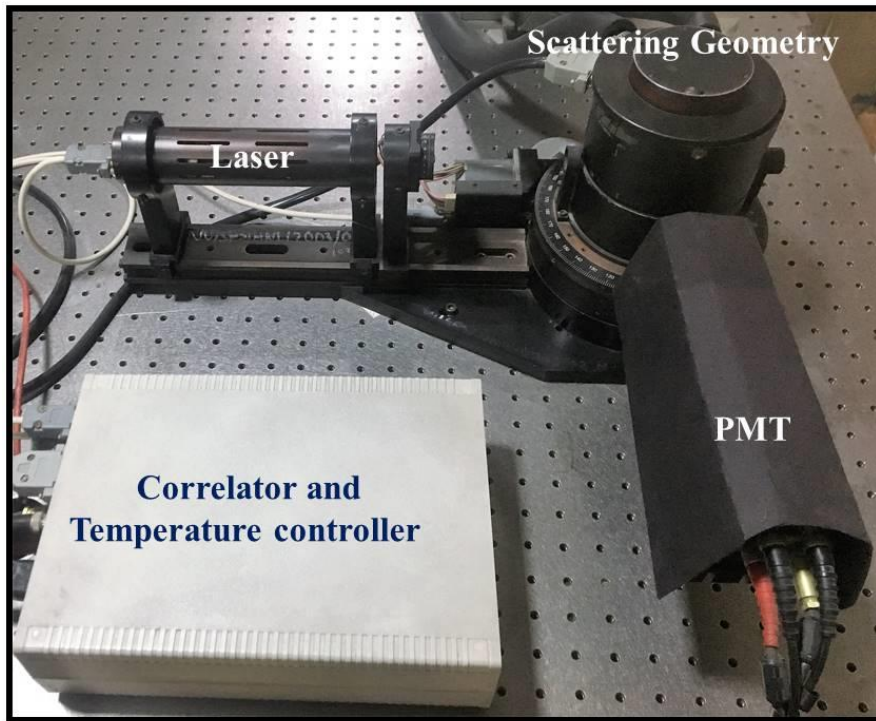


**Figure 2.4** Physical image of Photocor-light scattering instrument.

When this colloidal particle in the scattering geometry faces the electric field related to the light then there is induced local polarization within the molecules itself. These oscillating dipoles act as secondary source of radiation. This scattered light has various intensities depending upon the geometry and size of the scattering molecule. Therefore this scattering light contains plenty of information about the molecule. The size measured from dynamic light scattering is given by Stokes-Einstein relation which for a spherical particle is given by [14]

$$R_h = \frac{kT}{6\pi\eta_0 D} \quad (2.1)$$

Where  $R_h$  is hydrodynamic radius,  $D$  is translational diffusion coefficient,  $k_B$  is Boltzmann constant and  $\eta_0$  is solvent viscosity. If scattering particle is small in size then scattered intensity is less and if particle size is large then scattering intensity will be high.

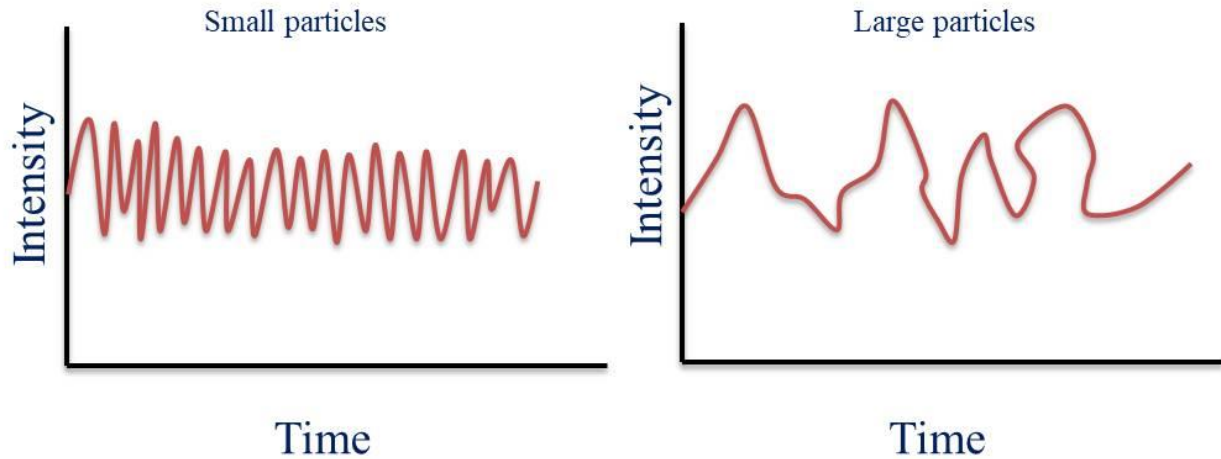


**Figure 2.5.** Intensity scattering profile for small and large particles

### Light Scattering Concept

When electromagnetic wave is incident on atom then energy and momentum of incident and scattering light changes. In the case of quasi-elastic scattering energy is nearly equal to incident energy i.e.

$$E_{\text{scattering}} = E_{\text{incident}} = \hbar\omega \quad (2.2)$$

Let incident and scattered light be denoted by wave vector  $\vec{k}_i$  and  $\vec{k}_s$  respectively. If refractive index of the medium is  $n$ , and  $\theta$  is the angle between  $\vec{k}_i$  and  $\vec{k}_s$ . Therefore, for the quasi-elastic scattering

$$|\vec{k}_i| = |\vec{k}_s| = \frac{2n\pi}{\lambda} \quad (2.3)$$

From above Fig. 2.6 the resultant wave vector,

$$\vec{k} = (\vec{k}_s - \vec{k}_i) \quad (2.4)$$

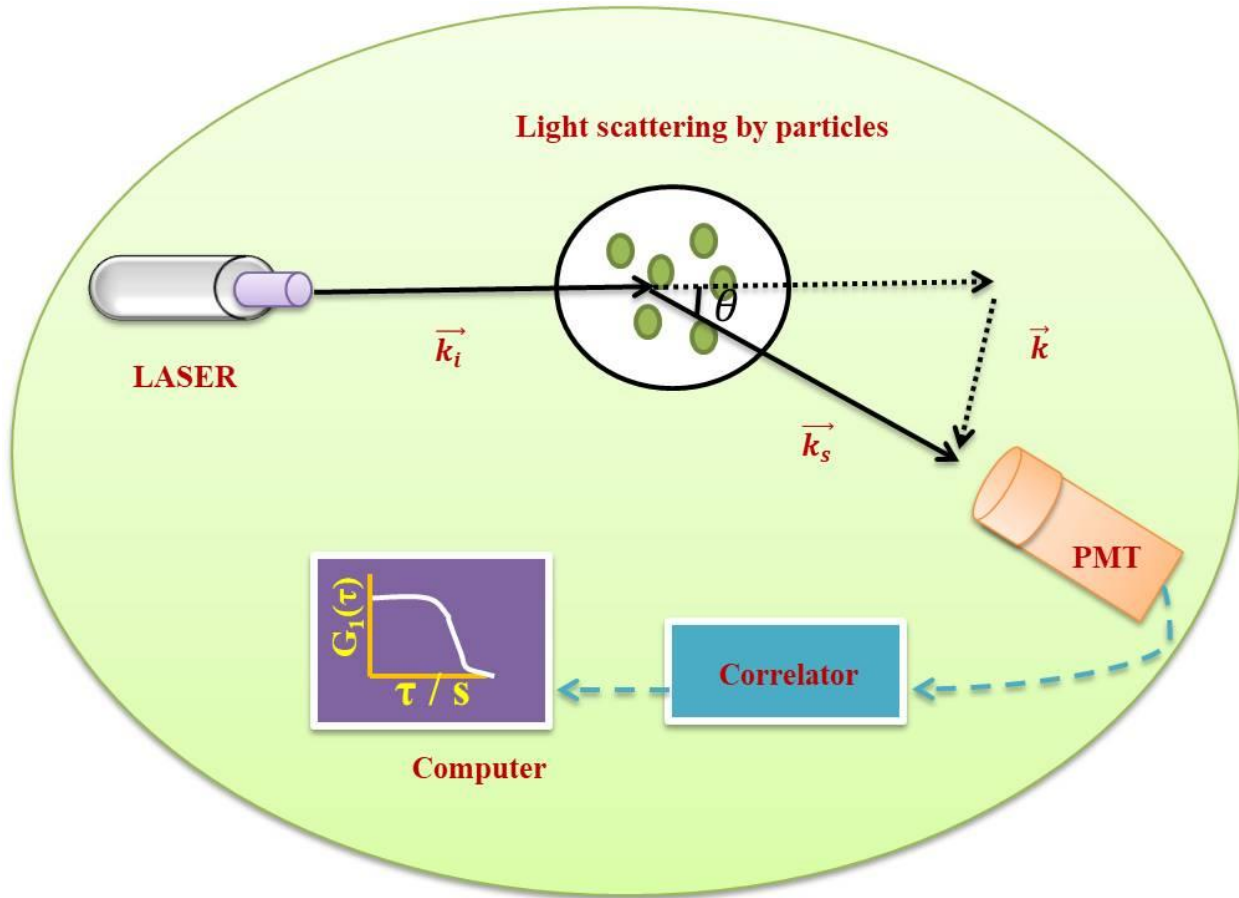


**Figure 2.6.** Schematic diagram for light scattering

Using cosine law on the triangle shown in Fig. 2.6

$$k^2 = |\vec{k}_s - \vec{k}_i|^2 \quad (2.5)$$

$$k^2 = k_s^2 + k_i^2 - 2 \vec{k}_s \cdot \vec{k}_i \quad (2.6)$$

$$k^2 = k_s^2 + k_i^2 - 2k_s^2 \cos \theta \quad (2.7)$$

$$k = \frac{4\pi n}{\lambda} \sin \frac{\theta}{2} \quad (2.8)$$

This is also known as Bragg condition which explains wave vector component of fluctuation that is corresponding to scattering at an angle  $\theta$ .

The random or Brownian motion of the particle is measured by light scattering. These scattering intensities have different intensity pattern corresponding to random motion of particles in the solution. Therefore the average intensity for the system is given as,

$$\langle I(t) \rangle = \lim_{T \rightarrow \infty} \frac{1}{T} \int_0^T I(t) dt \quad (2.9)$$

If the process is stochastic, the intensity autocorrelation [15,16] will be

$$\langle I(t)I(t + \tau) \rangle = \lim_{T \rightarrow \infty} \frac{1}{T} \int_0^T I(t)I(t + \tau) dt \quad (2.10)$$

In electric field correlation function is defined as

$$g_2(\tau) = \frac{\langle E_s(t)E_s^*(t+\tau) \rangle}{\langle |E_s(t)|^2 \rangle} \quad (2.11)$$

Similarly, intensity correlation function is given by

$$g_2(\tau) = \frac{\langle E_s(t) E_s^*(t) E_s(t+\tau) E_s^*(t+\tau) \rangle}{|\langle |E_s(t)|^2 \rangle|^2} = \frac{\langle I(t)I(t+\tau) \rangle}{\langle I \rangle^2} \quad (2.12)$$

For isotropic medium scattered field is a stationary Gaussian process which yields the Siegert relation [17]

$$g_2(\tau) = 1 + |g_1(\tau)|^2 \quad (2.13)$$

General form of this relation is given by

$$g_2(\tau) = C_1 + C_2 |g_1(\tau)|^2 \quad (2.14)$$

Here  $C_1$  and  $C_2$  are constants if  $g_2(\tau)|_{z \rightarrow \infty}$ ,  $C_1$  = baseline and  $C_2$  is related to the coherence area factor with  $C_2/C_1$  is equivalent to signal to noise ratio, S/N ratio which is  $0 \leq \frac{S}{N} \leq 1$

Isotopic medium has only single relaxation mode for which field correlation can be given as

$$g_1(\tau) = e^{-\gamma\tau} \quad (2.15)$$

Here  $\gamma^{-1}$  is relaxation time of the particle in the solution corresponding to this diffusion coefficient is written as,

$$D = \frac{\gamma}{k^2} \quad (2.16)$$

This signifies the transport properties of the solute particle under Brownian motion.

### **Ergodic and Non ergodic Phase**

For the ergodic system or random process, time average is equal to ensemble average. Sol phase of any system is an ergodic state because of the random motion of the solute particles in the solution. For the gel phase the motion of particles is restricted i.e. scattering centers are localized near the mean position of the particle which is corresponding to restricted Brownian motion. Such system is known as non-ergodic system. For non-ergodic system Siegert relation is not valid. For such system the relation is written as [18]

$$g_2(\tau) = 1 + \beta' [2\chi(1 - \chi)g_1(\tau) + \chi^2(|g_1(\tau)|^2)] \quad (2.17)$$

Here  $\beta'$  is called coherence factor and  $\beta'_{\max} = 1$  and sometime known as S/N ratio.

$\chi$  is an ergodicity parameter (heterodyne parameter) which lies between 0 and 1.

If  $\chi = 1$ , then the system is ergodic in nature as in the case of sol phase for which Siegert relation holds good. For the motion restricted phase  $\chi < 1$  and  $g_2(\tau)$  depends only on  $2\chi(1 - \chi)$  term, therefore we have

$$g_2(\tau) \approx \frac{[g_2(\tau)-1]}{[2\beta'\chi(1-\chi)]} \quad (2.18)$$

Intercept calculated from  $[g_2(\tau) - 1]$  vs  $\tau$  at  $\tau \rightarrow 0$  yields  $\beta' 2\chi(1 - \chi)$  and  $\chi$  can be estimated.

Alternatively it can also be calculated from  $[g_2(\tau) - 1]$  vs  $\tau$  correlation height profile [19]

$$\chi = \lim_{t \rightarrow 0} g_2(\tau)|_{t \rightarrow 0} - \lim_{t \rightarrow \infty} g_1(\tau)|_{t \rightarrow \infty} \quad (2.19)$$

### 2.2.2 Small Angle Neutron Scattering

To probe microscopic structure small angle neutron scattering (SANS) and small angle X-ray techniques are utilized. In SANS is an elastic neutron scattering in which neutrons (wave length~ 0.5 nm) are scattered at small angle ( $1-10^0$ ) to study the unknown microscopic structure of the system [20]. As neutrons have magnetic moment and it is sensitive for isotopes in scattering, therefore it has advantage over small angle X-ray scattering. In this thesis, we have performed SANS at Bhabha Atomic Research Centre (BARC), Mumbai and Paul Scherrer Institute (PSI), Switzerland. There are various sources which generate neutrons such as spallation, nuclear reactors, radioisotopes, photo neutron and accelerator sources.

In BARC (Mumbai) SANS measurement was accomplished on spectrometer located at G.T. laboratory. Dhruva reactor is used as source for the neutrons. The wave vector ( $q$ ) range is  $0.18$  to  $3.0 \text{ nm}^{-1}$ . The neutron was passed through 2 mm thick and 0.7 ml quartz cell carrying the sample. The intensity  $I(q)$  vs wave vector ( $q$ ) correlation was obtained finally which carries microscopic information of the sample.

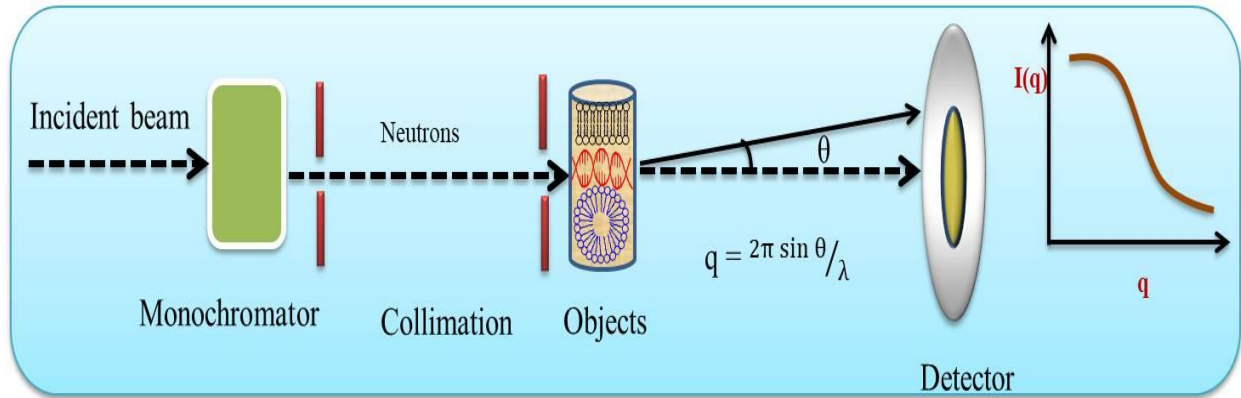


**Figure 2.7.** Schematic diagram for small angle neutron scattering

SANS setup is combination of three units,

- (1) Monochromator: Neutron beam produced from neutron source (flux  $\sim 10^{14} \text{ cm}^{-2}$ ) pass through monochromator to generate monochromatic wave with the resolution wave length 5 to 15 %.
- (2) Collimator: High collimation ( $0.5^\circ <$ ) is used in SANS. Collimator narrows or align the neutron beam (few meter) in particular direction.
- (3) Detector: Position Sensitive Detector (PSD) detect the scattered neutrons from the object or sample.

SANS-I facility of PSI (Switzerland) was also used for some of the measurements. The wavelength of neutron was  $8 \text{ \AA}$  with a resolution of 10%. The scattered neutrons from the samples were detected by using a large ( $96 \times 96 \text{ cm}^2$ ) area  $^3\text{He}$  detector. All the samples (2 mm thick and 0.7 ml quartz cell) were measured at two sample-to-detector distances of 2 and 8 m to cover a  $q$  range of  $0.07 - 2.5 \text{ nm}^{-1}$ . All the samples were prepared on heavy water for good resolution.



## Theory of neutron scattering

Neutron scattering involve a techniques to measure microscopic structure of soft materials. It's the techniques in with neutron emitted from source interact with target which is required to study. As scattering angle of such interaction are very small so referred as small angle scattering. Therefore sans scattering wave vector  $q$  is given as [20],

$$q = \left(\frac{4\pi}{\lambda}\right) \sin \theta/2 \quad (2.20)$$

Where  $q$  is wave vector,  $\theta$  is scattering angle and  $\lambda$  is wave length of incident neutron beam

The scattering intensity is given as [21]

$$I(q) = P(q)S(q)\phi \quad (2.21)$$

Where  $P(q)$  is known as form factor,  $S(q)$  is structure factor and  $\phi$  is known as density of particles.

- (1) Form factor: Form factor is deal with each scattered particle (shape and size) and corresponding to nuclear density. It can be defined as

$$P(q) = \langle |F(q)|^2 \rangle \quad (2.22)$$

Where

$$F(q) = \oint (\rho - \rho_0) e^{iqr} dV, \quad (2.23)$$

Here,  $\rho$  is density of scattering length

- (2) Structure factor: It is corresponding to spatial distribution of center of mass and defined as

$$S(q) = \langle \sum e^{iq(r_a - r_b)} \rangle, \quad (2.24)$$

where  $r_a - r_b$  is position vector of particle inside the material.

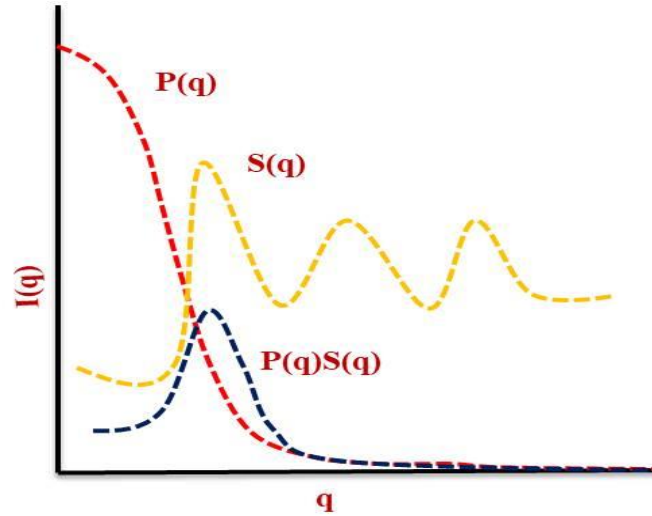


**Figure 2.8** Plot for form factor  $P(q)$ , structure factor  $S(q)$  and scattering intensity.

For dilute medium  $S(q)$  taken as 1 (no inter particle interference)

Hence, 
$$I(q) = P(q)\phi \quad (2.25)$$

For small  $q$  regime  $qR_g < 1$ , where  $R_g$  denotes the radius of gyration and form factor decays exponentially which is written as [22]

$$P(q) = \exp\left(-\frac{q^2 R_g^2}{3}\right) \quad (2.26)$$

This approximation is known as Guinier approximation which yields the form of scattering particles i.e. shape and size.

Mean field theory explains that for low wave vector  $q$  structure factor corresponding to correlation length (mass size) can be estimated by [23],

$$S(q) = \frac{S(0)}{1 + \xi^2 q^2} \text{ if } \xi q \ll 1 \quad (2.27)$$

This is Ornstein-Zernike (O-Z) function, which gives the information about mass size,  $\xi$ .

Small angle X-ray (SAXS) experiment was performed on a Anton Paar SAXSpace instrument (USA). This instrument uses line collimated sealed tube as X-ray source (Cu-K $\alpha$ ) which operates at 40 kV, 50 mA. 2D CCD (pixel size 24 micron) was used to monitor scattering

intensity in the transmission mode geometry, and the span for scattering wave vector  $q$  ( $=4\pi/\lambda \sin(\theta/2)$ ,  $\lambda$  is X-ray wavelength and  $\theta$  is scattering angle) ranged from 0.01 to  $0.65 \text{ \AA}^{-1}$ .

### 2.2.3 Rheology

A material can have two properties elasticity and viscosity. Elasticity is defined as an ability of any material to store energy in the form of deformation. Viscosity corresponds to resistance of flow and in which dissipation of deformational energy during flow. Therefore any material can show either elastic or viscous behavior. It is known as viscoelastic behavior of the material. Therefore viscoelastic properties of materials are studied by Rheology [24]. Force per unit area or deformation force defines the stress. Strain on material is expressed as displacement of sample after deformation.

Rheology measurement was done on AR-500 stress controlled rheometer manufactured by T.A. instruments, UK. In rheometer there are two kind of geometries are used cone- plate with  $2^\circ$  angle and plate of 20, 40 and 60 mm diameter and parallel-plate  $0^\circ$  angle and 20, 40 and 60 mm plate diameter.



**Figure 2.9** Physical image of AR-500 rheometer.

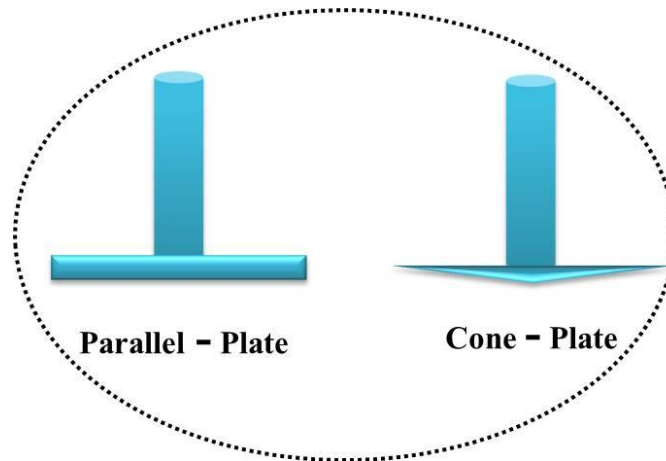


**Figure 2.10** Sketch for parallel-plate and cone-plate geometry.

### **Working Principle**

Rheometer can have two approaches [25,26],

1. Controlled stress: Strain rate is measured by applying the stress to the sample.
2. Controlled rate: Stress is generated by applying the strain rate to the sample.

Mechanical components of rheometer such as air bearing gives support to drive shaft and geometry. Geometry produces small stress on the sample and further this response from sample is measured by the sensor. Stress from instrument is controlled by controlled torque motor and other internal electronics and the stress applied on sample by sensor which measures the displacement. Optical encoder is quite sensitive to measure wide range of angular deflection. For temperature controlled measurement peltier plate was also used. In peltier plate for cooling, external water supply was connected.

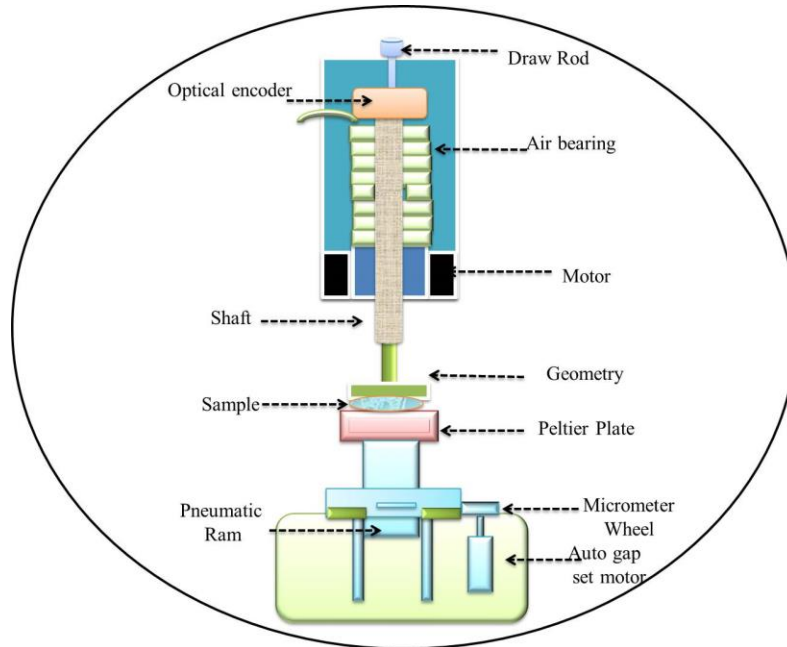


**Figure 2.11** Diagram of rheometer

## Operational Modes

### (1) Flow mode of operation

In flow mode of operation study of deformation is carried out at constant frequency. On the basis of flow there are three types of fluids

- (a) Newtonian
- (b) Time independent non-Newtonian fluid
- (c) Time dependent non-Newtonian fluid

In Newtonian fluid shear viscosity does not vary with deformation. If the fluid viscosity is shear rate dependent and does not depend on time of shear, it is known as non-Newtonian fluid with time independent. In such fluid shear thinning or thickening take place. In the shear thinning viscosity of fluid decreases with enhancement in shear rate. Shear thickening occurs if

both viscosity and shear rate increases simultaneously. If the fluid viscosity is not only depend on shear rate but also dependent on shear time is known as non-Newtonian fluid with time dependent. In such fluid thixotropy and rheopexy take place [27]. In thixotropy, on applying constant shear rate or stress viscosity of material decreases with time and it recovers gradually occurs while removing shear or stress rate. In rheopexy viscosity increases with time if same thing happens.

### (1) Oscillatory test

#### Frequency sweep measurement

In frequency sweep measurement (at fix Temperature) at varying frequency martial response is measured while keeping stress or strain constant. Storage or elastic modulus  $G'$ , loss modulus  $G''$  (viscous modulus) and phase angle  $\delta$  is plotted with varying frequency range ( $\omega$ ) (typically for gel, 0.1 to 100 rad  $s^{-1}$ ). If  $G' > G''$  them it is corresponding to elastic properties of materials such as for gel system [28].

For oscillatory strain on the sample is given by

$$\gamma(t) = \gamma_0 \cos(\omega t) \quad (2.28)$$

and the corresponding stress is given as

$$\sigma(t) = \sigma_0 \cos(\omega t + \delta) \quad (2.29)$$

If the material act as an ideal elastic material according to Hook's Law stress is proportional to the amplitude of strain and both are in same phase.

Therefore,

$$\sigma(t) = G\gamma_0 \cos(\omega t) \quad (2.30)$$

Where  $G$  is known as shear modulus

If the material act as an ideal fluid material according to Newton's Law stress is proportional to the derivative (rate) of strain and stress lead strain by  $\pi/2$  (out of phase).

$$\sigma(t) = \eta\omega\gamma_0 \cos(\omega t + \frac{\pi}{2}) \quad (2.31)$$

Where  $\eta$  is known as viscosity

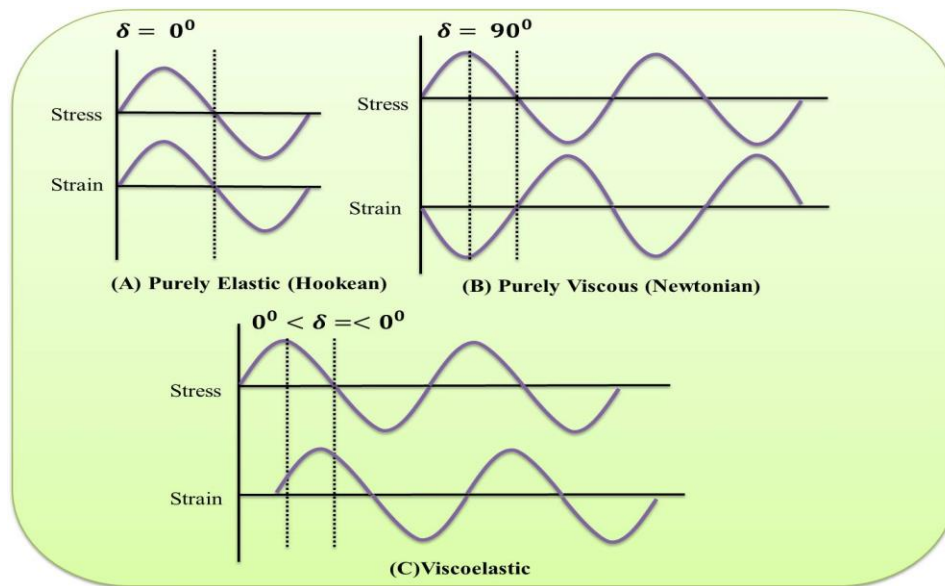


**Figure 2.12** Difference between elastic, viscous and viscoelastic material

Therefore, for viscoelastic material there is shift in phase between stress and strain. The stress for viscoelastic material has two component (in phase) elastic ( $\sigma'$ ) and (out of phase) viscous stress ( $\sigma''$ ) with strain.

Hence,

$$\sigma(t) = \frac{\sigma_0 \cos(\delta)}{\gamma_0} \gamma_0 \cos(\omega t) + \frac{\sigma_0 \sin \delta}{\gamma_0} \gamma_0 \sin(\omega t) \quad (2.32)$$

$$G' = \frac{\sigma_0 \cos(\delta)}{\gamma_0} \quad (2.33)$$

$$G'' = \frac{\sigma_0 \sin \delta}{\gamma_0} \quad (2.34)$$

Therefore, total deformation is measured by complex modulus

$$G^* = G' + iG'' \quad (2.35)$$

$G'$  denotes to elasticity of material which is corresponding to ability of energy storage by material and  $G''$  denotes to viscous nature of material which is corresponding to loss of energy as heat from material. Material damping due to vibration or sound is given by

$$\tan \delta = \frac{G''}{G'} \quad (2.36)$$

$\tan \delta$  should be less than 1 for viscoelastic materials like gel.

### Temperature Sweep measurement

In temperature sweep process storage ( $G'$ ) and loss modulus ( $G''$ ) is measured corresponding to temperature at a fixed frequency. Here transition temperature of viscoelastic material is probed. This transition temperature is also known as melting temperature.

#### 2.2.4 Viscometer

Viscosity measurement was performed on a SV-10, Sine wave vibro viscometer. It consists of two plates which vibrate at 30 Hz frequency and the amplitude of these was uniformly maintained via feedback electric current. The viscosity of the sample corresponds to uniform amplitude produced by electric current derived through vibrating plates at constant frequency.



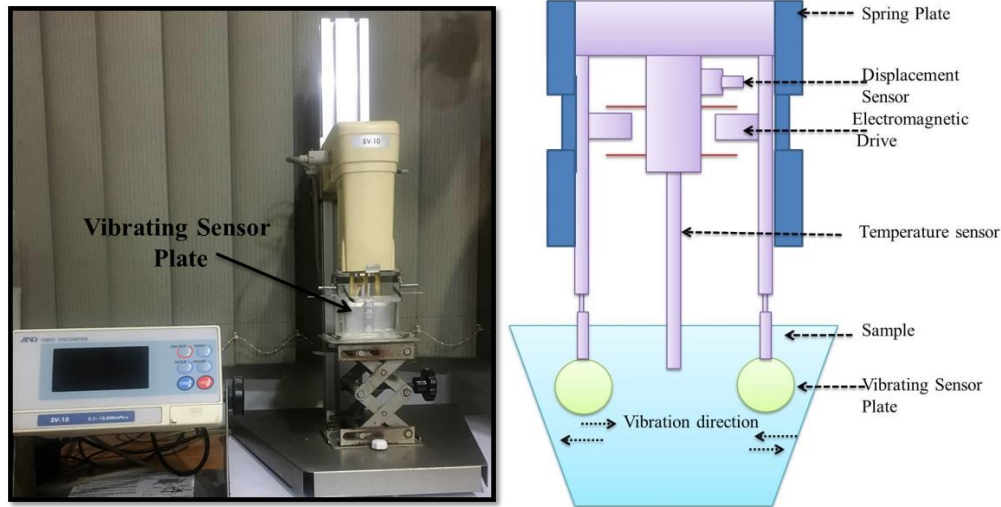


**Figure 2.13** Physical image of vibro viscometer and working sketch of visometer.

### 2.2.5 Electrophoresis

The charged particles that are mobile under electric field are the processed through what is known as Electrophoresis. When electric field is applied these charge particles move with velocity corresponding to this potential is measured by Zeta potentiometer. In biopolymers with change in pH effective charge develops. Total charge on the particles occurs from the ionization which has effect on the nearby interfacial regions of these charge particles. Near this region opposite charged particles are attached to counter ions (Stern layer). Moving away from this region counter ions and some other same polarity (co-ions) ions are distributed because of motion of solvent molecules thermally. This region is known as Shear plane (Fig. 2.14). The potential on the surface of shear plane is known as zeta potential [29].

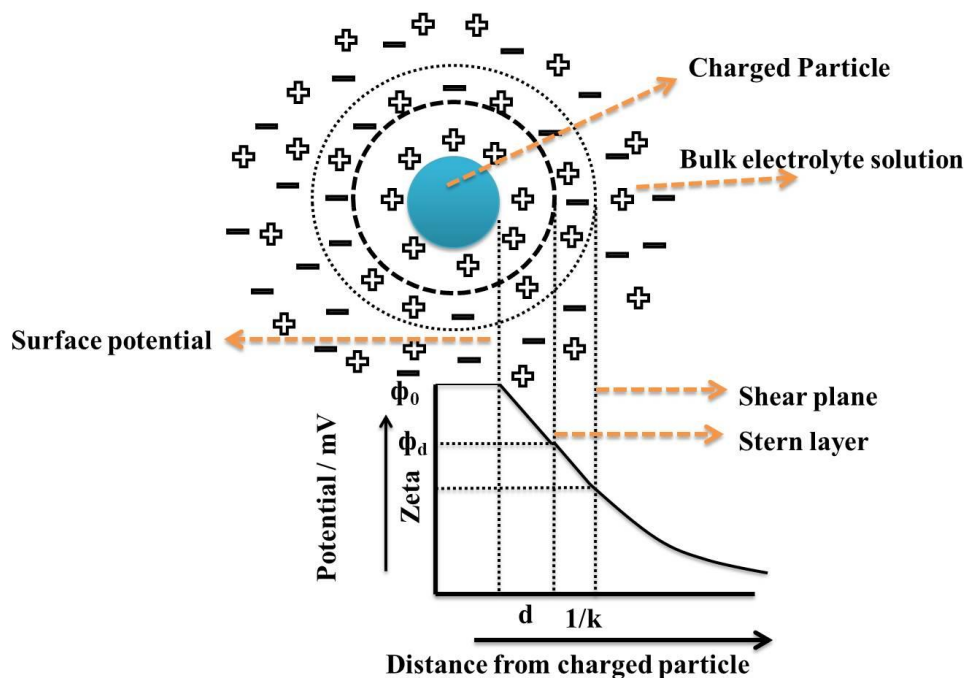


**Figure 2.14** Plot for double layer showing various potentials.

The Zeta potential measurement was performed on ZC-2000, Microtec instrument, Japan.

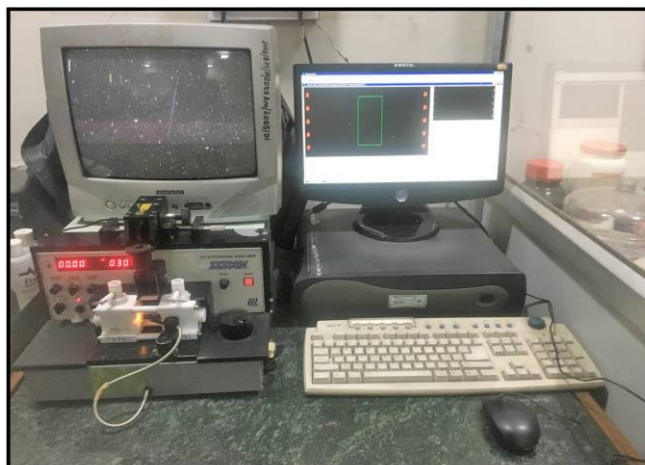


**Figure 2.15** Physical image of Zeta potentiometer.

## 2.2.6 FTIR

Fourier transform infrared spectroscopy is used to identify certain function group in the unknown molecule. This is a vibrational spectroscopic technique. When any molecule exposed to

a particular wave length of light due to rotation in the chemical bond, asymmetric stretching or vibration in the molecule it generates a resonant spectrum for the molecule [30].

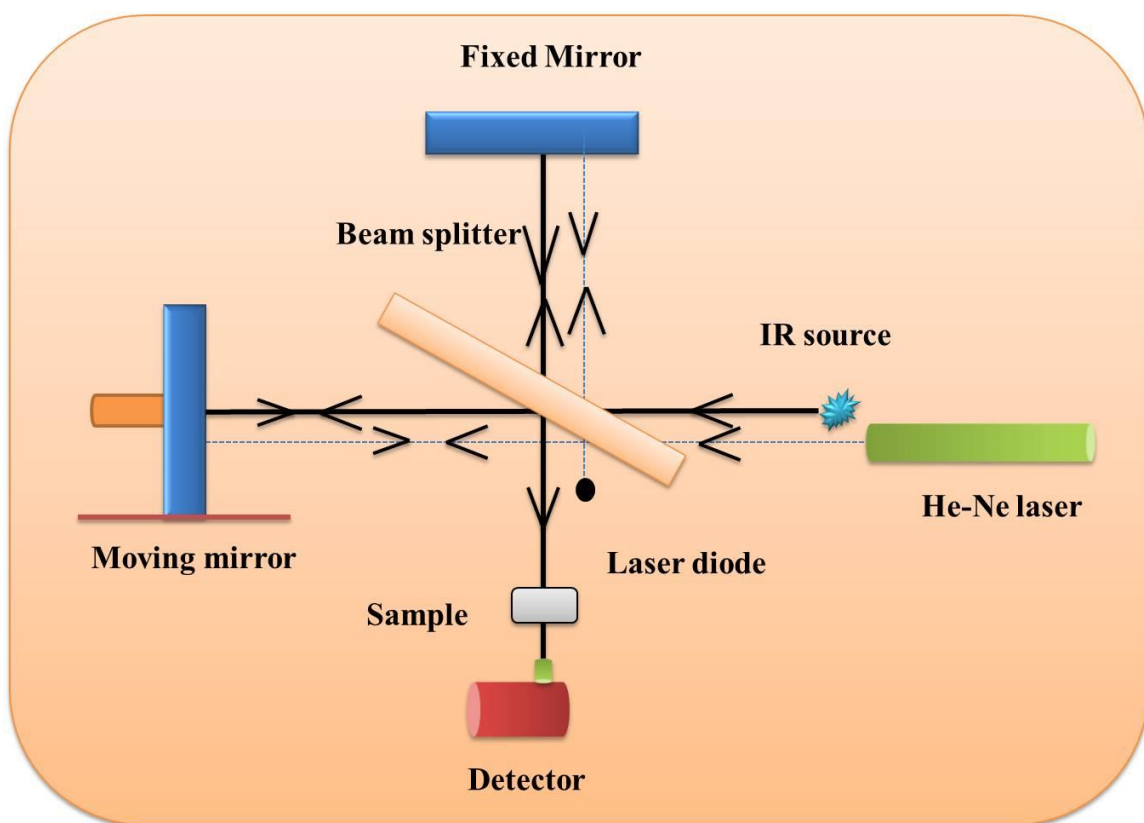


**Figure 2.16** Sketch for working of FTIR

The working of FTIR shown in the Michelson interferometer an arranged is illustrated in Fig. 2.16. He-Ne laser acts as a light source. Other half of the laser light is reflect in  $90^{\circ}$  and hits the mirror which is fixed and other half is pass through beam splitter and hits the mirror which can move freely. These split beam again recombine and show interference pattern because of different distance travelled by them. They pass through the sample and resulting interferogram is collected by detector. The frequency domain of this interferogram is analyzed by Fourier transformation. FTIR is used for compositional analysis of organic, inorganic and polymers etc.

## 2.2.7 Scanning Electron Microscope

In Scanning electron microscope (SEM) high energy electron beam is used to scan the sample for microscopic imaging [31].

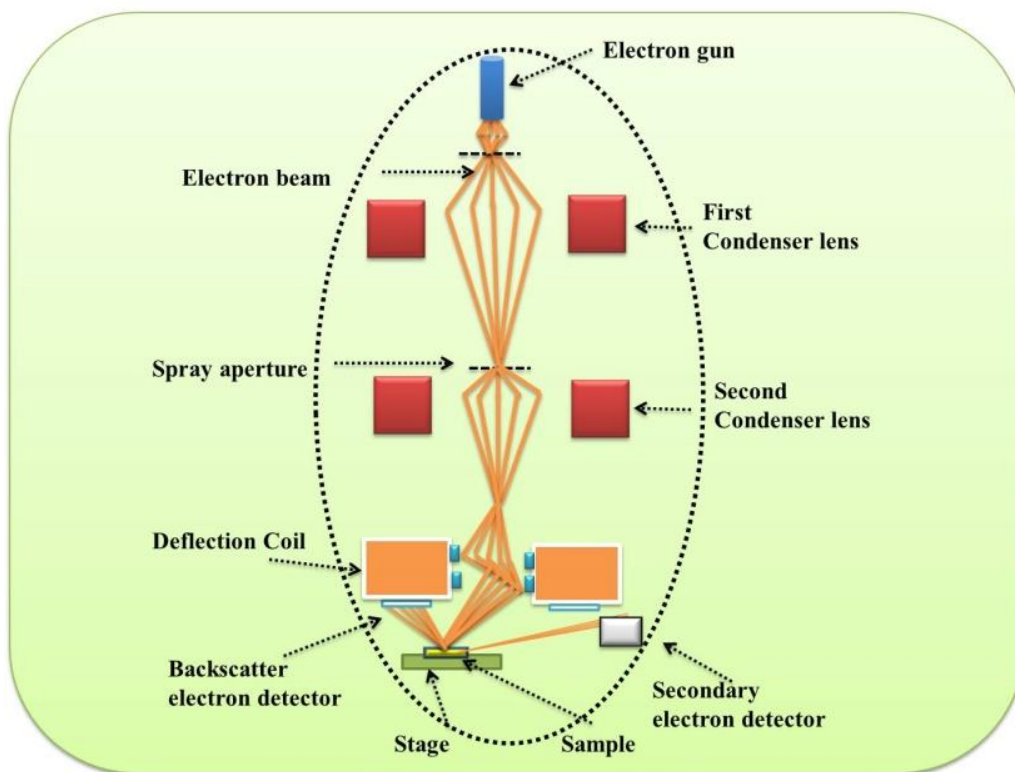


**Figure 2.17** Sketch for working of SEM

When these high energy electrons incident on the atoms of sample both elastic and inelastic scattering take place. Elastic scattering corresponds to back scattered electron and inelastic scattering produces secondary electrons. Secondary electrons which are less in energy generated from the surface of the sample leading to high resolution image in the nanometer range. In this thesis ZEISS-EVO-40 SEM is used for imaging of the sample. For SEM imaging freeze dried sample with gold coating (to make it conducting) was used.



**Figure 2.18** Physical image of ZEISS-EVO-40 SEM.

(Image Source: <http://www.angelfire.com/in3/usicjnu/sem.JPG>)

### **2.2.8 Transmission Electron Microscope**

Transmission electron microscope (TEM) is used to form images at high resolution and magnification [31]. An object of thickness 100 nm can be resolved less than de Broglie wavelength of electrons. It is used generally to get very small size like quantum dots and nanoparticles.

Transmission electrons pass through the samples and provide internal structure of the object. 50-150kV supply pass-through cathode generates beam of electrons. The condenser lens focuses the beam on the specimen. At the bottom the unscattered electrons forms shadow of images on fluorescent screen through magnetic projector lenses.

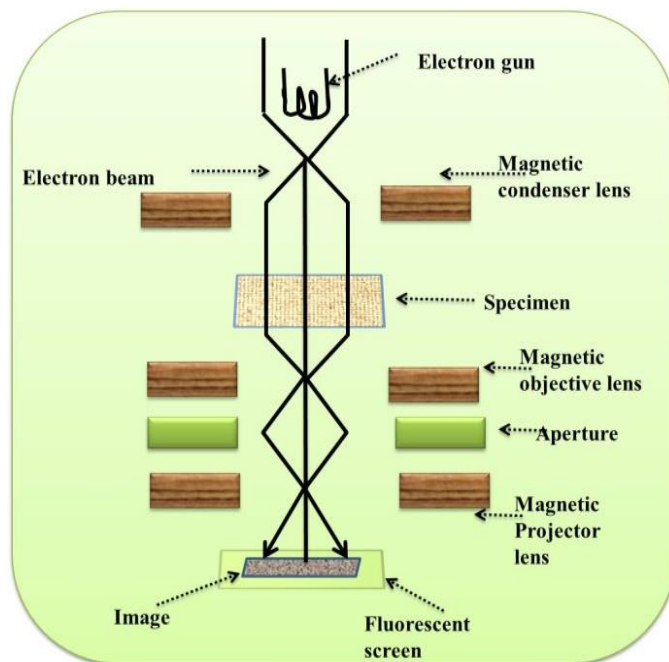


**Figure 2.19** Sketch for working of TEM

In this work the TEM images were taken from TEM JEOL-2100F instrument and sample was prepared on carbon coated Cu-grid by drop casting method.



**Figure 2.20** Physical image of TEM JEOL-2100F

(Image Source: <http://www.angelfire.com/in3/usicjnu/tem.jpg>)

## 2.2.9 UV-vis Spectroscopy

UV visible spectroscopy is also known as absorption spectroscopy. Molecule shows absorption peak when it ( $\pi$  or nonbonding electrons) absorbs light in the UV-visible region of electromagnetic spectrum to transit from ground state to excited state. According to Beer-Lambert law [32], the absorbance is dependent on the concentration of absorbing sample and the optical path length

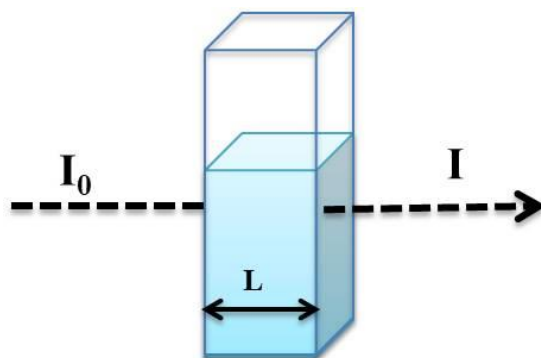


**Figure 2.21** Sketch for UV light passing through the sample

The transmittance is given as  $T = I/I_0$  (2.37)

$$\%T = 100(I/I_0) \quad (2.38)$$

Therefore absorbance,

$$A = \ln \left[ \frac{I_0}{I} \right] = \epsilon cL = -\ln T \quad (2.39)$$

Where  $I_0$  = Incident light intensity at given waave length

$I$  = transmitted light intensity

$c$  = concentration of sample

$L$  = optical path length of covered by light through the sample

$\epsilon$  = absorptivity of the reference sample

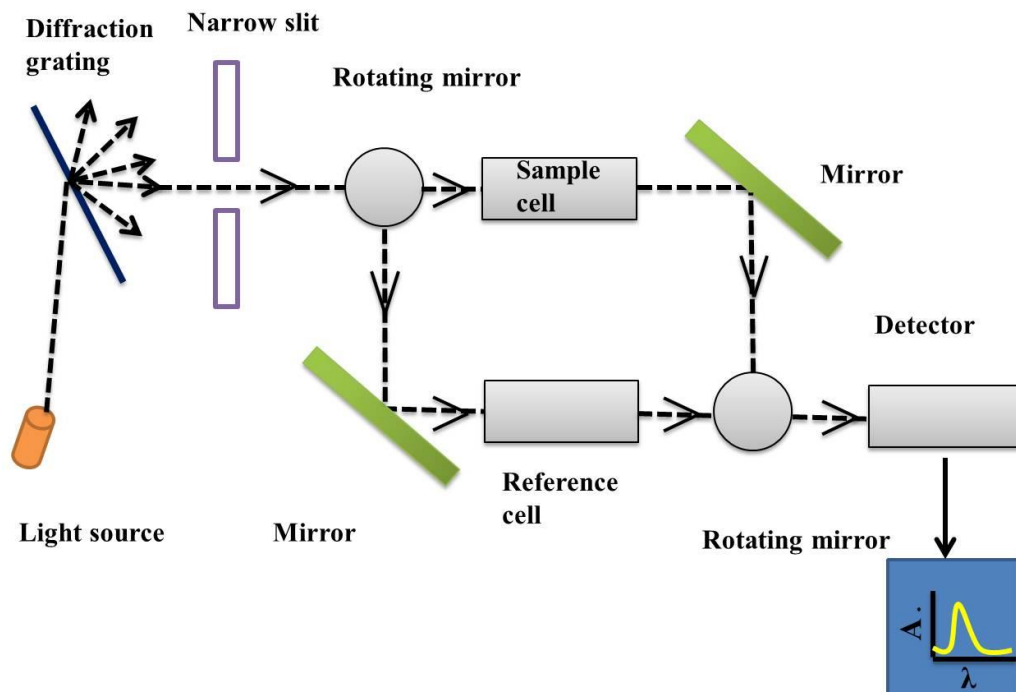


**Figure 2.22** Sketch for working of UV spectrophotometer



**Figure 2.23** Physical image of UV spectrophotometer (Cary-60, Agilent)

In this work Agilent Technologies- Cary 60 spectrophotometer (USA) was used. This instrument consists of light source, sample holder, gratings, mirrors and detector. The



electromagnetic radiation passes from both sample and reference by rotating mirror. The detector measures the absorbance signal corresponding to electromagnetic radiation with respect to reference.

### 2.2.10 Fluorescence Spectroscopy

When a light beam is incident on a molecule it moves from ground state ( $S_0$ ) to the excited singlet ( $S_1$  or  $S_2$ ) or triplet state ( $T_1$ ) by absorbing the light. This molecule can come back to ground state by several ways [33],

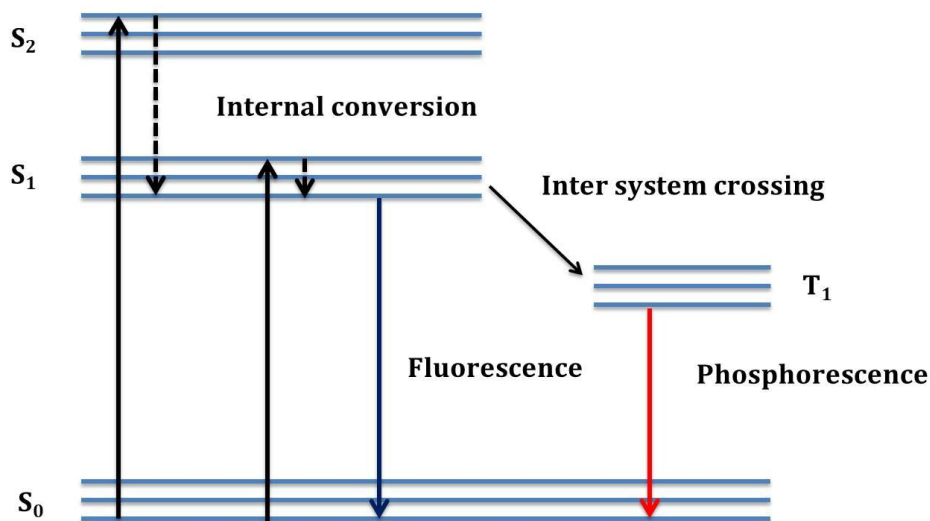


**Figure 2.24** Jablonski diagram for fluorescence

- (1) It transfers energy to another molecule either by collision or loss of energy radiative to the surrounding molecules.
- (2) By intersystem crossing from excited singlet state to triplet state and then comes to ground state. This phenomenon is known as phosphorescence.

(3) When molecule loses its energy partially (via conformational changes) and relaxed to lowest vibrational energy levels. This process is called internal conversion. The molecule returns the ground state by emitting light. This phenomenon is known as Fluorescence.

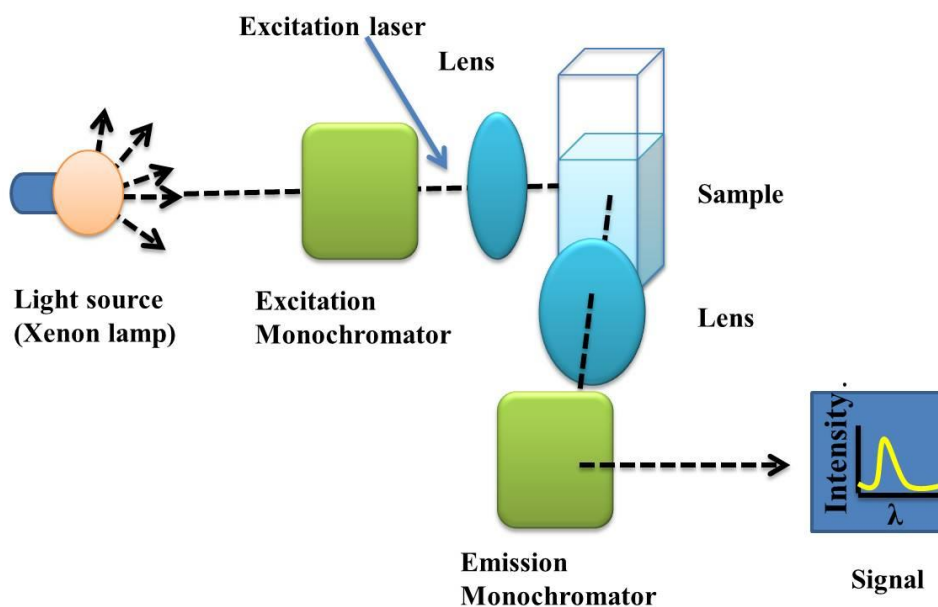


**Figure 2.25** Sketch for working of fluorescence spectrophotometer

In this work Agilent Technologies- Cary Eclipse fluorescence spectrophotometer (USA) is used. It has xenon lamp (60-75 kW) which act as light source. Two monochromators are used one is excitation monochromator and other one is emission monochromator. The light passes through the excitation monochromator and fall on the lens, this lens focus the excited beam on the sample. After transmitting from sample it is again focus by next lens and pass through emission monochromator. Finally a required spectrum is obtained on the display.



**Figure 2.26** Physical image of fluorescence spectrophotometer (Cary Eclipse, Agilent)

### 2.2.11 XRD

X-ray diffraction (XRD) is a technique used for the characterization of structure of crystal. The X-ray generated from cathode tube interact with electrons of the atom which are symmetrically arranged in the crystal plane. The interaction of this monochromatic radiation with sample forms constructive interference when it follows Bragg's condition given by [34]

$$2d\sin\theta = n\lambda \quad (2.40)$$

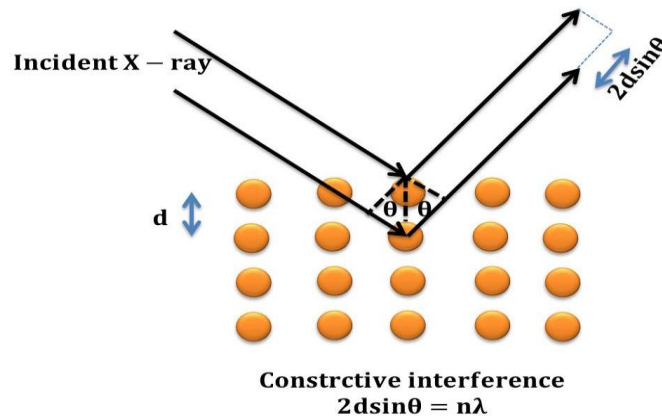


**Figure 2.27** Diagram for X-ray diffraction

Where  $\theta$  is diffraction angle,  $d$  is interpleader lattice spacing and  $\lambda$  is wave length of X-ray radiation.

In this work the measurement was performed on PANalytical X'PERT PRO diffractometer. The wavelength of radiation is  $1.54 \text{ \AA}$  and operating voltage is 45 kV. The thin film or powder sample was made on sample holder then it was kept in the shielding chamber. X-ray incident from Xray tube and fall in the sample the diffracted beam from the sample is collected by the detector. The angle between incident and diffracted beam is  $2\theta$ .



**Figure 2.28** Physical image of PANalytical X'PERT PRO diffractometer. (Image Source: <http://www.angelfire.com/in3/usicjnu/xrdpdr.jpg>)

### 2.2.12 Cyclic -Voltammetry

Electrochemical sensing is a technique used for the study of electrochemical properties of various analytes such as urea, glucose and cholesterol etc. It involves redox reaction, oxidation, stability of reactants and kinetic studies of reaction process. In this thesis, electrochemical sensing of analytes via cyclic voltammetry (CV) studies on a Autolab Potentiostat/ Galvanostat (Eco Chemie, Netherlands) was carried out. It has three electrodes working electrode, counter electrode and reference electrode. These are connected with potentiostat.

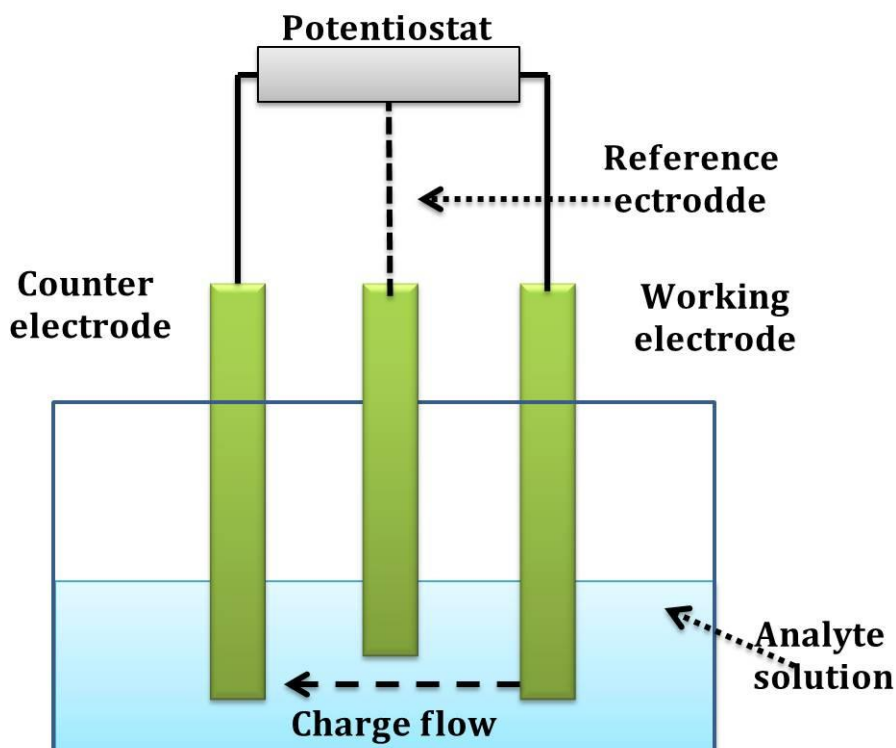


**Figure 2.29** Sketch for working of Cyclic voltametry

When external potential is applied between working and counter electrode charge flow takes place through the analyte due the oxidation and reduction of substance taking place. Ag/AgCl is taken as reference electrode. Reference electrode has constant potential and plays role in reversible half reaction which shows Nernstian behavior.



For counter electrode Platinum (Pt) wire is used and it passes the current to working electrode. The dominant peak current (cathodic and anodic) of cyclic voltammetry signal corresponds to peak potential  $E_c$  and  $E_a$  which shows either reaction is reduction or oxidation.

If the reaction is reversible then separation of peak is given by the following relation

$$\Delta E = |E_a - E_c| = 2.303 \frac{RT}{nF} = \left( \frac{0.0592}{n} \right) V \quad (2.42)$$

If the reaction is irreversible,

$$\Delta E > \left( \frac{0.0592}{n} \right) V$$

Randles-Sevcik relation gives the peak current for the reversible reaction [35]

$$i_p = 2.86 \times 10^5 n^{3/2} A C D^{1/2} V^{1/2} \quad (2.43)$$

Here,  $i_p$  is know as peak current and  $n$  is number of electrons,  $A$  is the area of electrode,  $C$  is concentration,  $D$  shows diffusion coefficient and  $V$  is scan rate.

### 2.2.13 Atomic Force Microscopy

To get the topographic image, roughness and growth profile in the nanometer range of sample atomic force microscopy (AFM) is used. AFM consists of cantilever, probe, laser photodiode sensor and piezoelectric tube. Laser falls on the cantilever and goes back to photodiode sensor.

The force exerted by probe depends on the cantilever's spring constant which follows Hooks law. In this work Atomic force microscope (AFM) was performed by alpha 300 RA WITec instrument GmbH, Germany.

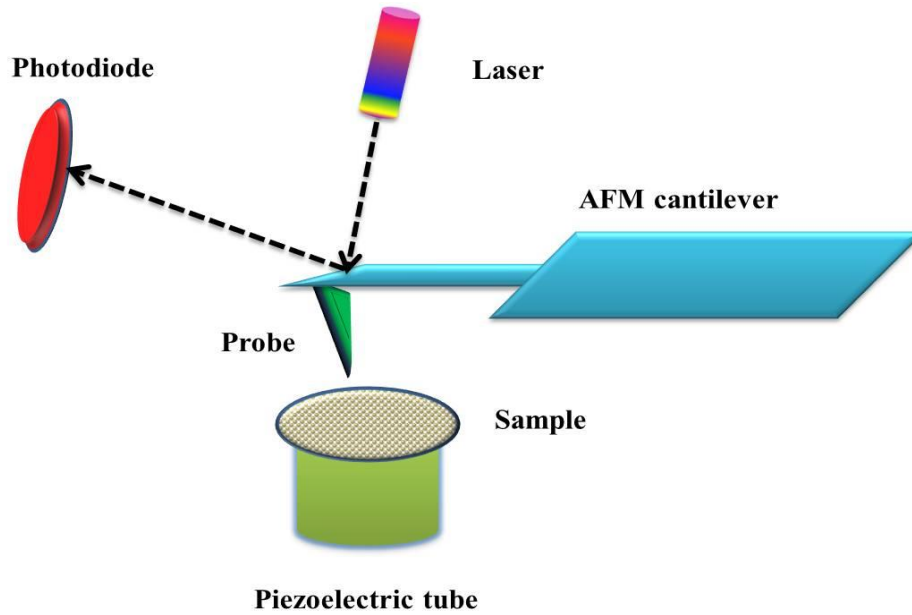


**Figure 2.30** Sketch for working of AFM



**Figure 2.31** Physical image of Alpha 300 RA WITec instrument. (Image Source: [www.witec.de](http://www.witec.de))

The van der Waals force [36] between probe and sample is responsible for the topographic image of the sample. When probe moves over the sample under this force the

deflection experienced by cantilever is measured by photodiode. Finally, the topographic image generated is seen in the display of monitor.

#### **2.2.14 Confocal Imaging**

Confocal imaging is a fluorescence microscopy. In it laser light illuminates only single spots rather than whole sample. This light emitted from the particular spots only reaches to the detector to generate image of the sample because pinhole present on the path way of the emitted light restricts or blocks other signals. In this thesis fluorescent cells were taken in the confocal microscope *FluoView™ FV1000*.

#### **2.2.15 Gamma Irradiation**

The  $\gamma$ -irradiation of the samples was done at the  $\gamma$ -irradiation chamber (model GC 1200, BRIT, India) at the Inter University Accelerator Center, New Delhi. In this instrument Cobalt-60 (1.33MeV) is used as a source of radioactive material in the lead shielded  $\gamma$ -chamber when the samples were exposed to different doses (0 - 100 Gy) of radiation. Energy of incident  $\gamma$ -irradiation was 6.8 KGy / hr.

### **2.3 References**

- [1] K. Tanaka and Y. Okahata, J. Am. Chem. Soc., **118**, 10679 (1996).
- [2] S. Zamenhof, Methods Enzymol. **3**, 696 (1957).
- [3] J. Marmur and P. Doty, J. Mol. Biol. **5**, 109 (1962).
- [4] M. J. Earle and K. R. Seddon, Pure Appl. Chem. **72**, 1391 (2000).
- [5] J. Dupont, R. F. De Souza, P. A. Z. Suarez, and A. Hydroformylation, Chem. Rev **102**,



- 3667–3692 (2002).
- [6] R. D. Rogers and K. R. Seddon, *Science* **302**, 792 (2003).
- [7] P. Wasserscheid, *Nature* **439**, 5635 (2006).
- [8] W. Leitner, *Nature* **423**, 930 (2003).
- [9] C. M. Vaz, L. A. de Graaf, and W. J. Mulder, *Adhesives, Coatings, and Bioplastics from Protein Sources* (Wiley Online Library, 2018).
- [10] S.-Z. Wang and A. Esen, *Plant Physiol.* **81**, 70 (1986).
- [11] R. Shukla and M. Cheryan, *Ind. Crops Prod.* **13**, 171 (2001).
- [12] Q. Zhong and M. Jin, *Food Hydrocoll.* **23**, 2380 (2009).
- [13] Y. Luo and Q. Wang, *J. APPL. POLYM. SCI* **40696**, 1 (2014).
- [14] J. Stetefeld, S. A. Mckenna, and T. R. Patel, *Biophys. Rev.* **8**, 409 (2016).
- [15] E. Hadji, M. Sakho, E. Allahyari, O. S. Oluwafemi, and N. Kalarikkal, *Dynamic Light Scattering (DLS)* (Elsevier Ltd, 2017).
- [16] B. J. Berne and R. Pecore, *Dynamic Light Scattering with Applications to Chemistry, Biology and Physics* (John Wiley & Sons, INC, New York, 1976).
- [17] H. Voigt and S. Hess, *Physica A* **202**, 145 (1994).
- [18] E. Geissler, *Dynamic Light Scattering* (Clarendon Press: Oxford, England, 1993).

- [19] N. Joshi, K. Rawat, and H. B. Bohidar, *J. Phys. Chem. B* **118**, 6329 (2014).
- [20] B. Hammouda, S. Krueger, and C. J. Glinka, *J. Res. Natl. Inst. Stand. Technol.* **98**, 31 (1993).
- [21] S. H. Chen, *Ann. Rev. Phys. Chem* **37**, 351 (1986).
- [22] B. Hammouda, *J. Appl. Cryst.* **43**, 716 (2015).
- [23] T. Matsunaga, T. Sakai, Y. Akagi, and U. Chung, *Macromolecules* **42**, 6245 (2009).
- [24] H. A. Barnes, *A Handbook of Elementary Rheology* (University of Wales, Institute of Non-Newtonian fluid Mechanics, Aberystwyth, 2000).
- [25] V. S. Rudraraju and C. M. Wyandt, *Int. J. Pharm.* **292**, 53 (2005).
- [26] S. Ravindranath and S.-Q. Wang, *J. Rheol. (N. Y. N. Y.)* **52**, 957 (2008).
- [27] A. Potanin, *J. Rheol. (N. Y. N. Y.)* **48**, 1279 (2004).
- [28] J. De Vicente, *Rheology* (InTech, Croatia, 2012).
- [29] B. J. Kirby and E. F. Hasselbrink, *Electrophoresis* **25**, 187 (2004).
- [30] D. M. Byler and H. Susi, *Biopolymers* **25**, 469 (1986).
- [31] P. J. Goodhew, J. Humphreys, and R. Beanland, *Electrom Microscopy and Analysis* (Taylor & Francis Group, New York, 2000).
- [32] F. Swinehart, *J. Chem. Educ.* **39**, 333 (1962).

- [33] A. Jablonski, *Nature* **131**, 839 (1933).
- [34] C. G. Pope, *J. Chem. Educ.* **74**, 129 (1997).
- [35] N. Joshi, K. Rawat, P. R. Solanki, and H. B. Bohidar, *Sens. BIO-SENSING Res.* **5**, 105 (2015).
- [36] F. J. Giessibl, *Rev. Mod. Phys.* **75**, 949 (2003).

## CHAPTER-3

---

### DNA hydrogel and ionogel and low concentration ionogel and Gamma irradiated ionogel

**Abstract:** In this chapter DNA based hydrogels, ionogels have been discussed. Their phase transition study has been probed with the help of DLS, viscosity, rheology and neutron scattering measurements. Further effect of Gamma ray irradiation on DNA ionogel has been studied.

#### 3.1 Introduction

DNA is found to be an extraordinary biopolymer because it can be used as a molecular tool to construct many other objects such as nano devices, periodic arrays and genetic engineering templates. DNA takes part in various biological activities [1]. DNA hydrogels are eco-friendly because these are biocompatible and biodegradable. Unlike other hydrogels, DNA hydrogels are different in terms of efficiency and strong branched cross-linking [2]. The benefit of it is one can achieve gelling under physiological conditions that allows for the encapsulation of drugs, proteins and mammalian cells in the sol phase instead of drug-loading step and denaturing conditions [3]. A strongly interactive PVA and DNA cryogel was prepared and it showed a good mechanical resistance due to its heterogeneous porous structure [4]. Metals like As, Ni and Cr etc act as a crosslinker for DNA which are known carcinogens [5,6]. Polyacrylamide based DNA gel was used for release of nanoparticles in drug delivery application [7]. DNA based hydrogels also showed thermal and enzymatic responses under specific temperature conditions and some control over building sites of DNA [8]. DNA hydrogels have a wide range of biomedical applications such as drugs in pharmaceuticals and tissue regeneration [9]. Lee et al have mentioned that silk worm and spiders gave the evidence for the formation of DNA hydrogel

---

**This chapter is Adapted from:** Pandey et al., J.Appl. Biotechnol. Bioeng. **2**, 144 (2017), Pandey et al., Phys. Chem. Chem. Phys. **19**, 804 (2017) and Pandey et al., Colloids and Surfaces A **538**, 184 (2018).

fibers [10]. DNA gels also shows swelling behavior and DNA release .Surfactant and protein like lysozyme also took part in the formation of gels without crosslinker [9] . DNA based physical and chemical gels have shown strain hardening [11]. Physical gels of DNA were prepared by only heating and cooling process while for chemical gels crosslinker (EGDA) was used. Viscoelastic nature and swelling behavior of DNA gels were reported earlier [12,13]. Relaxation time for DNA strands was also probed by Liu et al on the basis of oscillatory flow mode and stress relaxation [14].

DNA hydrogel relaxation dynamics has been found to be hierarchical in concentration [15]. The differential shrinking of hydrogels in presence of NaBr and cationic surfactant has been reported [16]. Rheological behavior of DNA gels showed storage and loss modulus are frequency independent which is due to dominance of viscoelastic relaxation of the networks at lower frequencies [17].

Hierarchical self-assembly in DNA gels is the primary factor which distinguishes and makes it versatile. At appropriate concentration and controlled flexibility, one-pot self-assembly of DNA gives rise to very small nanometer range tetrahedral, dodecahedra and bucky-ball size complex structures. Therefore, self-assembly of DNA allows formation of complex 3-D structures [18]. Theoretically, DNA gels can be explained by worm like chain model [11]. Tissue regeneration application due to biocompatibility and permeability of hydrogel, one can design the required three-dimensional constructions [19]. In spite of the availability of a large volume of literature on DNA, the micro-structural probing of their hydrogels by SANS remains poorly explored. In this work microscopic structure of DNA hydrogels were studied by using SANS [20] to develop a common idea of hierarchical self-organization of these networks.

Considering the importance of the DNA hydrogels in various biomedical and tissue engineering application this study can be helpful.

Organic salts having melting point less than 100 °C are called ionic liquids. These are thermally stable, non-flammable and highly conductive [21–24]. The ILs are found as good stabilizers for biopolymers due to availability of nitrogen-containing cations, such as imidazolium, and inorganic or organic anions. Ionic liquids as electrolytes or in the form of composites are being used for electrochemical based sensor applications. IL based DNA ionogel consists of two types of ILs, short and long chain {1-ethyl-3-methylimidazolium chloride [C2mim][Cl]} and {1-octyl-3-methyl imidazolium chloride [C8mim][Cl]} which are used in drug delivery and tissue engineering applications. Many reports reveal that DNA encapsulation can be used either in gene therapy or chitosan microsphere based delivery vehicles [25,26].

ILs are introduced in to polymer/biopolymer solutions to form ionogels with physically or chemically cross-linked networks that can absorb large amount of water without being dissolved [27,28]. It was observed that these ionogels originated from a homogeneous sol due to the availability of imidazolium head groups which strongly interact with biopolymer molecule *via* hydrogen bonding, electrostatic and  $\pi - \pi$  interactions [29]. Ionogels are used as chemiresistive transducer materials for the detection of volatile organic compounds (VOCs). Different types of ILs, when encapsulated in silica gel network produced specific resistive response due to their differential molecular interaction between ionic liquids and VOCs [30]. Use of DNA hydrogels in controlled drug delivery, tissue engineering, 3D cell culture, and cell transplant therapy is reported in the literature [31]. Lee et al have used DNA hydrogels to create an electrical circuit where water acts as a switch [32]. Xiong et al have extensively discussed the applications of hydrogels in the development of sensors and logic gates among others [33].

Angelova et al (2011) demonstrated lipidopolymeric self-assembled nanocarriers with tunable nanochannel size, morphology, and hierarchical inner organizations that provided potential vehicles for the predictable loading and release of therapeutic proteins, peptides, or nucleic acids. They also studied the structure and dynamics of functionalized self-assembled lipid nanosystems during stimuli-triggered liquid-crystalline phase transformations [34]. The influence on the topology and internal structure of PEGylated lipid nanocarriers for neuronal transfection was investigated using synchrotron radiation SAXS and cryo-TEM studies [35]. Angelov et al (2012) described sterically stabilized DNA functionalized lipid nanocarriers using SAXS [36]. Angelov et al (2013) discussed the millisecond structural dynamics of DNA/Fusogenic lipid nanocarrier assembly [37]. In a separate investigation the significance of large channels in cationic PEGylated cubosome nanoparticles was explored by the same authors [38].

In most of the reported studies, DNA was present with a complementary surfactant, or polymer which favored formation of inter-polymer complexes largely through Coulombic interactions. We do not specifically emphasize hydrophobic interactions [39–41]. In this thesis DNA gels were prepared in the ionic liquid solutions, and we focus on enhancement of the gel properties of these new biomaterials. Since, ionogels have a wider window of temperature stability; these are good substitutes for hydrogels.

When it comes to the preparation of biomaterials, the major concern is to use minimum quantity of the nucleic acid which applies to DNA ionogels too. A pertinent question arises here; it is possible to reduce the gelation concentration of this biopolymer while retaining its gelation temperature and gel rigidity? In this work, we demonstrate that the gelation concentration could be reduced by as much as 85 % of its corresponding hydrogel value by preparing the gels in 1-octyl-3-methylimidazolium chloride ionic liquid. It is clearly shown that the gelation temperature

could be tuned between 52-72 °C and the storage modulus (gel rigidity) between 10±2 and 40±2 Pa by solely changing the DNA concentration from 0.3 to 1.0 % (w/v) at room temperature (25 °C). This remarkable reduction in DNA concentration, availability of a wide gel region with reasonable gel rigidity will pave the way for design of DNA based novel soft biomaterials with many advantages in terms of variety and processing. Furthermore, these physical gels are thermo-reversible with manageable crosslink density, and DNA being a highly functional molecule keeping the ssDNA safely embedded in a gel matrix at room temperature is an achievement. Considering the relevance of nucleic acids in artificial tissue designing, genetic engineering, pharmaceuticals, and molecular biology the importance of aforesaid results can be hardly stressed.

In the context of radiation based health risk evaluation, a few tens of milligray dose of ionizing radiation may have remarkable effect on cells integrity where such radiations may be arising from in medical diagnostic devices, radiation therapy and/or interventional radiology. Cancer and cardiovascular disease risk associated with natural background radiation and computer tomography (CT) scanning is already well known [42–45]. Structure of fragile biopolymers such as dsDNA may be affected by all ionizing radiations, where for instance, radiation can create oxidized bases causing DNA mutation and/or localized crosslinking [46–48]. Ionizing radiations dissociate water molecules present in the surrounding of DNA inside cell nucleus and the free radicals released from this dissociation can distort or even break the DNA strand [49–51]. Ionizing radiations like  $\gamma$ -rays are reported to alter the DNA structure to a considerable extent [52]. Certain changes have been noticed in the gel forming abilities of these irradiated biopolymers. For example, the mechanical strength of biopolymer hydrogels, and interpolymer complexes are influenced considerably which bearing on new tissue formation



[53]. In the case of agar and PVA based hydrogels decrease in physical crosslinking and increase in chemical crosslinking density with irradiation dose has been reported [54].

In this chapter we have studied DNA hydrogels, [C2mim][Cl] and [C8mim][Cl] based ionogels by different techniques. We have done comprehensively studied DNA and IL based gels, and evaluated their physical behaviour. Dynamic light scattering (DLS) measurement showed the relaxation dynamics of DNA ionogels, and it was found that both the relaxation dynamics and morphology were hierarchical in IL concentration. We have seen the effect of gamma irradiation dose on the DNA ionogels reported in [55]. Therefore the experimental achievements are helpful in our general understanding of self-organization of DNA ionogels.

## **3.2 Part [A]: DNA Hydrogel**

### **3.2.1 Sample preparation**

The salmon testis dsDNA sodium salt (2000 bp, molecular weight  $1.3 \times 10^6$  g/mol) was dissolved in D<sub>2</sub>O in different amounts (1-3% (w/v)) at 60 °C, followed by heating to 90 °C under stirring to denature the biopolymer. Finally, samples were gradually cooled to room temperature (25 °C) while their viscosity was measured in real time and the gels were subjected to SANS studies. Rigid gels were formed for DNA concentration,  $c^* \geq 2\%$  (w/v).

### **3.2.2 Result and Discussion**

#### **3.2.2.1 Sol-gel Transition**

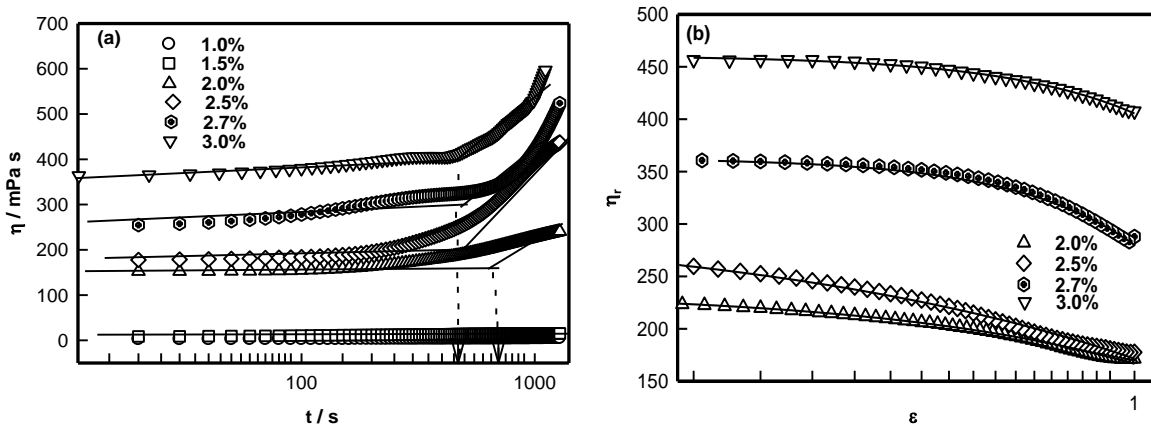
DNA solutions prepared with different DNA concentrations were analyzed for their characteristic sol-gel transition behavior. Time dependent evolution of viscosity  $\eta$  is shown in

Fig.3.1 for different samples. The time dependent growth of viscosity could be described by the scaling relation given by [56]

$$\eta_r = \varepsilon^{-k}; \quad t \rightarrow t_{gel} \quad (3.1)$$

Here, relative viscosity  $\eta_r = \eta/\eta_0$ ,  $\eta_0$  is solvent viscosity,  $\varepsilon = \left(1 - \frac{t}{t_{gel}}\right)$  and  $t_{gel}$  is gelation time.

The plot between  $\eta_r$  vs.  $t$  shown in Fig. 3.1(a), provided the characteristic time  $t_{gel}$  obtained from the change in slope which was found to decrease with DNA concentration.



**Figure 3.1.** (a) Temporal dependence of viscosity. The arrows indicate gelation time  $t_{gel}$ . (b) Relative viscosity  $\eta_r$ , as function of reduced time  $\varepsilon = (1-t/t_{gel})$ . Solid lines are fitting of data to eqn (3.1).

It was found that as the DNA concentration was increased from 1 to 3 %, the viscosity of DNA sol increased gradually due to the formation of interconnected physical networks. To fit relative viscosity data to time dependent power-law function was used and corresponding power-law exponent  $k$  was determined. Theoretical value for Rouse dynamics corresponds to  $k = 0.7$  for conducting, and  $k = 1.3$  for percolating gel network [57,58]. In our case,  $k = 0.13 \pm 0.02$ , implying invariance of the network growth process with DNA content. Although it was an indicative description of gelation, but on the basis of experimental data, it was possible to give a reasonable description to gelation kinetics. The gelation time was  $t_{gel} \approx 700$  s for 2% gel, which reduced to

350 s when the DNA concentration was 3%. This clearly indicated that at higher concentration due to the propensity of DNA strands the physical entanglement was highly favorable that caused earlier gelation.

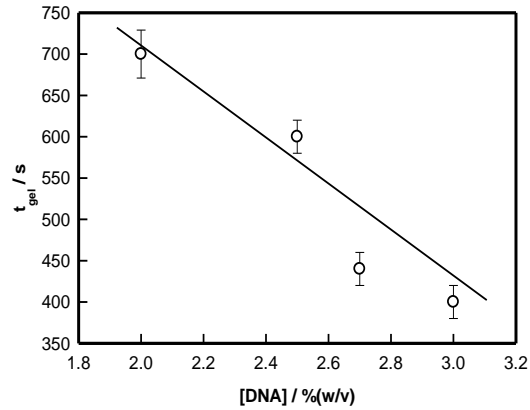


**Figure 3.2.** Variation of time of gelation  $t_{gel}$  as function of DNA concentration.

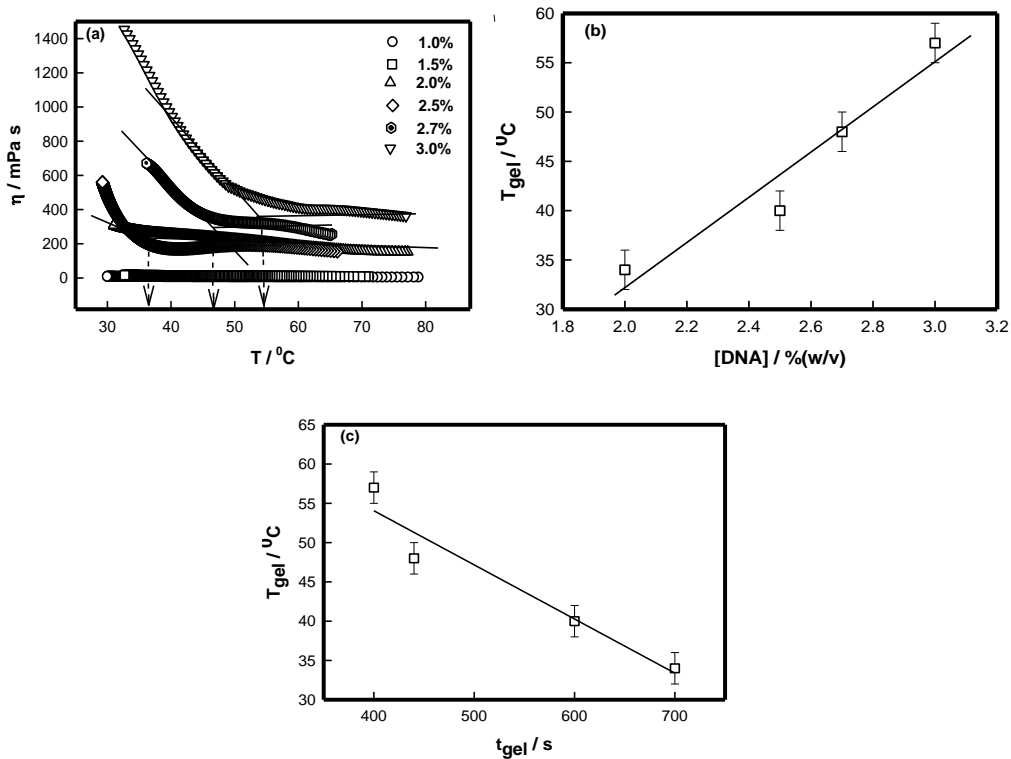


**Figure 3.3.** (a) Variation of viscosity with temperature shown for different DNA concentrations, and (b) variation of gelation temperature  $T_{gel}$  with DNA concentrations, and (c) temporal temperature dependence. Note the Newtonian cooling rate  $0.069 \text{ } ^\circ\text{C} / \text{s}$ .

No gelation transition was noticed when the biopolymer concentration was less than 2%. The temperature of gelation was 36 °C for 2% sample which enhanced to 57 °C for 3% DNA gels. It is remarkable to note that just by raising the concentration it was possible to increase the gelation temperature by 63 %. At the same time the gelation time reduced by almost 50%. Further, the data shown in Fig. 3.3(b), could be fitted to a straight line (chi-squared =0.99) with a slope of  $\approx 23$  °C/(w/v). The linear dependence of gelation temperature with DNA concentration was not reported hither to. This result will have significant bearing on the applications of DNA hydrogels.

### 3.2.2.2 Static Structure Factor

The static structure factor profiles obtained from different DNA hydrogel samples are shown in Fig. 3.4. The raw data was examined by checking their  $1/I(q)$  vs  $q^2$ , and  $1/\sqrt{q}$  vs  $q^2$  behavior which correspond to Ornstein-Zernike [59] and Debye-Bueche functions [60]. The statistical accuracy of this fitting was poor. The best fit to the data was found when it was fitted to an empirical function given by eqn 3.2. In this formalism, we have identified three ranges of scattering vectors  $q$ : (i) low  $q$ -range ( $0.05 \text{ nm}^{-1} \leq q \leq 0.11 \text{ nm}^{-1}$ ) was fitted to Guinier function given by  $I(q) \sim I_G \exp(-R_g^2 q^2/3)$  where  $R_g$  is known as radius of gyration of scattering moiety, (ii) in the intermediate  $q$ -range ( $0.12 \text{ nm}^{-1} \leq q \leq 0.21 \text{ nm}^{-1}$ ), power-law function was used for data fitting,  $I_{PL}(q) \sim q^{-\alpha}$  where  $\alpha$  is related to the geometry of scattering moiety, and (iii) in the high  $q$ -range ( $q \geq 0.22 \text{ nm}^{-1}$ ) the broad peak was fitted to a modified Lorentzian function given by,  $I(q) = I_{BP}/(1 + (q - q_0)/\xi)^m$  where  $q_0$  is related to peak position of scattered peak, and  $\xi$  is correlation length for polymer chain and  $m$  is a fitting parameter. Thus, the structure factor profile could be described by

$$I(q)=I_G \exp(-R_g^2q^2/3) + I_{PL}(q) \sim q^{-\alpha} + I_{BP}/(1 + (q - q_0) \xi)^m \quad (3.2)$$

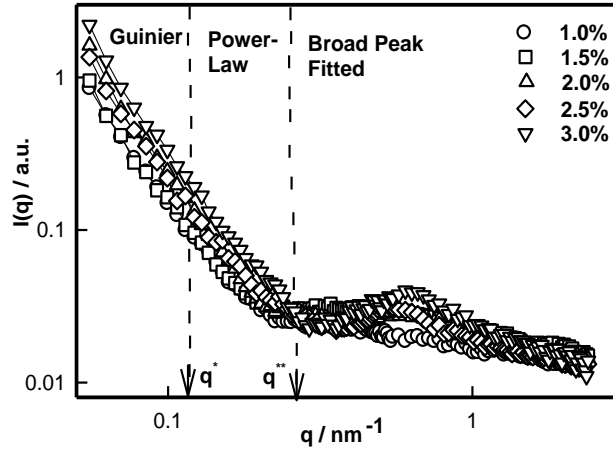


**Figure 3.4.** SANS correlation between static structure factor  $I(q)$  and scattering vector  $q$  for different DNA concentrations. These correlations are best fitted with Guinier, Power-Law and Broad peak (Lorentzian) functions in different  $q$ -ranges.

This mode of analysis yielded excellent chi-squared values ( $> 0.97$ ) in all the cases. The cross-over between low and intermediate, and intermediate and large- $q$  values are identified as  $q^*$  and  $q^{**}$ , respectively. These defined the signature length scales given by  $L^* \left( = \frac{2\pi}{q^*} \right)$  and  $L^{**} \left( = \frac{2\pi}{q^{**}} \right)$ , which plotted for different hydrogel samples. This biopolymer had an overlap concentration of  $c^* (\geq 2\%)$  above which the solution was in gel state (Fig.3.5). Remarkably, the value of  $L^*$  ( $= 50$  nm) coincides with the persistence length of DNA [61,62]. The  $L^{**}$  value was 26 nm in the sol, and about 22 nm in gel state (Fig.3.5). Thus, to a very good approximation,  $L^* \approx 2L^{**}$

In the low  $q$ -region ( $q < 3R_g^{-1}$ ) the scattering factor was approximated by Guinier-regime,

$$I(q) = I_G \exp(-R_g^2q^2/3) \quad (3.3)$$

where  $I_G$  is the structure factor at very low  $q$ , and the fitting yielded value of radius of gyration  $R_g \approx 40 \pm 3$  nm in the sol state independent of DNA concentration (Fig.3.6 (b)).

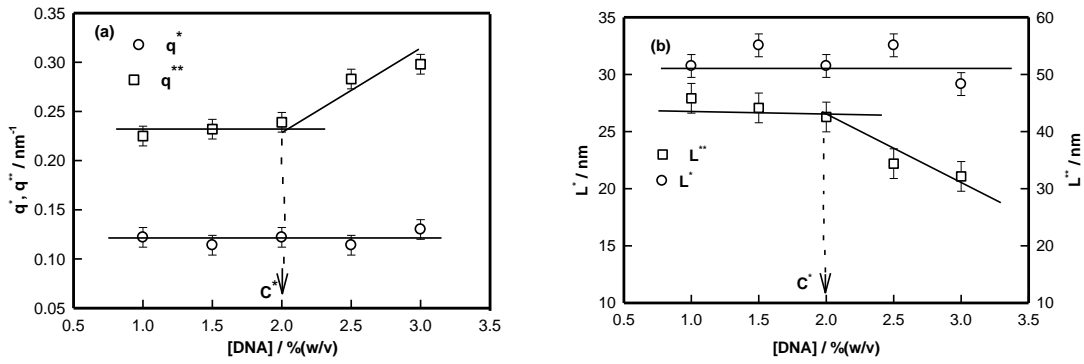


**Figure 3.5.** (a) Variation of  $q^*$  and  $q^{**}$  with different DNA concentrations. (b) Variation of  $L^*$  and  $L^{**}$  with different DNA concentrations. Overlap concentration  $c^*$  is clearly identified here (arrow).

According to scaling laws correlation length dependence of  $\xi$  with concentration is given as [63]

$$\xi = R_g \left(\frac{c}{c^*}\right)^{\frac{\nu}{1-3\nu}} \quad (3.4)$$

Where  $c^*$  ( $\approx 2\%$ ) is the typical overlap concentration and  $\nu$  is excluded volume exponent of the system. From this scaling relation, using  $\xi = 0.5- 3.3$  nm (deduced from eqn 3.6),  $R_g = 40$  nm, and  $c = 2\%$ , and scaling exponent obtained was  $\nu \sim 0.40- 0.45$ . Thus, in the sol state DNA strands were in the poor solvent environment, which changed to marginal solvent situation as the gelation temperature was reached. Therefore, the sol-gel transition was concomitant with change in the solvent quality for this biopolymer. Since, this change was in the favorable direction of solubility, there was no phase separation, but a clear transition to gel phase occurred due to a propensity in the physical entanglement of the DNA strands. We use eqn (3.4) with caution because it strictly applies to chemically cross-linked networks and gels. In the intermediate  $q$ -regime ( $0.12 \text{ nm}^{-1} \leq q \leq 0.21 \text{ nm}^{-1}$ ), power-law dependence of structure factor was defined by

$$I_{PL}(q) \sim q^{-\alpha} \quad (3.5)$$

The least-squares fitting of data yielded the value for  $\alpha \approx 2.2 \pm 0.1$  independent of DNA concentration (Fig.3.6 (b)), which attributed Gaussian chain behavior (theoretical value = 2) to these strands.

SANS data in the high  $q$ -region was described by a signature broad-peak, a profile normally noticed in scattering from amorphous soft materials. In this formalism, the typical distance between scattering heterogeneities is explained by  $d_0$  which is the peak position of the broad correlation peak located at  $q_0$ . The  $q_0$  value signifies the peak position of different morphologies such as in lamellar, cylindrical, spherical or for bi-continuous structures [64]. Here in the case of hydrogels one can see the significance of such a model. We identify  $d_0$  as average distance between the polymer-poor and polymer-rich regions. The following functional form (modified Lorentzian function) described the broad peak feature seen in our system which can be described by,

$$I_{BP}(q) = I_L / (1 + (q - q_0) \xi)^m \quad (3.6)$$

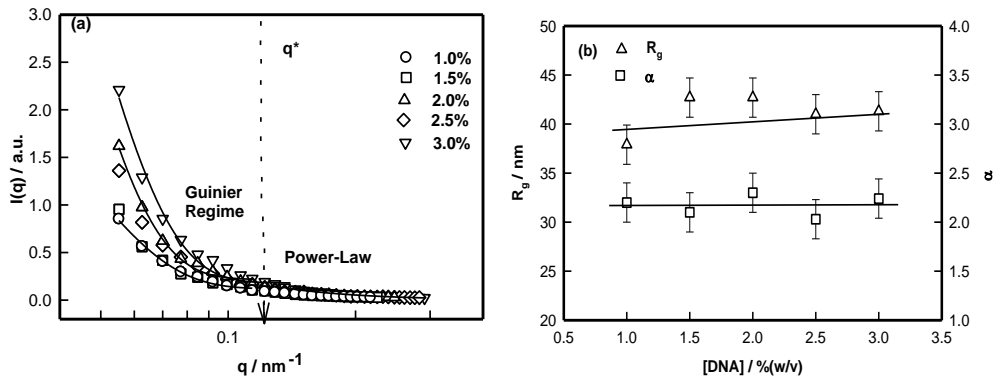


**Figure 3.6.** (a) Correlation for  $I(q)$  versus  $q$  fitted by Guinier and Power- Law functions for different DNA concentrations at room temperature.(b) variation of radius of gyration and geometrical scattering factor  $\alpha$  with different DNA concentration. Arrow demarcates the two regions.

Peak position  $q_0$  is related to  $d_0$  through the relation

$$d_0 = 2\pi / q_0 \quad (3.7)$$

Fig.3.7 data clearly shows that for the sample with 1% DNA concentration there was no correlation peak. As we increased the DNA concentration, the existence of broad peak became more prominent, and its position shifted to lower- $q_0$  value. Thus the value for  $d_0$  decreased from  $16.0 \pm 1.0$  to  $10.0 \pm 0.8$  nm which signified that the hydrogel system had become compact and dense. Incidentally, the value of the exponent  $m \approx 2 \pm 0.2$ .

Secondly, we found that with increase in DNA concentration (1 to 3%), the correlation length,  $\xi$  increased from 0.50 to 3.3 nm. It can be inferred that as DNA concentration increased there was formation of network structures due to physical entanglement of DNA strands, which was predominant at higher DNA concentrations. This corresponded to dominant scattering arising from these structures. This behavior is depicted in Fig.3.8, which, in addition, defines the overlap concentration  $c^*$ .

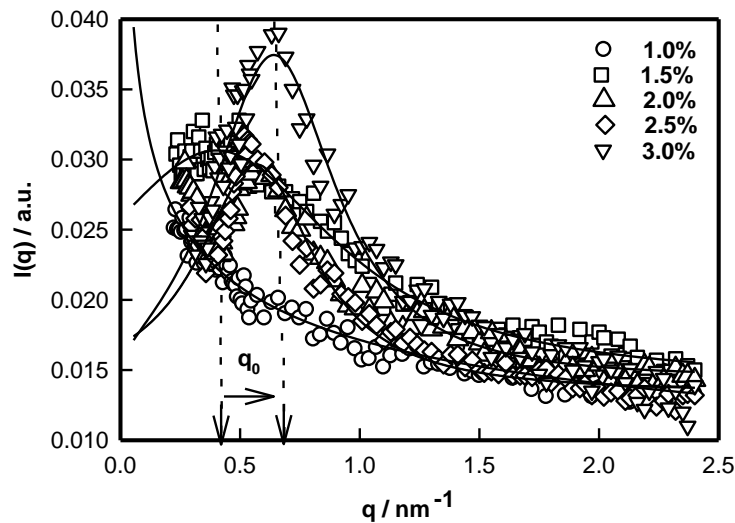


**Figure 3.7.** Correlation between  $I(q)$  versus  $q$  obtained from SANS measurement for high  $q$  regime performed on different DNA concentrations at room temperature. Note the red-shift of  $q_0$  (arrows).



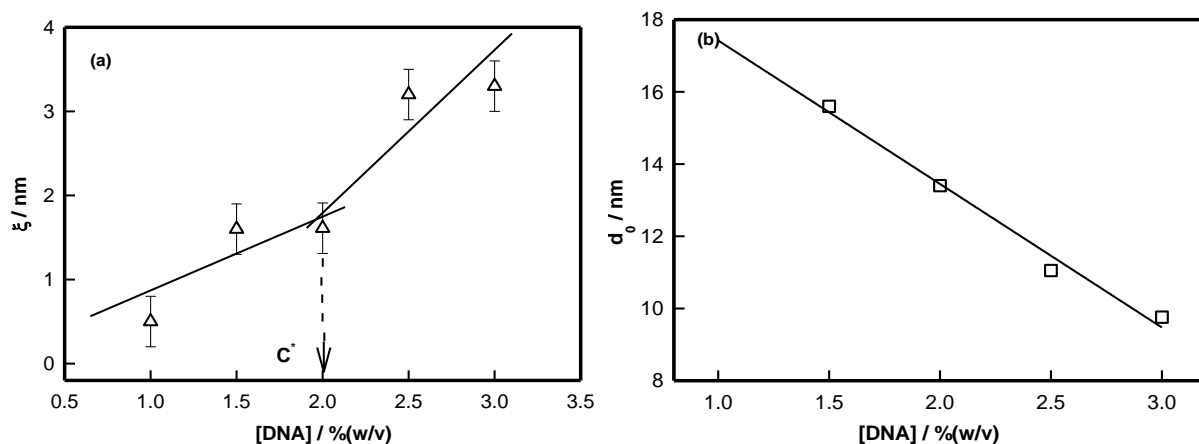
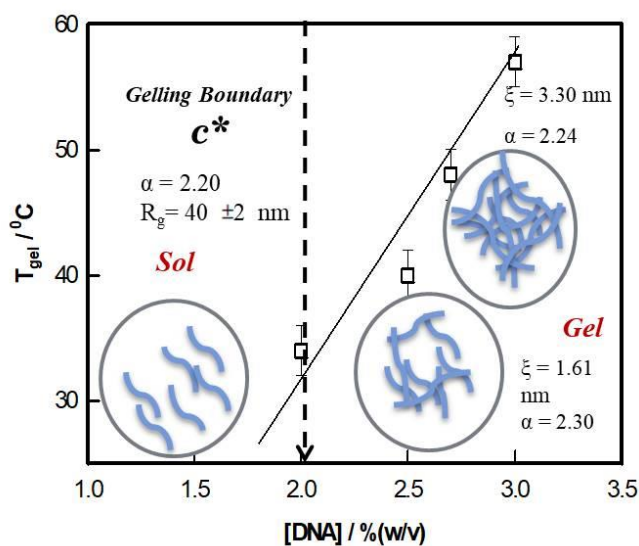


**Figure 3.8.** Variation of (a) correlation length with different DNA concentration. (b) d- spacing with different DNA concentrations.

Based on the SANS data, a schematic sol-gel phase diagram can be constructed which is shown in Scheme 3.1. In the sol state, the mean inter strand distance was  $d_0 = 16 \pm 1$  nm,  $R_g = 40 \pm 2$  nm and correlation length (distance of minimum approach)  $\xi = 0.5 \pm 0.04$  nm. These values changed to  $d_0 = 10.0 \pm 1.0$  nm and  $\xi = 3.3 \pm 0.4$  nm at the highest concentration used in this study. Thus, it was clearly seen that the self-assembly leading to the gelation involved at least five length scales.



**Scheme 3.1.** Schematic of sol- gel transition in DNA solution.

### 3.3 Part [B]: [C2mim][Cl] based Ionogel

#### 3.3.1 Sample preparation

The ionic liquid was dissolved in D<sub>2</sub>O in different amounts for making the stock solutions (1-5%). Stock solution of 1% of DNA was made by dissolving the supplied powder material in ionic liquid solutions at 60 °C followed by heating upto 90 °C under stirring to denaturate the DNA. Our experiments revealed that it was necessary to expose the DNA sols to a heating and cooling cycle to induce gelation in the system. Therefore all the sol samples were systematically heated to 90 °C, and then cooled to room temperature (25 °C). As per literature data at 90 °C, there is cooperative unraveling of the intertwined strands of double helix to single strands [35-42]. It is to be noted that ssDNA is not of much use in biology *per se*. However, we describe a DNA based biomaterial with gel-like properties to be possibly used as a matrix for drug and enzyme loading, wound healing and tissue engineering applications.

#### 3.3.2 Result and Discussion

##### 3.3.2.1 Scaling and Gelation time

The freshly prepared DNA ionosols were examined for their characteristic gelation behavior. Fig. 3.1 shows the temporal evolution of relative viscosity  $\eta_r$  ( $\eta_r = \eta/\eta_0$ ,  $\eta$  is solution and  $\eta_0$  is solvent viscosity) for different samples. This time dependent growth could be described by the scaling relation given by [56,57]

$$\eta_r = \varepsilon^{-k}; \quad t \rightarrow t_{\text{gel}} \quad (3.8)$$

where  $\varepsilon = \left(1 - \frac{t}{t_{\text{gel}}}\right)$  and  $t_{\text{gel}}$  is gelation time.

The relative viscosity vs. time data shown in Fig. 3.9 yielded the characteristic time  $t_{\text{gel}}$  deduced from the change in slope which was found to decrease with IL concentration.

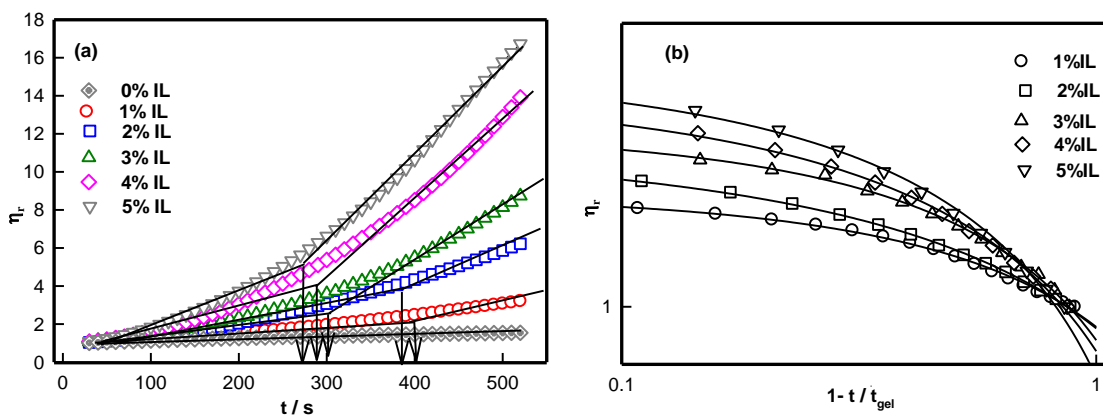


**Figure 3.9.** (a) Temporal evolution of relative viscosity. The arrows indicate gelation time  $t_{gel}$ . (b) Relative viscosity as function of reduced time  $\varepsilon = (1-t/t_{gel})$ . Solid lines in (b) are fitting of data to eqn (3.1).

It is clearly seen that as the IL concentration was increased from 1 to 5 %, the viscosity of ionosol increased systematically. It was due to the formation of DNA–IL clusters, and their interconnected networks with increase in IL concentration. The time dependent power-law growth function was used to fit the relative viscosity data to eqn (3.1) to determine the value of exponent  $k$ .

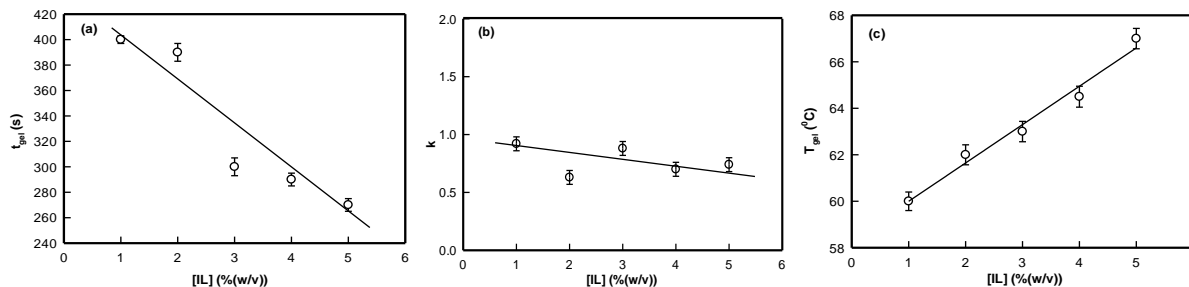


**Figure 3.10.** Variation of (a) gelation time  $t_{gel}$ , (b) exponent,  $k$ , and (c)  $T_{gel}$  as function of ionic liquid concentration.

The exponent  $k$  described the temporal growth of the networks (Fig. 3.10 (b)). Two observations can be clearly made: (i) it was remarkable to note that the gelation time,  $t_{gel}$  (1% IL) = 400 s decreased to  $t_{gel}$  (5% IL) = 260 s (a drop of 35%) (Fig. 3.10 (a)), and (ii) the value of  $k$

ranged between 0.6-0.9. Theoretically, Rose dynamics has shown that the exponent  $k = 0.7$  corresponds to conducting, and  $k=1.3$  to percolating gel network [56–58]. Therefore, on the basis of experimental data, it is possible to give a qualitative assessment of gelation kinetics. The exponent  $k$  decreased from 0.9 to 0.6 with increase in IL-concentration. Thus, the network which represented a conducting matrix ( $k \approx 0.9$ ), got reorganized into a percolating network when there was propensity of IL-molecules in the dispersion. This description is nothing more than indicative, and clearly requires more experimental data to be validated.

The temperature dependent viscosity data is presented in Fig. S1 (Ref. [55]) pertaining to the sols (ionosols) spontaneously cooling (below gelation temperature) to their gel states. It is clearly seen that as the IL concentration was increased from 1 to 5 %, the temperature of gelation increased systematically from 60 to 67 °C. The respective gelation time and temperature could also be correlated from Fig. S2 (Ref. [55]) data for different gelling samples. This large window of gelation temperature is remarkable, which could be achieved by addition of minute quantity of ionic liquid to the dispersion medium.

### 3.3.2.2 Dynamic Arrest and Ergodicity Breaking

All the gel samples were rigid except the one without IL which was in sol phase throughout .i.e. it did not flow on inversion of the sample cell. The samples were subjected to DLS experiments in a bid to study the relaxation dynamics of concentration fluctuations. The time dependent dynamic structure factor,  $g_1(\tau)$  were obtained from different samples. The dynamic structure factor determined from the treated intensity correlation function  $g_2(q, t)$  data could be described by,

$$g_1(q, t) = C \exp\left(-\frac{t}{t_f}\right) + (1 - C) \exp\left(-\frac{t}{t_s}\right)^\beta \quad (3.9)$$

Where  $C$  and  $(1-C)$  are relative amplitudes of the two modes and  $\beta$  is stretch parameter which is defined as width of distribution function that uniquely characterized the structure factor  $g_1(q,t)$ , and  $t_f$  and  $t_s$  are the relaxation times corresponding to fast and slow mode relaxations. The variation of different modes of relaxation frequencies with waiting time  $t_w$  for various samples is depicted in Fig. 3.11

The analysis of the DLS data also yielded the value for the fast and slow mode relaxation times  $\tau_f$  and  $\tau_s$ , respectively. These data are plotted as function of waiting time  $t_w$  pertaining to each gel sample (Fig. 3.11). The fast mode relaxation time did not change with  $t_w$  regardless of increase in IL concentration. However; the slow mode exhibited a sharp increase at specific waiting time dependent on IL content. This increase can be attributed to dynamic arrest of the networks. It was remarkable to note that the time of arrest was almost same as the ergodicity breaking time,  $\tau_{EB}$  (to be discussed). Therefore, the transition to non-ergodicity was a dynamic process that was predominantly manifested in the dynamic structure factor data.

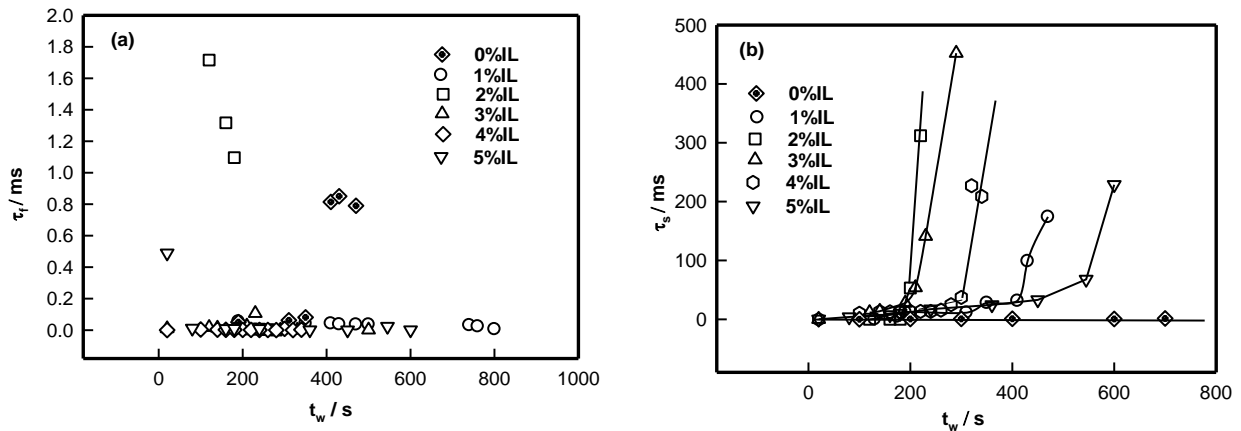


**Figure 3.11.** Plot of different modes of relaxation frequency with waiting time,  $t_w$  shown for samples with different IL concentrations. (a) Note the invariance of fast mode relaxation time with  $t_w$  or IL concentration. (b) The slow mode relaxation time showed sharp up-turns at the time of dynamic arrest (arrows).

For an ergodic state, the dynamic structure factor  $g_1(t)$  relaxes to the value 0 (at  $t \rightarrow \infty$ ) from its initial value of 1 ( $t = 0$ ). For a nonergodic state, ergodicity parameter  $\chi$  or the signal to noise ratio i.e. signal modulation for  $g_1(q,t)$  is given by [65,66]

$$\chi = g_1(q,t) |_{t \rightarrow 0} - g_1(q,t) |_{t \rightarrow \infty} = 1 \quad (3.10)$$

Signal modulation lies between 0 to 1 for a nonergodic state due to dynamic arrest of scattering moieties and it has been seen in various soft matter systems such as polymer and colloidal gels, glasses etc [66,67]. The measured  $g_1(q, t)$  data was fitted to eqn (3.9) to determine  $t_f$ ,  $t_s$  and  $\beta$  parameters, in addition to the ergodicity parameter  $\chi$ . A representative plot of nonergodic parameter  $\chi$  and stretch exponent  $\beta$  are shown in the Fig. 3.12 which shows a transition from ergodic to non ergodic state defined by an ergodicity breaking time  $\tau_{EB}$ .

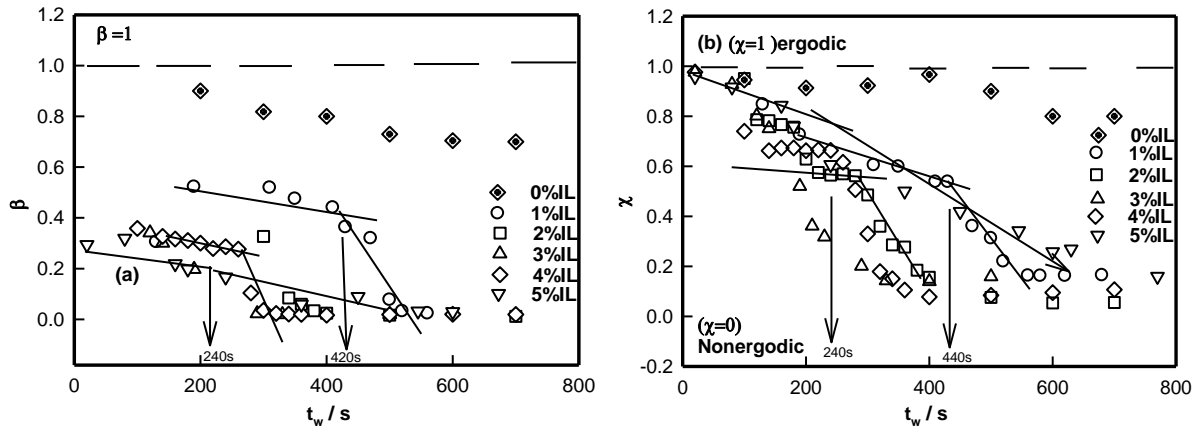


**Figure 3.12.** (a) Variation of stretch parameter  $\beta$  with waiting time  $t_w$  for different IL concentrations. (b) Variation of  $\chi$  as a function of waiting time,  $t_w$ . The point where there is a slope change in the value of  $\chi$  is defined as a ergodicity breaking time  $\tau_{EB}$  shown for different IL concentrations.

It is remarkable to note that both  $\beta$  and  $\chi$  reveal identical ergodicity breaking time  $\tau_{EB}$ , which is shown in Fig. 3.13 (a). When  $\tau_{EB}$  and  $t_{gel}$  were correlated (Fig. 3.13 (b)), we clearly noticed a linear dependence implying ergodicity breaking time was same as gelation time.

Therefore, gelation referred to the dynamic arrest of the IL-cladded DNA strands that organize to yield an interconnected gel network.

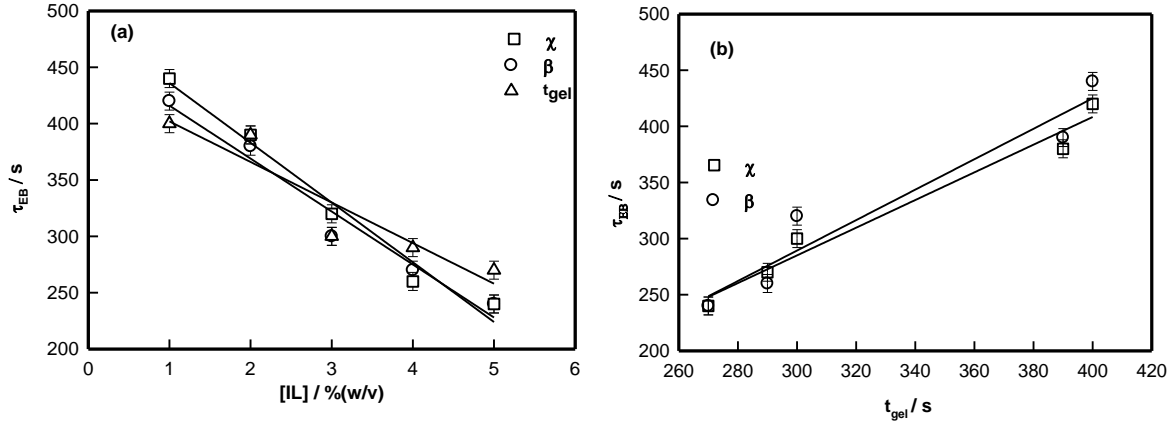


**Figure 3.13.** (a) Variation of ergodicity breaking time (from  $\chi$  and  $\beta$ ) and time of gelation with different IL concentrations. (b) Variation of ergodicity breaking time (from  $\chi$  and  $\beta$ ) with time of gelation  $t_{gel}$ .

### 3.3.2.3 Static Structure Factor

To map the microscopic internal structure of the ionogel samples, small angle neutron scattering (SANS) was used as a probe. The static structure factor profile for samples made with different IL concentrations is shown in Fig. 3.14 (a). The  $I(q)$  vs  $q$  data was first analyzed using the following protocols: (i)  $1/I(q)$  vs  $q^2$  and (ii)  $\sqrt{1/I(q)}$  vs  $q^2$  plots which did not yield clear straight lines or a set of two straight lines with different slopes. The best fit was obtained when the  $I(q)$  data was fitted to following empirical functional form

$$I(q) \approx I_{PL}q^{-\alpha} + \frac{I_{OZ}}{(1+q^2\xi^2)} + I_{GP} \exp\left(\frac{-R_c^2q^2}{2}\right) \quad (3.11)$$

(Power-law) + (Ornstein-Zernike) + (Guinier-Porod)

Here,  $I_{PL}$ ,  $I_{OZ}$  and  $I_{GP}$  are  $q$ -independent pre-factors. This permitted the scattering profile to be split into three distinct  $q$ -regions.

The low- $q$  region ( $0.06 \text{ nm}^{-1} \leq q \leq 0.19 \text{ nm}^{-1}$ ) was fitted to a Power-law function, intermediate- $q$  region ( $0.19 \text{ nm}^{-1} \leq q \leq 0.53 \text{ nm}^{-1}$ ) was fitted to Ornstein-Zernike function, and asymptotic range at  $q \rightarrow \infty$  ( $q \geq 0.53 \text{ nm}^{-1}$ ) was fitted to Guinier-Porod function. Here,  $\alpha$  is related to the geometry of the scattering moiety.

At equilibrium, for polymers in a good solvent, the mean-field theory describes that the structure factor of concentration fluctuation is defined by Ornstein Zernike (O-Z) function [68]. Here,  $\xi$  is correlation length or mesh size of the network. It was possible to probe the intermediate- $q$  domain because of high resolution of spectrometer available in PSI. In far- $q$  domain called the asymptotic regime, the chain cross-section makes a finite contribution to measured structure factor. In the Guinier-Porod formalism, at  $q \rightarrow \infty$  the structure factor is described by

$$I(q) \sim \exp(-R_c^2 q^2 / 2) \quad (3.12)$$

Where  $R_c$  is cross sectional radius of DNA strands.

The analysis of SANS data yielded  $\alpha$  value in between  $1.8 \pm 0.1$  and  $2.1 \pm 0.1$  (Fig. 3.14 (b)) for 1-5% (w/v) ionogels, and 2.8 for DNA sols. The value of  $\alpha = 2$  corresponds to Gaussian coil type structure while at  $\alpha = 2.6$  the conformation is closer to diffusion limited aggregation clusters in 3D-space.

Further, in the intermediate- $q$  region data was analyzed by Ornstein-Zernike relation that emerged from density fluctuations existing in the condensed phase [68]. The average mesh size or correlation length of these fluctuation was given by  $\xi = 3 \pm 0.7 \text{ nm}$  for different ionogel samples, and a smaller mesh size for sols,  $\xi = 0.73 \text{ nm}$ . The correlation length of only DNA sol (0% IL) was 76.7% less than that of DNA ionogels. The asymptotic regime was analyzed using



eqn (3.12). The cross-section of DNA strands determined was,  $R_c = 1.7 \pm 0.1$  nm independent of IL concentration.

The characteristic cross-over lengths referred to the boundaries between the various  $q$ -regions mentioned earlier, are designated as  $q^*$  and  $q^{**}$  in Fig. 3.14 (a). Therefore, the length scales  $L^* \left( = \frac{2\pi}{q^*} \right)$  and  $L^{**} \left( = \frac{2\pi}{q^{**}} \right)$  were determined to be equal to  $33 \pm 5$  nm and  $12 \pm 1$  nm, respectively. This revealed that inter particle distance decreased as the mesh-like structures appeared within the ionogels.

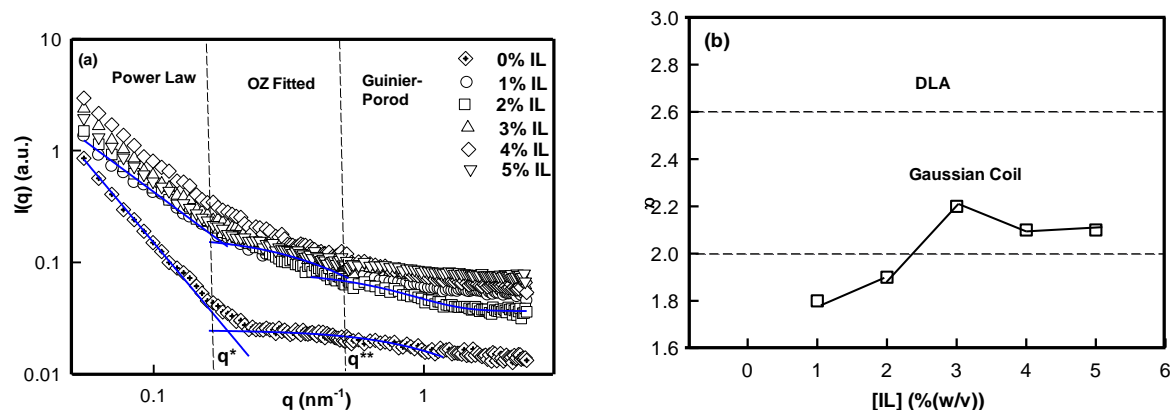


**Figure 3.14.** (a) Static structure factor  $I(q)$  measured by SANS for IL%(w/v) samples. Curves were fitted with power law, Ornstein-Zernike (OZ) function and Guinier-Porod function in different  $q$ -regions.(b) Variation of geometrical scattering factor  $\alpha$  with IL concentration.

It was pertinent to note that rod-like DNA strand, when got cladded with IL-molecules lost their rigidity to assume Gaussian coil conformation due to localized surface charge neutralization. Thus, the binding of positively charged imidazolium head groups to DNA resulted in softening the stiffness of the nucleic acid. DNA-protein binding has shown similar results earlier [61,69,70].

### 3.3.2.4 Rheology

The ionogel samples were subjected to dynamic rheology studies to evaluate their viscoelastic properties. Linear viscoelastic theory predicts that the storage modulus  $G'$  exhibits a frequency dependent dispersion behavior given by [71]

$$G'(\omega) = G_0 \omega^n \quad (3.13)$$

The exponent  $n$  lies between 0 and 2, with  $n=0$  corresponding to Hookean solid, and  $n=2$  representing a Maxwellian viscoelastic matter. Chemically cross-linked matured gels exhibit Hookean solid-like behavior, and  $G'$  is independent of frequency (exponent ' $n$ '=0). In physical gels (like in the present case) intense viscoelastic behavior is observed, and these do show frequency dependence, which we observed. At gelation point, the storage and loss moduli have the same exponent ( $G'(\omega) = G''(\omega) \sim \omega^n$ ). This dispersion data is depicted in Fig. 3.15.

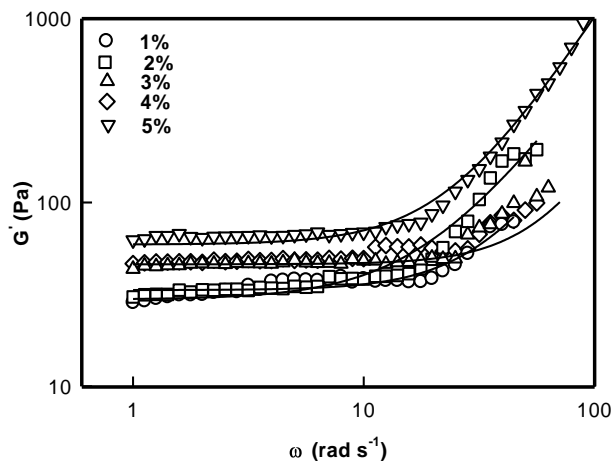


**Figure 3.15.** Storage  $G'(\omega)$  modulus of DNA ionogel is plotted as a function of frequency. Solid line is fitting to eqn (3.13).

Lodge et al have explained the self assembly of ion gels of tri-block copolymers and have extensively discussed the viscoelastic behavior of these chemically crosslinked gels [72]. Fig.

3.15 is a log-log plot depiction of eqn (3.13). Thus, the exponent ‘n’ could be determined from the slope of the line:  $\log G'(\omega) = G_0 + n \log \omega$ .

Two observations are clearly made from this data: (i) the low frequency storage modulus,  $G_0$  given by value of  $G'(\omega)$  at lowest frequency used in the experiment showed a characteristic dependence with  $G_0$  assuming a value  $\sim 27$  Pa for 1% and it sharply increased to  $\sim 70$  Pa for [IL]=5 % sample, and (ii) we found that the value of  $n=1.8 \pm 0.2$  was universal. These results clearly indicated that these ionogels were viscoelastic in nature irrespective of their actual [IL] concentration (Fig. 3.16, n-data) which constrained the self assembly of DNA to be hierarchical (Fig. 3.16,  $G_0$  data).

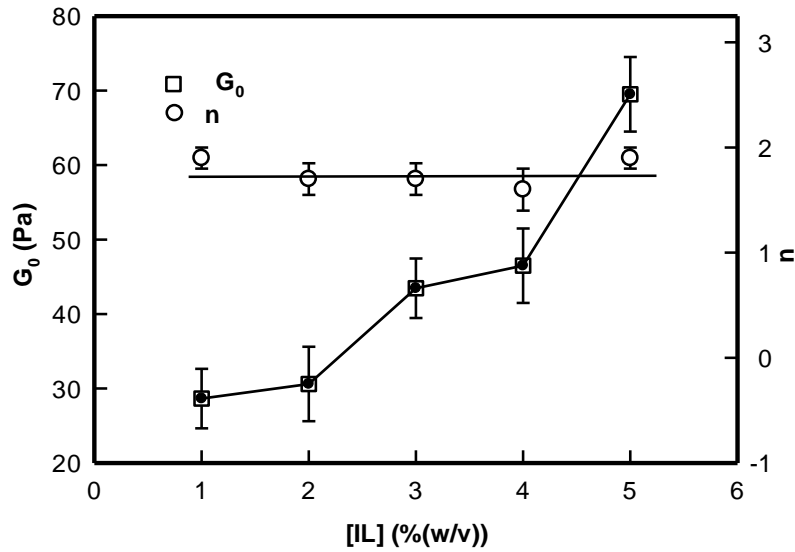


**Figure 3.16.** Variation of rigidity modulus  $G_0$  and frequency exponent  $n$  of ionogels shown as function of IL concentration. Solid lines are guide to the eye.

The gel phase can be visualized as a transient polymer network of viscoelastic length,  $\zeta_{el}$  through the relation given by [73]

$$G_0 \sim k_B T / \zeta_{el}^3 \quad (3.14)$$

The data in hand yielded  $\zeta_{el} \approx 45 \pm 3$  nm for  $[IL] = 1-3$  %; 38 nm for  $[IL] = 4\%$  and 35 nm for  $[IL] = 5\%$  ionogels. Thus, the networks got more compact with increase in IL concentration which imparted higher values to its storage modulus.

In the next step, isochronal temperature sweep experiments were carried out to characterize the melting profiles of these gels [55]. It was remarkable to observe that sharp transitions were found at two distinct temperatures. We shall refer to these as  $T_{melt}$  and  $T_{gel}$ , respectively. These  $T_{gel}$  values were consistent with the same determined from viscosity experiments. This is illustrated in Fig. 3.17. It was remarkable to note that  $T_{gel}$  could be raised (shifted) by  $\approx 7$  °C because of the presence of a tiny volume fraction of ionic liquid. Therefore, the ionogels are associated with a gelation zone that spans from 60 to 67 °C which will enable design of more flexible DNA based biomaterials in future.

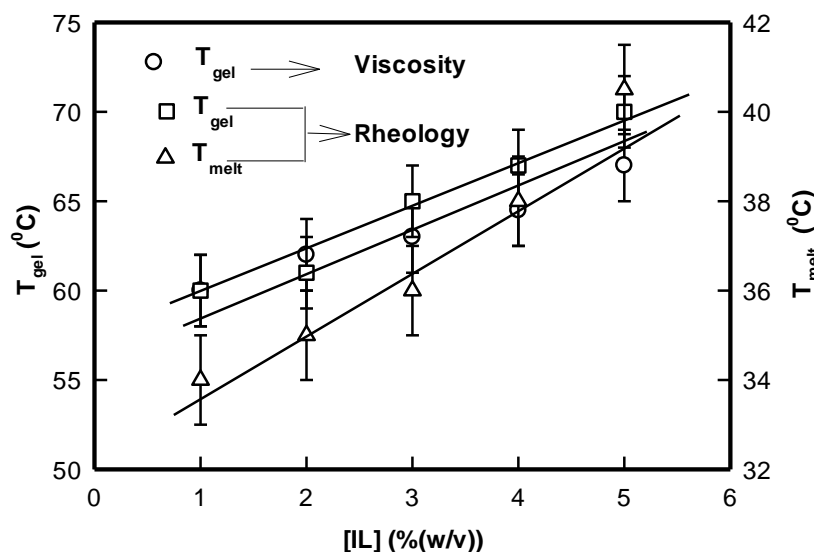
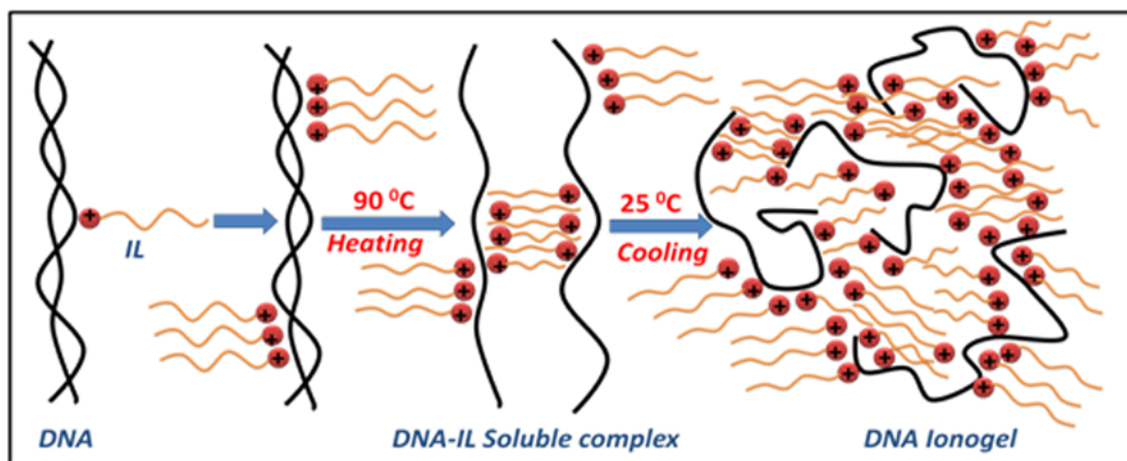


**Figure 3.17.** Variation of temperature of melting,  $T_{melt}$  and gelation,  $T_{gel}$  of DNA ionogels as a function of IL concentration obtained from rheology and viscosity.

Let us discuss the significance of  $T_{\text{melt}}$ . We did not observe an equivalent of  $T_{\text{melt}}$  from the viscosity data may be due to the poor resolution of the viscometer apparatus. However, it can be argued that initial self-organization of IL-cladded DNA strands formed primary transient networks with a characteristic enthalpy defined by  $T_{\text{melt}}$ . This temperature increased from 34 °C for 1% to 40 °C for 5% ionogel. Further,  $G_0$  value noted a decrease of typically 40% as this temperature was approached. Compared to this the drop in  $G_0$  value was almost 100% as  $T_{\text{gel}}$  was approached. Clearly, the gelation transition that occurred at  $T_{\text{gel}}$  was associated with a larger enthalpy compared to the melting transition encountered at  $T_{\text{melt}}$ . A schematic representation of DNA-ionogel is depicted in scheme 3.2.



**Scheme 3.2.** Schematic representation of formation of DNA ionogels (not to scale).

### 3.4 Part [C] [C8mim][Cl] based Low concentration DNA gel discussion

#### 3.4.1 Sample preparation

All ionogel samples were prepared by dissolving deionized water at 90 °C under constant stirring followed by normal cooling to room temperature, 25 °C. A set of ten samples were prepared with DNA concentration ranging from 0.1 to 1.0 % with the concentration gap of 0.1

between successive samples while keeping the IL concentration fixed at 1% (w/v). The presence of ionic liquid molecules hinders the base pairing leading to formation of ssDNA strands cladded with IL molecules ref. [55]. All gel samples appeared optically clear at room temperature. All concentrations are in (w/v) unless otherwise stated. Although the gel systems studied in this paper are hydrogels, we will refer to these as ionogels as ionic liquids were added as a second component to the continuous phase. These stock solutions appeared optically transparent to the eye. All measurement procedures were performed at room temperature (25 °C), and relative humidity in the laboratory was less than 50%.

### **3.4.2 Result of Discussion**

#### **3.3.2.1 Universality of sol-gel transition**

As the gelling sols were allowed to cool to room temperature from 90 °C, the cooling path was expected to follow the Newtonian cooling profile. During this process considerable reorganization of ssDNA strands took place; these IL cladded DNA strands formed physical crosslinks that led to the formation of finite size networks and gradually the system moved towards gelation. After the samples reached room temperature, these were inverted to notice for the flow of the meniscus. Samples that could sustain their weight against gravity (non-flowing meniscus) were the gel samples. The time-dependent growth of this network structure defined the gelation kinetics. This pathway was captured by continuous viscosity measurement performed on these samples.

For cross-linked polymer networks and gels, the scaling theory predicts universal growth exponents for various physically measurable parameters like, viscosity, network size, shear

modulus etc. as the sol approaches the gel phase [56,57]. In our case, the relevant scaling relation is given by (for  $t \rightarrow t_{gel}$ )

$$\eta_r \sim \varepsilon_1^{-k_1} \quad (3.15)$$

Here  $\eta_r = \eta/\eta_0$  and the sol and solvent viscosity are designated as  $\eta$  and  $\eta_0$  respectively. The reduced time  $\varepsilon_1 = \left(1 - \frac{t}{t_{gel}}\right)$ ,  $t < t_{gel}$ . Clearly, at the gel point  $t=t_{gel}$  the sol would exhibit a very high viscosity value. This data is shown in Fig. 3.18 (a) which was fitted to eqn (3.15) to determine the value for the exponent  $k_1$ . Analysis revealed  $k_1 = 0.50 \pm 0.10$  independent of DNA concentration. The observed value for  $k_1$  may be visualized qualitatively in the frame work of percolation theory [56,57]. This theory predicts that for Zimm dynamics (hydrodynamic interactions are neglected)  $k_1=0.7$  and for Rouse dynamics (hydrodynamic interactions are inclusive)  $k_1=1.3$ . Our value for  $k_1=0.5\pm 0.1$  is closer to Zimm model for network growth. Since, the value of this exponent remained invariant of DNA concentration, the existence of a universal pattern of self-assembly of DNA in the continuous medium cannot be ruled out.

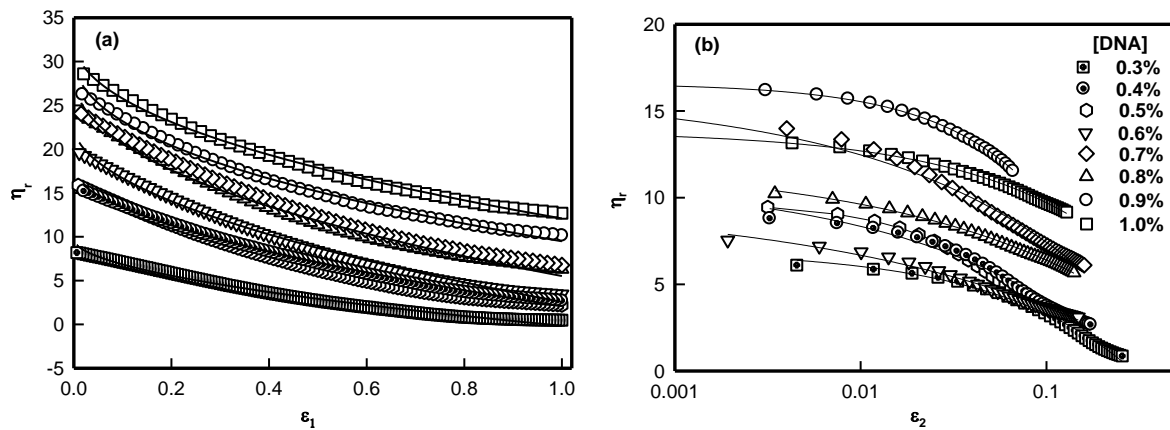


**Figure 3.18.** (a) Temporal evolution of relative viscosity shown as function of scaled time  $\varepsilon_1 = (1-t/t_{gel})$ . (b) Relative viscosity shown as function of scaled temperature  $\varepsilon_2 = (T/T_{gel}-1)$ . Solid lines are fitting of data to eqns. (3.15) and (3.16).

As has been mentioned earlier, gelation was induced by cooling the hot ionosol from 90 °C to room temperature of 25 °C. The variation of relative viscosity  $\eta_r$  with temperature is shown in Fig. 3.18 [74]. Once again, it is possible to scale the temperature axis using the relation ( $T \rightarrow T_{gel}$ )

$$\varepsilon_2 = \left( \frac{T}{T_{gel}} - 1 \right), T_{gel} < T \quad (3.16)$$

Here the gelation temperature  $T_{gel}$  was approached from  $T=90$  °C. Correspondingly, it was possible to define the temperature dependent evolution of relative viscosity  $\eta_r$  through a scaling relation equivalent to eqn (3.15) given by

$$\eta_r \sim \varepsilon_2^{-k_2} \quad (3.17)$$

The least squares fitting of data shown in Fig. 3.18 (b) to eqn (3.17) yielded the scaling exponent  $k_2 = 0.6 \pm 0.2$ . Once again  $k_2$  showed invariance with DNA concentration implying universal self-organization of ssDNA strands in the gelling sol. A second observation was dependence of  $T_{gel}$  on the DNA concentration (Fig. 3.19 (a)). When DNA content was increased from 0.30 to 1.0 %,  $T_{gel}$  increased systematically from 52 to 72 °C following a linear dependence given by

$$T_{gel} = T_0 \left( 1 + K_{T_{gel}} [DNA] \right) \quad (3.18)$$

Here  $T_0$  refers to  $T_{gel}$  at  $C^*$  which was the gelation concentration of DNA (=0.3%) in the IL solution. Since, the sol-gel transition was basically a process of re-organization of ssDNA strands in the ionic liquid solution,  $K_{T_{gel}} (\approx 0.52(\% w/v)^{-1})$  is a measure of intermolecular interaction (nearest neighbour). This large window of gelation temperature is remarkable, which could be achieved by addition of minute quantity of ionic liquid to the dispersion medium, the volume fraction of which did not exceed (0.01).



The respective gelation time  $t_{gel}$  changed in the range from 800 s to 300 s decreasing with DNA concentration (Fig. 3.19 (a)). Interestingly, gelation temperature could be correlated to gelation time to generate a linear dependence (slope= $0.03^{\circ}\text{C}\cdot\text{s}^{-1}$ ) shown in Fig. 3.19 (b) which implied early gelation for more concentrated sol samples. This observation is logical because with the propensity of ssDNA strands formation of a physically entangled network is highly probable because of closer proximity between the strands. At lower biopolymer concentration, this probability is much reduced, and hence the network formation will take much longer time. The dependence of  $t_{gel}$  was found to be linear with DNA concentration, and it was possible to describe this dependence through the relation given by

$$t_{gel} \text{ or } \tau_{EB} = t_0 \left( 1 + K_{t_{gel}} \text{ or } K_{\tau_{EB}} [\text{DNA}] \right) \quad (3.19)$$

As before we define  $t_0$  as gelation time for the sample corresponding to  $[\text{DNA}]=C^*$ . Fitting of data shown in Fig. 3.19(a) yielded  $K_{t_{gel}} = 0.78 (\% \text{ w/v})^{-1}$ . Relevance of ergodicity breaking time  $\tau_{EB}$  will be discussed later.

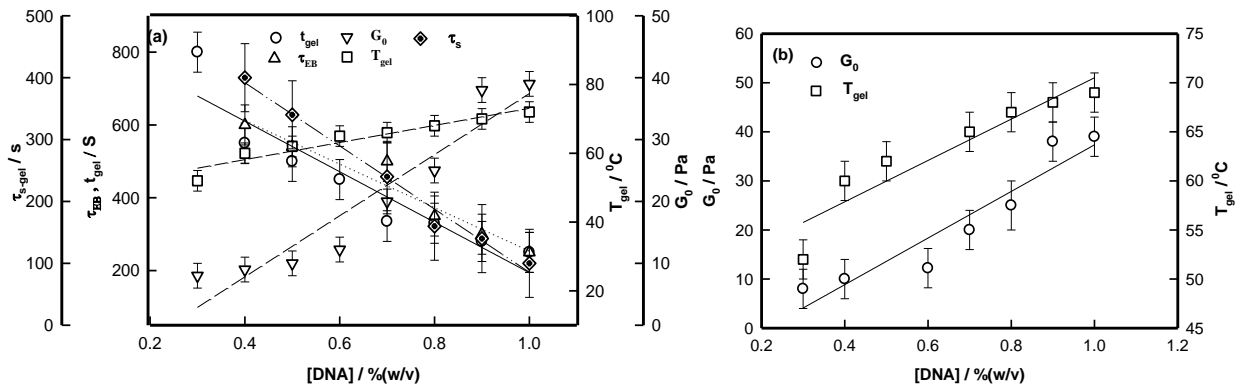


**Figure 3.19.** (a) Variation gelation time  $t_{s-gel}$  or  $t_{gel}$ , ergodicity breaking time  $\tau_{EB}$ , storage modulus  $G_0$ , and gelation temperature  $T_{gel}$  as function of [DNA] concentration and (b) variation of storage modulus  $G_0$ , and gelation temperature  $T_{gel}$  with [DNA] concentration. Solid lines are linear fitting of the data. See text for details.

### 3.3.2.2 Viscoelastic Behavior

The viscoelastic attributes of soft matter is best probed by dynamic oscillatory measurements (rheology). The ionogel samples were subjected to the following two distinct types of investigations: (i) isothermal frequency, and (ii) isochronal temperature sweep tests. The first yields the elastic response to applied variable shear deformation while the second test maps the melting profile of the material concerned. Linear viscoelastic theory defines the storage modulus of elasticity  $G'$  to scale with frequency of shear rate  $\omega$  given by [71,75]

$$G' \sim \omega^n \quad (3.20)$$

For a Hookean solid  $n=0$ , and it approaches as a value of 2 for a Maxwellian viscoelastic material. This dispersion data is depicted in Fig. 3.20 (a) and analysis of the data using eqn (3.20) gives value for  $n = 1.75 \pm 0.25$  independent of nucleic acid concentration. This clearly establishes the Maxwellian viscoelastic attributes of the soft ionogels. The gel rigidity is an important parameter for any potential application which is determined from the low-frequency storage modulus  $G_0$  given by

$$G_0 = \lim_{\omega \rightarrow 0} G'(\omega) \quad (3.21)$$

The variation of  $G_0$  with DNA concentration is illustrated in Fig. 3.20 (a) and  $G_0$  was found to increase from  $10 \pm 2$  Pa (for 0.3% DNA) to  $40 \pm 2$  Pa (for 1% DNA). Any gel with gel modulus value so low can be clearly defined as a soft gel. A coherent picture that emerges from this study revealed that the re-arrangement of ssDNA strands in the gel matrix was universal in self-assembly (because  $n$  was invariant), but was hierarchical in the biopolymer concentration (because rigidity increased with DNA concentration).

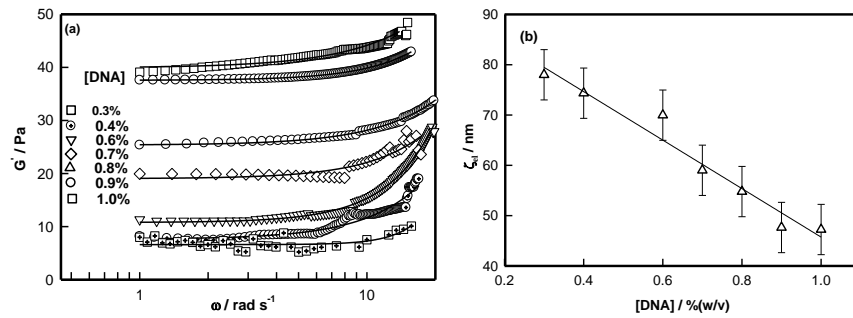


**Figure 3.20.** (a) Variation of elastic storage modulus  $G'$  shown as function of frequency, and (b) dependence of viscoelastic length on DNA concentration. Solid lines are fitting of data to eqns.(3.20) and (3.23), respectively.

Physically,  $G_0$  is a measure of elastic energy stored in the network of typical size  $\xi_{el}$ , which is often referred to as viscoelastic length is given by [73]

$$\xi_{el} = \sqrt[3]{\frac{K_B T}{G_0}} \quad (3.22)$$

Interestingly, this length parameter showed a linear dependence with DNA concentration with a negative slope (Fig. 3.20 (b)). This data could be represented by

$$\xi_{el} = \xi_0 + K_{\xi_{el}} [DNA] \quad (3.23)$$

Here,  $\xi_0$  is the viscoelastic length at  $[DNA] = C^*$ . The analysis of the data fitting inferred that  $K_{\xi_{el}} = 48.21 \text{ nm}/(\% [DNA])$  implying a monotonic decrease in the viscoelastic length with nucleic acid content. For the 1% DNA ionogel sample  $\xi_{el} = 45 \text{ nm}$  which increased to 79 nm for 0.3% sample.

The thermal profiling of these gels were conducted using isochronal temperature sweep experiments the data of which are presented in Fig. 3.21(a). In this study, the temperature dependent variation of  $G_0$  was measured. When the gel undergoes a phase transition (gel to sol) or melting transition (uncoiling of interpolymer complexes) a change in enthalpy is involved, which is manifested as a sharp change in the value of  $G_0$ . In Fig. 3.12(a), this is indicated by

arrows. Two clear transitions were detected, one in the low temperature (between  $\approx 40$ - $50$   $^{\circ}\text{C}$ ) and another in the higher temperature region (between  $50$ - $80$   $^{\circ}\text{C}$ ). These will be referred to as  $T_{\text{melt}}$  and  $T_{\text{gel}}$ , respectively.

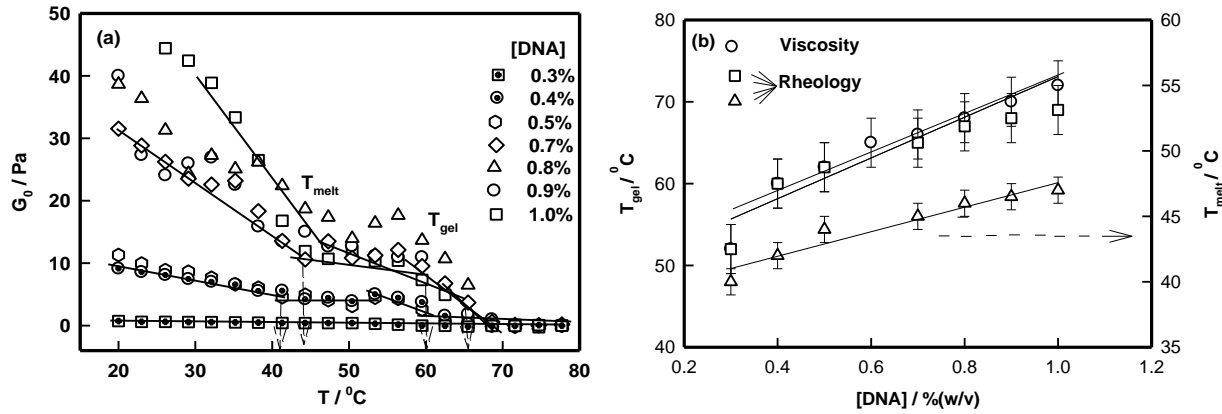


**Figure 3.21.** (a) Temperature dependent variation of  $G_0$ . Note the change in slope indicated by dotted arrows which correspond to  $T_{\text{melt}}$  and  $T_{\text{gel}}$  (see text for details). (b) Variation of temperature of melting,  $T_{\text{melt}}$  and gelation,  $T_{\text{gel}}$  of ionogels as a function of DNA concentration obtained from rheology and viscosity measurements.

Earlier works on DNA hydro- and ionogels have established that  $T_{\text{gel}} \approx 55$ - $60$   $^{\circ}\text{C}$  [15,55,76]. The other transition observed at lower temperature ( $T_{\text{melt}}$ ) was not reported earlier which we shall discuss later. It was remarkable to note that slopes of  $T_{\text{gel}}$  and  $T_{\text{melt}}$  versus [DNA] plots were linear with a value of  $K_{T_{\text{gel}}} = 0.52$   $^{\circ}\text{C}(\% \text{ w/v})^{-1}$  and  $K_{T_{\text{melt}}} = 0.33$   $^{\circ}\text{C}(\% \text{ w/v})^{-1}$  when the data were fitted to eqn (3.24).

$$T_{\text{gel/melt}} = T_{0_{\text{gel/melt}}} \left( 1 + K_{T_{\text{gel/melt}}} [\text{DNA}] \right) \quad (3.24)$$

Here the  $T_{\text{gel}}$  or  $T_{\text{melt}}$  temperatures for [DNA] =  $C^*$  is represented as  $T_{0_{\text{gel/melt}}}$ . The observed slope value implied that the gelation (also melting) temperature would increase by as much as  $2.4$   $^{\circ}\text{C}$  when the [DNA] was raised by a mere  $0.1\%$  (w/v). This would offer significant ability to

users to design tailored DNA gels for pharmaceutical applications. The parameter  $\Delta T = (T_{gel} - T_{melt})$  defines the gelling region during which reorganization of DNA strands occur in order to generate an interconnected network. Data in Fig. 3.21(a) yields  $\Delta T \approx 12^\circ C$  independent of DNA concentration indicating that the self-assembly process was universal.

The viscosity data could not capture the transition pertaining to  $T_{melt}$  that resided in the typical temperature window of 40-50  $^\circ C$  may be due to the poor resolution offered by the instrument. It needs to be noted that at  $T_{gel}$  the  $G_0$  value dropped by typically 80%, while at  $T_{melt}$  it was closer to 50%. Since,  $G_0$  is a measure of elastic energy per unit volume, it accounts for transition enthalpy directly. Therefore, the change in enthalpy at  $T_{gel}$  was much larger than the same at  $T_{melt}$ . Since, the gelation transition involved a distinct enthalpy, it may be construed as a first-order phase transition.

### 3.3.2.3 Relaxation Dynamics

The structural phase transition occurring during gelation was probed by dynamic light scattering measurements where the density fluctuations were captured in the dynamic structure factor (electric field correlation,  $g_1(\tau)$ ) data. It was noticed that the correlation functions did not relax to their equilibrium values at large delay times for measurements taken after  $t > t_{gel}$  which clearly implied dynamic arrest of the fluctuations. Therefore, the sample in the sol state (ergodic state,  $\lim_{\tau \rightarrow \infty} g_1(\tau) = 0$ ) transitioned to the non-ergodic state ( $\lim_{\tau \rightarrow \infty} g_1(\tau) > 0$ ) on gelation, where the ergodicity was broken precisely at gelation time. We shall refer to this characteristic time as ergodicity breaking time  $\tau_{EB}$ . Such behavior has been noticed in several gelling systems pertaining to polymers and colloids [77,78]. The state of ergodicity of a sample can be quantified from the measured  $g_1(\tau)$  data as follows [77,78]

$$\lim_{\tau \rightarrow 0} g_1(\tau) - \lim_{\tau \rightarrow \infty} g_1(\tau) = \chi \quad (3.25)$$

Clearly,  $0 \leq \chi \leq 1$  implying that when  $\chi$  value deviates from 0 and approaches 1, the sample moves from an ergodic to a non-ergodic state. In the present case these two states are identified as ionosols, and their gels. The evolution of the dynamic structure factor with waiting time  $t_w$ , ( $t_w \rightarrow t_{gel}$ ) is shown [74]. The  $\chi$ -parameter obtained from the data is plotted in Fig. 3.22(a) which indicates a distinguishable transition at well-defined time, called ergodicity breaking time  $\tau_{EB}$ . Fig. 3.22 (a) shows plot of  $\tau_{EB}$  and  $t_{gel}$  as function of DNA concentration, and the excellent linearity is endorsed by eqn. 3.24 which yielded  $K_{\tau_{EB}} = 0.70 \text{ s}(\% w/v)^{-1}$ . A second observation was  $t_{gel} \approx \tau_{EB}$  to a remarkable accuracy which implied that the gelation process was concomitant with dynamic arrest of density fluctuations in the samples.

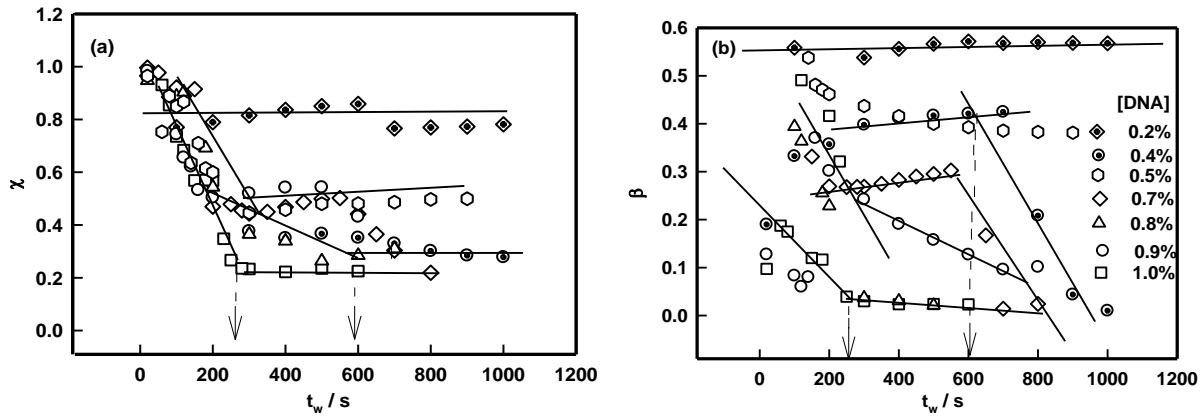


**Figure 3.22.** (a) Variation of  $\chi$  with waiting time  $t_w$  for different DNA concentration. (b) Variation of stretch parameter  $\beta$  as a function of waiting time,  $t_w$ . The point where there is a change in the value of  $\chi$  (arrows) defines the ergodicity breaking time  $\tau_{EB}$  for plot (a) and  $\tau_\beta$  for plot (b).

The  $g_1(t)$  data was empirically fitted to the following function given by

$$g_1(t) = A \exp\left(-\frac{t}{\tau_f}\right) + (1 - A) \exp\left(-\frac{t}{\tau_s}\right)^\beta \quad (3.26)$$

where the strengths of fast and slow modes, and their relaxation times are defined as  $A$ , and  $(1-A)$ , and  $\tau_f$ , and  $\tau_s$ , respectively.

In the analysis of  $g_1(t)$  data from DLS experiments, at long wavelengths in the gel regime, the first term on the right-hand side, which is the short-time behavior defines the cooperative diffusion. This relaxation originates from the concerted diffusive motion of polymer chains/segments relative to the solvent [68,79,80].

The variation of  $\tau_f$  with waiting time  $t_w$  is shown in Fig. 3.23 (a) which is invariant of DNA concentration.

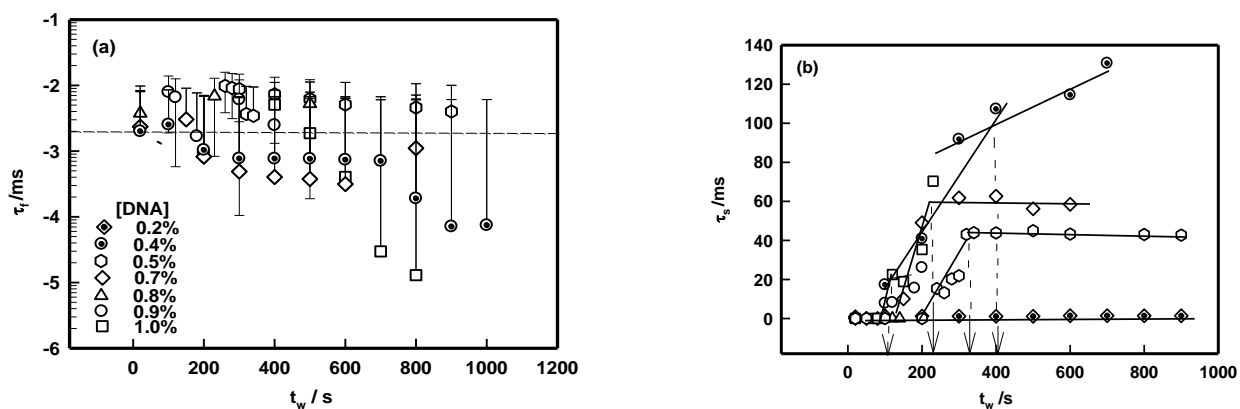


**Figure 3.23.** Plots of relaxation time of fast (a), and slow modes (b) with waiting time,  $t_w$  shown for different DNA concentration. Note the invariance of fast mode relaxation time,  $\tau_f$  with DNA concentration. The slow mode relaxation time,  $\tau_s$  showed change of slope at the time of dynamic arrest (arrows).

The slow mode relaxation time was typically 1000 times larger than the corresponding fast mode values. Fig. 3.23 (b) data indicates initial increase in the  $\tau_s$  value followed by a plateau for all samples where the diffusion process remained arrested. This increase occurred at a time

that exactly corresponded to the  $t_{\text{gel}}$  (see Fig. 3.19 (a)). We shall refer to this as  $\tau_{\text{s-gel}}$ . Remarkably, it was found that  $t_{\text{gel}} \approx \tau_{\text{EB}} \approx \tau_{\text{s-gel}} \approx \tau_{\beta}$ .

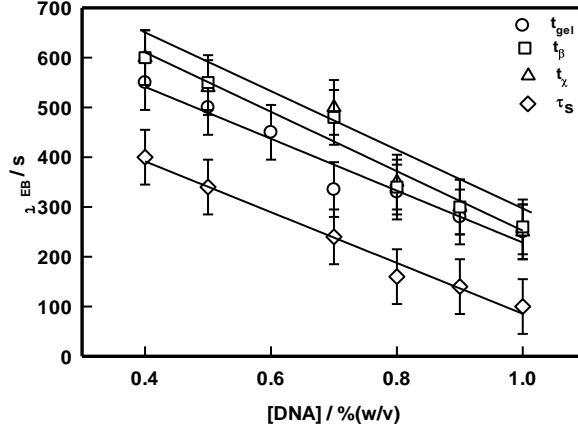


**Figure 3.24.** Combined plot of ergodicity breaking time (deduced from  $\chi$ ,  $\beta$  and  $\tau_{\text{s}}$ ) and  $t_{\text{gel}}$  with DNA concentration for ionogel samples. Note that  $\tau_{\text{s}}$  determined ergodicity breaking time was about 300 s lower than others, See text for details.

The onset time of this arrest was measured (shown as arrows) and it could be correlated with the  $t_{\text{gel}}$  and  $\tau_{\text{EB}}$  data (Fig. 3.24). Indeed, the  $\tau_{\text{s}}$  determined ergodicity breaking time was about 300 s faster than others. This difference can be explained as follows: viscosity and rheology are macroscopic studies and these probe the fluidity (or viscoelasticity) over a typical length scale of microns while in the DLS studies the samples are probed on a length scale  $\sim 1/q$ , which is  $\sim 500$  nm. Thus, the dynamics registered in the slow mode pertained to “local motion” of the moieties on submicron length scale. Therefore, it can be argued that the dynamic arrest of fluctuations were initiated locally on submicron length scales that eventually spread to microscopic dimensions pervading the whole space with waiting time.

The slow mode relaxation was expressed as a stretched exponential function in eqn (3.26) with a characteristic exponent  $\beta$ . It defines the heterogeneous dynamics of disordered systems. In fact,  $0 \leq \beta \leq 1$ , accounts for the width of the distribution of relaxation times and it is interpreted



as a measure of inhomogeneity or disorder effects present in the sample. The specific value of  $\beta$  depends on the topological dimension of the inhomogeneity. The mean relaxation time  $\bar{\tau}$  in this framework is given by [81,82]

$$\tau_s = \bar{\tau} = \frac{\tau}{\beta} \Gamma\left(\frac{1}{\beta}\right) \quad (3.27)$$

Where  $\Gamma\left(\frac{1}{\beta}\right)$  is the gamma function. In this framework, the slow mode relaxation time  $\tau_s$  is often associated with the chained is engagement relaxation. We determined the value of this exponent  $\beta$  by fitting the  $g_1(\tau)$  data to eqn (3.26) and the obtained values are plotted in Fig. 3.22(b) which is very revealing. Again, one observes a sharp change in slope in the  $\beta$  versus  $t_w$  plot occurring at certain characteristic times  $t_\beta$  which is plotted in Fig. 3.24, and it shows remarkable match with  $t_{\text{gel}}$  and  $\tau_{\text{EB}}$  data implying that  $t_\beta$  was an alternative measure of ergodicity breaking time. Further, it implied that topological dimension of the inhomogeneity changed as gelation was approached. Thus, we have estimated the ergodicity breaking time from three independent properties of the dynamic structure factor and these were found to be identical, i. e.  $t_{\text{gel}} \approx \tau_{\text{EB}} \approx t_\beta$ .

### 3.3.2.4 Small Angle neutron Scattering

Microstructure of low concentration DNA ionogels were probed by small angle neutron scattering (SANS). The statics structure factor data for different samples is shown in Fig. 3.25. This data was divided into three distinct regions: (i) Power-law ( $0.0552 \leq q \leq 0.1951 \text{ nm}^{-1}$ ), (ii) Ornstein- Zernike ( $0.2024 \leq q \leq 0.6317 \text{ nm}^{-1}$ ) and (iii) Guinier-Porod ( $0.6609 \leq q \leq 2.3480 \text{ nm}^{-1}$ ) on the basis of best-fit criteria. Thus,

$$I(q) = I_{\text{PL}} q^{-\alpha} + \frac{I_{\text{OZ}}}{(1+\xi^2 q^2)} + I_{\text{GP}} \exp\left(-\frac{R_c^2 q^2}{2}\right) \quad (3.28)$$

The Power-law, Ornstein- Zernike and Guinier-Porod functions are represented by the first, second and third term of LHS in eqn (3.28), respectively.

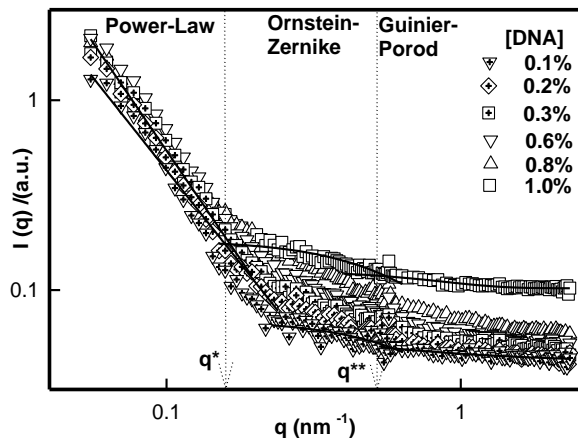


**Figure 3.25.** Static structure factor profile for different samples determined from SANS experiments. Solid lines are fitting of the data to eqn (3.28).

Here  $I_{PL}$ ,  $I_{OZ}$  and  $I_{GP}$  are  $q$  independent pre-factors, and  $\alpha$  corresponds to geometry of scattering moiety,  $\xi$  is mess size or correlation length and  $R_c$  is cross sectional radius of DNA. The analysis of SANS data for low  $q$  region ( $0.0552 \leq q \leq 0.1951 \text{ nm}^{-1}$ ) analysed by Power-law function gives the value of  $\alpha \approx 2.0 \pm 0.1$  (Fig.3.26 (a)), a result, which is consistent with the Gaussian coil type conformation.

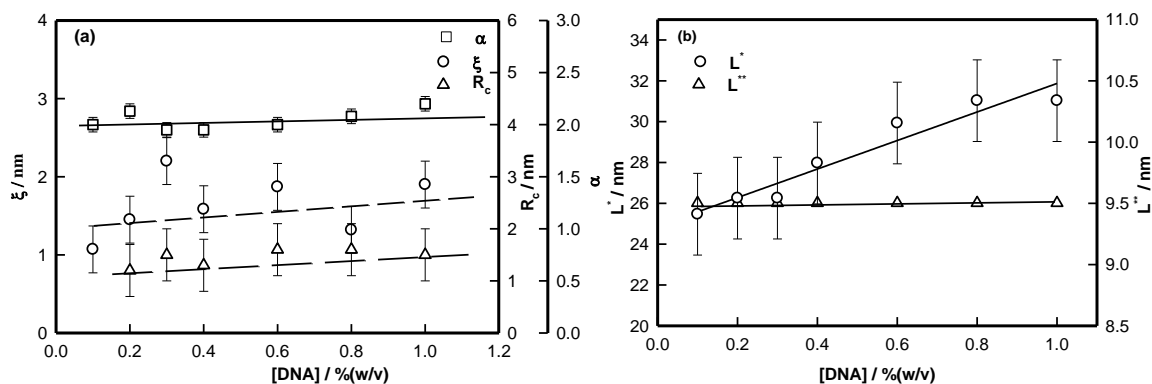
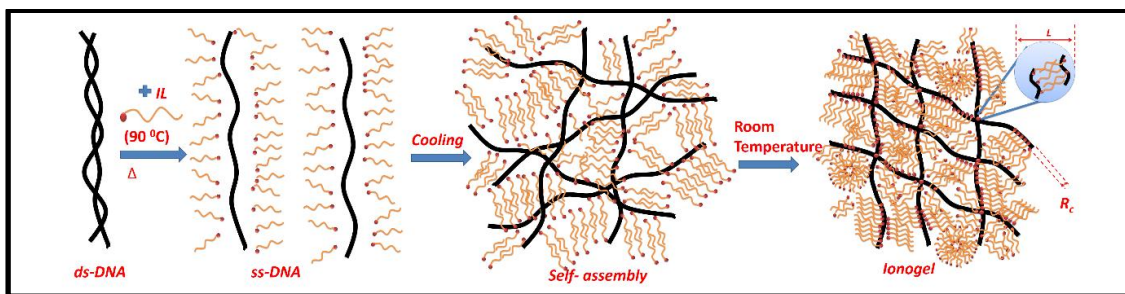


**Figure 3.26.** (a) Variation of  $\alpha$ ,  $\xi$  and  $R_c$ , and (b) crossover lengths  $L^*$  and  $L^{**}$  shown for different DNA concentrations. Solid lines are linear fit of data. See text for details.

Ornstein - Zernike (OZ) model was used to determine the mesh size of the samples which was best fitted in intermediate scattering regime ( $0.2024 \leq q \leq 0.6317 \text{ nm}^{-1}$ ). The value obtained was  $\xi \approx 1.5 \pm 0.5 \text{ nm}$ . Far  $q$ - domain reveals the chain cross section of coil. The Guinier- Porod relation yielded the cross-section radius  $R_C$ . The fitting of data in this asymptotic range ( $0.6609 \leq q \leq 2.3480 \text{ nm}^{-1}$ ) assigned a value to  $R_C \approx 1.4 \pm 0.3 \text{ nm}$ . The length scales  $L^* (=2\pi /q^*)$  and  $L^{**} (=2\pi /q^{**})$  or characteristic crossover lengths corresponding to the boundaries between various regions was determined from the SANS data (Fig. 3.26 (b)). The power-law to OZ crossover was located at  $L^* = 26 \pm 4 \text{ nm}$ . This boundary demarcated the persistent region from the gel domain. On the other hand, the crossover from the gel to the Porod region was detected at  $L^{**} = 10 \pm 2 \text{ nm}$ , and it remained invariant of DNA concentration. The typical persistence length of DNA is  $l_p = 50 \text{ nm}$  [15]. Therefore, the  $l_p \approx 2L^* \approx 5L^{**}$ . These structural parameters are compared with same of other type of DNA gels, and the differential behaviours are highlighted in Table 3.1.

### 3.3.2.5 Phenomenology of Gelation

dsDNA sample which was heated to  $90 \text{ }^\circ\text{C}$  in water to dissociate the base pairs. Hot IL was added to this preparation to quench the base pair binding sites (nucleotides) with the imidazolium head groups of the IL molecules. Hydrogen bonds were formed between the nucleotides and nitrogenous groups present in the imidazolium component of IL. This cladding helped in keeping the two ssDNA strands separate, and renaturation was avoided. Further, the hydrophobic tails of IL molecules overlapped to avoid contact with water forging labile hydrophobic bonds between pairs of ssDNA chains. This allowed for the physical entanglement of the chains to come into existence. This has been conceptualized in a schematic shown in Scheme 3.3.



**Scheme 3.3.** Representation of self-assembly and formation of DNA ionogels.

The theory of polymer solutions correlates the mesh size of the gel network to solvent quality through the relation given by [68,79,80]

$$\xi = R_g \left( \frac{C}{C^*} \right)^{-\left( \frac{\nu}{1-3\nu} \right)} \quad (3.29)$$

Here, the radius of gyration of the polymer chain is  $R_g$  ( $\approx 150$  nm for DNA [7]), polymer concentration is  $C$ , molecular weight is  $M$ , and  $\nu$  is the molecular weight exponent ( $R_g \sim M^\nu$ ). In our case,  $\xi = 1.5 \pm 0.5$  nm, which yields  $\nu = 0.38 \pm 0.05$ . Similar calculations done for DNA hydrogel using ref. [15,76] data, and for DNA ionogel (in 1-octyl-3-methylimidazolium chloride solution, [C2mim][Cl]) using ref. [55] data assigns  $\nu = 0.34$  (to hydrogel) and 0.42 (to [C2mim][Cl] ionogel) samples. Thus, within experimental error, one observed a universal value for the solvent quality parameter ( $\nu = 0.37 \pm 0.05$ ) indicating the gelation transition was in fact a first-order phase transition involving deterioration of solvent quality from good ( $\nu > 0.5$ , for ionosol) to poor ( $\nu < 0.5$ , for ionogel) solvent environment.

The relative comparison of [C8mim][Cl] based ionogel with [C2mim][Cl] based ionogel and corresponding hydrogel of DNA are listed in Table 3.1.

**Table 3.1:** Comparison of physical parameters of DNA hydrogel, [C2mim][Cl] and [C8mim][Cl] based ionogel.

S. No.	Parameters	Hydrogel	Ionogel in [C2mim][Cl]	Ionogel in [C8mim][Cl]	Significance of this work
1	$C_{gel}$ / % (w/v)	2%	1%	0.3%	Low gelation concentration
2	$T_{gel}$ ( $^{\circ}$ C)	34	60	55-75	Tunable gel region
3	$T_{melt}$ ( $^{\circ}$ C)	-	40	45-47	Wider gel domain
4	$G_0$ (Pa)	20 $\pm$ 2	29 $\pm$ 2	10 $\pm$ 2 to 40 $\pm$ 2	Tunable gel strength
5	$\xi$ (nm)	1.6 $\pm$ 0.5	3.0 $\pm$ 0.5	1.5 $\pm$ 0.5	Constricted network

Table-3.1 data indicates several advantages of the ionogels undertaken for study in this work. The special feature of attaining gelation at such remarkably lower DNA concentration will enable widening of the application potential of this biomaterial.

### 3.5 Part [D]: Effect of $\gamma$ -radiation on DNA ionogel: Structure-property evaluation

#### 3.5.1 Sample preparation

DNA was dissolved in deionized water at 60 $^{\circ}$  C and heated up to 90 $^{\circ}$  C under continuous stirring to obtain a optically clear solution. Then, these sols were allowed to cool to room temperature 25 $^{\circ}$ C and these were ready for  $\gamma$ -irradiation with doses of 20 to 100 Gy. The irradiation of the samples was done at the  $\gamma$ -irradiation chamber (model GC 1200, BRIT, India) at the Inter University Accelerator Center, New Delhi. In this instrument Cobalt-60 (1.33 MeV) is used as a source of radioactive material in the lead shielded  $\gamma$ -chamber when the samples were exposed to different doses (20 - 100 Gy) of radiation. Energy of incident  $\gamma$ -irradiation was 6.8 KGy /hr. 1%

(w/v) of ionic liquid was added to these  $\gamma$ -irradiated DNA sols which on waiting turned into gels.

In the absence of IL, these solutions did not gel.

### **3.5.2 Result and Discussion**

#### **(A) Gamma Irradiated DNA solution**

##### **3.5.2.1 Secondary Structure**

The procured nucleic acid samples had dsDNA with a well specified base pair designation. The biological activity of this molecule was heavily affected on exposure to ionizing radiation due to secondary structure alteration. The pertinent query is do these  $\gamma$ -irradiated DNA strands undergo gelation? This was ascertained systematically in this study. Therefore all gamma treated samples was taken for CD measurement.

The UV-Vis spectroscopy data of  $\gamma$ -irradiated DNA-IL samples exhibited characteristic absorption peaks at 260 nm. The data analysis revealed that there was change in amplitude of the peak when radiation dose was increased from 0 to 100 Gy of radiation dose. Since, the fragmented DNA had distorted base-pairs the net absorbance at 260 nm became weaker and weaker as the extent of fragmentation increased. This is clearly seen from Fig. 3.27.

The binding to secondary structure of DNA is seen in many biological processes. Therefore,  $\gamma$ -irradiated DNA sol was subjected to investigation of circular dichroism in order to find the effect of binding on the helix content. The obtained fuzzy data of CD made it difficult for any quantitative analysis of secondary structure of the DNA. Therefore UV visible spectroscopy was chosen as an alternative option for representative information for secondary structure taken at 260 nm.

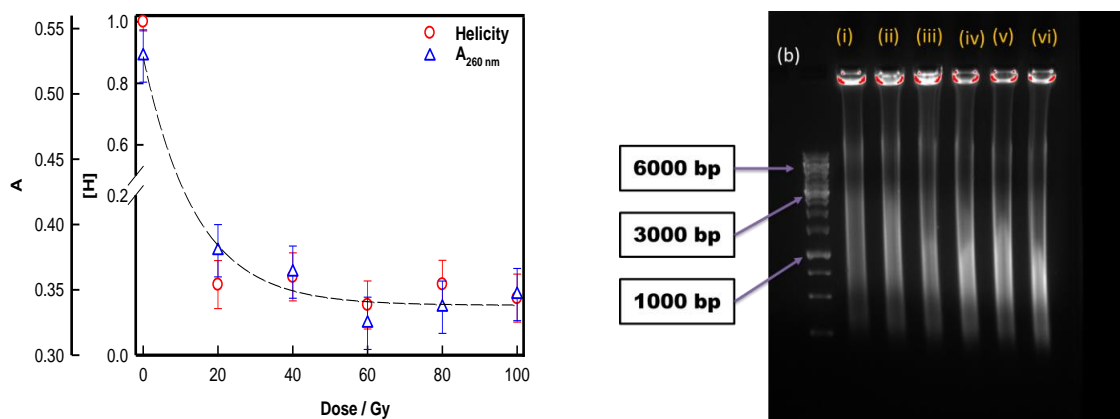


**Figure 3.27.** (a) Absorbance and helicity for DNA ionogel at different  $\gamma$ -irradiation dose. (b) Agarose gel electrophoresis showing the confirmation of fragmentation of DNA. (i) – (vi) represent samples exposed to radiation dose of 0, 20, 40, 60, 80, and 100 Gy.

The representative helicity [H] is defined as

$$[H] = |A_m - A_c| / |A_s - A_c| \quad (3.30)$$

Here it is assumed that the DNA has a helicity proportional to the UV absorbance value  $A_s$ .  $A_m$  and  $A_c$  shows the absorbance of the sample and ssDNA solution, respectively.  $A_c$  was measured on a DNA solution heated to 60 °C. Fig. 3.27 shows that DNA helicity decreased as  $\gamma$ -irradiation dose increased. Loss of helicity could be directly related to DNA fragmentation. This was ascertained from gel electrophoresis studies.

### 3.5.2.2 Agarose gel electrophoresis

Sambrook *et al* [83] have described Agarose gel electrophoresis protocol for DNA. DNA samples were inserted in 1% agarose gel which was prepared in 40mM Tris-Acetate and 1.0 mM EDTA (1X TAE) buffer (pH = 8) by heating then cooling to 45 °C. 0.5  $\mu\text{g ml}^{-1}$  ethidium bromide was used to stain the gel. Gel electrophoresis study was carried out at 5 V/cm in TAE buffer.

Gamma treated DNA sample was visualized on transilluminator at 302 nm. The molecular weight determined by ultracentrifugation was equivalent to for 2000 bp. The dose dependent fragmentation pictures are depicted in Fig. 3.27(b). It was clearly confirmed that the fragmentation of DNA. This data clearly indicated that  $\gamma$ -radiation induced fragmentation in DNA.

## (B) Gelling behavior of Gamma treated Solutions

### 3.5.2.3 Viscosity Measurement

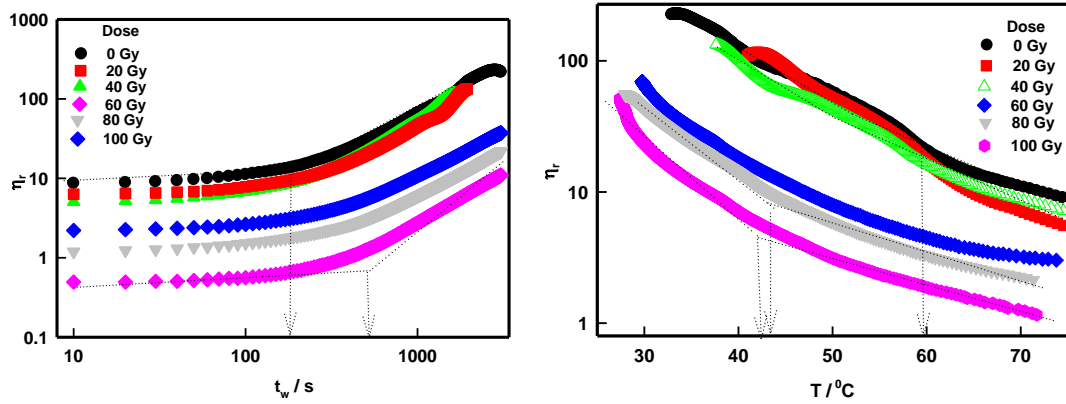


**Figure 3.28.** (a) Change in relative viscosity  $\eta_r$  with (a) waiting time  $t_w$  and (b) temperature for ionogels made with different  $\gamma$ -irradiation dose.

1% (w/v) ionic liquid was added to gamma treated DNA sols. To map the gelation behavior of these samples (Fig. 3.8 (a)) temporal evolution of relative viscosity  $\eta_r$  ( $= \eta / \eta_0$ , where  $\eta$  is solution and  $\eta_0$  is solvent viscosity) and temperature dependent relative viscosity (Fig. 3.28 (b)) was characterized for different samples. The slope obtained corresponding to time of gelation  $t_{gel}$  when one used the scaling relation to describe the network growth which is given by,

$$\eta_r = \varepsilon^{-k}, \quad t < t_{gel} \quad (3.31)$$

Where  $\varepsilon = t / t_{gel}$  and  $k$  is a universal scaling exponent.



It was found that when the radiation dose increased from 0 to 100 Gy, the viscosity of ionic sol decreased continuously. The relative viscosity data was fitted by scaling relation given by eqn 3.31 and we obtained a power-law exponent  $k$  that described the time-dependent growth of the network (Fig. 3.29 (a)). Interestingly it is seen that as radiation dose increased from 0 to 60 Gy the time of gelation increased from 400 s to 600 s and after that it changed to 800s as the dose reached 100 Gy. The value of exponent  $k$  (Fig. 3.29 (b)) varied 0.6 to 0.7 all the while. For cross-linked gels, the Rose dynamics gives the value of  $k = 0.7$  for conducting network and 1.3 for percolating network [56–58]. Therefore, the obtained value of  $k$  gives qualitative analysis of gelation kinetics.

The temperature dependent viscosity data is shown in Fig. 3.28 (b) reflect that on raising the radiation dose from 0 to 100 Gy the temperature of gelation decreased from  $60^{\circ}$  to  $43^{\circ}$  C. Therefore increase in radiation dose within same samples was able to tune the temperature of gelation (by  $\sim 17^{\circ}$ C).

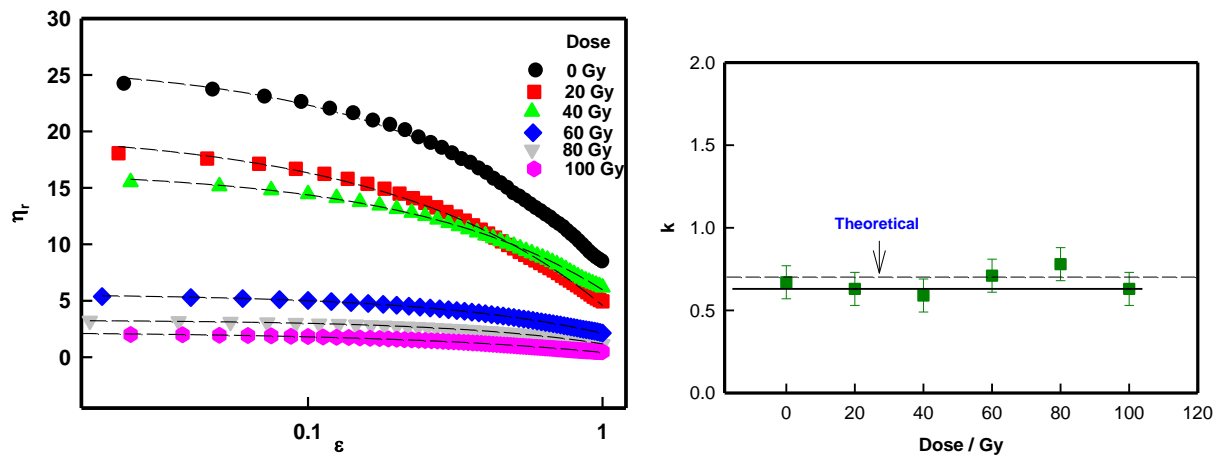


**Figure 3.29.** (a) Variation of relative viscosity  $\eta_r$  with (a) reduced time ( $\epsilon = 1 - t/t_{gel}$ ) and (b) power law fitting exponent  $k$  for different  $\gamma$ -irradiated samples.

### 3.5.2.4 Dynamic Arrest

The relaxation dynamics in these ionic liquid based samples were probed by dynamic light scattering with the objective to map the growth kinetics. For this study the heated ionosol samples (~60<sup>0</sup> C) were subjected to DLS measurements. The intensity correlation functions were systematically measured and collected until the samples became gel. The measured normalized intensity correlation function was converted to dynamic structure factor  $g_1(t)$  using the protocol given by [84]. The best least-squares fitting to the structure factor data was obtained for the following mathematical function

$$g_1(t) = A \exp\left(-\frac{t}{t_f}\right) + (1 - A) \left[ \exp\left(-\left(\frac{t}{t_s}\right)^\beta\right) \right] \quad (3.32)$$

Here A and (1-A) are relative amplitude of the two relaxation modes having relaxation times  $t_f$  (fast) and  $t_s$  (slow), respectively, and  $\beta$  is stretch parameter or width of the slow mode relaxation time distribution function. There is transition from ergodic (or random) to non-ergodic (or arrested) state when gelation occurs in the system and mobility of polymer chains get severely restricted. Due to the ensuing crosslinking network relaxation modes dominate. This arrest behavior can be captured from the dynamic structure factor data. The ergodicity parameter  $\chi$  can be determined from the from the following relation

$$\chi = \lim_{t \rightarrow 0} g_1(t) - \lim_{t \rightarrow \infty} g_1(t) \quad (3.33)$$

The value of  $\chi$  lies between 0 and 1. For an ergodic system  $\chi=1$  and it approaches 0 as dynamic arrest is reached. Change in ergodicity and stretch parameter with waiting time  $t_w$  for different irradiated samples is shown in Fig. 3.30. The ergodicity breaking time  $\tau_{EB}$  (qualitatively same as gelation time,  $t_{gel}$ ) varies from 440 to 1500 s. Which means as radiation dose increased from 20 to 100 Gy transition from random to arrested phase became slower. Therefore, highly fragmented DNA strands were difficult to gel.

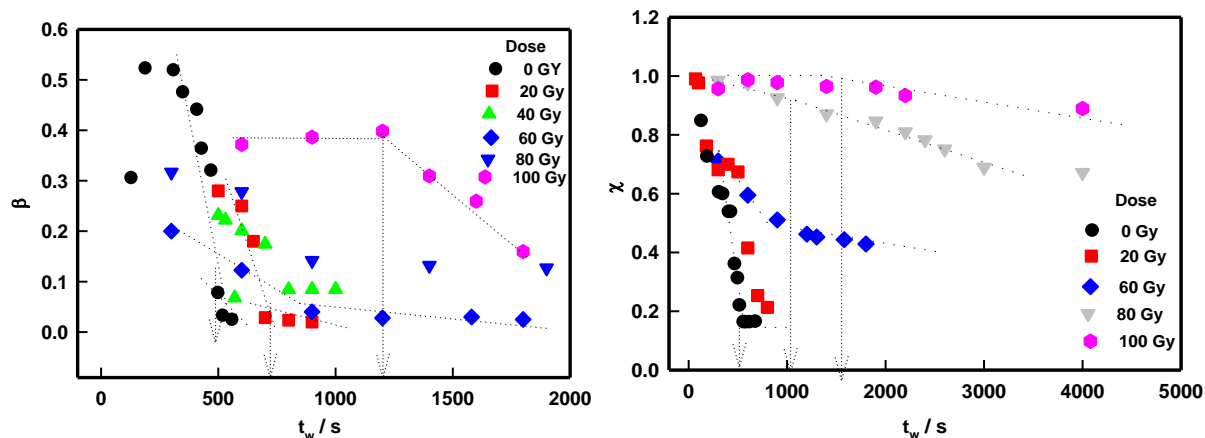


**Figure 3.30.** (a) Variation of stretched parameter  $\beta$  and (b) ergodicity parameter  $\chi$  with waiting for different radiated samples. Arrows indicate ergodicity breaking time.

Ergodicity breaking time determined from DLS and viscosity measurement (gelation time) were found to be linearly dependent on the dose of gamma radiation (Fig. 3.31). Therefore, the network growth and gelation *per se* got effected due to the structural change in DNA caused by exposure to gamma radiation.

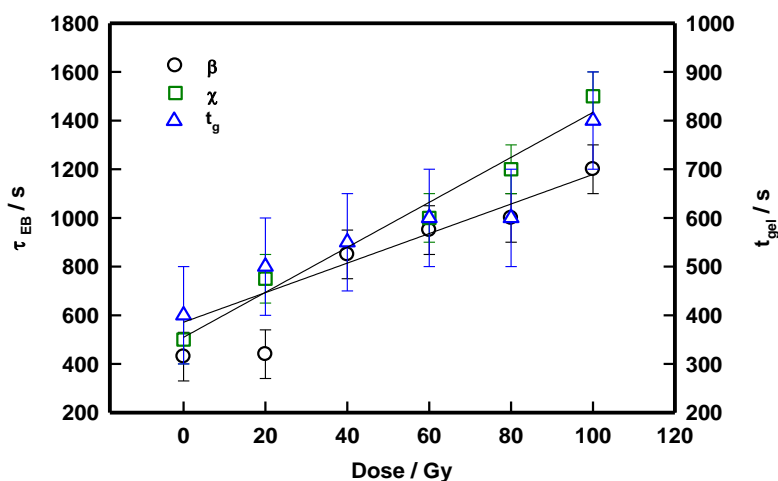


**Figure 3.31.** Variation of ergodicity breaking time  $t_{EB}$  (determined from  $\beta$  and  $\chi$ ) and time of gelation  $t_{gel}$  (determined from viscosity measurement) shown for different  $\gamma$ -irradiated samples.

### 3.5.2.5 Viscoelastic properties

Viscoelastic characteristics of  $\gamma$ -irradiated ionogels were probed by rheology measurement. The dispersion profile of the storage modulus  $G'$  exhibited a frequency  $\omega$  dependent behavior given by the scaling law [71,73,75]

$$G'(\omega) \sim \omega^n \quad (3.34)$$

Where the exponent  $n$  varies between 0 (Hookean solid) and 2 (Maxwellian viscoelastic material). The dispersion behavior of  $G'(\omega)$  is depicted in Fig. 3.32, and the data was fitted to power law eqn (3.33) which yielded the value of the exponent  $n$ . For ionogels  $n = 1.60 \pm 0.4$  indicating the viscoelastic nature of this material. Further,  $G' \gg G''$  for all the cases which implied the materials were gels.

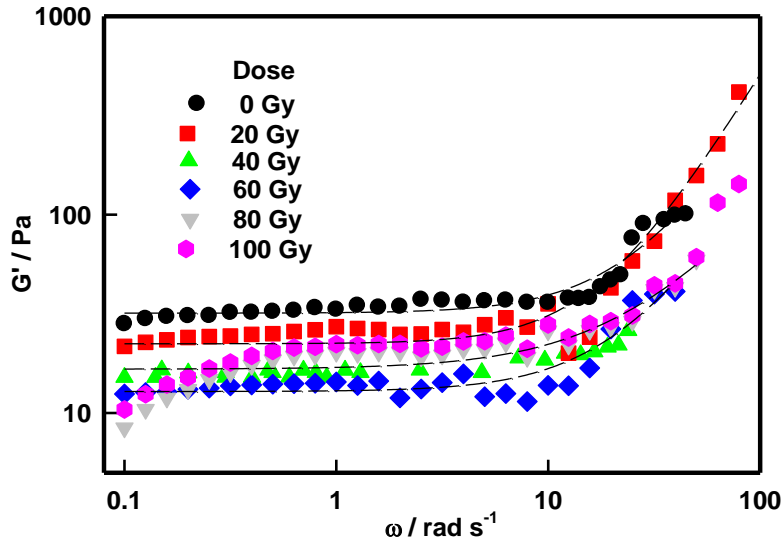


**Figure 3.32.** Variation of storage modulus  $G'$  with frequency for different  $\gamma$ -irradiated ionogels. Solid lines are fitting of the data to eqn (3.34).

The low frequency storage modulus,  $G_0$  is given by

$$G_0 \approx \lim_{\omega \rightarrow 0} G'(\omega) \quad (3.35)$$

This accounts for the rigidity of the gel. The data in Fig. 3.33 shows that  $G_0$  decreased from 30 Pa (at 0 Gy) to  $\approx 10$  Pa (at 100 Gy) clearly indicating loss of network structures due to radiation.

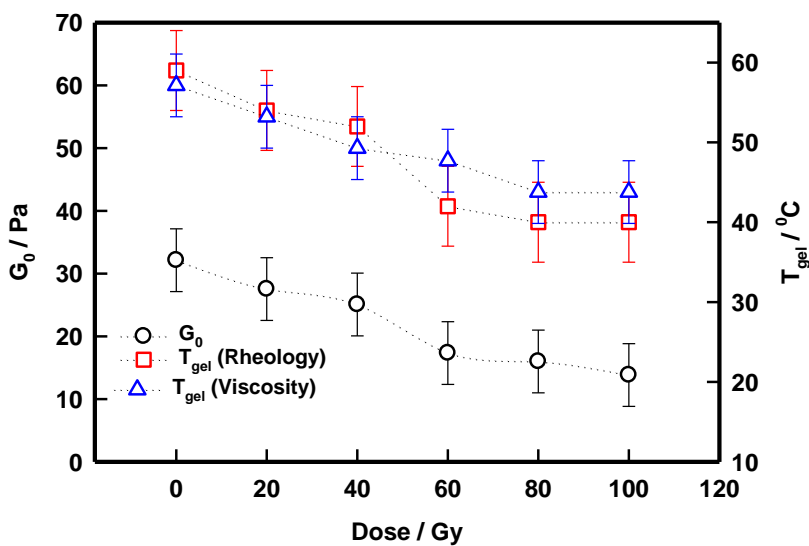
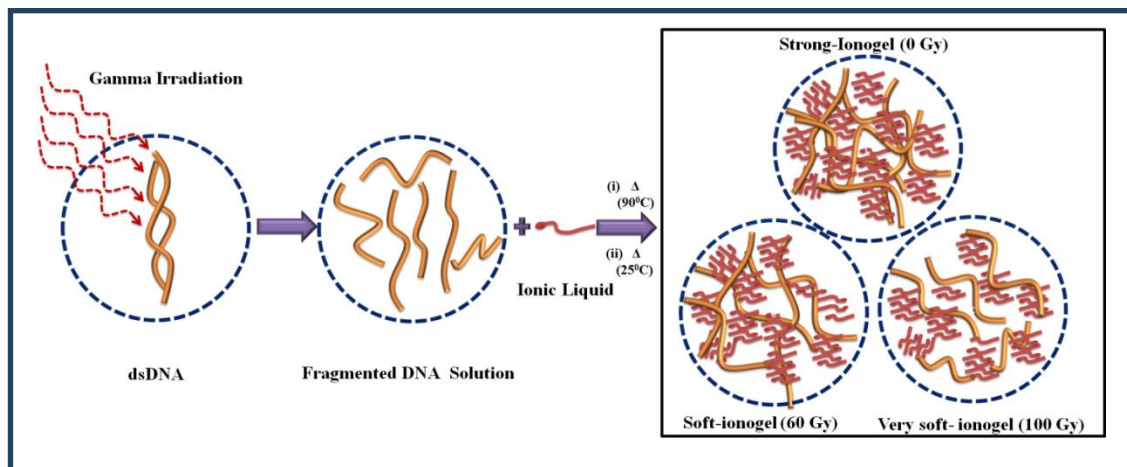


**Figure 3.33.** Variation of  $T_{gel}$  (from viscosity and rheology) and low frequency storage modulus  $G_0$  of ionogels prepared from different exposure of  $\gamma$ -radiation.

Thus, the dosage dependent gel softening was noticed in all the samples and at higher dosage the gels exhibited substantially lower strength. Thus, the fragmented DNA could not contribute to the formation of a homogeneous network structure that could sustain large mechanical deformation.

The melting profiles of these gels were deduced from the isochronal temperature sweep studies. The distinguishable transitions were found at one particular temperature referred to as  $T_{gel}$ . In the case of ionogel samples  $T_{gel}$  reduced from  $60^{\circ}\text{C}$  at 0 Gy to  $40^{\circ}\text{C}$  at 100 Gy. This behavior is clearly shown in Fig.3.33, where some similarity is noticed with  $T_{gel}$  obtained from previously discussed viscosity data. It was important to note that  $T_{gel}$  could be decreased (shifted)

by  $\approx 20^{\circ}\text{C}$  at 100 Gy. Therefore, these ionogels can have custom-made gelation regions by adjusting the radiation dosage, which will may lead to design of novel DNA-based biomaterials.



**Scheme 3.4.** Schematic representation of formation of  $\gamma$ -radiation exposed DNA ionogels.

### 3.6 Conclusion

The conclusion of this chapter can be divided in four parts for different gels:

1. In DNA hydrogels, It was found that self-assembly of DNA strands precedes gelation transition. It was possible to extract micro-structural information about DNA strands with SANS measurement. The structure factor profile,  $I(q)$  vs  $q$  data, was divided into three different  $q$ -regions and were treated with specific fitting functions: (i) low- $q$  region ( $0.05\text{nm}^{-1} \leq q \leq 0.11\text{nm}^{-1}$ ),  $I(q) = I_G \exp(-R_g^2 q^2/3)$  (Guinier- regime); (ii) the intermediate  $q$ -region ( $0.12\text{nm}^{-1} \leq q \leq 0.21\text{nm}^{-1}$ ),  $I(q) \sim q^{-\alpha}$  (Power-law); and (iii) the asymptotic region ( $q \geq 0.22\text{nm}^{-1}$ ),  $I(q) = I_L/(1 + (q - q_0)\xi)^m$  (Broad Peak region where  $q_0$  is related to peak position of scattered peak and  $\xi$  is correlation length). The crossover between regions between (i) and (ii), and between (ii) and (iii) designated as  $q^*$  and  $q^{**}$  defined two other length scales,  $L^* = 2\pi/q^*$  (=50 nm independent of

concentration), and  $L^{**} = 2\pi/q^{**}$  (= 26 to 22 nm decreasing with increase in DNA concentration). From statistical analysis of the structure factor data, we obtained the radius of gyration value,  $R_g \approx 40 \pm 3$  nm. Assuming, the strands to be rod-like, the length of the strands  $L$  can be determined from,  $R_g^2 = L^2/12$  which gives  $L \approx 140$  nm which is quite realistic. In the high- $q$  region a broad correlation peak was detected, and the broad peak fitting analysis yielded correlation length,  $\xi$  increasing from 0.50 nm to 3.30 nm, and the inter strand spacing  $d_0$  decreasing from 15.6 to 9.8 nm as DNA content was increased from 1% to 3%. A clear overlap concentration  $c^* = 2\%$  (w/v) was found. DNA hydrogel was found to be consisting of hierarchy of structures with well-defined length scales that contribute uniquely to the scattering process. In summary; it has been shown that hierarchical structure of DNA hydrogels is replete with several self-organized assemblies, whose spatial extension is dependent on the biopolymer concentration.

**2.** For [C2mim][Cl] based DNA ionogels, the microscopic structure of sol and gel state of DNA-IL system was studied exhaustively as function of ionic liquid concentration. DNA (1% w/v) was in sol phase (it does not gel) which exhibited random Brownian motion and ergodicity. On addition of IL, there was gradual transition from random to arrested state because of ceased Brownian dynamics owing to the formation of IL-mediated network structures, which is a first order phase transition from ergodic to non-ergodic state. Inter-particle distance reduced, and mesh-like structures appeared in the presence of IL. Self-organization of DNA in IL solution occurred systematically driven mostly by electrostatic interaction. Note that presence of IL molecules, introduces enhanced possibility of hydrogen bonding, Coulombic interactions and hydrophobic forces. The self-assembly leading to gelation, observed in this work may be viewed as arising from an assortment of aforesaid forces. This has been conceptualized in a schematic representation shown in Scheme 3.2.

It is known that ssDNA can be prepared by heating the dsDNA stock solutions to 80 °C for 15 min followed by quenching to ice temperature that prevents its renaturation [9]. We followed the same procedure, but used charge quenching to keep the strands separated. The positively charged imidazolium head groups of IL molecules present in the solution were attracted towards the negatively charged phosphate groups on DNA due to electrostatic forces to form a monolayer of IL on the single strands. However, it should also be realized that the hydrophobic interaction between the alkyl group (ethyl-moieties) of the ionic liquid molecules and the hydrophobic nitrogenous bases in DNA also played a role (marginal). This prevented the re-naturation of the DNA strand. What followed was a self-assembly process, where the hydrophobic tails of IL were bound to DNA with similar units present in their neighborhood. This resulted in the formation of an amorphous network of IL-DNA clusters. Since the system was undergoing a sol-gel transition, the conclusion of formation of DNA-IL networks shown in Scheme 3.2 was logical. The low- $q$  region available to our SANS instrument did not yield a robust Guinier regime which could have yielded information about the physical size of these growing clusters. This phenomenological model is a conjecture. The relaxation dynamics was hierarchical within ionogels. The results draw our attention to very marginally understood self-organization of DNA in ionic liquid medium. Furthermore, the observation of increase in the gel strength leading to a close to 10 °C increase in the gelation temperature when the IL concentration did not exceed 5 % (w/v) was remarkable. Thus, we believe the results obtained will widen the potential application of DNA gels.

**3.** It is shown that 2000 bp DNA can undergo gelation and form a viscoelastic physical gel of moderate strength in 1-octyl-3-methylimidazolium chloride ionic liquid solution even when the nucleic acid concentration was as low as 0.3% (w/v), and the volume fraction of IL in the



continuous phase did not exceed 0.01. The gelation concentration of DNA hydrogels is  $\sim 2\%$  (w/v), thus we noticed physical gelation at a concentration that was  $\sim 85\%$  lower. These gels were endowed with gel rigidity ranging from 20 to 40 Pa, with gelation temperature spanning between 52 and 72 °C. Another striking feature was the remarkable linear dependence of gelation time  $t_{\text{gel}}$ , gel strength  $G_0$ , and gelation temperature  $T_{\text{gel}}$  with DNA concentration (0.3–1.0%). The sol-gel transition was captured as a dynamic arrest of the density fluctuations with a discernible ergodicity breaking time  $\tau_{\text{EB}}$ . It was noticed that  $t_{\text{gel}}$  was no different from  $\tau_{\text{EB}}$ . Thus, the reorganization of ssDNA strands leading to physical gelation was coincident with the corresponding alteration in the topological dimension of inhomogeneities in the gelling samples. Considering the importance of nucleic acid gels in pharmaceutical and biomedical applications, the aforesaid findings will be of major interest. Another important conclusion pertains to the ability of the user to create gels at such low DNA concentrations. Ionic liquid can be easily synthesized these days with sufficient purity. Though in our experiments, we have used commercially available IL in order to ensure error minimization. This study can be extended to locally prepared ILs. Additionally, IL is thermally stable, green solvent and highly conductive in nature compared to other additives [21,23,24,85,86]

**4.** We have systematically examined the gelation kinetics of  $\gamma$ -irradiated DNA solution in ionic liquid (IL) medium. It has been reported [55] that positive head (imidazolium) group of IL molecule interacts (electrostatic interaction) with negatively charged surface of DNA molecule and leads the formation of ionogel. Hydrophobic force between alkyl chain of 2-C in IL molecule and Nitrogenous bases in DNA also contribute on this network formation. It has been shown clearly that radiation processed ionogels have a structure-property relation very different from that of their hydrogels. It must be stressed that the DNA in gels were mostly in ssDNA

conformation. We followed the heat based denaturation protocol, but used charge quenching to keep the strands apart [9]. This has been conceptualized in a schematic representation shown in Scheme 3.4.

Though ionizing radiations are known to cause damage to the DNA double-strands their effect on gelation kinetics, and structure-property relation in such gels are issues very poorly understood. This study is a step in that direction. In summary, the results obtained will widen the scope of the DNA ionogels in applications.

### 3.7 References

- [1] F. Horkay and P. J. Basser, *Biomacromolecules* **5**, 232 (2004).
- [2] F. Xu, F. Xu, Q. Wang, Y. Zhou, Z. Ye, and W.-S. Tan, *Biochem.Eng.J.* **103**, 68 (2015).
- [3] S. H. Um, J. B. Lee, N. Park, S. Y. Kwon, C. C. Umbach, and A. D. Luo, *Nat. Mater.* **5**, 797 (n.d.).
- [4] A. Papancea, A. J. M. Valente, S. Patachia, M. G. Miguel, and B. Lindman, *Langmuir* **24**, 273 (2008).
- [5] Y. J. Cho, H. Y. Kim, H. Huang, A. Slutsky, I. G. Minko, H. Wang, L. V. Nechev, I. D. Kozekov, A. Kozekova, P. Tamura, J. Jacob, M. Voehler, T. M. Harris, R. S. Lloyd, C. J. Rizzo, and M. P. Stone, *J. Am. Chem. Soc.* **127**, 17686 (2005).
- [6] S. Dutta, G. Chowdhury, and K. S. Gates, *J. Am. Chem. Soc.* **129**, 1852 (2007).
- [7] T. Liedl, H. Dietz, B. Yurke, and F. Simmel, *Small* **3**, 1688 (2007).
- [8] Y. Xing, E. Cheng, Y. Yang, P. Chen, T. Zhang, Y. Sun, Z. Yang, and D. Liu, *Adv.*

- Mater. **23**, 1117 (2011).
- [9] M. C. Moran, M. G. Miguel, and B. Lindman, *Langmuir* **23**, 6478 (2007).
- [10] C. K. Lee, S. R. Shin, S. H. Lee, J. H. Jeon, I. So, T. M. Kang, S. I. Kim, J. Y. Mun, S. S. Han, G. M. Spinks, G. G. Wallace, and S. J. Kim, *Angew. Chemie - Int. Ed.* **47**, 2470 (2008).
- [11] N. Orakdogan, B. Erman, and O. Okay, *Macromolecules* **43**, 1530 (2010).
- [12] T. G. Mason, A. Dhople, and D. Wirtz, *Macromolecules* **31**, 3600 (1998).
- [13] Y. Murakami and M. Maeda, *Biomacromolecules* **6**, 2927 (2005).
- [14] Y. Liu, Y. Jun, and V. Steinberg, *Macromolecules* **40**, 2172 (2007).
- [15] N. Arfin, V. K. Aswal, J. Kohlbrecher, and H. B. Bohidar, *Polymer (Guildf)*. **65**, 175 (2015).
- [16] D. Costa, P. Hansson, S. Schneider, M. G. Miguel, and B. Lindman, *Biomacromolecules* **7**, 1090 (2006).
- [17] O. Okay, *J. Polym. Sci. Part B Polym. Phys.* **49**, 551 (2011).
- [18] Y. He, T. Ye, M. Su, C. Zhang, A. E. Ribbe, W. Jiang, and C. Mao, *Nature* **452**, 198 (2008).
- [19] C. Li, A. Faulkner-Jones, A. R. Dun, J. Jin, P. Chen, Y. Xing, Z. Yang, Z. Li, W. Shu, D. Liu, and R. R. Duncan, *Angew. Chemie - Int. Ed.* **54**, 3957 (2015).
- [20] J. Kohlbrecher and W. Wagner, *J. Appl. Crystallogr.* **33**, 804 (2000).

- [21] J. Dupont, R. F. De Souza, and P. A. Z. Suarez, *Chem. Rev.* **102**, 3667 (2002).
- [22] R. D. Rogers and K. R. Seddon, *Science* (80-. ). **302**, 792 (2003).
- [23] P. Wasserscheid, *Nature* **439**, 5635 (2006).
- [24] W. Leitner, *Nature* **423**, 930 (2003).
- [25] S. OzBas-Turan, C. Aral, L. Kabasakal, M. Keyer-Uysal, and J. Akbuga, *J.Pharm.Pharm. Sci.* **6**, 27 (2003).
- [26] C. Aral and J. Akbuga, *J. Pharm. Pharm. Sci.* **6**, 321 (2003).
- [27] J. Le Bideau, L. Viau, and A. Vioux, *Chem. Soc. Rev.* **40**, 907 (2011).
- [28] K. Haraguchi and T. Takehisa, *Adv. Mater.* **14**, 1120 (2002).
- [29] A. Sharma, K. Rawat, P. R. Solanki, and H. B. Bohidar, *Curr. Top Med. Chem.* **15**, 1257 (2015).
- [30] X. Zhu, H. Zhang, and J. Wu, *Sens. Actuat. B* **202**, 105 (2014).
- [31] J. B. Lee, S. Peng, D. Yang, Y. H. Roh, H. Funabashi, N. Park, E. J. Rice, L. Chen, R. Long, M. Wu, and D. Luo, *Nat. Nanotechnol.* **7**, 816 (2012).
- [32] S. H. Um, J. B. Lee, N. Park, S. Y. Kwon, C. C. Umbach, and D. Luo, *Nat. Mater.* **5**, 797 (2006).
- [33] X. Xiong, C. Wu, C. Zhou, G. Zhu, Z. Chen, and W. Tan, *Macromol. Rapid Commun.* **34**, 1271 (2013).
- [34] A. Angelova, B. Angelov, R. Mutafchieva, S. Lesieur, and P. Couvreur, *Acc. Chem. Res.*

- 44**, 147 (2011).
- [35] B. Angelov, A. Angelova, S. K. Filippov, G. Karlsson, N. Terrill, S. Lesieur, and P. Štěpánek, *Soft Matter* **7**, 9714 (2011).
- [36] B. Angelov, A. Angelova, S. Filippov, G. Karlsson, N. Terrill, S. Lesieur, and P. Štěpánek, *J. Phys. Conf. Ser.* **351**, (2012).
- [37] B. Angelov, A. Angelova, S. K. Filippov, T. Narayanan, M. Drechsler, P. Štěpánek, P. Couvreur, and S. Lesieur, *J. Phys. Chem. Lett.* **4**, 1959 (2013).
- [38] B. Angelov, A. Angelova, M. Drechsler, V. M. Garamus, R. Mutafchieva, and S. Lesieur, *Soft Matter* **11**, 3686 (2015).
- [39] H. Rosa, D. F. S. Petri, and A. M. Carmona-Ribeiro, *J. Phys. Chem. B* **112**, 16422 (2008).
- [40] I. S. Kikuchi, W. Viviani, and A. M. Carmona-Ribeiro, *J. Phys. Chem. A* **103**, 8050 (1999).
- [41] I. S. Kikuchi and A. M. Carmona-Ribeiro, *J. Phys. Chem. B* **104**, 2829 (2000).
- [42] G. M. Kendall, M. P. Little, R. Wakeford, K. J. Bunch, J. C. H. Miles, T. J. Vincent, J. R. Meara, and M. F. G. Murphy, *Leukemia* **27**, 3 (2013).
- [43] M. S. Pearce, J. A. Salotti, M. P. Little, K. McHugh, C. Lee, K. P. Kim, N. L. Howe, C. M. Ronckers, P. Rajaraman, A. W. Craft, L. Parker, and A. B. De González, *Lancet* **380**, 499 (2012).
- [44] O. Investigation, *Arch. Intern. Med.* **169**, 2078 (2009).

- [45] E. Picano and E. Vano, *Cardiovasc. Ultrasound* **9**, 1 (2011).
- [46] J. Cadet, J. L. Ravanat, M. TavernaPorro, H. Menoni, and D. Angelov, *Cancer Lett.* **327**, 5 (2012).
- [47] L. J. Eccles, P. O'Neill, and M. E. Lomax, *Mutat. Res.* **711**, 134 (2011).
- [48] J. F. Ward, *Prog. Nucleic Acid Res. Mol. Biol.* **35**, 95 (1988).
- [49] A. Asaithamby and D. J. Chen, *Mutat. Res. - Fundam. Mol. Mech. Mutagen.* **711**, 87 (2011).
- [50] B. Stenerlöv, K. H. Karlsson, B. Cooper, and B. Rydberg, *Radiat. Res.* **159**, 502 (2003).
- [51] J. . Milligan, J. Y. Ng, C. C. Wu, J. A. Aguilera, R. C. Fahey, and J. F. Ward, *Radiat. Res.* **143**, 273 (1995).
- [52] A. R. Peoples, K. R. Mercer, and W. A. Bernhard, *J. Phys. Chem. B* **114**, 9283 (2010).
- [53] H. J. Kong, D. Kaigler, K. Kim, and D. J. Mooney, *Biomacromolecules* **5**, 1720 (2004).
- [54] X. Yang, Z. Zhu, Q. Liu, X. Chen, and M. Ma, *Radiat. Phys. Chem.* **77**, 954 (2008).
- [55] P. K. Pandey, K. Rawat, V. K. Aswal, J. Kohlbrecher, and H. B. Bohidar, *Phys. Chem. Chem. Phys.* **19**, 804 (2017).
- [56] A. Aharony, *Introduction to Percolation Theory* (Taylor & Francis Group, London, 1994).
- [57] A. Stauffer, A. Coniglio, and A. Adams, *Adv. Polym. Sci.* **44**, 103 (1982).
- [58] L. DeArcangelis, E. Del Gado, and A. Coniglio, *Eur. Phys. J. E.* **9**, 277 (2002).

- [59] P. Debye and A. M. Bueche, *J. Appl. Phys.* **20**, 518 (1949).
- [60] B. Mohanty and H. B. Bohidar, *Euophys. Lett.* **76**, 965 (2006).
- [61] K. Rawat, J. Pathak, and H. B. Bohidar, *Phys. Chem. Chem. Phys.* **15**, 12262 (2013).
- [62] G. M. Mrevlishvili and D. V. Svintradze, *Int. J. Biol. Macromol.* **35**, 243 (2005).
- [63] B. Mohanty, V. K. Aswal, J. Kohlbrecher, and H. B. Bohidar, *J. Polym. Sci. Part B Polym. Phys.* **44**, 1653 (2006).
- [64] B. A. Simmons, G. C. Irvin, V. Agarwal, A. Bose, V. T. John, G. L. McPherson, and N. P. Balsara, *Langmuir* **18**, 624 (2002).
- [65] N. Joshi, K. Rawat, V. K. Aswal, and H. B. Bohidar, *Colloids Surfaces A Physicochem. Eng. Asp.* **501**, 55 (2016).
- [66] A. B. Rodd, D. E. Dunstan, D. V. Boger, J. Schmidt, and W. Burchard, *Macromolecules* **34**, 3339 (2001).
- [67] R. K. Pujala and H. B. Bohidar, *Soft Matter* **8**, 6120 (2012).
- [68] P.-G. DeGennes, *Scaling Concepts in Polymer Physics*, 2nd ed. (Cornell University Press, NY, 1985).
- [69] N. Arfin and H. B. Bohidar, *J. Phys. Chem. B* **116**, 13192 (2012).
- [70] K. Rawat, V. K. Aswal, and H. B. Bohidar, *J. Phys. Chem. B* **116**, 14805 (2012).
- [71] H. A. Barnes, *A Handbook of Elementary Rheology* (University of Wales, Institute of Non-Newtonian fluid Mechanics: Aberystwyth, 2000).

- [72] Y. He, P. G. Boswell, P. Bühlmann, and T. P. Lodge, *J. Phys. Chem. B* **111**, 4645 (2006).
- [73] A. Ajji and L. Choplin, *Macromolecules* **24**, 5221 (1991).
- [74] P. Kumar, K. Rawat, V. K. Aswal, J. Kohlbrecher, and H. B. Bohidar, *Colloids Surfaces A* **538**, 184 (2018).
- [75] J. D. Ferry, *Viscoelastic Properties of Polymers* (John Wiley & Sons, 1980).
- [76] P. . Pandey, K. Rawat, V. K. Aswal, J. Kohlbrecher, and H. B. Bohidar, *J. Appl. Biotechnol. Bioeng.* **2**, 144 (2017).
- [77] H. B. Bohidar and S. Ghosh, *Eur. Poly. J.* **36**, 2545 (2018).
- [78] P. Mongondry, J. F. Tassin, and T. Nicolai, *J. Colloid Interface Sci.* **283**, 397 (2005).
- [79] P. J. Flory, *Principles of Polymer Chemistry* (Cornell University Press, 1953).
- [80] H. B. Bohidar, *Fundam. Polym. Phys. Mol. Biophys.* **1** (2014).
- [81] B. Nyström and B. Lindman, *Macromolecules* **28**, 967 (1995).
- [82] W. Burchard and M. Eisele, *Pure Appl. Chem.* **56**, 1379 (1984).
- [83] J. Sambrook, E. F. Fritsch, and T. Maniatis, *Molecular Cloning* (Cold spring harbor laboratory press, New York, 1989).
- [84] J. Sharma and H. B. Bohidar, *Colloid Polym. Sci.* **278**, 15 (2000).
- [85] R. D. Rogers and K. R. Seddon, *Sci.* **302**, 792 (2003).
- [86] M. Villanueva, A. Coronas, J. García, and J. Salgado, *Ind. Eng. Chem. Res.* **52**, 15718 (2013).



## CHAPTER-4

---

### Complex Coacervation of dsDNA and in situ formed Zein nanoparticles

**Abstract:** In this chapter DNA-Zein complex coacervation was studied. We have also probed the effect of organic and inorganic salt produced ionic environment on the coacervation.

#### 4.1 Introduction

The electrostatic force between oppositely charged molecules initiates liquid-liquid phase separation which is known as coacervation transition [1,2]. To achieve dense liquid phase from homogeneous solution is known as coacervation [1]. Polymer rich phase separated from homogeneous solution is known as coacervate and remain part as supernatant. Phase separation occurs due to interaction of macromolecule carrying net opposite charge. The emerging polymer rich phase are achieved in various polyelectrolytes [3]. In recent past, complex coacervation has been seen in different macromolecular systems such as poly(dimethyldiallylammonium chloride)-BSA (bovine serum albumin) [4], gelatin- chitosan [5], gelatin- agar [6,7], gelatin-gelatin [8,9] and DNA-gelatin [10–12].

Free energy driven self-assembly of microscopic structure via nucleic acid has shown consolidated results [13]. DNA being one of the polyelectrolytes having the highest linear charge density, its association with other biomolecules is of considerable interest. Interaction between DNA, protein [14,15] and complementary charged ions [16] has shown amazing outcomes. The complex formation between rod like collagen complex and worm like DNA chain has reported by Mrevlishvili and Svintradze [14]. It was seen that overlapping hydrated shells of two

structures generates deduction in collagen triple helix and stabilize the duplex DNA chain. Structure of fibrils within the complexes of collagen depends on type of DNA (ssDNA or dsDNA) [15]. The dispersion of positively charged colloid shows following behavior with DNA [16], (i) for low concentration of colloid, DNA wraps the colloid and forms negatively charged DNA- colloid complex whereas (ii) for high concentration of colloid complexes show reverse charge that is positive. So there is an intermediate phase for the complex where the charge is fully neutralized and DNA-colloid condensation take place. Thus colloid concentration is a key factor for condensation. It has shown via Polycation (PC)-DNA interaction where complex charge state depends on DNA: PC charge ratio [17]. Protein binding with DNA occurs either in between functional group and phosphate sugar of DNA(Histone –DNA binding) or it depend on bases pair sequencing. Protein can interact to DNA via two ways either it bind directly to sugar-phosphate group of DNA or depend on base pair sequencing. Forces of interaction are mostly hydrogen bonding due to water molecule, ionic bonding, van der Walls and hydrophobic.

However, when it comes to a hydrophobic protein like Zein, the solvent nature introduces an additional factor into the abovementioned array of interactions

Zein is a hydrophobic water-insoluble plant protein extracted from corn (*Zeamays L.*) which consists of three fractions ( $\alpha$ ,  $\beta$  and  $\gamma$ ) that vary in molecular weight (MW) and solubility [18]. The  $\alpha$ -fraction has a of MW of 19-24 kDa, and it contains 75-80% of total protein content,  $\beta$ -fraction has molecular weight in the 17-18 kDa range and these contribute 10-15%, while the  $\gamma$ -zein has the highest molecular weight of 27 kDa and its contribution is limited to 5-10% [19,20]. The presence of more than 50% of non-polar residues like leucine, proline, alanine, and phenylalanine in its primary structure renders it hydrophobic, and water insoluble.

Regardless, its marginal amphiphilic nature facilitates its conjugation with polyelectrolytes. In addition, its unusual tertiary structure allows Zein to self-assemble into nanoparticles through pH control, liquid-liquid dispersion [21], solution enhanced dispersion, and phase separation processes [22]. In particular, the liquid-liquid dispersion method has been found useful to produce size selective zein nanoparticles of diameter 80–200 nm depending on the composition of the dispersion medium. This particular attribute of Zein has been exploited in this work.

As far as the effect of ionic environment on the coacervation is concerned several studies have revealed interesting features. Dubin and co-workers [23,24] have shown that for PE-colloid coacervation, the PE ( $\xi$ ) and colloid charge density ( $\sigma_c$ ) are related to Debye-Huckel screening length ( $\kappa$ ), by  $\xi\sigma_c = \kappa$ . Perry et al [25] studied the effect of salt type on coacervate formation using two vinyl polyelectrolytes, poly(acrylic acid sodium salt) and poly(allylamine hydrochloride), and confirmed the role of salt valence on the coacervate formation, while demonstrating the presence of significant secondary effects, which could be described by Hofmeister-like behavior. Wang et al [26] have shown the “salt suppression” and “salt enhancement” of coacervation. In the coacervation region, the electrophoretic mobility was found to be close to zero. At higher and lower ionic strengths, soluble complexes were positive or negatively charged, respectively. Interestingly, even in coacervating systems driven by surface selective patch binding mechanism ionic strength of the solution was seen to influence the binding profile [27].

In this thesis Zein nanoparticles (size 80-120 nm) that were remarkably generated *in situ*, and 2000 base pair dsDNA at 25 °C formed complexes and further leading complex coacervation with certain zein concentration.

Further we have studied the effect of organic and inorganic salt produced ionic environment on the coacervation process. The current study also proposes to resolve this issue. Three monovalent salts with same anion (Cl) were chosen for this study. Of the three salts explored two were organic salts (ionic liquids: 1-ethyl-3-methyl imidazolium chloride ([C2mim][Cl]) and 1-methyl-3-octyl imidazolium chloride ([C8mim][Cl])) and the third was an inorganic salt, NaCl. We have sought to investigate the effect of these salts on the coacervation profile of polydisperse ds-DNA with hydrophobic protein (zein) nanoparticles.

#### **4.2 Sample preparation**

Zein is best soluble in 80:20 ethanol: water. So, the stock solution of zein was prepared by dispersing the zein (powder, 1.5%) in 80:20 % ethanol: water binary solvent at room temperature by stirring it for 10 min. A series of solutions with varying zein concentration was prepared by dilution of the stock solution with required amount of water keeping the final volume same (one-shot addition) during which the ethanol concentration also changed. Thus, the samples with  $C_{\text{Zein}} = 0.1, 0.2, 0.3, 0.4$  and  $0.5$  % had ethanol content of 7, 14, 21, 28 and 35%. The pH of the stock was  $4.5 \pm 0.5$  which did not change after dilution with water.

DNA stock was prepared by dissolving DNA powder in double distilled deionized water at room temperature for an hour. Both the solutions appeared optically clear and transparent after preparation. Samples for experiment were prepared by mixing previously prepared Zein and DNA solutions ( $\text{pH} = 6.5 \pm 0.5$ ). In all the samples DNA concentration were maintained at 1% (w/v) while zein concentration were varied from  $C_{\text{Zein}} = 0$  to 0.5 % (w/v).

For salt dependent study zein concentration was 0.5% (w/v) and DNA concentration was 1% (w/v) maintained throughout the experiment. In the interacting solutions the salt

concentration was varied from  $10^{-4}$  to  $6 \times 10^{-1}$  M. It is to be noted that when any of the salts used in this study were added to DNA stock solution, the pH remained invariant. The coacervating solution had a pH of  $6.5 \pm 0.5$ , DNA concentration of 1% (w/v), zein concentration of 0.5% (w/v), and effective ethanol concentration was as 34 % (v/v) (on reverse calculation). Thus, the DNA and zein interacted in a given ionic environment in a milieu of 34:66 % (v/v) ethanol-water binary solvent at room temperature [28]. Same procedure was followed to prepare about 10 samples for each constituent salt. It may be noted that upon addition of zein solution to the DNA solution coacervation occurred instantaneously with clear phase separation of the polymer-rich phase from its supernatant.

## 4.3 Result and Discussion

### 4.3.1 DNA-Zein binding

The DNA solution was titrated with Zein solutions under mild stirring which instantaneously produced positively charged Zein nanoparticles (NPs) *in situ* that gave rise to sharp change in solution turbidity and viscosity, while keeping the pH of the solutions invariant at  $6.5 \pm 0.5$ . All these parameters were monitored continuously. Simultaneously, the zeta potential and particle sizing experiments were carried out on a duplicate solution. Fig. 4.1 depicts this data clearly which is quite revealing. The binding profile shows two distinguishable regions of interaction of DNA with Zein NPs: (i) in Region-I which ends at  $C_{zein}=0.2\%$  (w/v), the turbidity increase was very sharp, zeta potential decreased from -56 to -38 mV and apparent hydrodynamic size decreased from  $\approx 2100$  to 560 nm, and (ii) marginal change in the aforesaid properties was noticed when  $0.2 < C_{zein} < 0.5$  % (w/v) implying that a saturation binding condition had arrived.

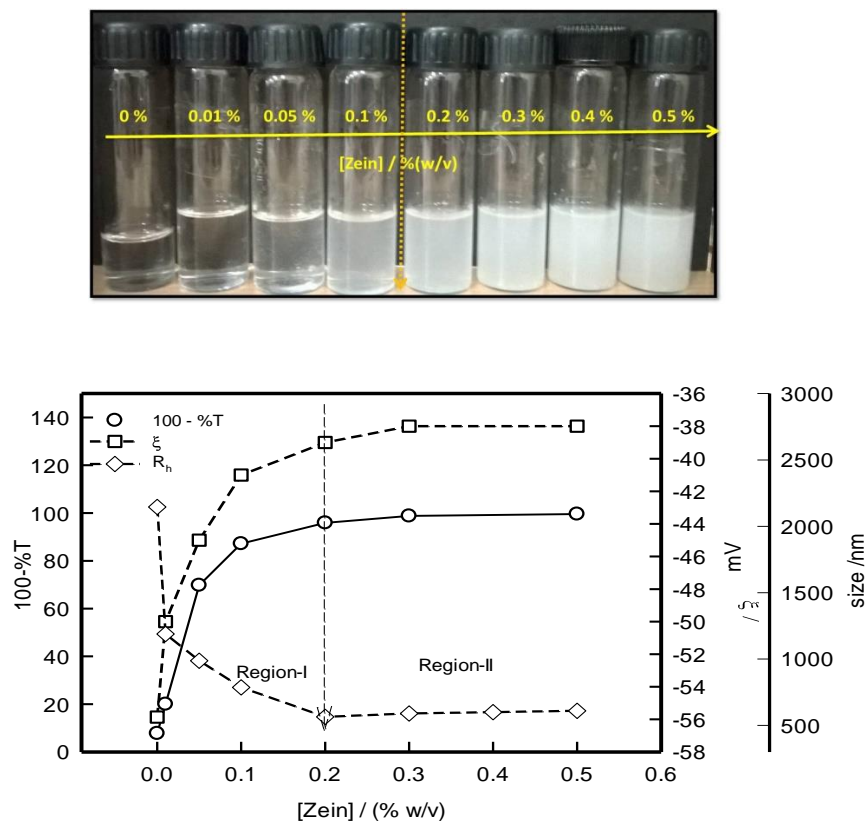


**Figure 4.1.** Variation of zeta potential, solution turbidity, and hydrodynamic radius  $R_h$  shown for different zein concentrations. DNA concentration was fixed at 0.01% (w/v). Notice the sharp change in slope at  $C_{Zein} \approx 0.2\%$  (w/v). The top row photographs depict the growth in turbidity as Zein concentration was increased.

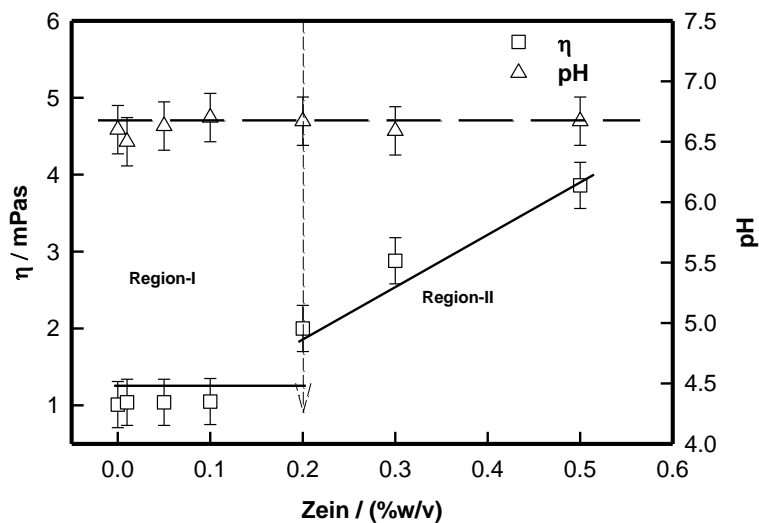


**Figure 4.2.** Variation of solution viscosity, and pH shown for different Zein concentrations. DNA concentration was fixed at 0.01% (w/v). Notice the invariance of pH, and sharp change in slope of viscosity at  $C_{Zein} \approx 0.2\%$  (w/v).

### 4.3.2 Condensation of DNA ( $C_{\text{Zein}} < 0.2\%$ (w/v))

Addition of multivalent counter-ions and non-solvents is known to condense DNA molecules [29–31]. Alternatively, an oppositely charged polymer can be used as a compacting agent, and for that complete charge neutralization of DNA may not be necessary [10–12]. The pH of the DNA- Zein mixed solutions were close to  $6.0 \pm 0.5$  invariant of protein concentration. At this pH, the zeta potential of DNA and Zein were measured to be -55 and +37 mV, respectively, which would facilitate their associative interaction via electrostatic forces, and in salt-free environment, in particular, such interaction led to the formation of soluble interpolymer primary complexes. The data in Fig. 4.1 clearly indicate that such binding zeta potential of DNA decreased (from -58 to -38 mV) during this interaction with the concomitant decrease in its apparent hydrodynamic size (from 2100 to 560 nm). In our experiments, large amount of Zein was required for the DNA condensation and its partial charge neutralization. This can be understood as. Firstly, because of the high charge ratio (DNA:Zein), more of Zein was required to bind and charge neutralize DNA backbone. Secondly, because of large and spherical structure of Zein, DNA will feel steric hindrance while attaching to incoming Zein molecule, regardless, the surface selective patch binding (SPB) of Zein to DNA backbone was realized. SPB mediated complex formation has been realized in many systems in the past [7,32–39].

In the SPB mechanism, the positively charged “patches” on the spherical Zein nanoparticles will preferentially bind to DNA overcoming the same charge repulsion between negatively charged “patches” on Zein and the DNA molecule. This interaction, which was electrostatic in nature, was supported by zeta potential data which depicts partial charge neutralization of DNA-Zein complex upon addition of Zein in Region-I. This can be referred to

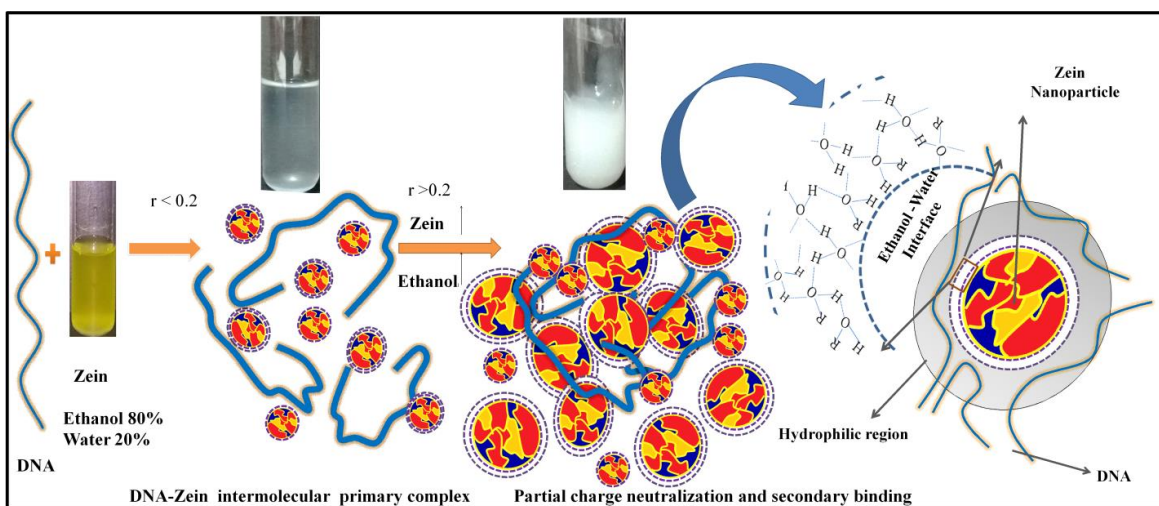
as primary binding. The inter-polymer complex formation in Region-I can be described as follows

$$[DNA] + (1 - x)[Zein NP] = [DNA - Zein NP]_{pc} + x[Zein NP] \quad (4.1)$$

which in terms of the zeta potential can be written as

$$\zeta_{DNA} + (1 - x)\zeta_{zein} = \zeta_{pc} + x\zeta_{zein} \quad (4.2)$$

The zeta potential of DNA, Zein, DNA-Zein primary complex are represented by appropriate suffices. Of the available Zein, a fraction  $(1-x)$  was bound to DNA to yield the DNA-Zein primary complex, and the remaining fraction  $x$  was available as free protein in the dispersion. When the appropriate data was used in eqn (4.1), one obtained,  $x \approx 1/6$  implying nearly 80 % of the available protein was bound to DNA strands in Region-I to cause DNA condensation while the rest 20 % was coexisting with the DNA-Zein complex in the dispersion as free protein. All this happened in the binary ethanol-water mixture (continuous phase) where organic phase content was 14% (v/v). Thus, the nucleic acid condensation was due to the combined effect of binding of 80 nm Zein nanoparticles to the DNA strand, and depletion of its aqueous hydration layer which was replaced by a water-ethanol interface (See Scheme 4.1).



**Scheme 4.1.** Illustration of DNA-Zein binding and replacement of aqueous hydration of DNA with ethanol-water interface.



Solvent hydrophobicity induced condensation of biopolymers in general has been realized in the past starting with the pioneering work of Timasheff in this field [40–42]. Interestingly, the solution viscosity  $\eta$  could not capture this conformational transition. The relative viscosity of the binary mixture changes marginally in the ethanol concentration window of 0-20 % [43], and the corresponding change in the dielectric constant of the medium was limited to not more than 10 % [44]. Thus, the condensation was a result of partial charge neutralization of the DNA strand and its exposure to a non-aqueous continuous medium.

#### **4.3.3 Complex coacervation ( $0.2 < C_{\text{Zein}} < 0.5\%$ (w/v))**

The data shown in Figs. 4.1 and 4.2 reveal a signature change in their profiles for  $C_{\text{Zein}} > 0.2\%$ . The solution turbidity increased marginally, and then saturated, and the viscosity rose sharply to double its value while the pH remained invariant. The zeta potential of the complex increased marginally and, then showed a plateau (at -38 mV) and the apparent hydrodynamic size did not change much. Interestingly, the turbidity did not decrease like in many other coacervating systems, because of the large negative zeta potential of the soluble complexes. Similar behavior had been noticed earlier in the case of DNA-gelatin A coacervation [10–12]. The behavior of the coacervating system in Region-II can be visualized as follows. The existing interpolymer primary complexes that were partially charge neutralized, as stated in the previous section, continued to attract more Zein nanoparticles for further binding and as a consequence turbidity and zeta potential kept increasing though marginally (secondary binding). In the Huggins theory of polymer solutions, the slope of the viscosity plot is related to the interaction between the dispersed particles [45]. This dispersion had a population of DNA-Zein complexes, and free Zein nanoparticles. The physical size of the complexes were at least 6-times larger than

Zein nanoparticles. Thus, the positive slope of the viscosity plot in Fig. 4.2 refers to strong inter-polymer-complex repulsion. However, since these complexes were negatively charged, these could attract positively charged Zein nanoparticles to facilitate secondary binding, and the manifestation of this was clearly reflected in the drastic increase in the viscosity value. The secondary binding in Region-II could be described as follows

$$[DNA - Zein NP]_{pc} + (1 - \gamma)[Zein NP]_{>80 nm} = [DNA - Zein NP]_{sc} + \gamma[Zein NP]_{>80 nm} \quad (4.3)$$

In terms of the zeta potential, the above can be expressed as

$$\zeta_c + (1 - \gamma)\zeta_{zein NP>80 nm} = \zeta_{cc} + \gamma\zeta_{zein NP>80 nm} \quad (4.4)$$

Here,  $(1-\gamma)$  is the fraction of available Zein nanoparticles of size more than 80 nm binding to primary complexes and suffix “sc” refers to the complex after secondary binding (secondary complexes). It needs to be emphasized that in Region-I, Zein nanoparticles of size 80 nm bind to DNA, while in Region-II, ~100 nm particles bind to existing complexes. Secondly, the electrostatic interactions operate in the continuous phase where ethanol content was between 20-35%, and the medium dielectric constant was between 50-60. Therefore, the secondary binding was less aggressive as the interaction potential was weaker. Substitution of the data in eqn (4.4) yields  $\gamma \approx 0.5$  implying close to 50% of the available protein nanoparticles were successfully attached to the secondary complexes with the rest remaining in equilibrium in the coacervating liquid as free nanoparticles. Partially charge neutralization precedes complex coacervation. In the present case, the secondary complexes in solution, because of their excess negative charge, strongly repelled each other and remained in stable turbid dispersion for sufficient amount of time inhibiting macroscopic liquid-liquid phase separation.

#### 4.3.4 Microstructure of coacervates

It was felt pertinent to evaluate the microstructural properties of the coacervate phase as function of Zein content of the material. Two methods were adopted for the viscoelastic profiling of these materials. To check the elastic response for variable shear deformation isothermal frequency, and to see its melting profiling isochronal temperature sweep tests were performed. The viscoelastic dispersion behavior of system is normally assessed from the frequency  $\omega$  dependent profiles of storage  $G'$  and loss modulus  $G''$  of elasticity [46,47]. In the most general definition, a power-law description given by  $G'(\omega) \sim \omega^{n'}$  adequately defines the system, where  $n' = 0$  refers to a Hookean solid, and 2 to a Maxwellian viscoelastic material. The dispersion behavior of the coacervates was measured in the frequency range of 0.1-100 rad/s (data not shown). The mechanical rigidity  $G_0$  of the material is a key parameter that owes its origin to interpolymer binding mechanism. This is determined from the low-frequency storage modulus  $G'$  given by

$$G_0 = \lim_{\omega \rightarrow 0} G'(\omega) \quad (4.5)$$

The variation of  $G_0$  and  $n'$  with Zein concentration is illustrated in Fig. 4.3. The value of  $G_0$  was found to increase from 3.0 Pa (for 0.01% Zein) to 30 Pa (for 0.5% Zein). The corresponding change in the value of  $n'$  was from 0.9 to 0.2. Two conclusions are easily made from this observation: (i) any material with  $G_0$  value so low can be clearly designated as soft matter, and (ii) reduction in the value of  $n'$  infers evolution of a elastic phase from a homogeneous viscoelastic solution. A coherent picture that emerged from this study revealed that the re-arrangement of dsDNA strands with Zein nanoparticles in the coacervate matrix was universal in self-assembly (because  $n'$  was invariant of protein concentration).

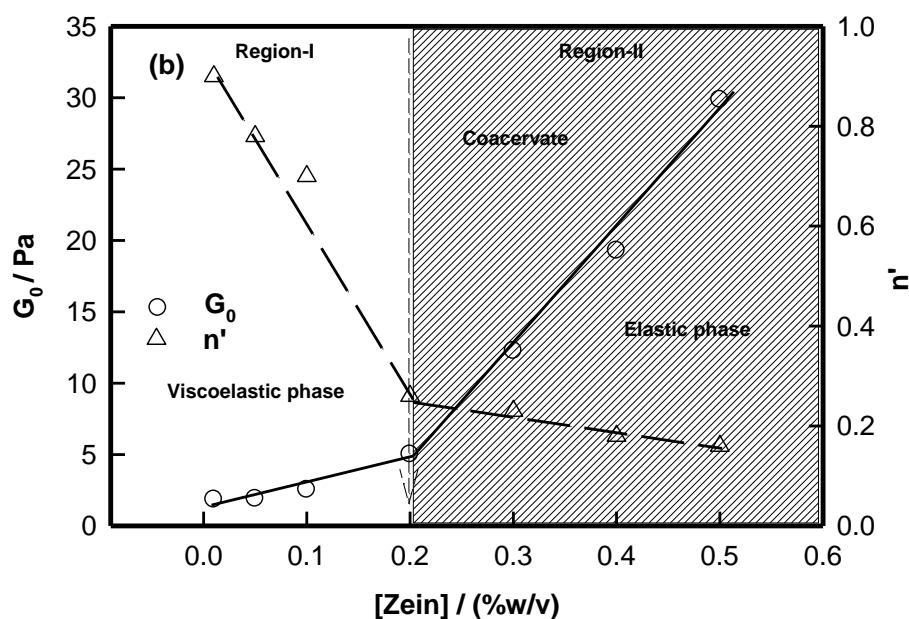


**Figure 4.3.** Variation of low frequency storage modulus  $G_0$  and  $n'$  shown as function of Zein concentration, where sharp change is seen at the coacervation at 0.2 % protein concentration.

The thermal profiling of these coacervates were conducted using isochronal temperature sweep experiments and the data is presented in Fig. 4.4. In this measurement, the temperature dependent variation of  $G_0$  was measured using a ramp of 3  $^{\circ}\text{C}/\text{min}$ . When the coacervates undergo a melting transition (from coacervate to sol) a change in enthalpy is involved, which is recorded as a sharp change in the value of material rigidity ( $G_0$ ). At the microscopic level, mechanical strength to the material arises from interpolymer binding. Thus, the thermal dissociation of bonds. Often this process is gradual leading to a smooth melting profile (Fig. 4). These transitions were detected at two signature temperatures, at the onset  $T_{\text{onset}}$  and at complete melting  $T_{\text{melt}}$  (shown as arrows in Fig. 4.4).

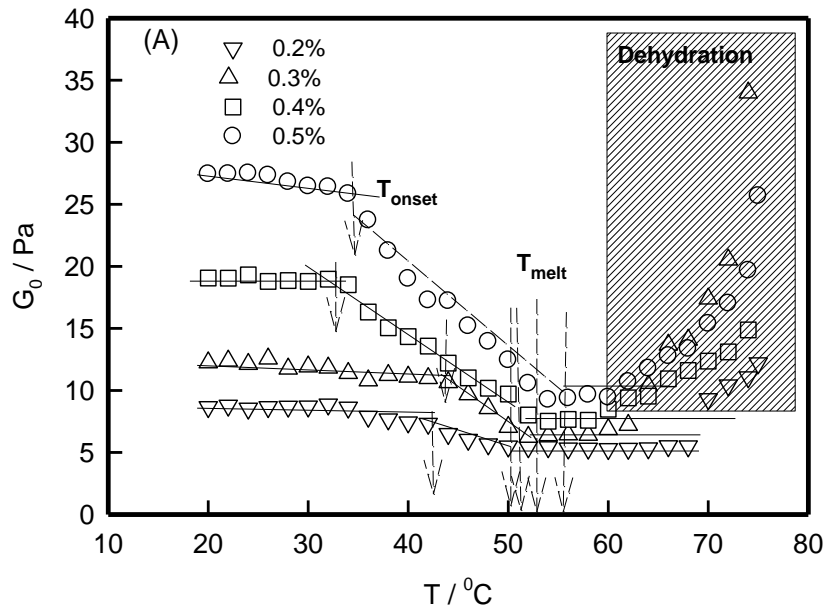


**Figure 4.4.** Variation of low frequency storage modulus  $G_0$  with temperature measured using a ramp of  $3^{\circ}$  C/min. Arrows indicate onset and melting points. Shadow region depicts sample dehydration (lines are guide to eye). See text for details.

The melting zone  $\Delta T = (T_{\text{melt}} - T_{\text{onset}})$  spread over a temperature of  $24 \pm 3^{\circ}$  C for 0.4 and 0.5 % Zein containing samples, whereas same for lower concentration samples was  $10 \pm 3^{\circ}$  C. The corresponding change in rigidity modulus,  $\Delta G_0 = (G_0^{\text{onset}} - G_0^{\text{melt}})$  was  $15 \pm 3$  Pa for higher, and  $7 \pm 3$  Pa for 0.3 and 0.2% Zein containing coacervate samples. Since,  $\Delta G_0$  is a measure of melting enthalpy per unit volume, it is reasonable to argue that coacervation required a minimum enthalpy of about 0.1 KJ/cc. For the sake of comparison, DNA hydro and ionogels have a typical gel strength in the range of 15-30 Pa [48]. DNA-gelatin coacervates, and those prepared in ionic liquid medium are associated with  $G_0$  values on the order of 1KPa [10–12]. Thus, the DNA-Zein interpolymer complexes (coacervates) were associated with much weaker binding. The variation of  $T_{\text{melt}}$  with protein content of coacervates is shown in Fig. 4.5.  $T_{\text{melt}}$  increases linearly with Zein concentration implying that interpolymer complexation was facilitated at higher protein content

of the coacervating solution. It has been already argued that in the secondary binding stage close to 50% of the available protein nanoparticles become part of the interpolymer complex leaving the rest in the dispersion to provide dynamical stability to the coacervate. Thus, there must be dynamic exchange of bound nanoparticles with their free population. Fig. 4.4 also depicts a region (shaded) where the  $G_0$  value was found to increase sharply beyond a certain temperature (typically 60 °C) which is attributed to the loss of solvent (sample dehydration) due to heating.

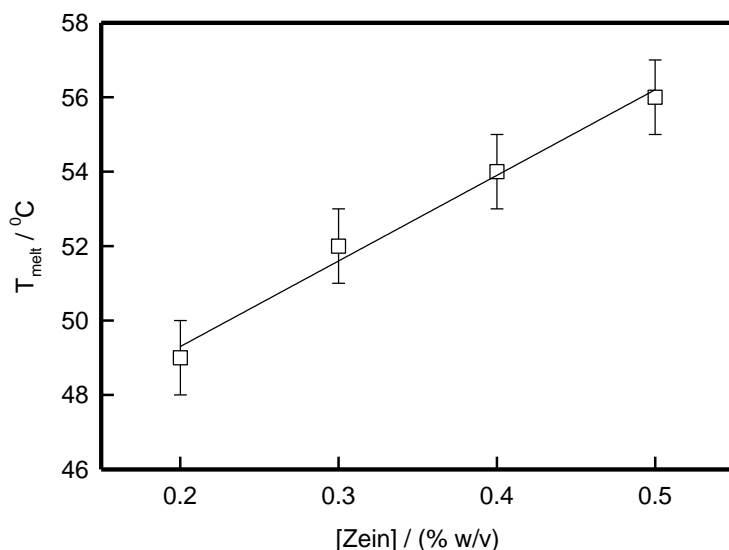


**Figure 4.5.** Melting temperature  $T_{\text{melt}}$  of coacervates shown for different Zein concentrations.

#### 4.3.5 Structure Factor

The static structure factor profiles obtained from SANS measurements performed on different coacervate samples are shown in Fig. 4.6. DNA is associated with a small scattering length compared to Zein, an approximate calculation showed that the difference of ten folds. Therefore, the neutron scattering data was dominated by contributions arising from the protein nanoparticles. Notice the poor scattering profile of the DNA sample in Fig. 4.6. In the data analysis protocol, the  $I(q)$  vs  $q$  data raw data was examined by checking their,  $1/I(q)$  vs  $q^2$ , and

$1/\sqrt{q}$  vs  $q^2$  behavior which correspond to Ornstein-Zernike [49,50] and Debye-Bueche functions [51], respectively. However, this did not yield good statistical accuracy. The best fit to the data was obtained when it was fitted to an empirical function given by eq. (6). In this formalism, we could identify two range of scattering vectors  $q$  : (a) intermediate- $q$  range,  $0.0171 \leq q \leq 0.0371 \text{ \AA}^{-1}$ , data was fitted to Debye-Bueche (D-B) function given by  $I(q) = I_{DB} / (1 + q^2\xi^2)^2$  where  $\xi$  is the characteristic heterogeneity length, and (ii) high- $q$  range,  $0.0393 \leq q \leq 0.3404 \text{ \AA}^{-1}$ , data was fitted to Guinier -Porod function given by,  $I = I_{GP} \exp(-R_c^2 q^2/2)$  where  $R_c$  is cross-sectional radius of the scattering moiety. Here,  $I_{DB}$  and  $I_{GP}$  are the amplitudes of the two scattering components. Thus, the structure factor profile could be adequately defined by

$$I(q) = I(q) = I_{DB} / (1 + q^2\xi^2)^2 + I_{GP} \exp(-R_c^2 q^2/2) \quad (4.6)$$

This treatment introduces a cross-over wave vector  $q^*$  that separates the two regions. This was determined, and was correlated to a signature length scale  $L^*$  of the system given by,

$$L^* = \frac{2\pi}{q^*} \quad (4.7)$$

The values of the two length scales  $\xi$  and  $L^*$  obtained from different coacervate samples are plotted in Fig. 4.7.

The analysis of the data revealed the following universal information: (i) mean heterogeneity size  $\xi$  was  $2.8 \pm 0.1 \text{ nm}$  ( $6.2 \text{ nm}$  for DNA),  $L^*$  was  $15 \pm 1 \text{ nm}$  ( $20 \text{ nm}$  for DNA), and  $R_c$  was  $0.8 \pm 0.1 \text{ nm}$  (for DNA).

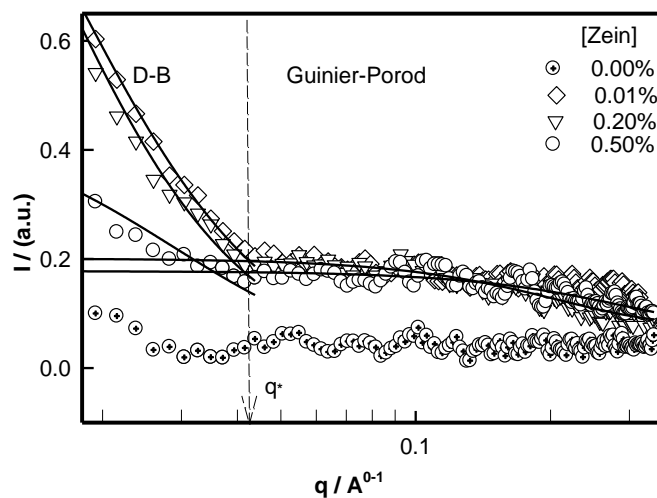


**Figure 4.6.** Static structure factor plot showing neutron scattering profiles of various coacervate samples. Solid lines are fitting of the data to eqn (4.6). Intermediate and high  $q$ -regions were fitted to Debye-Bueche (D-B) and Guinier-Porod functions, respectively.  $q^*$  separates the two regions.

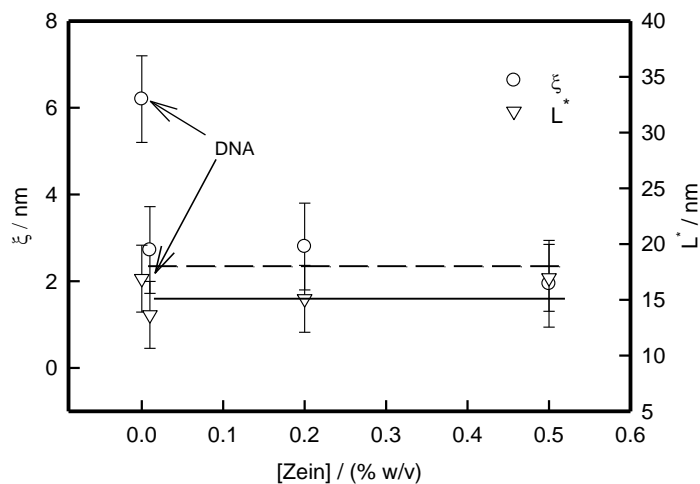


**Figure 4.7.** Variation of heterogeneity size, and crossover length for coacervate samples prepared with different Zein concentration.

Both  $\xi$  and  $L^*$  showed values that were independent of coacervate composition. This clearly emphasizes that the DNA-Zein interpolymers which constituted the building



blocks of the coacervate phase had a microstructure that was distinctively different from its individual components.

#### 4.3.6 Salt dependent Coacervation

The salt dependent coacervation was investigated using turbidity, zeta potential and particle size measurements the data for which are shown in Fig.4.9. There was a clear commonality in these three independently measured data sets which defines the distinctive binding patterns as function of salt concentration. These are identified as: (i) Region-I(A-B), salt content  $10^{-4}$  to 0.01M, (ii) Region-II(B-C), salt content 0.01 to 0.1M, and (iii) Region-III(C-D), salt content 0.1 to 0.6 M. The A-B region may be identified as primary binding zone where the association was very sharp and the three salts produced identical effect. The turbidity and zeta potential changed by barely 6-8 %, but the size of the interpolymer complexes increased from 120 to 150 nm (change of 25 %). Individual salt contributions were not discernible here. Since, the salt concentration was low in this region, the major force driving the associative binding was electrostatic.

In the B-C region (Fig. 4.9) zeta potential changed from -40 to -35, -21 and -26 mV respectively, for NaCl, [C2mim][Cl] and [C8mim][Cl] containing solutions. The corresponding change in the hydrodynamic radius  $R_h$  was from 150 to 280, 550 and 400 nm, respectively. Thus, during the secondary binding process, soluble complexes of DNA-zein had maximum size in [C2mim][Cl] solutions where the charge neutralization was the maximum. The growth gradients,  $d\zeta/d[salt]$  and  $dR_h/d[salt]$  were the highest for this IL. The particle size distributions are depicted in Fig. 4.8 for various samples pertaining to 0.1M salt concentration. Since the DNA sample was highly polydisperse with close to a Gaussian particle size distribution (Fig. 4.8(a)),

all inter-polymer complexes arising out of this material retain similar distribution pattern (Fig. 4.8(b-d)).

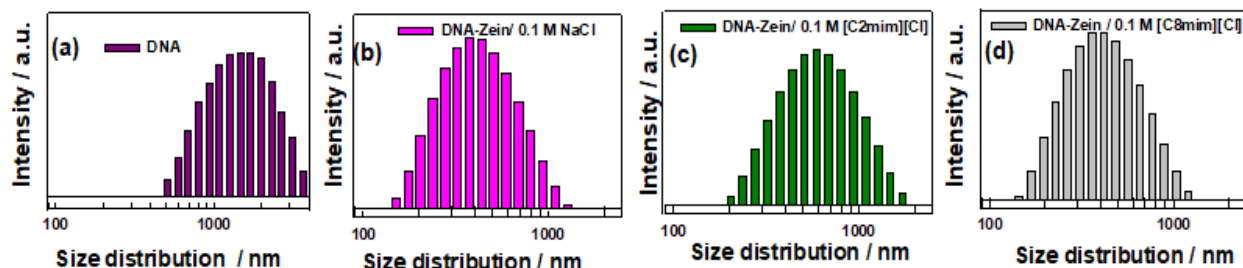


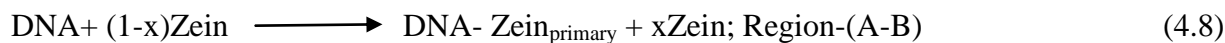
**Figure 4.8.** Representative particle size histograms of (a) 1% (w/v) DNA (mean=1100±180 nm), (b) DNA-zein/NaCl (mean=300±60 nm), (c) DNA-zein/[C2mim][Cl] (mean=500±90 nm) , and DNA-zein/[C8mim][Cl] (mean=400±80 nm) samples. Data for DNA sample was taken in salt-free solution.

In the B-C region, the ionic strength of the solution was varied between 0.01 to 0.1M, which decreased the Debye screening length from 3 to 1nm. Therefore, other interactions like hydrophobic and hydrogen bonding became dominant. The ILs bound to the DNA strand drain their alkane tails away from the electrostatic binding sites, and these offered possibility of hydrophobic binding with free zein nanoparticles. Since, NaCl is deficient in this, the secondary binding was poor in their case. The imidazolium head group of ILs contain N-atom which works as a H-bond partner with the amino acids located on zein surface. Both the aforesaid interactions facilitated preferential secondary binding in IL environment which was observed in our experiments. Between the two IL molecules, [C2mim][Cl] showed more binding because of the lower entropy cost involved. Such a description is consistent with the model proposed by Veis [52] and Tainaka [53] for conventional complex coacervation process, where it is shown that like-charged polyelectrolytes forms finite-sized aggregates which is driven by the cation- $\pi$  bond. In our case, the cations  $\text{Na}^+$ ,  $[\text{C2mim}]^+$  and  $[\text{C8mim}]^+$  can get involved in cation- $\pi$  interactions. Addition of anions at higher concentrations not only reduces the repulsion

significantly, but also generates attraction between the like-charged polyelectrolytes through non-electrostatic routes [54].

The binding-path C-D shown in Fig.4.9(a-c) represent saturation binding region pertaining to salt concentration more than 0.1M. The turbidity of the solution ( $\approx 96\%$ ), zeta potential of the complexes ( $\approx -36, -21$  and  $-26$  mV for NaCl, [C2mim][Cl] and [C8mim][Cl] salts respectively) and their corresponding size (280, 500 and 400 nm) remained invariant of salt concentration in this region.

Therefore, the salt concentration window in the B-C region was the most active regime for coacervation. In summary, the formation of interpolymer complexes between polyanion DNA and zein nanoparticles can be described as



(1-X) is the fraction of zein nanoparticles interacting with DNA to form the primary complex, which bind further to free-zein nanoparticles (a fraction 1-Y of the available free zein particles) at higher salt concentrations to yield soluble secondary complex.

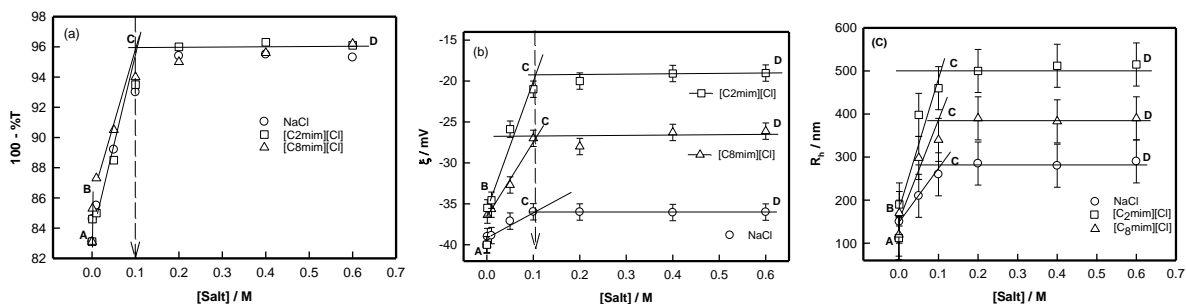


**Figure 4.9.** Variation of (a) turbidity (inset shows coacervate sample ), (b) zeta potential, and (c) hydrodynamic radius shown for different salt concentrations.

### 4.3.7 Fourier-transform infrared spectroscopy (FTIR)

The intermolecular interaction between DNA and zein was studied from the FTIR spectroscopy. The representative spectra of DNA, zein and their salt dependent complexes are shown in Fig.4.10. The spectra of zein shows a sharp absorption peak at  $3000\text{ cm}^{-1}$ , which resulted from the stretching of N-H of amides present in the amino acid residues. Other two characteristic absorption peaks were located at  $3458\text{ cm}^{-1}$  in zein due to -NH stretching and  $3726\text{ cm}^{-1}$  due to -NH band in DNA.  $1739\text{ cm}^{-1}$  is due to C = O band stretching. C = O and -N-H bonds were involved in the hydrogen bonding between different bases corresponding to the secondary structure of DNA which was prominent in [C2mim][Cl] based complexes.

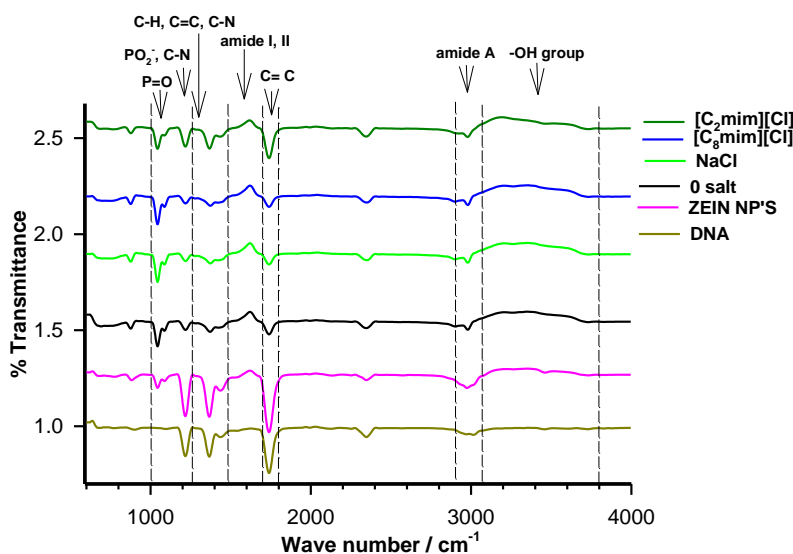


**Figure 4.10.** FTIR data shown for various samples. The samples were in their solution state and optical path length of the cell was kept same for all measurements.

Zein is hydrophobic in nature, the hydrophobic interaction was another driving force involved during the formation of zein-DNA complexes. It may be realized that though the DNA-bases themselves are not hydrophobic, but in the vicinity of planar face of each base, there is a region of finite hydrophobicity, which facilitates base-pair stacking, where water molecules would

otherwise organize themselves to form hydrogen bonds. We conjecture that zein hydrophobically interacts with these planar faces of nitrogenous bases.

FTIR Peaks in the frequency range  $3000 - 4000 \text{ cm}^{-1}$  arise from  $-\text{OH}$  stretching (Fig. 4.10). The  $\text{C}=\text{C}$  stretch in the base plane of nucleic acid result in the origin of  $1700\text{-}1800 \text{ cm}^{-1}$  bands. Peak at  $1215 \text{ cm}^{-1}$  corresponds to  $\text{PO}_2^-$  group in DNA. For Zein NP sample peak located at  $2970 \text{ cm}^{-1}$  represents amide A vibrations while the bands seen in the  $1500\text{-}1700 \text{ cm}^{-1}$  frequency range correspond to amide I, and amide II groups which arise from the peptide group. Further the peak at  $1220 \text{ cm}^{-1}$  is due to  $\text{C-N}$  stretching in the amino acids. Several changes were noticed when zein NP interacted with DNA. The  $\text{P}=\text{O}$  ( $1098 \text{ cm}^{-1}$ ) band stretch which originates from phosphate backbone of phosphodiester was significantly diminished implying hydrophobic interaction. In the DNA-zein complex, stretch in amide A became sharper, and bending in amide I and II were clearly noticeable. Further, there was a clear shift in the  $\text{C}=\text{C}$  vibrational band that corresponds to base plane of DNA. Data from samples containing IL revealed the presence of the bands  $1300\text{-}1500 \text{ cm}^{-1}$  arising from  $\text{C-H}$ ,  $\text{C}=\text{C}$  and  $\text{C-N}$  stretching vibrations of groups present in the IL molecules while forming the nucleic acid-protein complex. This categorically implied that there was differential binding between organic and inorganic salts.

#### **4.3.8 Viscoelastic properties of coacervates**

The viscoelastic attributes of the coacervate samples were probed through two different experimental protocols where the dispersion and temperature dependence behaviors of the storage  $G'$  and loss  $G''$  moduli were explicitly examined. Isothermal frequency sweep tests were performed at room temperature for varying shear deformations to monitor the dispersion

behavior of the coacervates (Fig.4.11), while isochronal temperature sweep tests were performed to observe their melting profiles (Fig.4.12).

In the Maxwellian model of linear viscoelastic theory, the storage modulus  $G'$  scales with frequency  $\omega$  with exponent 2 at low frequency and 0 at high frequency. For the loss modulus the corresponding exponents are 1 and -1, respectively. For more details on viscoelastic theory one may refer to refs. [55,56]. Thus, in the most general terms the dispersion behavior can be given by

$$G'(\omega) = G_0 \omega^n \quad (4.10)$$

Which is a power-law dependence of storage modulus in frequency. It is possible to express  $G''$  likewise.  $G_0$  is defined as strength of storage modulus at low frequency or mechanical rigidity. The exponent  $n = 0$  for a Hookean solid and 2 for Maxwellian viscoelastic material. The data shown in Fig. 4.11 was fitted to the eqn (4.10) and the best viscoelastic property was shown by [C2mim][Cl] containing samples, where  $n$  varied between 1.4 to 0.8 in the B-C region. For NaCl and [C8mim][Cl] samples the corresponding changes were from 0.8 to 0.1, and 0.6 to 0.1, respectively. Thus, it can be argued that the salts NaCl and [C8mim][Cl] effected coacervation in a way that yielded less hydrated and more inhomogeneous coacervates.

The rigidity modulus of the coacervate samples could be inferred from their low frequency storage modulus  $G_0$  data which is shown in Fig. 4.13 (a). There is again clear commonality in salt concentration dependence which unfolds as follows: (i) A-B region represents a overlapping zone where the material was quite soft with  $G_0$  maintaining a value less than 50 Pa for all three cases, (ii) B-C region exhibited maximum growth in rigidity with samples containing [C2mim][Cl] showing maximum  $G_0$  value of 250 Pa, as against 160 Pa for

[C8mim][Cl] and 130 Pa for NaCl samples. A homogeneous material can sustain larger shear deformation and hence, possesses higher rigidity modulus.

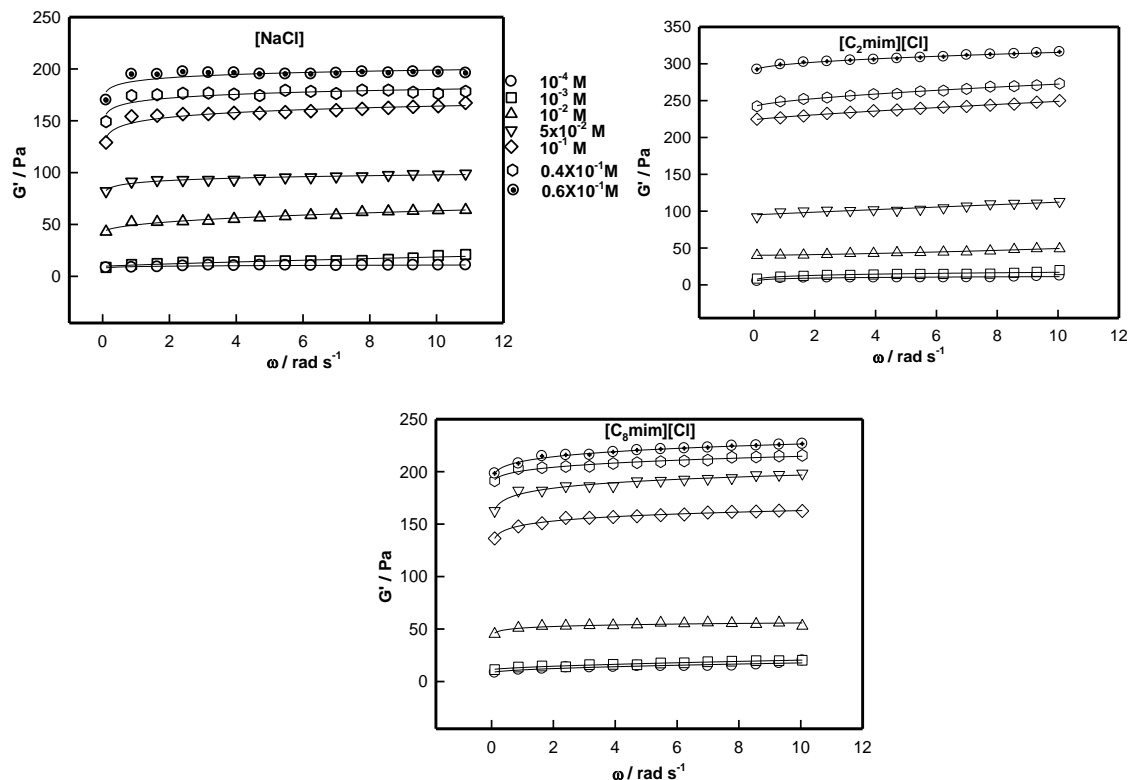


**Figure 4.11.** Variation of storage modulus with frequency for different salt concentrations.

The melting profiles of the coacervates are shown in Fig.4.12 where two clearly identifiable temperatures of transition are seen, namely the onset of melting occurring at  $T_{\text{onset}}$  and melting at  $T_{\text{melt}}$ . The melting region  $\Delta T = T_{\text{melt}} - T_{\text{onset}}$  was a function of solution ionic strength and the salt type. These values are listed in Table 4.1. The overall salt dependence of  $T_{\text{melt}}$  and  $T_{\text{onset}}$  is qualitatively similar to the profiles of  $G_0$  parameter. Higher melting temperature was for higher material rigidity  $G_0$  which is obvious.

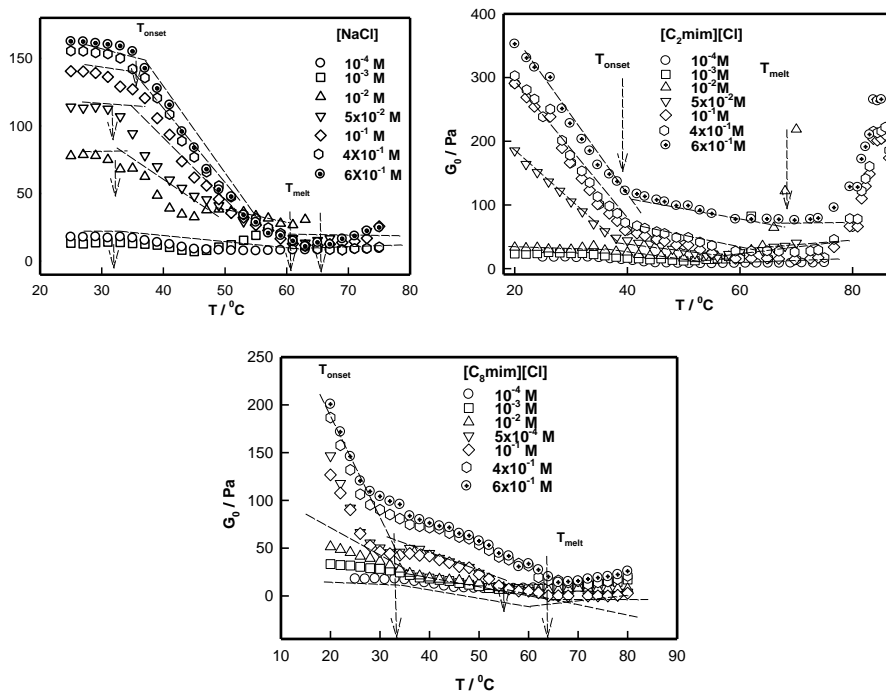


**Figure 4.12.** Variation of low frequency storage modulus  $G_0$  with temperature shown for different salt concentrations.

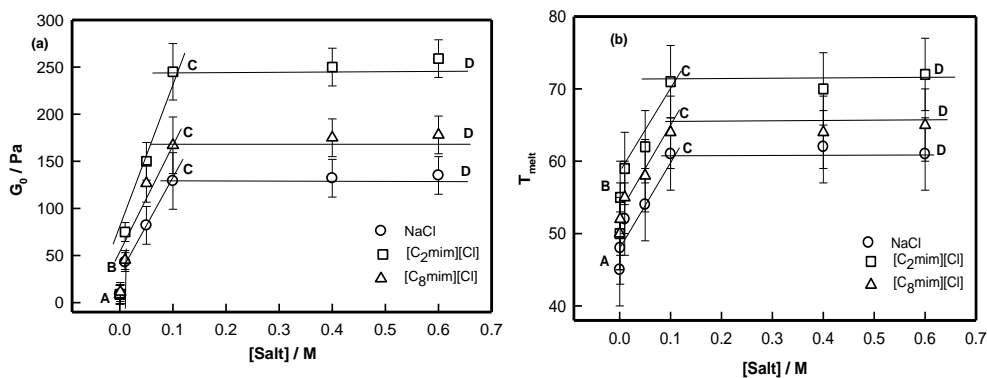


**Figure 4.13.** Variation of (a) rigidity modulus and, (b) melting temperature for different salt concentration.



Gibb's free energy ( $\Delta G$ ) is the key factor for transition from coacervate to solution state as the melting takes place. The transition region defined by  $\Delta T = (T_{melt} - T_{onset})$  was fitted to the Arrhenius equation given by

$$\Delta G_0(T) = \Delta G_0 \exp - (\Delta G/RT); T_{onset} < T < T_{melt} \quad (4.11)$$

Where  $\Delta G_0 = G_0(T_{onset}) - G_0(T_{melt})$ . The corresponding change in the free-energy of the system was determined from the data shown in Fig. 7(a) which revealed maximum change in free-energy occurred for [C8mim][Cl] samples both in the B-C and C-D regions. In addition, the commonality of salt concentration dependence on free-energy was noticed.

The rheology data can be used to obtain an estimate of the network density in a given material from the known  $G_0$  data. We probe this factor using the concept applicable for chemically assembled rubber elasticity where the network density is calculated from the equilibrium swelling experiments using the Flory model. This stipulates that the network density of the system  $\nu$  can be approximately determined from the relation given by

$$E \approx \left[ \frac{3\rho RT}{2M_e} \right] \quad (4.12)$$

where  $E$  is known as low deformation Young's modulus,  $\rho$  is rubber density, and  $M_e$  is the mean molecular weight of the polymer segment between cross-links. The dependence,  $\rho = \nu M_e$  and the fact that  $E \approx 3G_0$  (valid for an affine network), above equation can be reduced to

$$\nu \approx \left[ \frac{2G_0}{RT} \right] \quad (4.13)$$

To evaluate the relative network density  $\nu_r$  one may use

$$\nu_r = \left[ \frac{\nu}{\nu_0} \right] \quad (4.14)$$

Where  $\nu$  and  $\nu_0$  refer to the network density of salt and salt-free materials. The variation of  $\nu_r$  with salt content is shown in Fig. 4.14(b) which again follows the common description we noticed for other physical parameters. The network density was remarkably higher in samples containing [C2mim][Cl] salt.

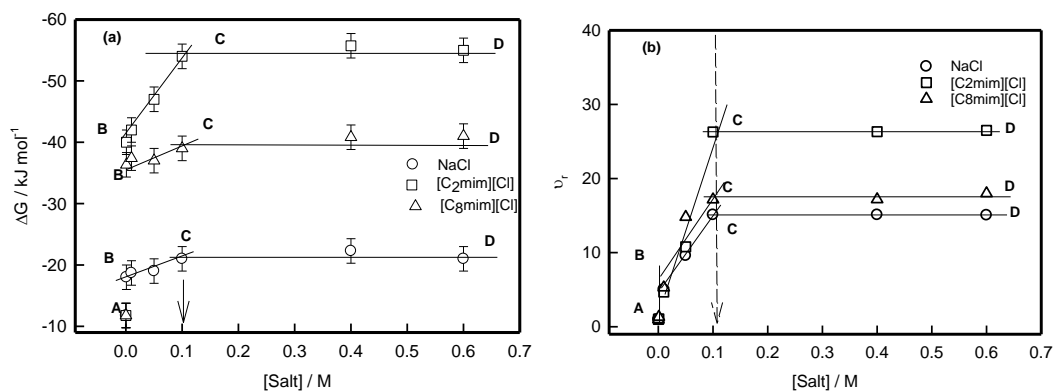
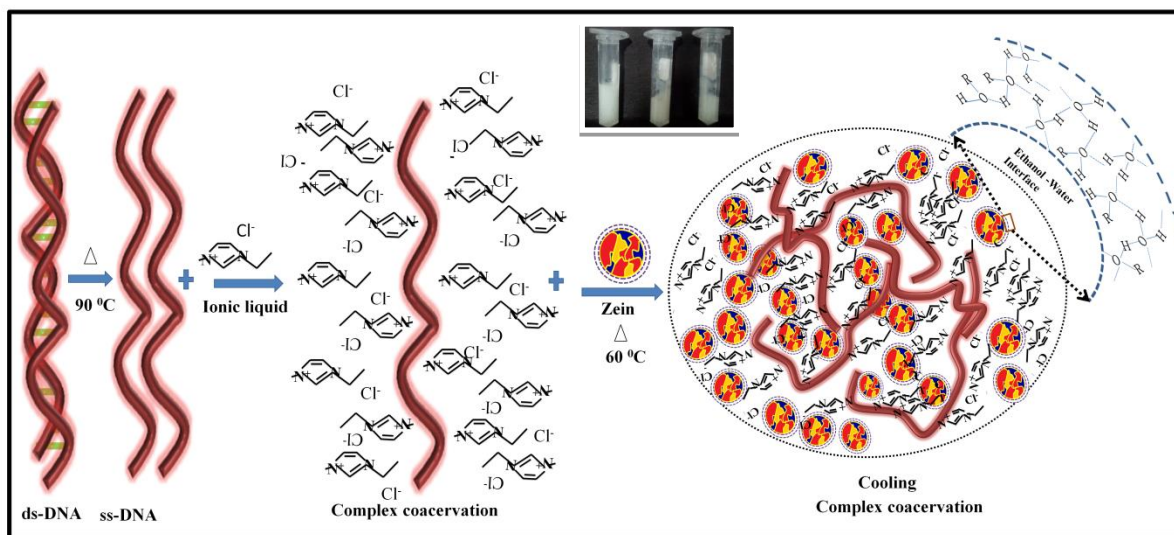


**Figure 4.14.** Variation of (a) Gibb’s free energy and (b) network density with ionic strength.

**Table 4.1.** Comparison for all coacervate properties in salt-free, and salty medium. DNA and zein data pertain to water and 80:20 % (v/v) ethanol-water medium. \*size of soluble complex

Parameter/sample	DNA	Zein	DNA-zein	[C <sub>2</sub> mim][Cl]	[C <sub>8</sub> mim][Cl]	NaCl
$G_0$ /Pa	----	----	28	9-300	9-200	9-140
$\Delta G_0$ /Pa	----	----	15±3	290±5	190±5	120±5
$T_{\text{onset}}/^\circ\text{C}$	----	----	42	35-40	34-38	32-35
$T_{\text{melt}}/^\circ\text{C}$	----	----	55	45-72	44-65	45-63
$\zeta$ /mV	-60	30	-38	-40 to -13	-40 to -23	-40 to -32
$R_h$ /nm	2100	80	170*	500*	400*	280*

The coherent picture that emerges from this study is the following: ssDNA binds to the head group of oppositely charged IL molecule that prevents base pairing. The alkane tails of ILs drain away from the polar binding sites which facilitates hydrophobic interaction between pairs of alkane tails of neighboring IL molecules. The self-assembly of this on a large scale causes interlinking of all DNA strands in a maze of supporting IL molecules. This strongly interacting assembly of DNA bound IL molecules create a polymer-rich region in the continuous medium which constitutes the supernatant. This is depicted schematically in Scheme 4.2. In the case of NaCl, no hydrophobic interactions prevail. Nonetheless, the cation- $\pi$  interaction is sufficiently dominant to cause coacervation.



**Scheme 4.2.**Representation of IL mediated complex coacervation. Inset shows pictures of ethanol-water networking.

#### 4.4 Conclusion

The complex coacervation of dsDNA, a polyanion, with a predominantly hydrophobic protein Zein was achieved by simply tuning the solvent hydrophobicity. The physical

conformation of the protein was a nanoparticle (size 80-120 nm) of low charge density that was formed *in situ* in the reacting mixture of aqueous DNA, and water-ethanol Zein solutions. Formation of interpolymer primary soluble complexes was facilitated by electrostatic interactions between the two biopolymers carrying net charge of opposite polarity, in the ethanol-water medium of low dielectric constant ( $\sim 60$ ). In this case 80 nm Zein NPs were bound to the DNA strand causing charge neutralization of the nucleic acid, and its concomitant condensation. The primary complexes were found to undergo associative interactions with Zein NPs of higher size ( $> 80$  nm) in a medium of 20-30% ethanol solution having much lower dielectric constant ( $\sim 50$ ) to generate soluble secondary complexes. Since, these complexes carried high negative charge (zeta potential of  $-38$  mV), a distinct mesophase separation was inhibited. Regardless, we observed coacervation, and the coacervate material exhibited its signature viscoelastic properties with characteristic melting profiles commensurate with Zein concentration (solvent hydrophobicity and nanoparticles size). This is the first observation of complex coacervation in a polyelectrolyte-protein nanoparticle system.

Further the coacervation in 1:1 inorganic and organic salt environment where the anion was  $\text{Cl}^-$ , for a DNA-protein system. The solution turbidity, size and zeta potential of interpolymer complex, rigidity modulus of the coacervate and its network density, all of these parameters exhibited qualitatively identical growth profiles with salt concentration. This observation is intriguing considering the fact that in addition to the dominant screened electrostatic interactions persisting between the pair of biopolymers, in the case of organic salts, in particular, other forces like hydrophobic and hydrogen bonding interactions did also played a significant role in the coacervation mechanism. Nonetheless the commonality in their binding profiles was universal. It was also found that organic salts of lower hydrophobicity facilitated

inter-polymer associations. Although, it has been widely reported that coacervation can be either favored or suppressed by increasing salt concentration, but the fact that there can be commonality in binding profiles in the environment of symmetric salts was not known hither to, which the present work unfolds.

#### 4.5 References

- [1] H. . Bungenberg de Jong and H. R. Kruyt, *Colloid Sci.* 232 (1949).
- [2] E. Tsuchida and K. Abe, *Intermacromolecular Complexes* (Springer, Heidelberg, 1982).
- [3] J. M. Park, B. B. Muhoberac, P. L. Dubin, and J. Xia, *Macromolecules* **25**, 290 (1992).
- [4] K. Kaibara, T. Okazaki, H. B. Bohidar, and P. L. Dubin, *Biomacromolecules* **1**, 100 (2000).
- [5] A. Gupta and H. B. Bohidar, *J. Phys. Chem. B* **111**, 137 (2007).
- [6] S. S. Singh, V. K. Aswal, and H. B. Bohidar, *Int. J. Biol. Macromol.* **41**, 301 (2007).
- [7] S. Boral and H. B. Bohidar, *J. Phys. Chem. B* **114**, 12027 (2010).
- [8] A. Tiwari, S. Bindal, and H. B. Bohidar, *Biomacromolecules* **10**, 184 (2009).
- [9] D. J. Burgess, *J. Colloid Interface Sci.* **140**, 227 (1990).
- [10] N. Arfin and H. B. Bohidar, *J. Phys. Chem. B* **116**, 13192 (2012).
- [11] N. Arfin, V. K. Aswal, and H. B. Bohidar, *RSC Adv.* **4**, 11705 (2014).
- [12] K. Rawat, V. K. Aswal, and H. B. Bohidar, *J. Phys. Chem. B* **116**, 14805 (2012).

- [13] A. E. Smith, *Nature* **214**, 1038 (1967).
- [14] G. M. Mrevlishvili and D. V. Svintradze, *Int. J. Biol. Macromol.* **35**, 243 (2005).
- [15] M. Kaya, Y. Toyama, K. Kubota, Y. Nodasaka, M. Ochiai, M. Nomizu, and N. Nishi, *Int. J. Biol. Macromol.* **35**, 39 (2005).
- [16] T. T. Nguyen and B. I. Shklovskii, *J. Chem. Phys.* **115**, 7298 (2001).
- [17] E. Gurovitch and P. Sens, *Phys. Rev. Lett.* **82**, 339 (1992).
- [18] C. M. Vaz, L. A. de Graaf, and W. J. Mulder, *Adhesives, Coatings, and Bioplastics from Protein Sources* (Wiley Online Library, 2018).
- [19] S. Z. Wang and A. Esen, *Plant Physiol.* **81**, 70 (1986).
- [20] R. Shukla and M. Cheryan, *Ind. Crops Prod.* **13**, 171 (2001).
- [21] Q. Zhong and M. Jin, *Food Hydrocoll.* **23**, 2380 (2009).
- [22] Y. Luo and Q. Wang, *J. APPL. POLYM. SCI* **40696**, 1 (2014).
- [23] K. W. Mattison, P. L. Dubin, and I. J. Brittain, *J. Phys. Chem. B* **102**, (1998).
- [24] J. M. Park, B. B. Muhoberac, P. L. Dubin, and J. Xia, *Macromolecules*, **25**, 290 (1992).
- [25] S. L. Perry, Y. Li, D. Priftis, L. Leon, and M. Tirrell, *Polymers (Basel)*. **6**, 1756 (2014).
- [26] Y. Wang, K. Kimura, Q. Huang, P. L. Dubin, and W. Jaegar, *Macromolecules* **32**, 7128 (1999).
- [27] J. Pathak, E. Priyadarshini, K. Rawat, and H. B. Bohidar, *Adv. Coll. Int. Sci.* **250**, 40

- (2017).
- [28] P. K. Pandey, P. Kaushik, K. Rawat, and P. L. Dubin, *Soft Matter* **13**, 6784 (2017).
- [29] U. Micka and K. Kremer, *Europhys. Lett.* **38**, 279 (1997).
- [30] V. A. Boomfield, *Biopolymers* **31**, 1471 (1991).
- [31] S. M. Melnikov, M. O. Khan, B. Lindman, and B. Jonsson, *J. Am. Chem. Soc.*, **121**, 1130 (1999).
- [32] M. Antonov, M. Mazzawi, and P. L. Dubin, *Biomacromolecules* **11**, 51 (2010).
- [33] M. W. Liberatore, N. B. Wyatt, M. Henry, P. L. Dubin, and E. Foun, *Langmuir* **25**, 13376 (2009).
- [34] C. Sanchez, G. Mekhloufi, and D. Renard, *J. Colloid Interface Sci.* **299**, 867 (2006).
- [35] Y. Xu, M. Mazzavi, K. Chen, L. Sun, and P. L. Dubin, *Biomacromolecules* **12**, 1512 (2011).
- [36] K. Chen, Y. Xu, S. Rana, O. R. Miranda, P. L. Dubin, V. M. Rotello, L. Sun, and X. Guo, *Biomacromolecules* **12**, 2552 (2011).
- [37] A. B. Kayitmazer, S. P. Strand, C. Tribet, W. Jaegar, and P. L. Dubin, *Biomacromolecules* **8**, 3568 (2007).
- [38] A. B. Kayitmazer, D. Seeman, B. B. Minsky, P. L. Dubin, and Y. Xu, *Soft Matter* **9**, 2553 (2013).
- [39] E. Kizilay, S. Maccarrone, F. Elaine, A. D. Dinsmore, P. L. Dubin, and F. Foun, *J. Phys.*

- Chem. B **115**, 7256 (2011).
- [40] S. N. Timasheff, *Adv. Protein Chem* **51**, 355 (1998).
- [41] S. N. Timasheff, *Biochemistry* **31**, 9857 (1992).
- [42] S. N. Timasheff, *PNAS* **99**, 9721 (2002).
- [43] B. Mohanty and H. B. Bohidar, *Phys. Rev. E* **69**, 1 (2004).
- [44] B. Mohanty and H. B. Bohidar, *Int. J. Biol. Macromol.* **36**, 39 (2005).
- [45] H. B. Bohidar, *Fundam. Polym. Phys. Mol. Biophys.* 1 (2014).
- [46] J. E. Martin, D. Adolf, and J. P. Wilcoxon, *Phys. Rev. Lett.* **61**, 2620 (1988).
- [47] J. E. Martin and D. Adolf, *Ann. Rev. Phys. Chem* **42**, 311 (1991).
- [48] P. K. Pandey, K. Rawat, V. K. Aswal, J. Kohlbrecher, and H. B. Bohidar, *Phys. Chem. Chem. Phys.* **19**, 804 (2017).
- [49] K. Okana, K. Wada, K. Kurita, and H. Fukuro, *J. Appl. Cryst.* **11**, 507 (1978).
- [50] T. Cosgrove, S. J. White, A. Zarbakhsh, R. K. Heenan, and A. M. Howe, *Langmuir* **11**, 744 (1995).
- [51] P. Debye and A. M. Bueche, *J. Appl. Phys.* **20**, 518 (1949).
- [52] A. Veis, *Adv. Coll. Int. Sci.* **167**, 2 (2011).
- [53] T. K, *Biopolymers* **19**, 1289 (1980).
- [54] K. Tanaka and Y. Okahata, *J. Am. Chem. Soc.*, **118**, 10679 (1996).



- [55] H. A. Barnes, *A Handbook of Elementary Rheology* (University of Wales, Institute of Non-Newtonian fluid Mechanics: Aberystwyth, 2000).
- [56] J. D. Ferry, *Viscoelastic Properties of Polymers* (John Wiley & Sons, 1980).

## CHAPTER-5

---

### Green and Enzyme-free DNA ionogel based platform for Urea detection

**Abstract:** In this chapter 1-ethyl-3-methylimidazolium chloride based ionogel electrode has used for sensing of urea.

#### 5.1 Introduction

Living beings release urea from their body as a waste material which is excreted through renal clearance. The breaking down of proteins to amino acids (amino acid catabolism), which is basically a digestion process, in the body results in the production of waste ammonia ( $\text{NH}_3$ ) which is toxic. The blood urea nitrogen (BUN) test determines the kidney health. It does this by measuring the amount of urea nitrogen in the blood. The BUN normal test range lies between 7 and 21 milligrams per deciliter of blood for a healthy individual. Urea level in serum needs to be in the normal range of 3 to 7 mM, and higher level of urea may cause renal deficiency in the body requiring the patients to undergo hemodialysis [1].

Thus, urea is a very important analyte which must be detected early to cope with kidney problems including renal failure, hepatic failure, urinary tract blockage and nephritic syndrome [2]. Many sensors have been fabricated in the past for the detection of urea which are mainly conductimetric, amperometric, potentiometric or spectroscopic methods [3]. In optical sensors there is no need for a reference sample, and the sensing is not influenced by electromagnetic interference [4]. Enzymatic method of detection [5–8] or immunoassays [9,10] are the commonly used techniques to detect Urea in pathology laboratories. Nanostructured nickel/cobalt hydroxide based electrodes were used for urea detection using cyclic voltametry in

the past [11]. Srivastava et al have used titania-zirconia based nanocomposite materials for urea detection [12].

In this work, we have used DNA ionogel [13] as substrate electrode for sensing of urea in aqueous samples in *in vitro* experiments. A remarkable aspect of the study arises from the simplicity of the electrode design and non-enzymatic mode of detection that makes the approach facile and cost-effective. Here DNA ionogel platform for the urea detection in aqueous samples in an enzyme-free milieu.

## **5.2 Sample preparation**

DNA ionogel were prepared by dissolving 1% (w/v) DNA in 1 to 5 % (w/v) ionic liquid [C2mim][Cl] solutions at 60 °C followed by heating upto 90 °C under stirring to denaturate the DNA then cooled to room temperature (25 °C).

### **5.2.1 Preparation of DNA ionogel/ITO electrodes**

The working electrode was prepared by drop casting method, where a drop of the ionosol was uniformly coated by dispersing of 50 µl of the suspension on the ITO plate that had a covered surface area of 0.25 cm<sup>2</sup> which created a thin gel film. The electrochemical behavior of the prepared electrodes were monitored and, and optimized for best response. Maximum current was detected for the sample with ionic liquid concentration of 4% (w/v). Except for a few experiments (standardization of IL concentration) all other experiments were performed on thin films containing 1% (w/v) DNA and 4% (w/v) ionic liquid. Stock solutions of 10 mM of different analytes used in the study such as urea (U), oxalic acid (OA), cholesterol (CHOX) and dextrose (DEX) were separately prepared in deionized water and store at 4 °C when not in use.

### 5.3 Result and Discussion

Initially scan rate and IL concentrations were optimized for maximum current response. Thereafter, electrochemical studies were conducted for different analytes (urea, oxalic acid, gallic acid, cholesterol, dextrose and citric acid) in the concentration range of 0.02-0.2 mM.

#### 5.3.1 Optimization of electrode parameters

DNA ionogel/ITO electrode was operated in the -0.20 to 0.4 V range. As the concentration of IL in the mixture had significant effect on the electrochemical properties, we first investigated the effect of varying IL concentration on peak current. Fig. 5.1 shows the change in CV profile for DNA ionogel/ITO electrode in comparison to bare ITO electrode. Fig. 5.2(b) shows maximum increase in cathodic current  $I_c$  at IL = 4.0% (w/v), then a plateau followed by a decrease. The highest peak current was obtained at 4.0% IL concentration indicating that this particular concentration had superior electron transfer properties and sensitivity compared to samples with other concentrations. Therefore, all further experiments were performed under these conditions.

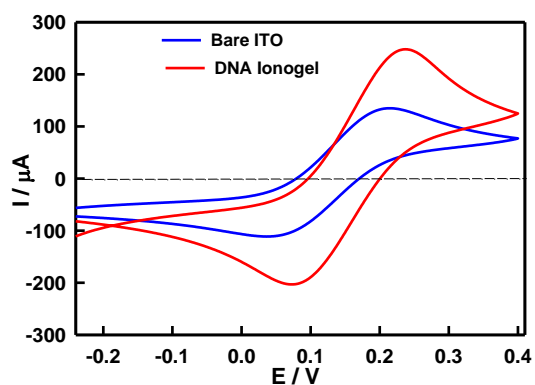


**Figure 5.1.** Comparative CV profile of DNA ionogel/ITO and bare ITO electrodes.

It was found the the CV profile of bare ITO and DNA ionogel/ITO electrodes at a scan rate of 50 mV/s in order to map the electrochemical behavior in Zobell's solution. Fig. 5.1 suggested that the presence of a film on the ITO surface and there was a reduction in electron transfer accessibility by the film compared to ITO electrode [14,15].

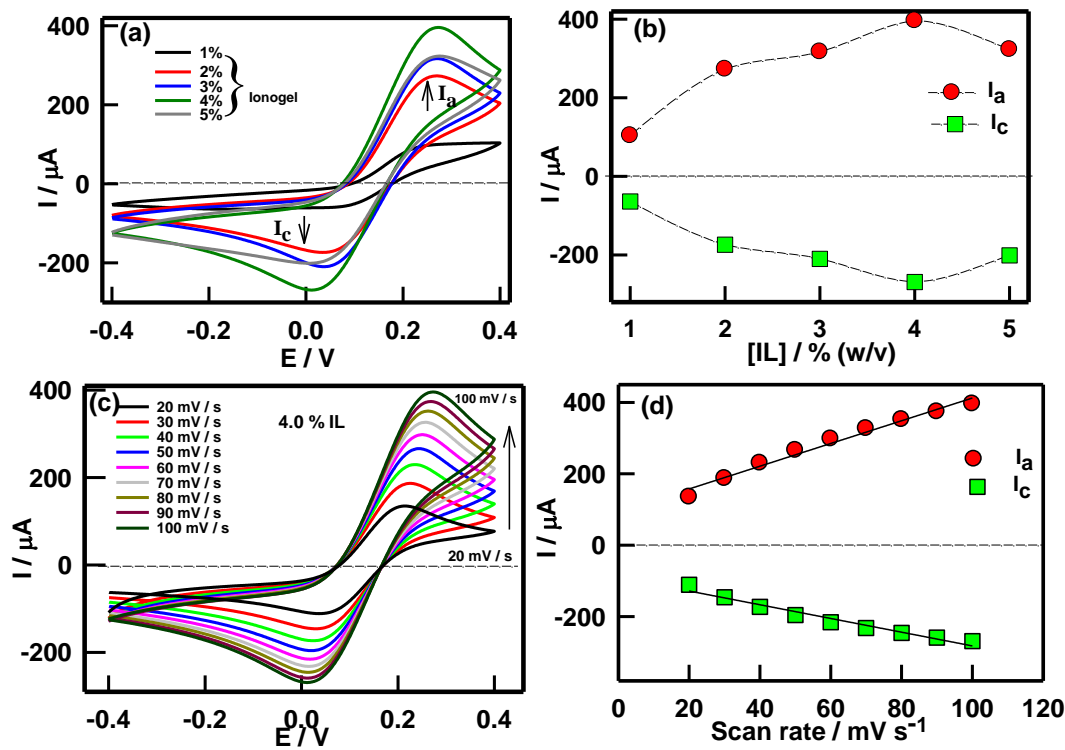


**Figure 5.2.**(a) CV response of ionogel electrode with 1% to 5% (w/v) IL concentration. (b) anodic and cathodic current with IL concentration and peak current is maximum for 4% (w/v) sample, (c) Cyclic voltammograms of DNA ionogel at different scan rates. (d) Peak current is shown having linear dependence with scan rate (mV/s) with a  $\chi^2$  value of 0.99.

Thereafter, the effect of scan rate on peak current was estimated. Fig. 5.2(a) exhibits CV profile of DNA ionogel/ITO electrode in the potential range of -0.4 to 0.4 V. Fig. 5.2(c) depicts the scan rate (10 to 50 mV/s) dependence, where an increase in peak current was observed with increasing scan rate. The peak currents  $I_a$  and  $I_c$  were noticed to be linearly increased (Fig. 5.2(d)) with scan rate with  $\chi^2$ -value of 0.99. Thus, the electrochemical reaction was confirmed to

be a diffusion driven process. Furthermore, the peak separation potential was independent of scan rate that suggested that diffusion controlled redox reaction occurred in the DNA ionogel/ITO electrode.

### 5.3.2 Detection of analytes

The sole objective of the present study was to analyze the potential ability of the ionogel electrodes towards bio-analyte detection. Therefore, electrochemical response of most sensitive ionogel (4% IL) electrode was used as the working electrode to monitor response from different analytes. The tested concentration range of these analytes varied from 0.02-0.2 mM and with 50 mV/s was the fixed scan rate. The variation in peak current ( $I_a$  and  $I_c$ ) with varying analyte concentration was observed to determine the response of the electrode towards the tested analytes. A single DNA ionogel/ITO electrode was used for the whole concentration range for a given analyte. Distinct changes in CV profile were observed in the case of urea while no major changes were seen in the case of other tested analytes. The anodic peak current was observed to increase with increasing concentration of urea. Additionally, a shift of anodic peak current towards higher potential was seen with increasing urea concentration. Fig. 5.3(a) shows the CV of DNA ionogel/ITO electrode on treatment with varying urea concentration. It clearly indicated increase in the oxidation ( $I_a$ ) and reduction ( $I_c$ ) current on treatment with urea, and thus suggested that the electrocatalytic reaction was because of urea presence. No change in the peak current was found for other analytes even at very high concentration of 0.2 mM..

On plotting the anodic and cathodic peak current for urea with respect to its concentration, a linear relationship was observed with a least-square fitting  $\chi^2$  value of 0.97 and 0.98, respectively (Fig. 5.3(b)). For the linear detection range (0.02 to 0.2 mM), detection limit was found to be

0.01 mM and the sensitivity of ionogel electrode towards urea was calculated from the slope of peak current which was 6.25 mA/mM cm<sup>2</sup>.

**Table 5.1.** Comparison of different urea sensors which suggests that our system presents a very high sensitivity compared to the existing enzymatic and non-enzymatic modes of detection.

S. No.	Electrode composition	Detection range (mM)	Detection limit (mM)	Reference
<i>Enzymatic</i>				
1.	Urs-GLDH / ZnO-CH/ITO	10.8–16.6	1.30	[16]
2.	PNVK/SA/urease LB film	0.5 – 68.0	0.50	[17]
3.	Urease + polyurethane-acrylate	0.2 – 6.0	0.20	[18]
4.	Urease/MSA-QDs	0.01 – 100.0	0.01	[19]
<i>Non-enzymatic</i>				
5.	Pyrrrole/Pt	0.08–1.44	1.11	[20]
6.	GA-NC/ITO	0.10–20.0	7.70	[21]
7.	Chitosan-MIP	10 <sup>-9</sup> –10 <sup>-7</sup>	10 <sup>-9</sup>	[22]
8.	ZnO/Ag/glass	0.001-24.0	0.01	[23]
9.	Cellulose-SnO	0.1-42.0	0.50	[24]
10.	DNA-ionogel/ITO	0.02-0.2	0.01	Present work

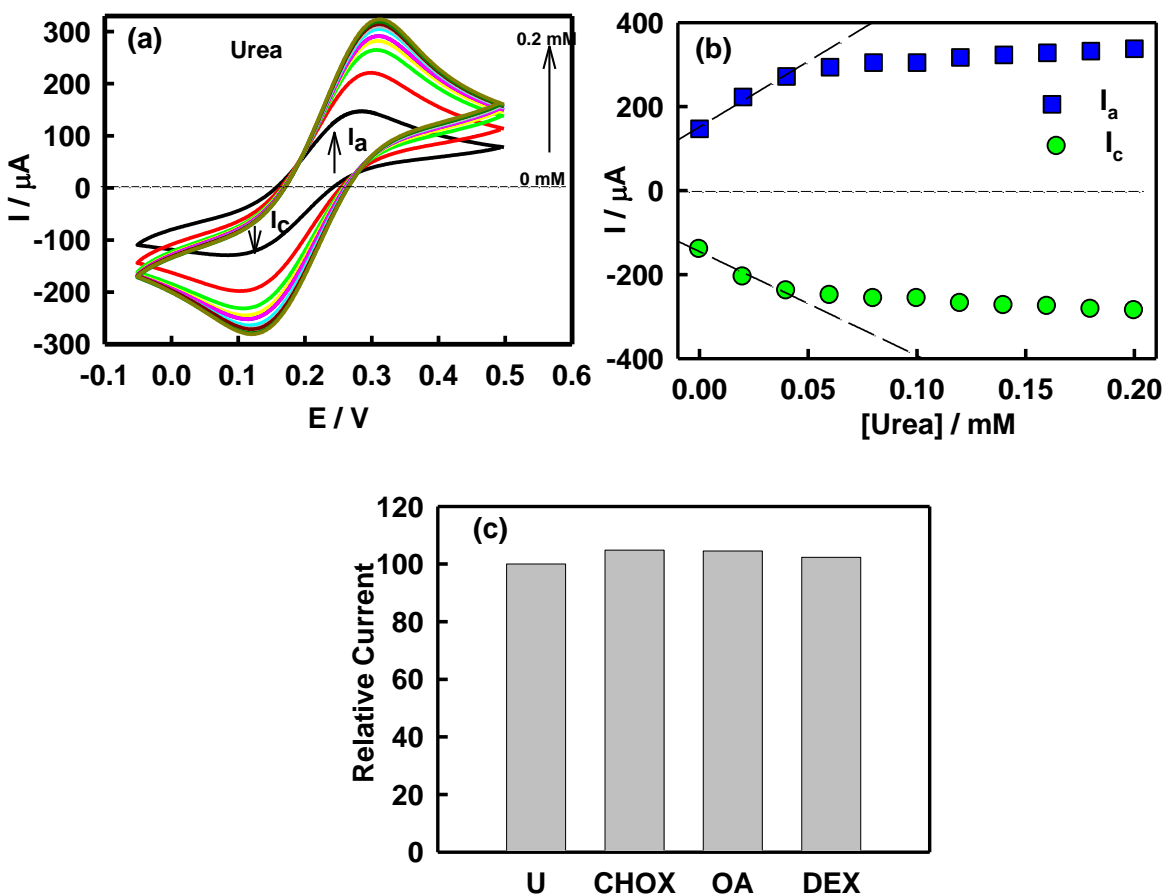
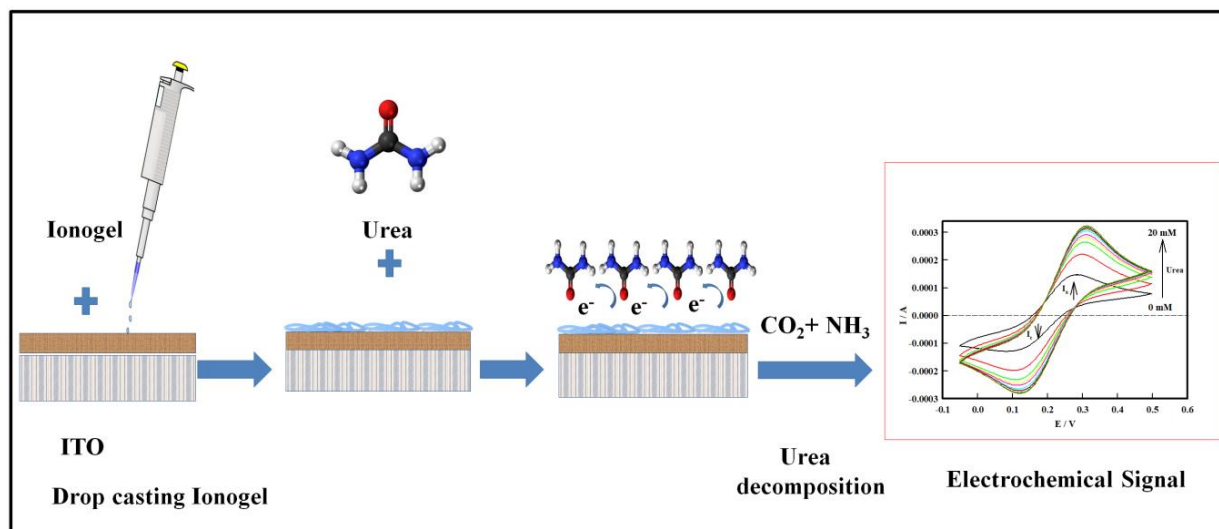


**Figure 5.3.** (a) Cyclic voltammograms of DNA ionogel in presence of varying concentration of urea analyte, (b) Linear dependence of current as a function of urea concentration showing the sensitivity of the system in the range of 0.02-0.06 mM urea, (c) Interference in presence of 1:1 ratio of urea and test analyte.

Enzymatic mode detection involving urease enzyme depends on the catalytic hydrolysis of urea and measuring the ions used or generated in the process. In the present method, a non-enzymatic approach is proposed where changes in electrochemical current was observed when the electrode was treated with increasing concentration of urea. Thus, a similar process to that of enzymatic reaction occurs where on interaction with the electrode, decomposition of urea occurs thereby generating  $\text{NH}_3$ , which subsequently gets converted to  $\text{NH}_4^+$ , that is responsible for the increase



in peak current. A representative mechanism of urea detection by DNA ionogel/ITO electrode is presented in Scheme 5.1.



**Scheme 5.1.** Representative illustration of the mechanism of electrochemical sensing of urea by DNA ionogel/ITO electrode.

The selectivity of electrode towards urea was inferred from the interference study (Fig.5.3(c)). It was observed that in presence of different analytes (CHOX, OA and DEX) electrode was remarkably selective towards urea. In this study 10 mM concentration of urea and different analytes of same concentration were mixed in 1:1 (v/v) ratio and their redox behavior was monitored. It was found from the peak current of CV data that ionogel/ITO electrode was selective for urea and did not show notable response against other analytes (Fig. 5.3(c)).

### 5.3.3 FTIR

Fourier-transform infrared spectroscopy (FTIR) shows the structural and conformational changes that occurred after binding to the urea with in ionogel (Fig. 5.4). FTIR data was analyzed on the

basis of variation in the peak intensity. The sample showed broad band located at  $700\text{ cm}^{-1}$  was due to  $=\text{C-H}$  bending or  $\text{C-Cl}$  stretch. Peak at  $1200\text{ cm}^{-1}$  and  $1350\text{ cm}^{-1}$  was corresponding to the imidazolium ring and the  $\text{CH}_2$  bend in the spectra. Peak,  $1740.49\text{ cm}^{-1}$  was due to  $\text{C=O}$  stretch coming from DNA or carbonyl functional group of urea. FTIR peak at  $3020\text{ cm}^{-1}$  was corresponding to stretching vibration of  $-\text{N-H}$ . Peak at  $3470$  was from  $-\text{OH}$  stretching (hydration layer) and  $3775\text{ cm}^{-1}$  due to  $-\text{NH}$  band in DNA. Peak at  $983\text{ cm}^{-1}$  was due to the phosphate symmetric vibration within the ionogel.

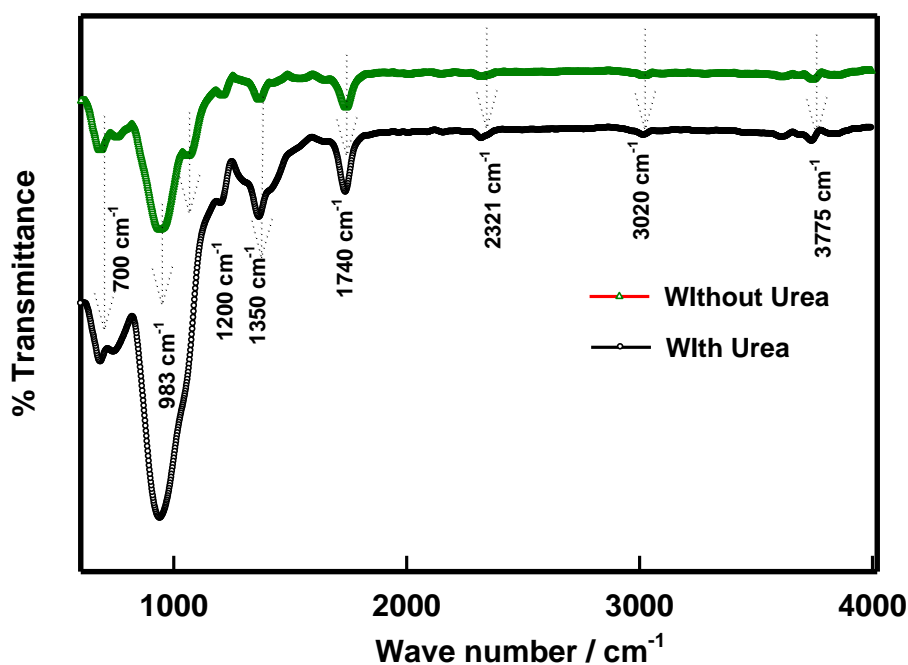


**Figure 5.4.** FTIR spectra for various samples. See the text for details.

### 5.3.4 Surface Morphology characterization

The information about surface morphology of DNA ionogel electrode was observed from the scanning electron microscope pictures. Fig. 5.5 (a) describes the layered shaped morphology of

ionogel /ITO thin film. Image (b) shows morphological changes in the electrode because of electrochemical response of electrode towards urea.

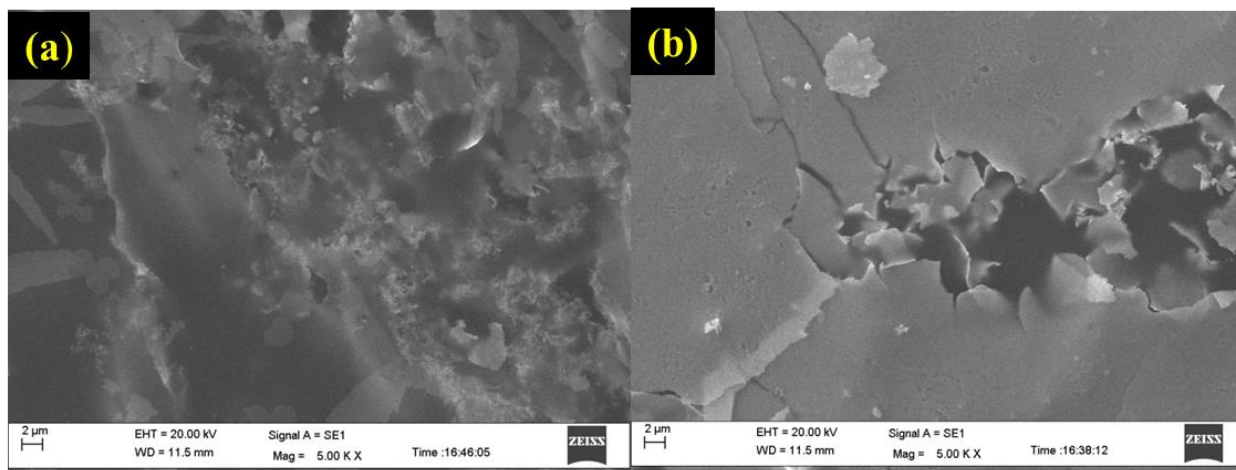


**Figure 5.5.** SEM images for (a) ionogel/ITO electrode, (b) change in morphology after urea detection

## 5.4 Conclusion

The present study focused on the development of a DNA ionogel based detection platform. The thin film of this ionogel was uniformly deposited and dried on an ITO glass plate, and used as working electrode for highly selective and sensitive detection of urea. The electrode exhibited a very high sensitivity of  $6.25 \text{ mA mM}^{-1} \text{ cm}^{-2}$  with detection limit of 0.01 mM. Here sensing provides a new platform for enzyme-free and sensitive detection of urea. This study must be extended to include pathological samples in future in order to validate this platform for clinical applications.

## 5.5 References

- [1] S. G. Ansari, H. Fouad, H. S. Shin, and Z. A. Ansari, *Chem. Biol. Interact.* **242**, 45 (2015).
- [2] R. K. Srivastava, S. Srivastava, T. N. Narayanan, B. D. Mahlotra, R. Vajtai, P. M. Ajayan,

- and A. Srivastava, *ACS Nano* **6**, 168 (2012).
- [3] A. Maaref, H. Barhoumi, C. Martelet, and R. M. Baker, *Sens. Actuators B* **123**, 679 (2007).
- [4] P. Bhatia and B. . D. Gupta, *Sens. Actuators B* **161**, 434 (2012).
- [5] W. Y. Lee, S. R. Kim, and T. H. Kim, *Anal. Chim. Acta* **404**, 195 (2000).
- [6] M. Stred'anský, A. Pizzariello, S. Stred'anská, and S. Miertuš, *Anal. Chim. Acta* **415**, 151 (2000).
- [7] M. L. Hamlaoui, K. Reybier, M. Marrakchi, N. Jaffrezic-Renault, C. Martelet, R. Kherrat, and A. Walcarius, *Anal. Chim. Acta* **466**, 39 (2002).
- [8] M. Santandreu, S. Solé, E. Fàbregas, and S. Alegret, *Bioelectron. Biosens.* **13**, 7 (1998).
- [9] A. P. Deng, J. T. Chen, and . H. J. Huang, *Acta Anal. Chim.* **461**, 49 (2002).
- [10] S. B. Adeloju, S. J. Shaw, and G. G. Wallace, *Anal. Chim. Acta* **341**, 155 (1997).
- [11] M. Vidotti, M. R. Silva, R. P. Salvador, S. I. C. de Torresi, and L. H. Dall'Antonia, *Electrochim. Acta* **53**, 4030 (2008).
- [12] S. Srivastava, M. A. Ali, P. R. Solanki, P. M. Chavhan, M. K. Pandey, A. Mulchandani, A. Srivastava, and B. D. Malhotra, *RSC Adv.* **3**, 228 (2013).
- [13] P. K. Pandey, K. Rawat, V. K. Aswal, J. Kohlbrecher, and H. B. Bohidar, *Phys. Chem. Chem. Phys.* **19**, 804 (2017).
- [14] N. Joshi, K. Rawat, P. R. Solanki, and H. B. Bohidar, *Biochem. Eng. J.* **102**, 69 (2015).

- [15] N. Joshi, K. Rawat, P. R. Solanki, and H. B. Bohidar, *Sens. Bio-Sensing Res.* **5**, 105 (2015).
- [16] P. R. Solanki, A. Kaushik, A. A. Ansari, G. Sumana, and B. D. Malhotra, *Appl. Phys. Lett.* **93**, 163903 (2008).
- [17] R. Singhal, A. Gambhir, M. K. Pandey, S. Annapoorni, and B. D. Malhotra, *Biosens. Bioelectron.* **17**, 697 (2002).
- [18] B. Lakard, G. Herlem, S. Lakard, A. Antoniou, and B. Fahys, *Biosens. Bioelectron* **19**, 1641 (2004).
- [19] C. P. Huang, Y. K. Li, and T. M. Chen, *Biosens Bioelectron* **22**, 1835 (2007).
- [20] S. Mondal and M. V. Sangaranarayanan, *Sensors Actuators B* **177**, 478 (2013).
- [21] A. Sharma, K. Rawat, H. B. Bohidar, and P. R. Solanki, *Appl. Clay Sci.* **146**, 297 (2017).
- [22] H.-T. Lian, B. Liu, Y.-P. Chen, and X.-Y. Sun, *Anal. Biochem.* **426**, 40 (2012).
- [23] R. Ahmad, N. Tripathy, and Y.-B. Hahn, *Sensors Actuators B* **194**, 290 (2014).
- [24] J.-H. Kim, S. Mun, H.-U. Ko, G.-Y. Yun, and J. Kim, *Nanotechnology* **25**, 092001 (2014).

## CHAPTER-6

---

### Concentration Dependent 1-Octyl-3 Methylimidazolium Chloride based DNA ionogel: Application as Citric Acid Sensor

**Abstract:** In this chapter concentration dependence of 1-octyl-3 methyl imidazolium ionic liquid based DNA ionogels was prepared and these ionogel have been used to fabricate citric acid sensor.

#### 6.1 Introduction

Earlier pH triggered and fast responding DNA hydrogel was demonstrated for sustainability under different pH conditions [1]. It is desired because of its biocompatible and low cytotoxic nature. Different lengths of DNA chains form stable assembly with cationic colloidal particles [2]. Graphene oxide was used to form multifunctional DNA hydrogel with high rigidity, biocompatible, self-healing property [3]. Supramolecular polypeptide -DNA hydrogel with high rigidity modulus was used for 3D printing [4].

DNA is polyanionic in nature and repel each other because of columbic repulsion. Therefore, for physical entanglement to take place a cross linker is required such as EGDA [5]. Polymerase enzyme based DNA meta- hydrogel is used in electrical circuit in which water plays a role of ON-OFF switch [6]. Interaction of DNA and multi-walled carbon nanotube leads to the formation of self-assembled DNA-hybrid hydrogel [7]. Comparative study of ds-DNA and ss-DNA with cation have been extensively explored and it is concluded that ss-DNA collapse more than ds-DNA [8]. DNA functionalized hydrogel was used to detect mercury from the environment because of its hazardous effects [9]. Stable DNA Hydrogel fibers could be prepared

in the presence of ionic liquid without high temperature [10]. Surfactant CTAB and lysozyme protein solution assemble DNA gel particles with ss-DNA or ds-DNA [11]. DNA hydrogel can hold Au nanoparticle inside its matrix [12]. Cross linking of DNA gel with organic salt such as  $\text{CaCl}_2$  shows deduced osmotic pressure [13]. Relaxation dynamics and rheological properties of DNA hydrogels was consistently explored and microscopic changes in the hydrogels were probed by neutron scattering technique [14,15].

Sui et al have shown poly(ferrocenylsilane) in presence of poly ionic liquid forms nanogels [16]. It was seen that block copolymer forms self-assembled spherical or worm like micelles in ionic liquid [17]. Ionic liquid based biopolymer gel has high viscosity and melting temperature. It has also capacity to dissolve cellulose powder which is generally insoluble in water and other solvents [18]. At very low concentration of DNA, ionogel was also formed [19]. Self-assembly of triblock copolymer was studied with the help of rheology. It was found that gels formed in presence of ionic liquid are stable at high temperature ( $100^{\circ}\text{C}$ ) [20].

Pandey et al have demonstrated DNA ionogels and studied their time dependent structural dynamics, viscoelastic properties and microscopic structures [21]. These ionogels are used in the manufacture of lithium ion batteries, fuel cells, solar cells, electrochemical sensor, biosensors, actuators and drug release vehicles etc. [22]. Here, we have studied concentration dependence of 1-octyl-3 methyl imidazolium ionic liquid based DNA ionogels and these ionogel have been used to fabricate citric acid sensor for the biomedical application purpose.

## **6.2 Sample preparation**

DNA was dissolved in different concentration (0.1% to 1.0 % (w/v)) of IL aqueous solution such a way that final concentrations of DNA remain 1% (w/v). These samples heated upto  $90^{\circ}\text{C}$ .

Finally on cooling at room temperature an optically clear sample was obtained for rheology and SANS study [23].

**Table 6.1** Data indicates the ionic liquid threshold undertaken for study in this work comparing with earlier one. The special features of attaining gelation depend on ionic liquid concentration.

DNA%(w/v)	[C2mim][Cl] %(w/v)	Remark	[C8mim][Cl] %(w/v)	Remark
1%	1%	Gel	1%	Gel
1%	3%	Gel	3%	Sol
1%	5%	Gel	5%	Sol

## 6.3 Result and Discussion

### 6.3.1 Viscoelastic Behavior of ionogels

The Rheological characterization of samples was probed by following two distinct approaches [24,25]. Initially the variation of shear modulus to probe elastic behavior of these gels an isothermal frequency sweep test was performed (Fig. 6.1(a)), and later temperature dependent study of different gel samples was probed by isochronal temperature sweep test (Fig. 6.2(a)). The photograph of these samples is shown in Fig. 6.1(b). Power-law dependence of elastic modulus on shear rate frequency  $\omega$  is given by the relation [26,27]

$$G' \sim \omega^n \quad (6.1)$$

Above equation yields the exponent  $n = 0.8 \pm 0.4$  when fitted to data in Fig. 6.1(a). When  $\omega \rightarrow 0$ , the gel strength  $G_0$  can be described as,



$$G_0 = \lim_{\omega \rightarrow 0} G'(\omega) \quad (6.2)$$

The value of  $G_0$  changes from  $10 \pm 4$  Pa to  $60 \pm 10$  Pa on increasing the IL concentration from 0.1% (w/v) to 1.0% (w/v). Therefore, as IL concentration increases the gel rigidity increased because of the closer network formation.

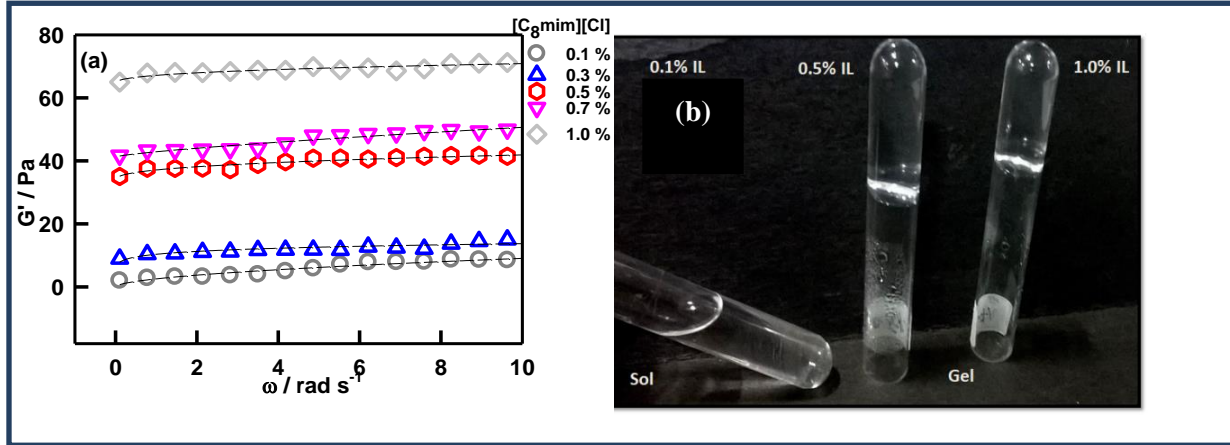


**Figure 6.1.** (a) Frequency dependent behavior of elastic storage modulus with different IL concentration and (b) photograph of ionosol and ionogels.

Viscoelastic length  $\xi_{el}$  is depend on rigidity, which is given by [28]

$$\xi_{el} = \sqrt[3]{\frac{K_B T}{G_0}} \quad (6.3)$$

For the 0.1% IL sample  $\xi_{el} = 120$  nm which reduced to 40 nm for 1.0 % IL sample.

The temperature sweep data of these gels gives clearly two transition regions which are clearly depicted in Fig. 6.2(a). The initial transition point was found between temperature 35-40 °C ( $T_{melt}$ ) and  $T_{gel}$  was located in the higher temperature region (53-62 °C).

From Fig. 6.2(b), it can be easily interpreted that all  $G_0$ ,  $T_{melt}$  and  $T_{gel}$  are linearly dependent with IL concentration. The gelation is associated with enthalpy change which is corresponding to first order phase transition.

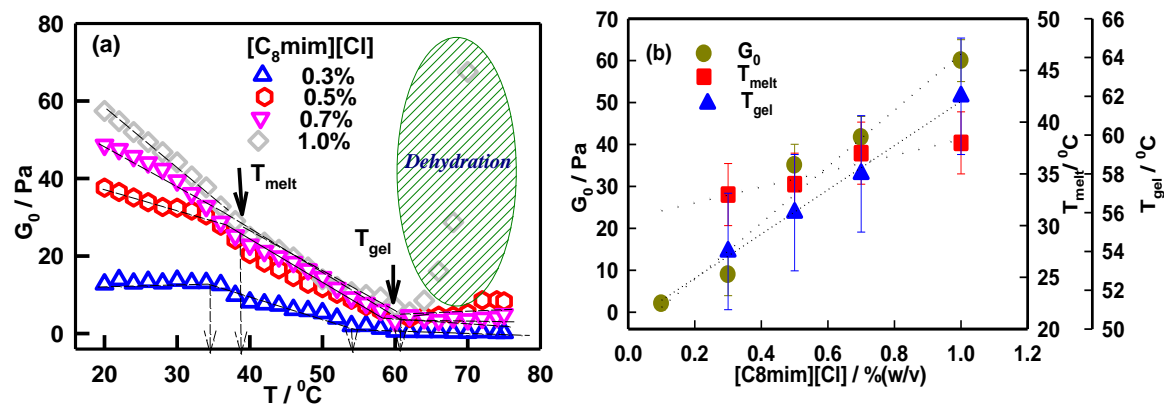


**Figure 6.2.** (a) Temperature dependent profile for storage modulus  $G_0$ . Change in slope depicts the transition temperature, referred as  $T_{melt}$  and  $T_{gel}$ . (b) IL concentration dependent variation of  $G_0$ ,  $T_{melt}$  and  $T_{gel}$ .

Linear fitting of  $G_0$ ,  $T_{melt}$  and  $T_{gel}$  with respect to IL concentration, shows change in these parameter per (w/v) IL concentration. The determined values are

$$G_0 = 67.16 \text{ Pa/ \% (w/v)}, T_{melt} = 7.66 \text{ }^\circ\text{C/ \% (w/v)}, T_{gel} = 11.40 \text{ }^\circ\text{C/ \% (w/v)}$$

### 6.3.2 Microscopic Information

The  $I(q)$  Vs  $q$  structure factor data is shown in Fig. 6.3. The data was defined in two distinct regions. These regions are best fitted by Power-law ( $0.0552 \leq q \leq 0.1140 \text{ cm}^{-1}$ ), Broad-Peak ( $0.1290 \leq q \leq 1.180$ ) and fluctuations given by,

$$I(q) = \text{Power Law} + \text{Broad Peak} + \text{Fluctuations}$$

$$I(q) = I_{PL}q^{-\alpha} + \frac{I_{BP}}{[1+\xi|q-q_0|^m]} + B \quad (6.4)$$

The first two terms of above equation are corresponding to power law and broad peak functions and B denotes to the fluctuations. The eqn (6.4) yields the parameters such as  $I_{PL}$ ,  $\alpha$ ,  $I_{BP}$ ,  $\xi$ ,  $q_0$  and m. where  $I_{PL}$  and  $I_{BP}$  are pre-factors.  $\alpha$  denotes the structural geometry of scattering moiety,  $\xi$  is corresponding to correlation length of polymer network,  $q_0$  identifies the broad peak position, m

is obtained from fitting of broad peak relation or also known as modified Lorentz equation. The boundary between two regions is defined by  $q^*$  value [Fig. 6.3].

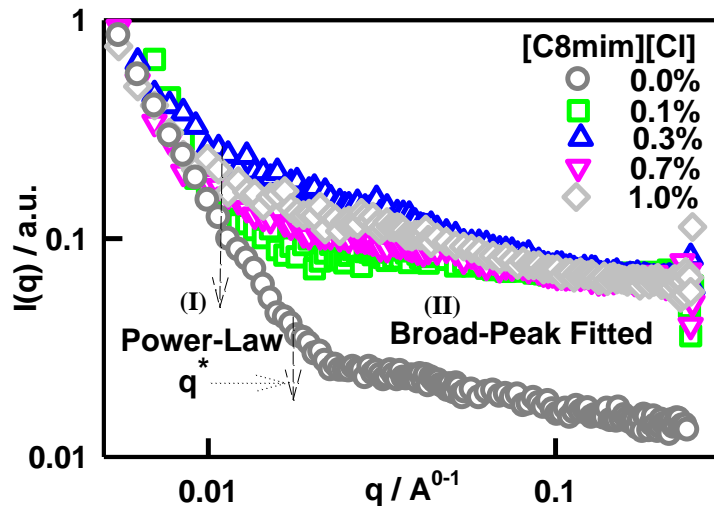


**Figure 6.3.**  $I(q)$  versus  $q$  structure factor correlation profile for different ionogels.

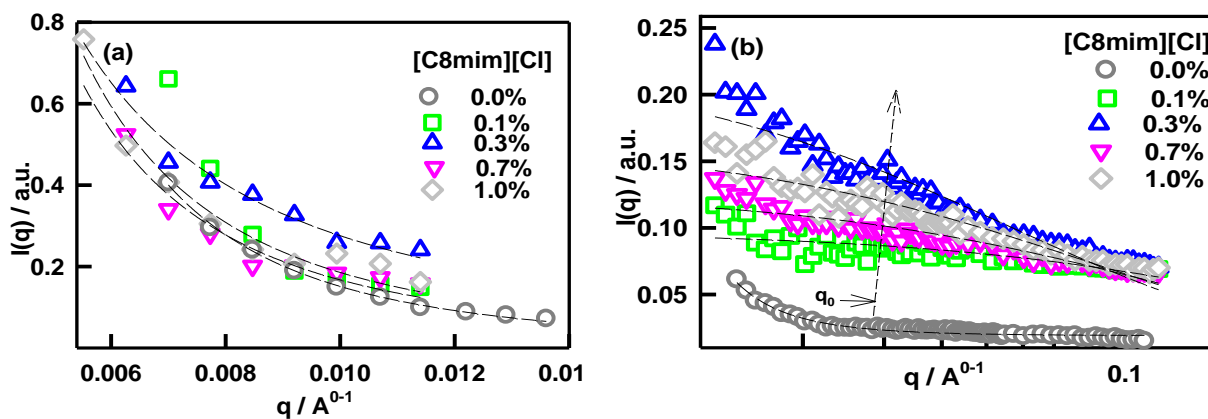


**Figure 6.4.** Distinct structure factor profile fitted by (a) Power-law and (b) broad peak functions. Plotted lines are showing fitting of the data.

From the fitting of low-  $q$  region obtained value of  $\alpha$  is  $2.5 \pm 0.3$ , Fig. 6.5(a) which shows the Gaussian chain as scattering moiety.

In high  $q$ -region there is appearance of broad peak which is interpreted by broad peak fitting function, which yields the value of correlation length  $\xi$  for gel network. In this case it varies from 3.5 nm to 1 nm (see Fig. 6.5(a)). That is with IL concentration, correlation length decreases. This is corresponding to compact network formation. The peak position of structure factor profile  $q_0$  shifts rightwards with IL concentration. This is correlated by  $d$ -spacing or  $d_0$  ( $= 2\pi/q_0$ ) value of microscopic structure. It is defined by distance between polymer rich to poor region of ionogel network. Therefore there is formation of close packing or compact networks within ionogels with higher IL concentration [29,30].

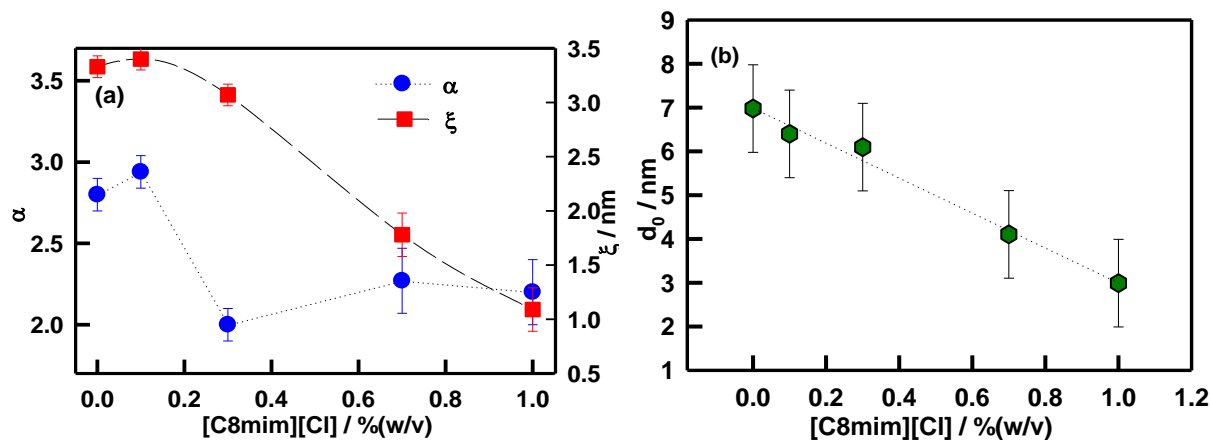


**Figure 6.5.** (a) Variation of  $\alpha$ ,  $\xi$  and (b)  $d$ -spacing for different IL concentrations.

### 6.3.3 Preparation of DNA ionogel-ITO electrodes

The thin film of DNA ionogel-ITO electrode was prepared by drop casting method, where a drop of the ionosol was uniformly coated by dispersion of 50  $\mu$ l of the suspension onto an ITO plate that had a covered surface area of 0.25  $\text{cm}^2$  which created a thin film. The films were then allowed to dry at room temperature for about 24 hours. The electrochemical behavior of the

prepared electrodes was monitored and the maximum current was detected for the sample with ionic liquid concentration of 0.7% (w/v). Except for a few experiments (standardization of IL concentration) all other experiments were performed on thin films containing 1% (w/v) DNA and 0.7% (w/v) [C8mim][Cl].

### 6.3.4 Fourier transform Infrared spectroscopy (FTIR) and surface morphology

The DNA Ionogel/ITO electrode showed broad band located at  $757.1\text{ cm}^{-1}$  is due to =C-H bending or C-Cl stretch. Peak at  $1217.6\text{ cm}^{-1}$  and  $1361.9\text{ cm}^{-1}$  is corresponding to the imidazolium ring and the  $\text{CH}_2$  bend in the spectra. The C-H bond stretch in ionic liquid attached to DNA strand. Peak at  $1529.8\text{ cm}^{-1}$  is because of C=C stretch,  $1471.2\text{ cm}^{-1}$  is due to C-H bending.  $1740.5\text{ cm}^{-1}$  is due to C=O stretching in DNA or carboxylic acid functional group of citric acid.

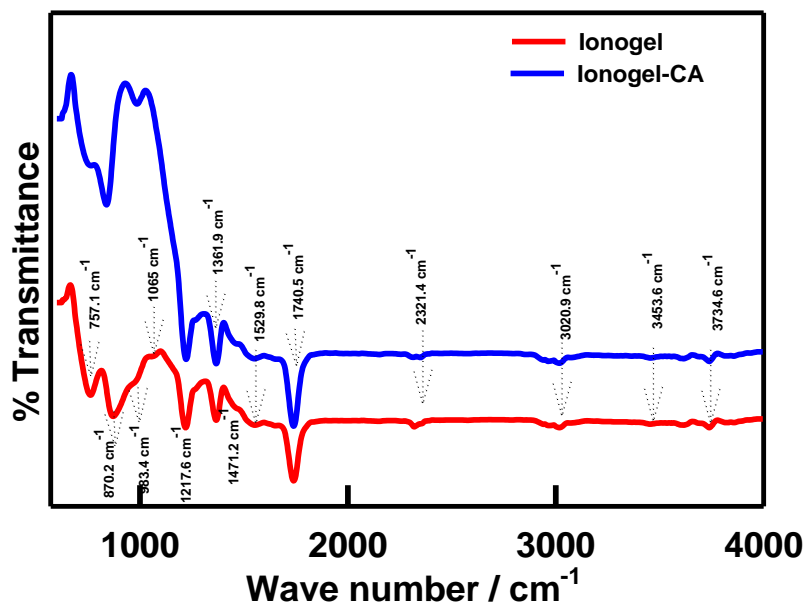


**Figure 6.6.** FTIR spectra without and with analyte.

Peak at  $3020\text{ cm}^{-1}$  originates from -N-H stretching vibration and  $3453\text{ cm}^{-1}$  due to -OH stretching vibration and  $3734.6\text{ cm}^{-1}$  due to -NH band in DNA ionogel. Distinct changes in the

spectra occurred on treatment with citric acid, basically changes in intensity of peaks was observed which established the interaction between the electrode and citric acid. Peak at  $983.4\text{ cm}^{-1}$  is due to phosphate symmetric vibration within the ionogel. In the presence of citric acid, there is major change or stretch in the peak  $1065\text{ cm}^{-1}$ ,  $788\text{ cm}^{-1}$  and  $1361.9\text{ cm}^{-1}$ .

The surface morphology of electrodes without and citric acid was characterized using scanning electron microscope (SEM) is shown in Fig. 6.7 (a) were describes the branched shaped morphology of ionogel thin film. Image (b) shows surface morphology of electrode with Citric acid. This change in surface morphology is caused by transfer citric acid – ionogel interaction. Details discussion of analytic detection is given further.

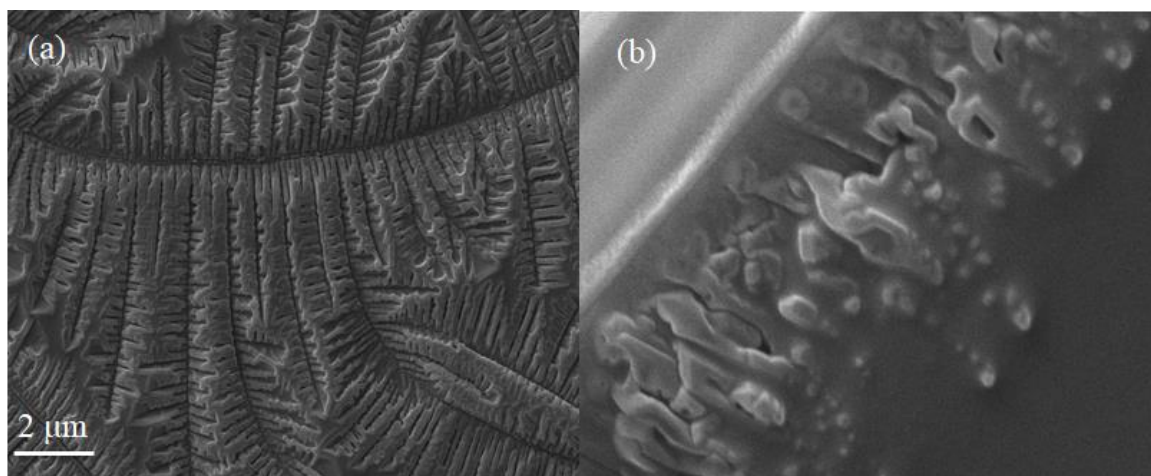


**Figure 6.7.** SEM images (a) without and (b) with analyte.

### 6.3.5 Optimization of parameters

In electrochemical sensing of analytes three electrode cell were operated in  $-0.05$  to  $0.5\text{ V}$  potential. The three electrodes were used such as (DNA ionogel-ITO) as a working electrode, Platinum wire as supplementary electrode and Ag/AgCl as a reference electrode. The CV studies were conducted using Zobel's solution ( $3.3\text{ mM K}_4\text{Fe(CN)}_6$ ,  $3.3\text{ mM K}_3\text{Fe(CN)}_6$  and  $0.1\text{M}$

KCl). Scan rate, ionogel concentration and analyte concentration were standardized by repeating the experiments thrice under similar experimental conditions.

Initially we investigated the CV profile of bare ITO and DNA ionogel-ITO electrode at a scan rate of 50 mV/s in order to understand the electrochemical behavior in Zobell's solution and observed that the peak current of DNA ionogel/ ITO electrode is higher than blank ITO. This suggested the presence of a film on the ITO surface and there was a reduction in electron transfer accessibility by the film compared to ITO electrode [31,32].

Later, the electrochemical response of DNA ionogel-ITO electrode was monitored in the potential range of -0.1 to 0.5 V. As the concentration of IL in the mixture had significant effect on the electrochemical properties, we first investigated the effect of varying IL concentration on peak current. Fig. 6.9(a) shows the CV profile of DNA ionogel-ITO electrode with varying IL concentration. Fig. 6.9(b) shows an increase in anodic current  $I_a$  at IL concentration 0.7% (w/v) and then decreases, and remained invariant thereafter. As the highest peak current ( $I_a$ , anodic and  $I_c$ , cathodic) was obtained at 0.7% IL concentration indicating that this particular concentration had superior electron transfer properties and sensitivity compared to samples with other concentrations. Therefore, all further experiments were performed under these conditions.

The different analytes used in the study were urea (U), oxalic acid (OA), gallic acid (GA), cholesterol (CHOX), Dextrose (DEX), and citric acid (CA). Stock solutions of 10 mM of these analytes were separately prepared in deionized water and store at 4 °C when not in use. The electron transfer kinetics of the electrode was analyzed using cyclic voltammetry (CV).

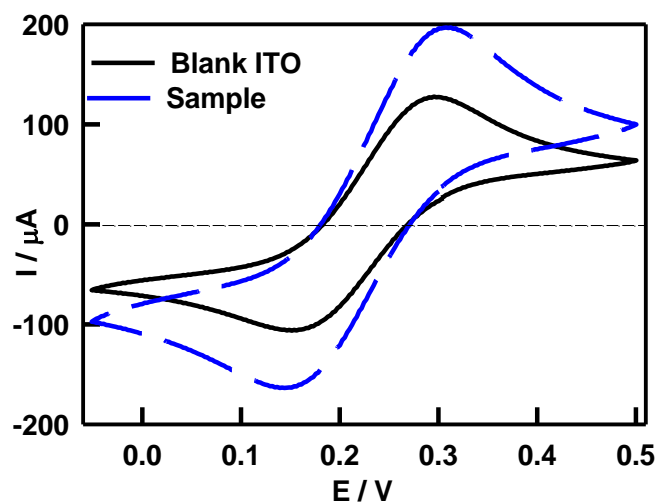


**Figure 6.8.** Cyclic voltammetric response of DNA ionogel and bare ITO.

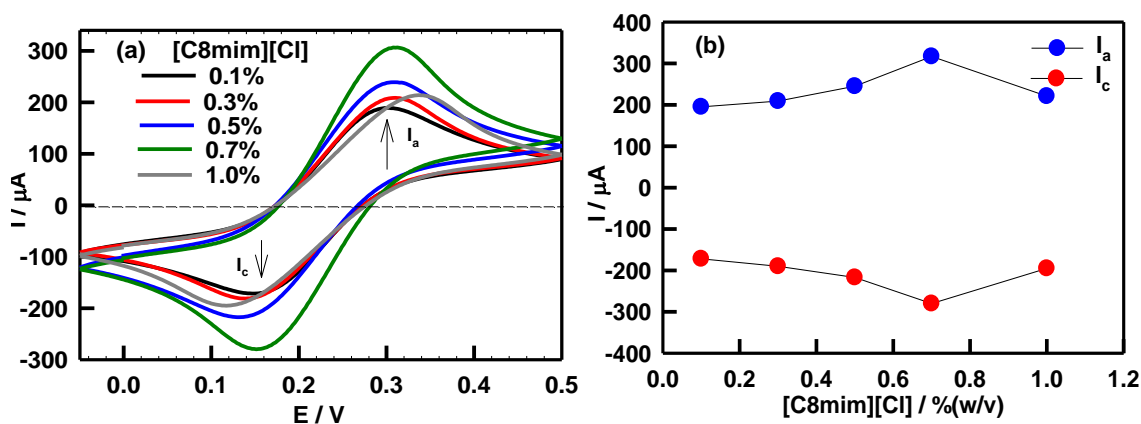


**Figure 6.9.** (a) Cyclic voltammetric response of DNA ionogel with different IL concentration varying from 0.1% to 1% (w/v) (b) Electrode Current ( $I_a$  and  $I_c$ ) dependence of IL concentration based ionogels.

Initially scan rate and ionogel concentration was optimized prior to detection study on analytes. Thereafter, electrochemical studies were conducted for different analytes in the concentration range of 0.02-0.20 mM. The electrochemical sensing profile suggested that the DNA ionogel-ITO electrodes were only selective for citric acid.



### 6.3.6 Detection of analytes

The sole objective of the study was to analyze the potential ability of the electrodes towards bioanalyte detection. We have studied detection abilities of DNA ionogels towards various bioanalytes in the concentration range of 0.02-0.2 mM at a fixed scan rate of 50 mV/s. The change in anodic and cathodic peak current with varying analyte concentration was observed to determine the response of the electrode towards tested bioanalytes. A single DNA ionogel-ITO electrode was used for the whole concentration range of a given analyte. Distinct changes in CV profile were observed in the case of citric acid while no major changes were seen in the case of other tested analytes. The anodic peak current was observed to increase with increasing concentration of citric acid. Additionally, a shift of anodic peak current towards higher potential was seen with increasing citric acid concentration. Fig. 6.10(a) shows the CV of DNA ionogel-ITO electrode on treatment with varying citric acid concentration. It clearly indicated increase in the oxidation ( $I_a$ ) and reduction ( $I_c$ ) current on treatment with citric acid and thus suggested that the electrocatalytic reaction was because of citric acid presence. No change in the peak current was found for other bioanalytes even at very high concentration of 0.2 mM (data not shown).

On plotting the anodic and cathodic peak current for citric acid with respect to its concentration, a linear relationship was observed with a least-square fitting  $\chi^2$  value of 0.97 and 0.98, respectively (Fig. 6.10 (b)). The linear detection range was found to be 0.02 to 0.08 mM and the sensitivity of electrode is calculated from the slop of current dependence of ionogel towards citric acid concentration. Therefore the calculated value of sensitivity is 12.25 mA/mM  $\text{cm}^2$ . Table 6.2 provides a comparative analysis of the different sensing platforms for citric acid detection and their sensitivity, which suggests that our system presents a very high sensitivity compared to the existing enzymatic and non-enzymatic modes of detection.

**Table 6.2. Comparison of different citric acid sensors.**

S.No.	Composition	Linear range / M	Detection limit / (mol L <sup>-1</sup> )	References
1.	Cobalt(II)-phthalocyanine modified carbon paste electrode	1 0.8–16.6	$2.54 \times 10^{-6}$	[33]
2.	Ion chromatography with suppressed conductivity detection	$(10.4-5205) \times 10^{-7}$	$3.13 \times 10^{-7}$	[34]
3.	Pyrolysis mass spectrometry	$5.21 \times (10^{-8}-10^{-1})$	$5.21 \times 10^{-9}$	[35]
4.	Reagent-injection spectrophotometry	$(3.0 - 600) \times 10^{-8}$	$3 \times 10^{-8}$	[36]
5.	DNA based Ionogel/ITO	$(0.02-0.2) \times 10^{-6}$	$1.5 \times 10^{-8}$	[Present Work]

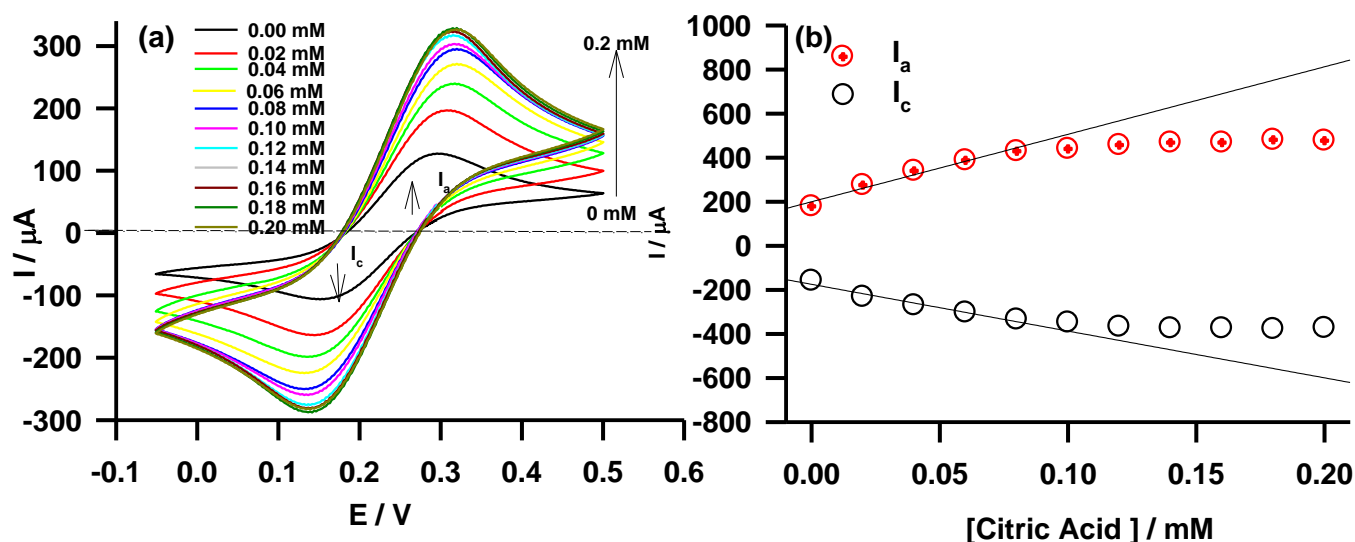


**Figure 6.10.** a) Cyclic voltammograms of DNA ionogel in presence of varying concentration of citric acid analyte b) Linear dependence of current as a function of citric acid concentration showing the sensitivity of the system in the linear range of 0.02-0.2 mM citric acid.

Enzymatic mode detection involving citrate lyase enzyme depends on the catalytic hydrolysis of citric acid and measuring the ions used or generated in the process. In the present method, a non-enzymatic approach is proposed where changes in electrochemical current was observed when the electrode was treated with increasing concentration of citric acid. Thus, a similar process to that of enzymatic reaction occurs where on interaction with the system, decomposition of citric acid occurs thereby generating Oxaloacetate, which subsequently gets converted to  $\text{COO}^-$  that is responsible for the increase in peak current. A representative mechanism of citric acid detection by DNA ionogel-ITO electrode is presented in Scheme 6.1.

The interference data for citric acid sensor shows that presence of other analyte does not affect the anode current  $I_a$  the sensor. Thus it can be concluded that the sensor is specific for citric acid inspite of the presence of other analytes in the same concentration (Fig. 6.11).

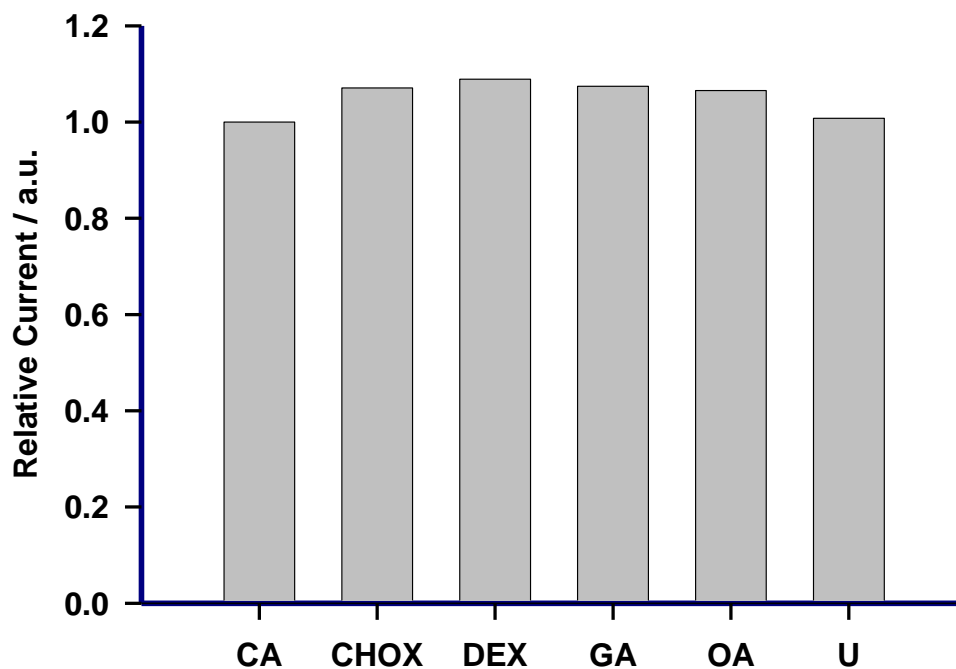
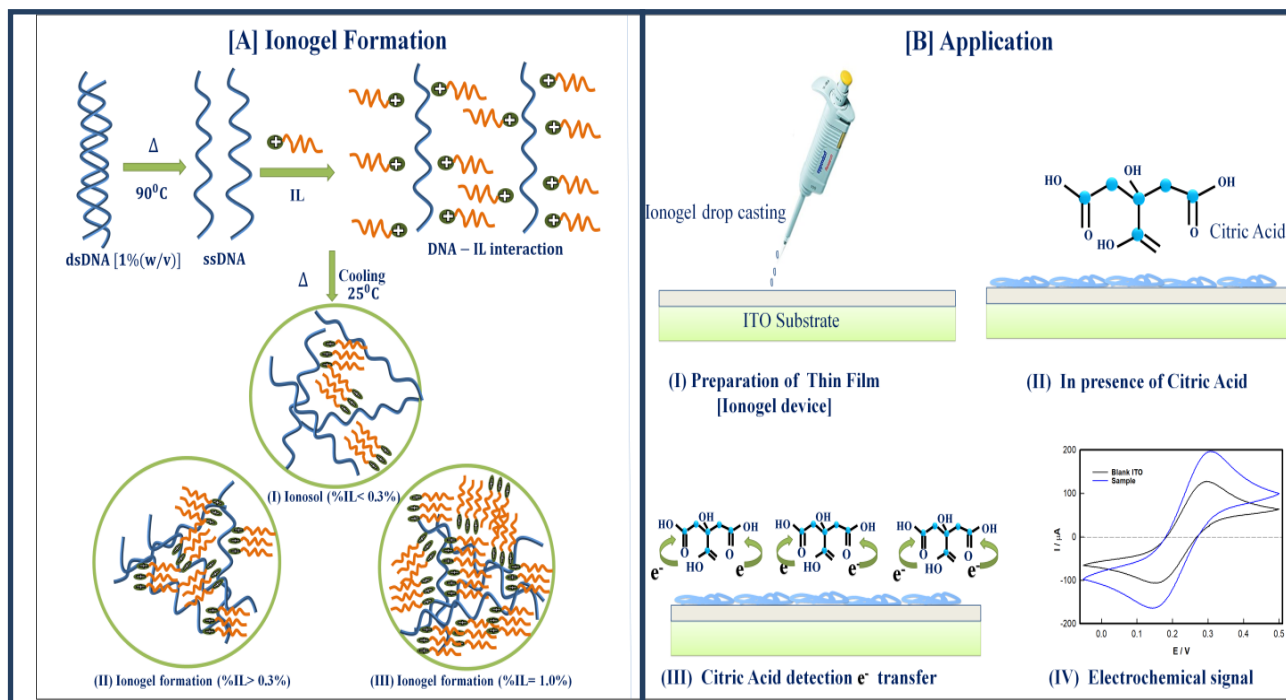


**Figure 6.11** Bar plot shows the effect of other analyte on citric acid sensing.



**Scheme 6.1.** Representative illustration of the mechanism of electrochemical sensing of citric acid by DNA ionogel-ITO electrode.

## 6.4 Conclusion

The tunability in IL concentration leads to sol to gel transformation of DNA solution. It was shown from rheology that these ionogels have been prepared with moderate (10 to 60 Pa) rigidity modulus with tunable, 52 to 62 °C gelation temperature. Microscopic structure has been evaluated by small angle neutron scattering which yield the value of correlation length (3 to 1 nm), geometry of scattering entity (Gaussian coil) and d spacing which is clearly depend on IL concentration. DNA is strong polyelectrolyte which bind with positive head group of IL which forms DNA-IL mediated ionogel network. Significance of DNA gels in biomedical and pharmaceuticals these ionogels have been utilized for bioanalyte sensing application.

The present study not only focused on the development of DNA ionogel system but also its has application in citric acid sensor in which DNA ionogel was uniformly deposited and dried on an ITO coated glass plate, and used as electrode for highly selective and sensitive detection of citric acid. The electrode exhibited a very high sensitivity of  $12.25 \text{ mA mM}^{-1} \text{ cm}^{-2}$  in the linear range of 0.02-0.08 mM citric acid. This sensing system provides a new platform for enzyme-free and sensitive detection of citric acid and holds promises in real time detection of clinical samples.

#### 6.4 References

- [1] E. Cheng, Y. Xing, P. Chen, Y. Yang, Y. Sun, D. Zhou, L. Xu, Q. Fan, and D. Liu, *Angew. Chem.* **121**, 7796 (2009).
- [2] H. Rosa, D. F. S. Petri, and A. M. Carmona-Ribeiro, *J. Phys. Chem. B* **112**, 16422 (2008).
- [3] Y. Xu, Q. Wu, Y. Sun, H. Bai, and G. Shi, *ACS Nano* **4**, 7358 (2010).
- [4] C. Li, A. Faulkner-Jones, A. R. Dun, J. Jin, P. Chen, Y. Xing, Z. Yang, Z. Li, W. Shu, D. Liu, and R. R. Duncan, *Angew. Chemie - Int. Ed.* **54**, 3957 (2015).
- [5] F. Topuz and O. Okay, *Biomacromolecules* **10**, 2652 (2009).
- [6] J. B. Lee, S. Peng, D. Yang, Y. H. Roh, H. Funabashi, N. Park, E. J. Rice, L. Chen, R. Long, M. Wu, and D. Luo, *Nat. Nanotechnol.* **7**, 816 (2012).
- [7] A. Zinchenko, Y. Taki, V. G. Sergeev, and S. Murata, *Nanomaterials* **5**, 270 (2015).
- [8] D. Costa, M. G. Miguel, and B. Lindman, *J. Phys. Chem. B* **111**, 10886 (2007).

- [9] N. Dave, M. Y. Chan, P.-J. J. Huang, B. D. Smith, and J. J. Liu, *J. Am. Chem. Soc.* **132**, 12668 (2010).
- [10] C. K. Lee, S. R. Shin, S. H. Lee, J. H. Jeon, I. So, T. M. Kang, S. I. Kim, J. Y. Mun, S. S. Han, G. M. Spinks, G. G. Wallace, and S. J. Kim, *Angew. Chemie - Int. Ed.* **47**, 2470 (2008).
- [11] M. C. Moran, M. G. Miguel, and B. Lindman, *Langmuir* **23**, 6478 (2007).
- [12] A. Zinchenko, Y. Miwa, L. I. Lopatina, V. G. Sergeyev, and Y. Murata, *ACS Appl. Mater. Interfaces* **6**, 3226–3232 (2014).
- [13] F. Horkay and P. J. Basser, *Biomacromolecules* **5**, 232 (2004).
- [14] N. Arfin, V. K. Aswal, J. Kohlbrecher, and H. B. Bohidar, *Polymer (Guildf)*. **65**, 175 (2015).
- [15] P. . Pandey, K. Rawat, V. K. Aswal, J. Kohlbrecher, and H. B. Bohidar, *J. Appl. Biotechnol. Bioeng.* **2**, 144 (2017).
- [16] X. Sui, M. A. Hempenius, and G. J. Vancso, *J. Am. Chem. Soc.* **134**, 4023–4025 (2012).
- [17] Y. He, Z. Li, P. Simone, and T. P. Lodge, *J. Am. Chem. Soc.* **128**, 2745 (2006).
- [18] A. Pinkert, K. N. Marsh, S. Pang, and M. P. Staiger, *Chem. Rev.* **109**, 6712 (2009).
- [19] P. Kumar, K. Rawat, V. K. Aswal, J. Kohlbrecher, and H. B. Bohidar, *Colloids Surfaces A* **538**, 184 (2018).
- [20] Y. He, P. G. Boswell, P. Bühlmann, and T. P. Lodge, *J. Phys. Chem. B* **111**, 4645 (2006).

- [21] P. K. Pandey, K. Rawat, V. K. Aswal, J. Kohlbrecher, and H. B. Bohidar, *Phys. Chem. Chem. Phys.* **19**, 804 (2017).
- [22] J. Le Bideau, L. Viau, and A. Vioux, *Chem. Soc. Rev.* **40**, 907 (2011).
- [23] J. Kohlbrecher and W. Wagner, *J. Appl. Crystallogr.* **33**, 804 (2000).
- [24] A. Aharony, *Introduction to Percolation Theory* (Taylor & Francis Group, London, 1994).
- [25] D. Stauffer, A. Coniglio, and A. Adams, *Adv. Polym. Sci.* **44**, 103 (1982).
- [26] J. D. Ferry, *Viscoelastic Properties of Polymers* (John Wiley & Sons, 1980).
- [27] H. A. Barnes, *A Handbook of Elementary Rheology* (University of Wales, Institute of Non-Newtonian fluid Mechanics, Aberystwyth, 2000).
- [28] A. Ajji and L. Choplin, *Macromolecules* **24**, 5221 (1991).
- [29] W. Burchard and M. Eisele, *Pure Appl. Chem.* **56**, 1379 (1984).
- [30] B. A. Simmons, G. C. Irvin, V. Agarwal, A. Bose, V. T. John, G. L. McPherson, and N. P. Balsara, *Langmuir* **18**, 624 (2002).
- [31] N. Joshi, K. Rawat, P. R. Solanki, and H. B. Bohidar, *Biochem. Eng. J.* **102**, 69 (2015).
- [32] A. Kaushik, P. R. Solanki, A. A. Ansari, G. Sumana, S. Ahmad, and B. D. Malhotra, *Sensors Actuators B Chem.* **138**, 572 (2009).
- [33] R. F. Nascimento, T. M. G. Selva, W. F. Ribeiro, M. F. Belian, L. CioAnghes, and V. B. Nascimento, *Talanta* **105**, 354 (2013).

- [34] B. M. DeBorbaa, J. S. Rohrera, and L. Bhattacharyya, *J. Pharm. Biomed. Anal.* **36**, 517 (2004).
- [35] A. Ghassempour, N. M. Najafi, and A. A. Amiri, *J. Anal. Appl. Pyrolysis* **70**, 251 (2003).
- [36] D. G. Themelis and P. D. Tzanavaras, *Anal. Chim. Acta* **428**, 23 (2001).



## CHAPTER-7

---

### Synthesis of water soluble MoS<sub>2</sub> Quantum Dot and Crosslinked DNA

#### Nanocomposite Hydrogels

**Abstract:** We have synthesized water soluble MoS<sub>2</sub> quantum dots. Further MoS<sub>2</sub> crosslinked DNA hydrogels were studied via different techniques.

#### 7.1 Introduction

Transition metal dichalcogenides MX<sub>2</sub> (where M = Mo, W and X= S, Se) has drawn much attention in the last few years. Graphene has zero bandgap with good, thermal and electrical properties. There is blue shift in size dependent color spectrum in graphene [1]. Molybdenum disulfide (MoS<sub>2</sub>) which is similar to graphene, but persists with a tunable bandgap that makes its electrical and optical properties extraordinary. It has shown pre-eminent role in semiconductor electronics, photonics and power harvesting applications [2–4]. It is extensively used as a lubricant material in hydrogen evolution reaction, and in photocatalysis [5]. Transition from bulk to monolayer of MoS<sub>2</sub> that is indirect to direct bandgap transition leads to the emergence of luminescence properties in this material [6] because quantum size effect is correlated to electronic band structure. Synthesis of water soluble or oil-free quantum dots are generally emphasized for their biocompatibility. Recently, water soluble MoS<sub>2</sub> quantum dots were prepared via bottom up approach by using (NH<sub>4</sub>)<sub>6</sub>Mo<sub>7</sub>O<sub>24</sub>·4H<sub>2</sub>O and Na<sub>2</sub>S as precursors and 1,4-diaminobutane as capping agent [7]. Use of photothermal therapy has been demonstrated where optical energy is converted into the heat energy to combat tumor cells [8]. Highly sensitive and responsive nature of MoS<sub>2</sub> based hybrid phototransistor devices that benefits from the synergism

of 2D-MoS<sub>2</sub> and 0-D MoS<sub>2</sub> semiconductors has been demonstrated [9]. MoS<sub>2</sub> QD based biosensor has been developed to detect hyaluronidase [10]. Room temperature single layer MoS<sub>2</sub> has shown mobility comparable to the graphene nano-ribbons and very low power dissipation transistors could be made using this material [11].

Graphene oxide based multifunctional DNA hydrogel showed good mechanical strength. The functional groups of DNA tend to interface with other molecules and this rapid communication between DNA and ligands help in better property of the resultant composite material [12–14]. Quantum dot based DNA hydrogel has shown multifunctional use in enzyme-responsive drug delivery process and cell targeting [15]. Quantum dot used as a crosslinking agent in hydrogel act as photonic beads for level free detection of DNA [16]. DNA based meta-hydrogel has shown applications in diverse fields such as flexible circuit design, electric switching, cell therapy and drug release [17]. DNA based two terminal device has been used for sensing of basidiomycetes from its current-voltage profile [18].

Herein, we have characteristics of a MoS<sub>2</sub> quantum dot crosslinked DNA hydrogels. When suitably embedded in a DNA hydrogel matrix, these QDs acted as excellent pseudo-crosslinkers that enhanced gel strength, and melting temperature of the nanocomposite gel, regardless of the fact that the biopolymer and the QD had charge of same polarity

There is general lack of understanding of the interactions that exist between nanoparticles and polyelectrolytes of same polarity which limits the possibility to customize this new class nanocomposite material. This work attempts to shed some light on the nature of this interaction.

## **7.2 Sample preparation**

### **7.2.1 Synthesis of MoS<sub>2</sub> quantum dots**

The easiest method for MoS<sub>2</sub> quantum dot synthesis was a single-step process in which ammonium tetrathiomolybdate ((NH<sub>4</sub>)<sub>2</sub>MoS<sub>4</sub>) was used as the precursor which was mixed with 50 mL of water and ultrasonicated for 15 min. After addition of 0.25g of L-cysteine to this solution it was ultrasonicated for another 10 min. After ultrasonication this solution was transferred to Teflon lined stainless steel autoclave and maintained at 200<sup>0</sup> C for 24 h. The obtained purified (by centrifugation and followed by dialysis) water soluble MoS<sub>2</sub> quantum dots were used for all the measurements.

### **7.2.2 Synthesis of fluorescent DNA nanocomposite hydrogel**

[DNA] (2% (w/v)) was dissolved in deionized water and heated to 90<sup>0</sup> C for 30 min, resulting in a homogeneous and optically clear solution. Synthesized MoS<sub>2</sub> QDs (12 to 60 mM) was then added to the hot DNA solution such that the final concentration of DNA was 1.0% (w/v) in the DNA-MoS<sub>2</sub>suspension. These samples were allowed to cool to room temperature which formed a gel and the gel could support its own weight when the sample cell was inverted. When observed under UV light these gels showed blue fluorescence.

## **7.3 Result and Discussion**

### **7.3.1 Morphology and structure of MoS<sub>2</sub> QDs**

The mean size of quantum dots estimated from TEM analysis was 3.1 nm (Fig.7.1(a)). In Fig. 7.1(b) uniformly distributed QDs, are clearly seen and the inset shows size distribution

histogram. The XRD pattern is depicted in Fig. 7.1(c). HRTEM (Fig. 7.1(d)) image clearly shows diffraction fringes (Fig. 7.1(e)) which was used for crystal plane spacing determination which was found to be 0.19 nm.

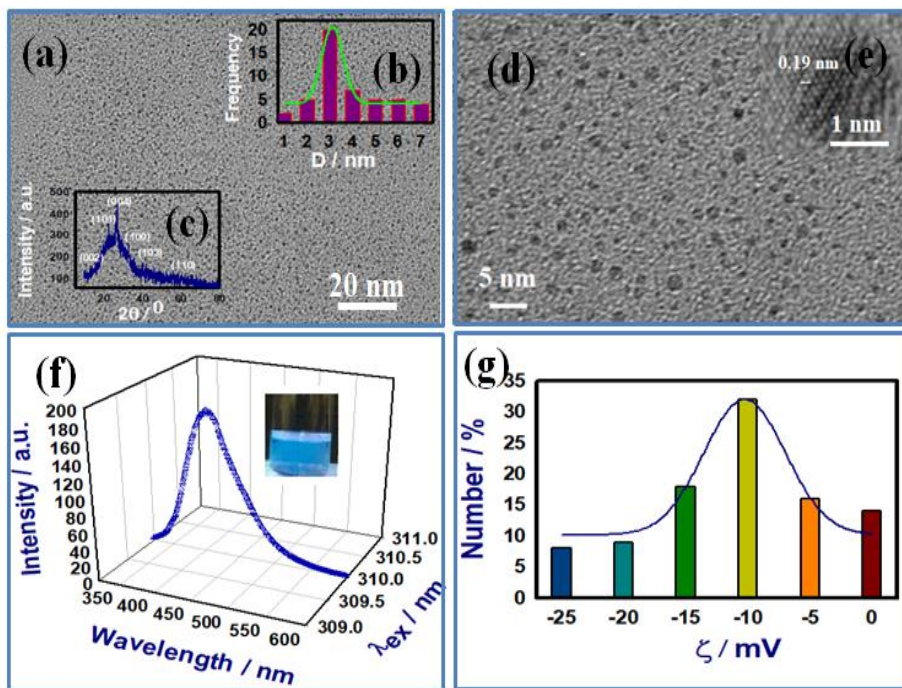


**Figure 7.1.** (a) TEM image at 20 nm scale, (b) shows the size distribution histogram, (c) XRD data of synthesized MoS<sub>2</sub> QDs, (d) TEM image at 5 nm scale (e) HRTEM image (f) Fluorescence at 400 nm under 310 nm UV- excitation wave length and (g) Zeta potential distribution.

In Fig. 7.1(c) X-ray diffraction pattern of the synthesized quantum dot is shown with clear diffraction peaks seen at 15<sup>0</sup>, 23<sup>0</sup>, 28<sup>0</sup>, 33<sup>0</sup>, 40<sup>0</sup> and 58<sup>0</sup> which are assigned to (002), (101), (004), (100), (103) and (110) diffraction planes of the crystalline MoS<sub>2</sub> structure. It was possible to apply Debye-Scherrer formula [19] to the XRD pattern to get an idea about average crystalline size. The mean crystalline size obtained was 7.4 nm.

The surface charge of MoS<sub>2</sub> quantum dots was confirmed from the zeta potential analysis shown in Fig. 7.1(g). The mean zeta potential of MoS<sub>2</sub> quantum dots and DNA were found to be -10

and -60 mV, respectively. Thus, the colloidal QDs were dispersed in the milieu of DNA strands in the aqueous medium in the sol state.

### 7.3.2 Bandgap

UV- visible spectra of MoS<sub>2</sub> quantum dot with the excitation absorption edge wavelength of 310 nm is obtained. When excited at this wavelength, it shows emission peak at 400 nm (Fig. 7.1(f)).

The optical bandgap energy was calculated from the Tauc equation given by [20]

$$(\alpha h\nu)^n = B(h\nu - E_g) \quad (7.1)$$

Here, absorption coefficient is given by  $\alpha$ , band tailing parameter is B, energy of photon is  $h\nu$ ,  $E_g$  is optical bandgap and  $n = 2, 3, 1/2$ , and  $1/3$  correspond to appropriate band to band transition.

Analysis of bandgap for MoS<sub>2</sub> for  $n = 2$  obtained by best linear fitting of Tau Plot. The bandgap calculated was 4.25 eV.

Under the 310 nm excitation of UV light, a blue luminescence could be observed at 400 nm.

### 7.3.3 Viscoelasticity of nanocomposite hydrogels

The viscoelastic behaviour of soft matter is best probed by rheology. The nanocomposite gels were subjected to isothermal frequency sweep, and isochronal temperature sweep experiments to profile these materials. The dispersion behavior of gel samples is explained by linear viscoelastic theory under small deformation approximation. The storage modulus  $G'$  exhibits a frequency dependent dispersion behavior given by [21]

$$G'(\omega) = G_0 \omega^n \quad (7.2)$$

Here  $G_0$  is the strength of elastic modulus at  $\omega \rightarrow 0$ . The exponent  $n$  varies between 0 and 2. It is 0 for a Hookean solid and 2 for Maxwellian viscoelastic matter in the low frequency regime. The

experimentally determined dispersion behavior of storage modulus  $G'$  is depicted in Fig. 7.2(a). The dependence of exponent  $n$  and  $G_0$  on QD concentration is shown in Figs.7.2(b,d). It is inferred from the data shown in Fig. 7.2(d) that  $G_0$  had value of 9 Pa for 12mM MoS<sub>2</sub> QD and it sharply increased to ~ 40 Pa for 60 mM sample, and the corresponding value of  $n$  varied from 0.2 to 0.05. It is to be noted that the without MoS<sub>2</sub> QD the sample was a sol. Therefore, the QDs acted as physical crosslinkers in the DNA sol to generate a strong nanocomposite gel. The synergy of this interaction can be gauged from the fact that the gel strength increased with QD content. It was clearly seen that these QD based DNA hydrogels were viscoelastic in nature irrespective of their MoS<sub>2</sub> QD content, but these became more rigid at higher crosslinker concentration ( $0.05 < n < 0.23$ , Fig. 7.2(b)).

Previously reported  $G_0$  value for DNA hydrogel was  $20 \pm 2$  Pa at 2 % (w/v) DNA concentration and for ionogel it was  $29 \pm 2$  Pa at 1 % (w/v) concentration [12,13]. The present gel showed a highest value of 40 Pa for  $G_0$  indicating the crosslinking potential of the used QDs. Fig. 7.2(c) shows an interesting interdependence between melting temperature and gel strength, and their variance with QD content. This clearly establishes the synergetic crosslinking potential of the used QDs in the DNA sol milieu.

The elastic free energy stored in a network per unit volume is determined by its  $G_0$  value. When this energy is equated with the thermal energy, it defines a characteristic length scale called the viscoelastic length. This length is a key parameter for a self-assembled network, which is given by  $\zeta_{el}$  [22]

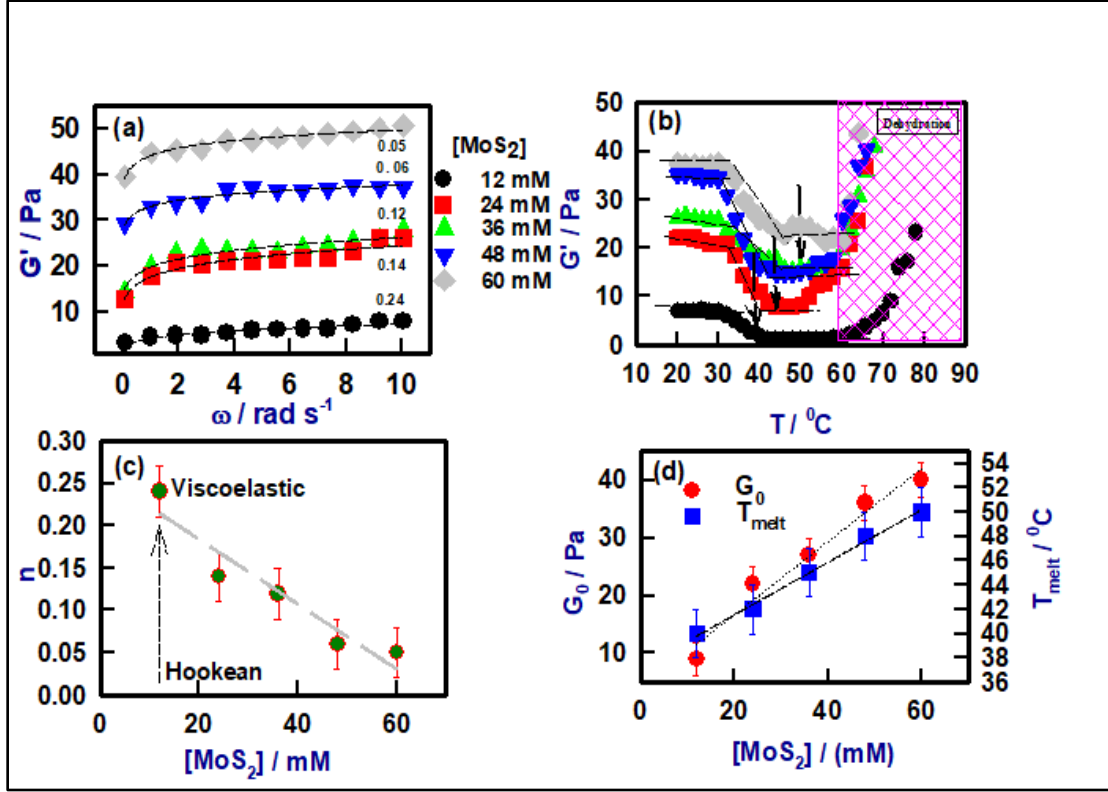


**Figure 7.2.** (a) Storage  $G'(\omega)$  modulus of nanocomposite gel plotted as function of frequency, (b) variation of power-law exponent  $n$  with QD concentration, (c) temperature sweep profile, and (d) variation of gel strength  $G_0$  and  $T_{melt}$  with QD concentration.

$$G_0 \sim k_B T / \zeta_{el}^3 \quad (7.3)$$

This length varies from  $\zeta_{el} \approx 77$  nm for 12 mM QD sample to 49 nm for 60 mM QD nanocomposite gel. Therefore, the formed networks are denser at higher MoS<sub>2</sub> concentration. The temperature sweep measurements (Fig. 7.2(c)) show transitions which can be referred to as gel melting temperature,  $T_{melt}$ . The  $T_{melt}$  value increased from 40 to 50<sup>0</sup> C with MoS<sub>2</sub> concentration indicating sufficient synergy between DNA strands and quantum dots. Therefore, the melting temperatures of the nanocomposite gels can be tuned by increasing QD concentration as required by the application.

### 7.3.5 Dynamics and ergodicity

In sol-gel transition involves significant change in the diffusion dynamics due to the altered density fluctuations which are hierarchical in both time and length scales. The time scale relaxation is best captured from the dynamic structure factor data. In an experiment, this information is contained in the electric field auto-correlation function  $g_1(q, \tau)$ . To study the relaxation dynamics all samples were subjected to DLS experiments. The time dependent dynamic structure factor,  $g_1(q, t)$  obtained from different samples and a representative plot is shown in Fig. 7.3(a). It is well known that the  $(g_1(t)|_{t=0} - g_1(t)|_{t=\infty}) = \chi$  defines the signal modulation. For a sample of scattering moieties exhibiting Brownian dynamics,  $\chi = 1$  and the correlation function relaxes to its equilibrium value indicating manifestation of ergodicity in the sample. On the contrary, for arrested systems, correlation function does not relax fully and  $\chi < 1$ , which infers non-ergodicity. Therefore, from the measured correlation function data it was possible to evaluate the  $\chi$ -parameter, and hence, determine the ergodic state of the system (representative data is shown in Fig. 7.3(b)). It is clearly seen that there was ergodicity breaking as gel phase was approached which inferred transition of Brownian to arrested dynamics.

This correlation data could be best described by the following function [23],

$$g_1(q, t) = A \exp - \left( \frac{t}{t_f} \right) + (1 - A) \exp - \left( \frac{t}{t_s} \right) \quad (7.4)$$

Where  $A$  and  $(1-A)$  are relative amplitudes of the two modes of relaxation.  $t_f$  and  $t_s$  are the relaxation times corresponding to the fast and slow mode.



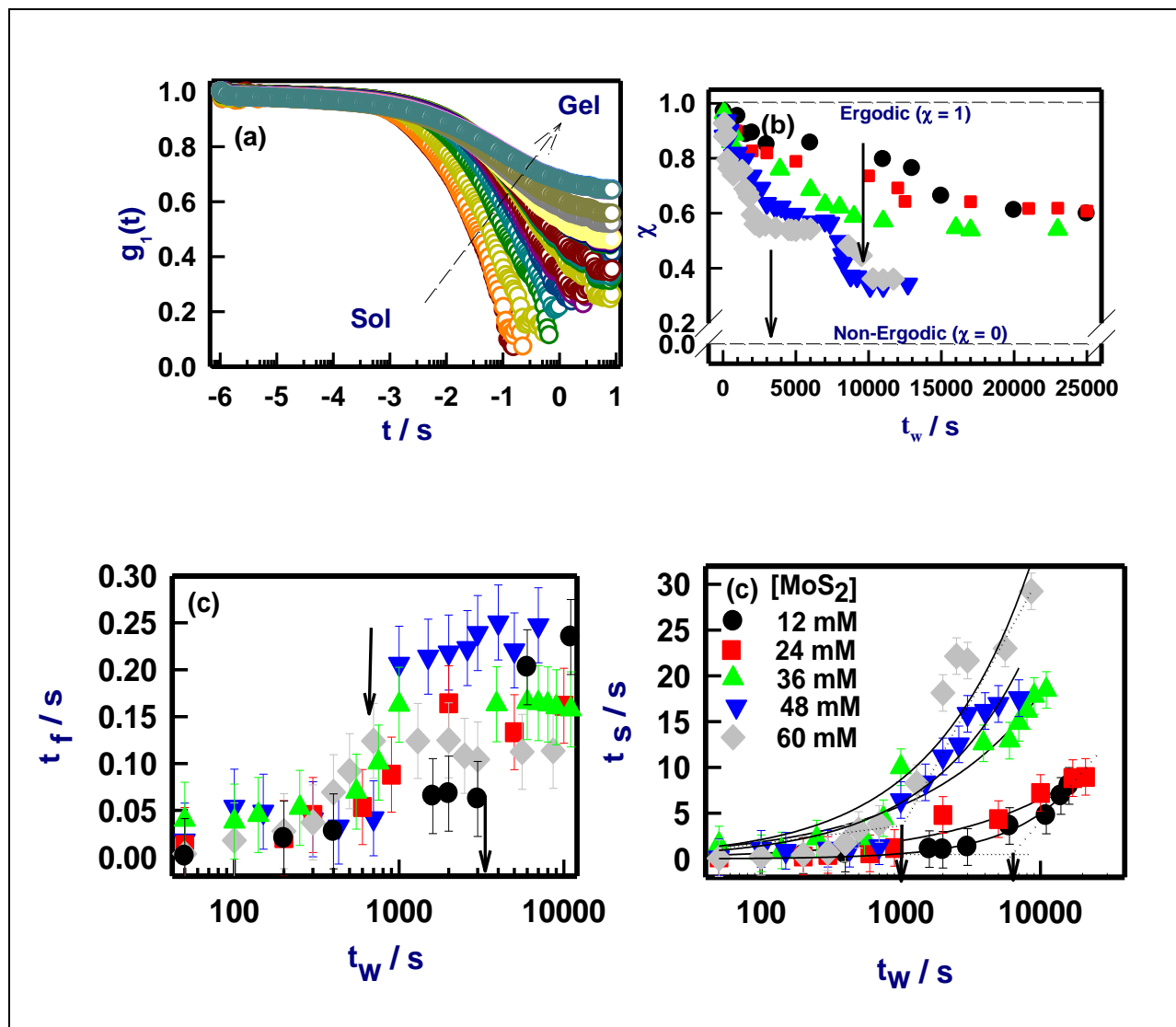


**Figure 7.3.** Plot of (a) correlation function, notice the incomplete relaxation as gel state was approached, (b) variation of sample ergodicity with time, (c) fast and (b) slow mode relaxation times shown as function of waiting time  $t_w$ . At  $t_w = 0$ , the samples were in sol state, and at  $t_w = t_{\text{gel}}$  gelation occurred (arrows).

The value for the fast and slow mode relaxation times  $\tau_f$  and  $\tau_s$  were determined from the fitting of correlation functions to eqn 7.4. These relaxation times are plotted (Fig. 7.4) with waiting time  $t_w$  to estimate gel transition time or ergodicity breaking time ( $\tau_{\text{EB}}$ ) which corresponds to the time required for the network formation to take place ( $t_{\text{gel}}$ ). There was a

discernible change in the fast and slow mode relaxation times with  $t_w$  with increase in QD concentration. The fast mode changed abruptly at  $t_w = t_{gel}$  which corresponds to the ergodicity breaking time ( $\tau_{EB}$ ). It may be noted that for  $t > \tau_{EB}$ , the Brownian dynamics changes to arrested dynamics, hence a break in ergodicity was envisaged. On the contrary, the slow mode relaxation time showed a clear increase with waiting time. This change can be predicted by ceased Brownian motion within the system and the data could be fitted to a power-law function given by

$$t_s \sim t_w^m \quad (7.5)$$

The exponent  $m$  increased from 0.60 to 0.94 with QD concentration implying that at higher crosslinker density (QD content) gelation occurred earlier.

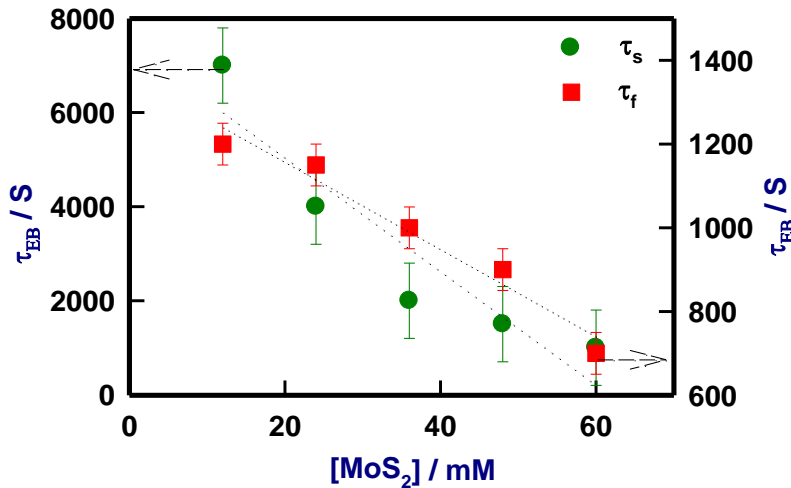


**Figure 7.4.** The variation of ergodicity breaking time  $\tau_{EB}$  obtained from fast and slow mode of relaxation with QD concentration. The  $\tau_{EB}$  determined from the  $\chi$ -parameter was not too different (Fig. 7.3(b)).

Figure 7.4 illustrates the linear dependence of  $\tau_{EB}$  with QD concentration. Secondly, the fast mode was seen to freeze much earlier than the slow mode.

### 7.3.5 Small Angle X-Ray Scattering

To map the microscopic internal structure of the nanocomposite hydrogels SAXS technique was used where the static structure factor was measured. The scattered intensity versus wave vector  $q$  profile is depicted in Fig. 7.5(a). The  $I(q)$  vs  $q$  data was first analyzed using the following

protocols:  $1/I(q)$  vs  $q^2$  and  $\sqrt{1/I(q)}$  vs  $q^2$  plots. The best fitting was obtained for the fitting function  $1/I(q)$  vs  $q^2$ . This analysis showed two distinct slopes pertaining to two distinct  $q$ -domains ( $q^* = 0.24$  and  $q^{**} = 1.7 \text{ nm}^{-1}$ ) for every single structure factor data. This allowed the data to be split into three distinct fitting functions corresponding to three distinct  $q$ -regions given by

$$I(q) \approx I_{PL} q^{-\alpha} + \frac{I_{OZ}}{(1+q^2\xi^2)} + I_{GP} \exp\left(\frac{-R_G^2 q^2}{2}\right) \quad (7.6)$$

(Power-law) + (Ornstein-Zernike) + (Guinier-Porod)

Here,  $I_{PL}$ ,  $I_{OZ}$  and  $I_{GP}$  are  $q$ -independent pre-factors. These split regions are low  $q$ -region ( $0.10 \leq q \leq q^* = 0.23 \text{ nm}^{-1}$ ), intermediated  $q$ -region ( $q^* \leq q \leq 1.67 \text{ nm}^{-1}$ ) and high  $q$ -region ( $q \geq q^{**} = 1.7 \text{ nm}^{-1}$ ). These distinct regions were best fitted by Power-law (PL), Ornstein-Zernike (O-Z) and Guinier-Porod (GP) functions respectively (eqn 7.6). Power-law fitting yielded  $\alpha$ , which gives information about geometry of the scattering object. It has been suggested by mean-field theory that for the polymers in good solvent, O-Z formulation can describe the structure factor of concentration fluctuation at equilibrium [24]. Therefore, mesh size,  $\xi$  was obtained from O-Z relation for polymer network at intermediate  $q$ -region. To know the cross-sectional radius of scattering moiety, it was necessary to focus in the high  $q$ -region of the structure factor data. This  $q$ -domain is described by the Guinier-Porod relation.

The analysis of SANS data yielded  $\alpha = 0.06 \pm 0.03$  (Fig. 7.7 (b)). The value of  $\alpha < 1$  corresponds to rod like scattering objects.

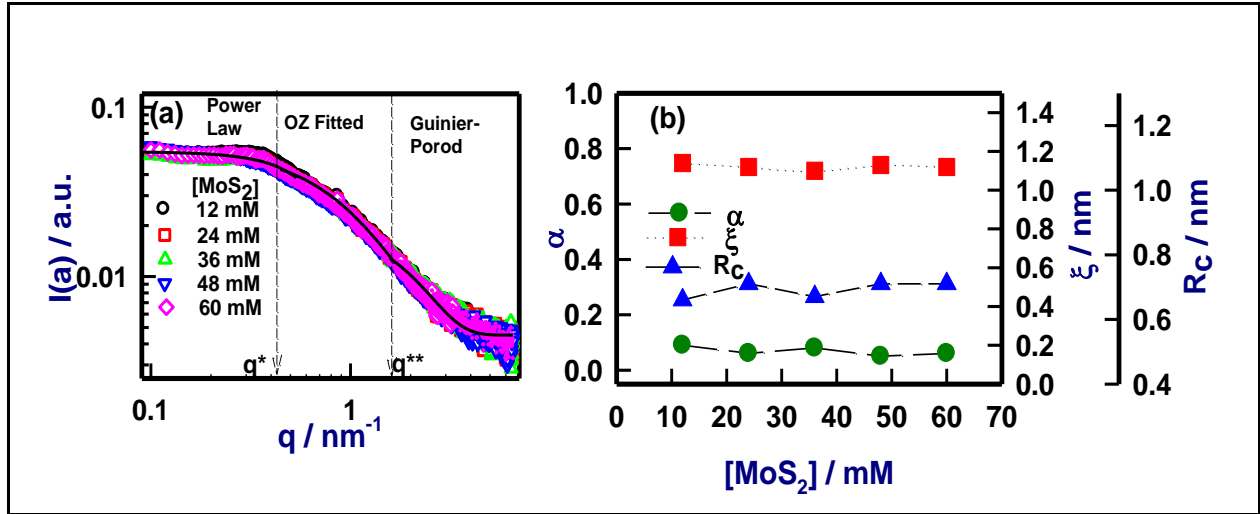


**Figure 7.5.** (a) Static structure factor  $I(q)$  measured by SAXS for gel samples. Curves were fitted with power-law, Ornstein-Zernike (OZ) function and Guinier-Porod function in different  $q$ -regions. (b) Variation of geometrical scattering factor  $\alpha$ , mesh size  $\xi$  and cross sectional radius  $R_c$  with QD concentration. See text for details.

Further, scattering by dense phase is probed by O-Z relation which yields the value of mesh size or correlation length  $\xi = 1.12 \pm 0.02$  nm. For far  $q$ -region or asymptotic region cross-sectional radius  $R_c$  was obtained from G-P function which had a value of  $0.7 \pm 0.1$  nm independent of  $\text{MoS}_2$  concentration. The boundaries between different  $q$ -regions (Fig.7.5(a)) are defined by  $q^*$  and  $q^{**}$ . These wave vectors correspond to two characteristic lengths given as,

$$L^* = 2\pi / q^* \quad \text{and} \quad L^{**} = 2\pi / q^{**} \quad (7.7)$$

Therefore, we obtained  $L^* = 26 \pm 4$  nm and  $L^{**} = 4 \pm 0.6$  nm, respectively. Thus,  $L^{**}$  was close to the size of the QDs. It was possible to conjecture a self-assembly model based on the observed results, which is illustrated in Scheme 7.1. It appears that  $\text{MoS}_2$  QDs locate themselves

at DNA overlap junctions creating rigid crosslink nodes. When observed under UV radiation, these QDs glow to provide a fluorescence signal.

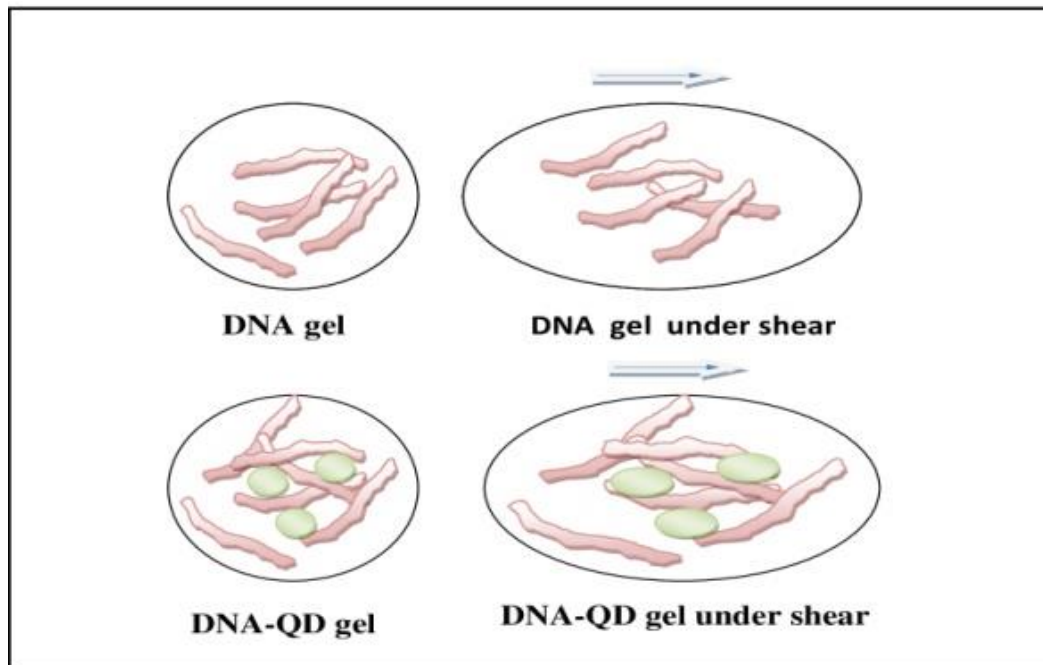
### **7.3.5 Phenomenology of pseudo-crosslinking**

The zeta potential measurements revealed that both the DNA and the QDs were negatively charged. Now the question arises how do these QDs, which are negatively charged, work as crosslink junctions between predominantly negatively charged DNA strands? The science of Wigner glass (and gel) is known for a long time in the literature where self-organization in a repulsive electrostatic environment prevails [25–27]. Such systems have shown interesting aging dynamics and evolution of non-ergodicity. Cross-over from a completely relaxed correlation function (system obeying Brownian dynamics) to an incomplete state (system obeying arrested dynamics) has been observed which is designated as the ergodicity breaking time. These systems also reveal a fast diffusion coefficient (short time behavior) that is correlated to the escape of the particles from the “cage”. The accompanied slow mode diffusivity referring to long time behavior pertains to reversible trapping of the particles in a localized region in space.

Our system is physically similar to the colloidal dispersion discussed above except that there is a low volume fraction of negatively charged colloidal particles dispersed in a heterogeneously distributed ensemble of large linear charge density DNA strands of same polarity. The QDs would prefer to locate themselves in pockets where there is least repulsion, since the DNA strands due to their anisotropic character create an inhomogeneous solution microscopically, such pockets abound. An inhomogeneous dispersion of rod-like particles in its gel state will show a lower shear modulus due to the preferred alignment of these rods along the shear direction. If a certain amount of colloidal particles are added to this dispersion, these particles

will occupy the free-volumes available between the randomly distributed rods in the dispersion, and reduce the free-volume in the overall sample. If a low frequency and low amplitude shear is applied to the gel of this system, the rods will no longer be able to align along the shear direction due to the static hindrance offered by the QDs, and the DNA-QD assembly will collectively respond to the shear deformation. In the gel state, such a situation will lead to manifestation of higher storage modulus which was noticed in our case. Thus, the QDs act as pseudo-crosslinkers and this makes the system sustain higher level of elastic deformation. Because the overall environment is still repulsive, it is not unreasonable to define this self-assembled system as a “Wigner-like gel”. It may be recalled that, we observed ergodicity breaking when arrested dynamics took over from the Brownian dynamics close to gelation transition. Both the fast and slow mode diffusivity revealed aging dynamics during this process alike in Wigner systems. Therefore, there is much similarity between the colloidal Wigner glass and our nanocomposite gel. This is depicted in the Schematic 7.1.

Rance et al [28] studied the interaction between multi-walled carbon nanotubes (MWCNT) and gold nanoparticles of same polarity and observed that van der Waals forces caused adsorption of the nanoparticles on the nanotube surface. We, however, rule out the possibility of van der Waals interaction playing any possible role in our system primarily because these forces are very weak at room temperature. Therefore, a gel network crosslinked through such interaction may not sustain a shear deformation to yield a large storage modulus of ~40 Pa which was observed in our system.



**Scheme 7.1.** Scheme shows the DNA hydrogel microstructure (top) and same in presence of MoS<sub>2</sub> QD (bottom). Because of non-existent crosslinks DNA gels do not sustain shear deformation (low storage modulus) whereas its pseudo-crosslinked nanocomposite gel exhibits elastic response to applied shear (large storage modulus).

## 7.4 Conclusion

Hydrophilic MoS<sub>2</sub> quantum dots were synthesized and their physical properties were characterized by different techniques. These nanomaterials could be used for inducing gelation in low concentration DNA solutions much below the gelation concentration of the nucleic acid. Rheological studies of these nanocomposite hydrogels revealed enhanced gel strength and higher melting temperature implying synergy between the hydrated biopolymer and the colloidal QD. The dynamic arrest appeared in the system as the sol approached gel phase and it was captured from the dynamic structure factor data. The microscopic internal structure was probed from small angle X-ray scattering.

## 7.5 References

- [1] S. Kim, S. W. Hwang, M.-K. Kim, D. Y. Shin, D. H. Shin, C. O. Kim, S. B. Yang, J. H. Park, E. Hwang, S.-H. Choi, G. Ko, S. Sim, C. Sone, H. J. Choi, S. Bae, and B. H. Hong, *ACS Nano* **6**, 8203 (2012).
- [2] H. Dong, S. Tang, Y. Hao, H. Yu, W. Dai, G. Zhao, Y. Cao, H. Lu, X. Zhang, and H. Ju, *ACS Appl. Mater. Interfaces* **8**, 3107 (2016).
- [3] Q. H. Wang, K. Kalantar-Zadeh, A. Kis, J. N. Coleman, and M. S. Strano, *Nat. Nanotechnol.* **7**, 699 (2012).
- [4] A. H. C. Neto, F. Guinea, K. S. Peres, N. M. R. Novoselov, and A. K. Geim, *Rev. Mod. Phys.* **81**, 109 (2009).
- [5] H. Wanga, Z. Lub, S. Xuc, D. Kong, J. J. Cha, G. Zheng, P.-C. Hsu, K. Yan, D. Bradshaw, F. B. Prinz, and Y. Cui, *PNAS* **110**, 19701 (2013).
- [6] D. Gopalakrishnan, D. Damien, and M. M. Shaijumon, *ACS Nano* **8**, 5297 (2014).
- [7] D. Haldar, D. Dinda, and S. K. Saha, *J. Mater. Chem. C* **4**, 6321 (2016).
- [8] J. Wang, X. Tan, X. Pang, L. Liu, F. Tan, and N. Li, *ACS Appl. Mater. Interfaces* **8**, 24331 (2016).
- [9] D. Kufer, I. Nikitskiy, T. Lasanta, G. Navickaite, F. H. L. Koppens, and G. Konstantatos, *Adv. Mater.* **27**, 176 (2015).
- [10] W. Gu, Y. Yan, C. Zhang, C. Ding, and Y. Xian, *ACS Appl. Mater. Interfaces* **8**, 11272 (2016).



- [11] B. Radisavljevic, A. Radenovic, J. Brivio, V. Giacometti, and A. Kis, *Nat. Nanotechnol.* **6**, 147 (2011).
- [12] P. K. Pandey, K. Rawat, V. K. Aswal, J. Kohlbrecher, and H. B. Bohidar, *Phys. Chem. Chem. Phys.* **19**, 804 (2017).
- [13] P. Kumar, K. Rawat, V. K. Aswal, J. Kohlbrecher, and H. B. Bohidar, *Colloids Surfaces A* **538**, 184 (2018).
- [14] Y. Xu, Q. Wu, Y. Sun, H. Bai, and G. Shi, *ACS Nano* **12**, 7358 (2010).
- [15] L. Zhang, S. R. Jean, S. Ahmed, P. M. Aldridge, X. Li, F. Fan, E. H. Sargent, and S. O. Kelley, *Nat. Comm.* **8**, 381 (2017).
- [16] Y. Zhao, X. Zhao, B. Tang, W. Xu, J. Li, J. Hu, and Z. Gu, *Adv. Funct. Mater.* **20**, 976 (2010).
- [17] J. B. Lee, S. Peng, D. Yang, Y. HoonRoh, H. Funabashi, N. Park, E. J. Rice, L. Chen, R. Long, M. Wu, and D. Luo, *Nat. Nanotechnol.* **7**, 816 (2012).
- [18] V. Periasamy, N. Rizan, H. M. JaberAl-Ta'ii, Y. S. Tan, H. A. Tajuddin, and M. Iwamoto, *Sci. Rep.* **6**, 29879 (2016).
- [19] A. L. Patterson, *Phys. Rev.* **36**, (1939).
- [20] J. Tauc, R. Grigorovici, and A. Vancu, *Phys. Stat. Sol.* **15**, 627 (1966).
- [21] H. A. Barnes, *A Handbook of Elementary Rheology* (University of Wales, Institute of Non-Newtonian fluid Mechanics: Aberystwyth, 2000).

- [22] A. Ajji and L. Choplin, *Macromolecules* **24**, 5221 (1991).
- [23] A. B. Rodd, D. E. Dunstan, D. V. Boger, J. Schmidt, and W. Burchard, *Macromolecules* **34**, 3339 (2001).
- [24] D.-G. DeGennes, *Scaling Concepts in Polymer Physics*, 2nd ed. (Cornell University Press, NY, 1985).
- [25] X. Meng, W. Hua and M. Massimo, *Soft Matter* **11**, 981 (2015).
- [26] D. Bonn, H. Tanaka, G. Wegdam, H. Kellay, and J. Meunier, *Eur. Letts.* **45**, 52 (n.d.).
- [27] R. Angelini, E. Zaccarelli, F. Augusto de Melo Marques, M. Sztucki, A. Fluerasu, G. Ruocco, and B. Ruzicka, *Nat. Comm.* **5**, (2014).
- [28] G. A. Rance, D. H. Marsh, S. J. Bourne, T. J. Reade, and A. N. Khlobystov, *ACS Nano* **4**, 4920 (2010).

## CHAPTER-8

---

### Fluorescent multipurpose DNA- Dots: Luminescent DNA gels, Cell Imaging and Dopamine Detection

**Abstract:** In this chapter we have discussed multifunctional properties of water soluble DNA- Dots.

#### 8.1 Introduction

Traditionally, Deoxyribonucleic acid (DNA) is a genetic information carrier but is also an interesting material in the field of soft material science. Functional DNA derivatives with different surface chemistry have been developed in the past for imaging, sensing and therapeutic applications [1]. Modification in DNA nanostructure has been utilized for the formation of Holliday Junctions, lattices, DNA tiles, stem loops and sticky ends, which have been widely used in the field of DNA nanotechnology [1]. Self-assembled systems based on DNA are also optimized in biomedical industry [1]. Further, DNA not only carries genetic code, but the hybridization of double stranded DNA provides a potent platform for the evolution of many types of nanostructures [2], where structures get engaged with DNA chain to create new self-assembled geometries. The stability of these structures depends on the interaction potential [3]. Crosslinking of DNA chains to form hydrogel is well known in the literature which have shown multidisciplinary applications in the field of pharmaceutical industry as drugs carriers, tissue regeneration agents, transplantation of cells etc [4]. It has been successfully used in the past in a designed electric circuit where the water molecules provided switching action [5]. To manufacture any desired hydrogel, hybridized DNA glues which are sequence-specific to binding, and programmable self-assembly DNA have been widely used [6]. Pandey et al have

reported low concentration DNA gelation where ionic liquid was acting as a crosslinker [7]. Nucleic acid based quantum size dots exhibit photoluminescence with lifetime (~10.44 ns) much longer than carbon based (< 0.5 ns) quantum dots [8]. Quantum dots have found applications in solar cells, photodetectors, cell bioimaging and fluorescent hydrogels [9–12].

Traditional dyes and fluorophores, which are currently used for biological imaging have the disadvantages of multiple synthetic steps, high cost of production, rapid photobleaching, small Stokes shift, short fluorescence lifetime, narrow excitation spectra, and broad emission band [13,14]. Latest developments in nanotechnology have generated high value optical probes [15]. Inorganic quantum dots have biomedical applications in biosensing, bioimaging and drug delivery [16]. However, in the recent times, Carbon Dots (CDs) and graphene QDs have emerged as new alternative luminescent nanomaterials, especially due to their low toxicity, high photoluminescence, high biocompatibility and low photobleaching properties [17,18]. Absence of heavy metals in CDs unlike the QDs bypasses the environmental hazards and health concerns [13]. The extremely small size of CD generates sufficient energy through Brownian motion to prevent aggregation, thus facilitating high solubility and aqueous stability. The environmental compatibility, excitation dependent emission, high photostability and aqueous solubility of the CDs do not require any further surface chemistry for reducing their toxicity or increasing their solubility and thus makes them excellent candidates for biomedical and bioimaging applications.

Earlier polymer based hybrid materials like  $\text{CuInS}_2$  quantum dots were used as electrochemical sensor for dopamine detection [19,20]. Organic electrochemical transistor made with different gate electrodes (multi-walled carbon nanotube- Chitosan hybrid, Graphite, Au and Pt based

electrode) were used to detect dopamine [21]. Recently PEDOT:PSS based sensor was used for selective detection of dopamine [22].

In this study, we synthesized DNA-dots (DD) from ds-DNA and investigated its multifunctional potential. Interestingly, we show for the first time the synthesis of fluorescent DNA hydrogel at low concentration with the DD working as crosslinker. Further these dots showed negligible toxicity and efficient internalization into the fungal cells, therefore have the potential for use as nontoxic fluorescent probe for cell imaging applications. The dots were also optimized for selective detection of dopamine using the electrochemical platform. Functional DNAs with different modifications hold promising applications.

## **8.2 Sample preparation**

**8.2.1 Synthesis of DNA Dots (DD).** The easiest method for DNA dots (DD) synthesis is a single step process in which salmon DNA (2% (w/v)) was used as precursor. It was heated to 60 °C under continuous stirring in magnetic stirrer for 1 h. After one hour, the resulting homogeneous solution was transferred to Teflon coated autoclave and kept overnight in heating oven at 200 °C. Finally the cooled obtained material purified by centrifugation at 1000 rpm followed by dialysis.

**8.2.2 Synthesis of Fluorescent DNA-DNA Dot hydrogel.** DNA 2% (w/v) was dissolved in deionized water and heated to 60 °C under stirring for 30 min, resulting in a homogeneous and optically clear solution. Previously synthesized DD sample (0.8 to 4% (w/v)) was then added to the hot DNA solution such that the final concentration of DNA was 1% (w/v) in the DNA-DD

sol. These samples were allowed to cool to room temperature to attain gelation (DNA –DD hydrogel), which was ascertained from the non-flowing meniscus of the nascent gel held inside a test tube, when inverted.

**8.2.3 Microbial Strains and Growth media.** *Candida albicans* SC5314 strain was used in this study and the strain description is given elsewhere [23]. The fungal strain was grown at 30°C in liquid YEPD broth containing 1% (w/v) Yeast extract, 2% (w/v) Peptone and 2% (w/v) Dextrose and for solid YEPD plates, 2.5% (w/v) Agar was added to the YEPD media. Strains were preserved at -80°C in 15 % (v/v) glycerol. Cells from frozen glycerol stocks were revived on YEPD plates at 30°C. Liquid media cell cultures were maintained at 30°C with continuous shaking at 140-150 rpm for 14-16 hrs and these exponentially growing cells were used for all the experiments. All experiments were performed in triplicates and the average of three independent experiments along with standard deviation was calculated for each assay. The student *t* test and *p* value were calculated using GraphPad Prism version 5.0 (GraphPad software, CA) to show the significance and reproducibility of experiments. The criterion of *p* value < 0.05 was considered as significant.

**8.2.4 Assessment of microbial toxicity of DNA Dots (DDs).** Broth microdilution dilution was used to assess the susceptibility of the microbial cells towards the DDs through determination of Minimum Inhibitory Concentration (MIC<sub>90</sub>; minimum concentration required to inhibit the growth of 90% of organisms), which was carried out in accordance with the recommendations of the Clinical and Laboratory Standard Institute (CLSI) as described elsewhere [24,25]. Cells grown for 14 - 16 hrs on agar plates (exponentially growing log phase cells) were re-suspended

in 0.9% saline to give an optical density of 0.1 at 600 nm ( $OD_{600}$ ), which corresponds to cell number  $0.5 - 1 \times 10^6$  cells/ml. The cells were further diluted 100-fold in YEPD medium to bring the final concentration of cells to  $0.5 - 1 \times 10^4$  cells/ml. These cells were then allowed to grow at 30°C with continuous shaking in the presence of various concentrations of DDs. The growth of the cells was evaluated both visually and by taking  $OD_{600nm}$  in a microtitre plate reader and compared with growth control (absence of DDs).

**8.2.5 Intracellular Reactive Oxygen Species (ROS).** Intracellular ROS in *Candida albicans* cells were detected using a fluorogenic cell permeant dye, DCFH-DA as previously reported with slight modifications [26]. This fluorescent probe measures the intracellular hydroxyl, peroxy and other reactive oxygen species (ROS). Cells were grown separately to mid exponential phase in the absence of DDs (control) and presence of DDs (4 and 8 mg/ml) and  $H_2O_2$  (10 mM). Then, the cells were harvested by centrifugation at 5000 rpm for 10 mins at 4°C and thorough washing twice with PBS buffer pH 7.4 to remove the media. Finally,  $10^7$  cells were re-suspended in 3 ml PBS pH 8.4. The fluorescent probe DCFH-DA (final concentration 10  $\mu$ M) was then added to each cell suspension and incubated at 30°C for 1 hr. Relative fluorescence (Rf) Intensity was measured in a Perkin Elmer L55 spectrofluorimeter at respective excitation and emission wavelengths of 488nm and 540nm with slit widths of 5 and 10 nm, respectively. The blank (absence of fluorescent probe) was maintained separately to avoid auto-fluorescence. To confirm the presence of ROS, the images of the fluorescent cells were taken in the confocal microscope *FluoView™ FV1000*.

**8.2.6 Cellular uptake of DDs by the fungal cells.** The internalization of the DDs in the fungal cells was assessed by measuring the cellular uptake of DDs according to a previously described protocol with modifications [27]. *Candida* cells grown till mid exponential phase were harvested and washed with PBS buffer pH 7.4 twice to remove the media. Then, cells were re-suspended in PBS pH 7.4 to a concentration of  $10^7$  cells/ml and incubated with DDs at concentration of 4 mg/ml. From this cell suspension,  $10^7$  cells were taken out at various time points viz. 30 min, 1 hr, 2 hrs, 4 hrs, 8 hrs and 14 hrs. The cells taken out were harvested and the supernatant was removed. The cells were thoroughly washed twice and the washed cells were resuspended in 1 ml PBS to measure their relative fluorescence Intensity (*R<sub>f</sub>*) in a Perkin Elmer L55 spectrofluorimeter at respective excitation and emission wavelengths of 350 and 450 nm with slit widths of 10 nm. The blank (absence of DDs) was maintained separately to avoid auto-fluorescence. Rhodamine 6G (R6G) was used at a concentration of 10  $\mu$ M as a positive control. The cellular uptake for R6G was monitored using spectrofluorimeter at respective excitation and emission wavelengths of 488 and 530 nm with slit widths of 10 nm.

**8.2.7 Fluorescence Microscopy.** To confirm the presence of DDs within the cells, the fluorescence within the cells were visualized under the Zeiss Imager Z1 apotome microscope after appropriate washing of the cells followed by mounting. For this, the *Candida* cells were incubated with DDs separately for 30 mins, 1 hr and 2 hrs at respective concentrations of 4 mg/ml and 8 mg/ml, followed by thorough washing of the cells and finally resuspended in PBS. Images were captured using cooled monochrome CDD camera AxioCam HRM using Axiovision Rel 4.8.1 software. Rhodamine 6G was used as a positive control at a concentration of 10 $\mu$ M.



**8.2.8 Electrochemical sensing.** Electrochemical sensing of analytes was performed via Cyclic voltammetry (CV) studies utilizing a three anode cell in the connected potential range of - 0.05 to 0.5 V. The three electrodes used were the working electrode (DNA-DD/ITO), Pt-wire was taken as an auxiliary electrode and Ag/AgCl was taken as reference. The CV studies were conducted using Zobel's solution (3.3 mM  $\text{K}_4\text{Fe}(\text{CN})_6$ , 3.3 mM  $\text{K}_3\text{Fe}(\text{CN})_6$  with 0.1 M KCl at pH 7). Analyte concentration was standardized by repeating the experiments thrice under similar experimental conditions.

The different analytes used in the study were Urea (U), Citric acid (CA), L-cysteine (L-Cys), Alanine (Ala), dopamine (Dop), Glutamine (Glu), and Glycine (Gly). 100 mM stock solution of these analytes were separately prepared in deionized water and store at 4°C when not in use.

### 8.3 Result and Discussion

As synthesized water soluble DD's were characterized by TEM and a typical image is shown in Fig. 8.1(A). The average size of DD was estimated using ImageJ software. The size histogram (Fig. 8.1(C)) showed that the average size was 3 nm and interplanar spacing for DD was 0.15 nm (Fig. 8.1(B)).

X-ray diffraction pattern of synthesized DDs depicted in Fig.8.1(D) shows intense diffraction peaks at  $2\theta^0$  which corresponds to (002) crystalline plane. Scherrer formula [28] gave estimation about average crystallite size (6 nm). The surface topography of DD film was studied after drop casting the dispersion of DD on a mica substrate followed by drying. The AFM image in Fig. 8.1(F) revealed the height profiles with the mean size of  $3 \pm 3$  nm.

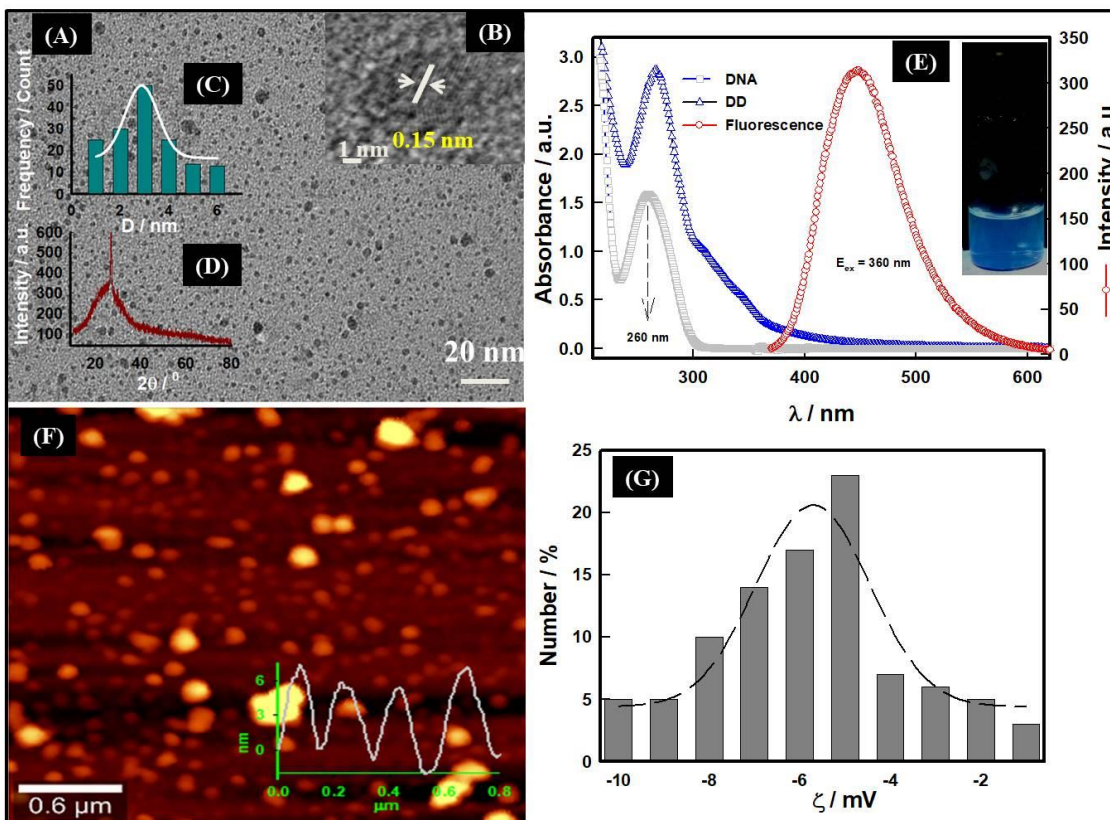


**Figure 8.1.** Characterization of DDs: (A) TEM image, (B) Interplanar spacing, (C) Size histogram obtained from TEM image analysis using imageJ software, (D) XRD pattern, (E) UV-fluorescence spectra (inset shows sample under UV-light), (F) AFM image (inset shows height distribution) and (G) Zeta potential histogram.

UV- visible spectra shown in Fig. 8.1(E) clearly shows signature absorption peak for DNA at 260 nm, and for DD at 260 and 360 nm. The optical band gap was determined by using Tauc's equation [29] given by,

$$(\alpha h\nu)^2 = \beta(h\nu - E_g) \quad (8.1)$$

Where  $\alpha$  is absorption coefficient, absorption coefficient is given by  $\alpha$ ,  $\beta$  is band tailing parameter,  $\nu$  is photon frequency,  $h$  is Planck's constant and  $E_g$  is required optical band gap. The band gap from linear fitting of plot  $(\alpha h\nu)^2$  vs  $h\nu$  yielded a value of 3.80. When the sample was

UV excited at 360 nm, a clear 450 nm blue fluorescence light was emitted which is depicted in Fig.8.1(E). The surface charge on the DDs was confirmed from the zeta potential histogram shown in the Fig. 8. 1(G), which ascribes a mean zeta potential of -6.5 mV to these particles.

### 8.3.1 Viscoelastic Properties of DNA-DD hydrogel

The viscoelastic profile of gel samples was evaluated from rheology using the following two different modes of analysis: (a) Isothermal frequency sweep studies were carried to evaluate the shear induced deformation of gel structure (Fig. 8.2(a)), and (b) Isochronal temperature sweep studies were performed to determine the melting profile of these gels. The storage modulus  $G'$  often displays a frequency  $\omega$  dependent dispersion behavior given by [30]

$$G'(\omega) = G_0\omega^{n'}; \quad G_0 = \lim G(\omega)_{\omega \rightarrow 0} \quad (8.2)$$

Here  $G_0$  is low frequency elastic modulus. It can be concluded from the data that  $G_0$  had a value of  $\sim 20$  Pa for a gel with 0.8% DD, and  $\sim 80$  Pa for 4 % sample, the corresponding value of  $n'$  was  $0.7 \pm 0.2$  (Fig. 8.2(C) and (D)). For comparison, the reported  $G_0$  value for DNA hydrogel is  $20 \pm 2$  Pa and for ionogel it is  $29 \pm 2$  Pa [7,31]. Thus, it can be stated that these DD based DNA hydrogels were highly viscoelastic in nature with attributes dependent on the DD content of the sample. It is to be noted that without the DD the samples would never gel. Therefore, these dots acted as crosslinkers in the DNA sol to generate a strong nanocomposite gel with tunable strength and melting temperature. The synergy of this interaction can be gauged from the fact that the gel strength increased with DD content.

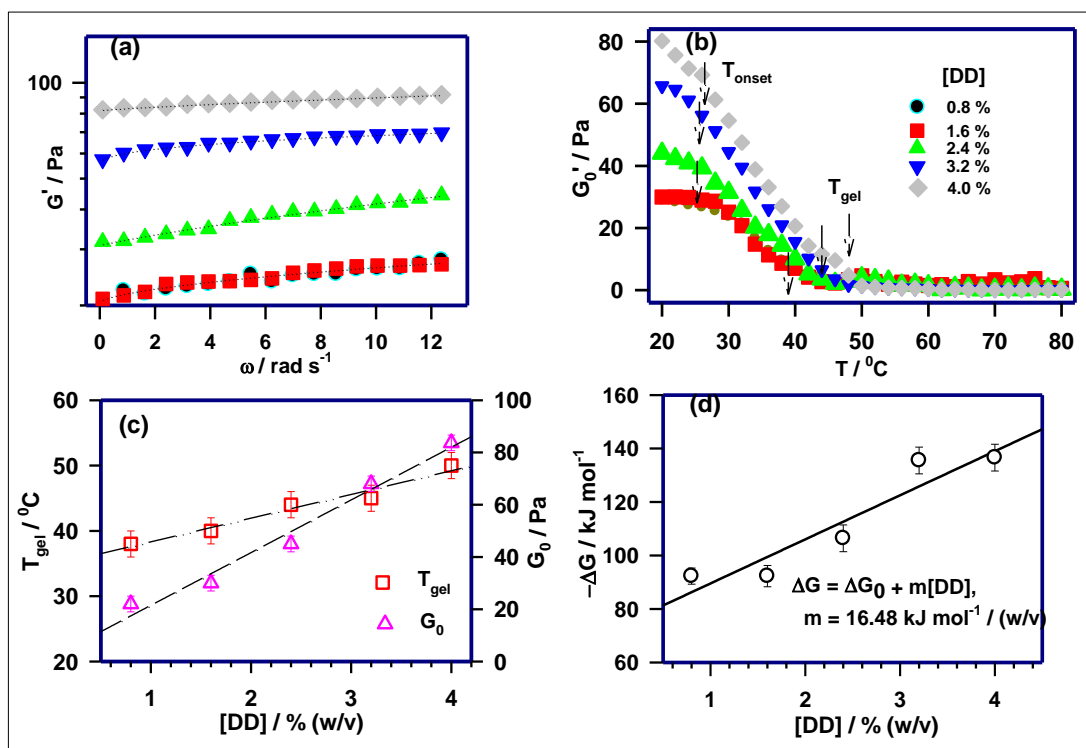


**Figure 8.2.** Viscoelastic Properties of DNA- DD nanocomposite hydrogel: (a) Storage modulus as a function of frequency, (b) Temperature sweep profile, (c) Variation of  $T_{gel}$  and storage modulus, (d) change in Gibbs free energy of gelation with DD concentration.

In the next step, the melting profiles of the gels containing different concentration of DDs were evaluated. This data is depicted in Fig. 8.1(B). Dependence of  $T_{gel}$  and  $G_0$  with DD content is clearly shown in Fig. 8.1(c), which shows that both  $T_{gel}$  and  $G_0$  increase highlighting the crosslinking efficiency of these dots, while retaining the viscoelastic nature of the gels.

The dot concentration [DD] could be correlated to the  $T_{gel}$  and  $G_0$  through the linear relations given by

$$T_{gel}(DD) = T_{gel}(o) + m_{gel}[DD] \quad (8.3)$$

$$G_0(DD) = G_0(o) + m_{G_0}[DD] \quad (8.4)$$

Where  $[DD]=0$  concentration values are represented as  $T_{gel}(0)$  and  $G_0(0)$ , and the concentration coefficients are  $m_{gel}$  and  $m_{G_0}$ , respectively. The least-squares fitting of the data yielded:  $T_{gel}(0) = 34.7^{\circ}C$ ,  $G_0(0) = 1.33 Pa$ ,  $m_{gel}=3.6$  and  $m_{G_0}=20.2$  with chi-squared value  $\sim 0.98$ .

The elastic energy stored in a network per unit volume is determined by its  $G_0$  value. When this energy is equated with the thermal energy, it defines a characteristic length scale called the viscoelastic length. The length is a key parameter corresponding to self-assembled network, which is given by  $\zeta_{el}$  [32]

$$G_0 \sim k_B T / \zeta_{el}^3 \quad (8.5)$$

This length varied from  $\zeta_{el} = 58 nm$  for 0.8% (w/v) of DD based DNA-DD hydrogel sample to 37 nm for 4% (w/v) DD hydrogel. Therefore, the formed networks were denser at higher DD concentration. The temperature sweep measurement Fig.8.2(c) showed transition which can be referred as gelling temperature,  $T_{gel}$ . The  $T_{gel}$  value increased from 40 to 50<sup>o</sup> C with DD concentration indicating sufficient interaction between DNA strands and DD. Therefore, the gelling temperatures of the nanocomposite gels can be tuned by altering the DD concentration as required for the application. During the melting process the equilibrium gel makes a thermodynamic transition to an equilibrium sol state. Therefore, the melting profile between  $T_{onset}$  and  $T_{gel}$  region (see Fig. 8.2(b)) can be described by the Arrhenius relation given by

$$\Delta G_0(T) = \Delta G_0 \exp - \left( \frac{\Delta G}{RT} \right) \quad (8.6)$$

Where,  $\Delta G_0 = G_0(T_{onset}) - G_0(T_{gel})$ ,  $R$  is universal gas constant and  $T$  is temperature in Kelvin, and  $T_{onset} < T < T_{gel}$  is the melting region which was fitted to eqn (8.6). The estimated Gibbs free energy of gelaton  $\Delta G$  varied from -90 to 140  $kJmol^{-1}$  with increase in DD concentration, which clearly indicated more favorable networking in DNA gels. This reiterates

our contention that these dots acted as crosslink junctions inside the gel matrix. The corresponding enthalpy ( $\Delta H$ ) and entropy ( $\Delta S$ ) change were estimated from

$$\Delta G = \Delta H - T\Delta S \quad (8.7)$$

and the known values of free-energy. This analysis yielded  $\Delta H = -119 \text{ kJ mol}^{-1}$  and  $\Delta S = -5.16 \text{ J K}^{-1}$ . Thus, it was remarkable to note that DNA solution (1% (w/v)) transformed into a DNA hydrogel assisted by crosslinking junctions provided by DNA dots.

### 8.3.2 Morphology of DNA-DD hydrogel

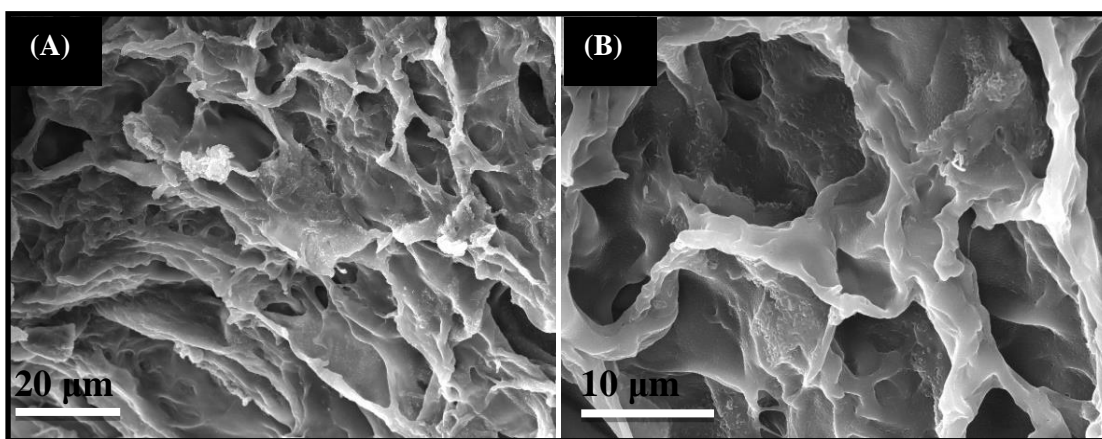


**Figure 8. 3.** Morphology of DNA- DD hydrogel: (A) FESEM image with 20  $\mu\text{m}$  and (B) 10  $\mu\text{m}$  scale bar resolution.

The morphology of hydrogel was obtained from FESEM images shown in Fig. 8.3. Interconnected networks and hierarchical porous structures were observed for these hydrogels, which again suggested that the DNA dots assisted in the evolution of a self assembled network structures from a solution that would otherwise not form a gel. A qualitative profile of the networks seen in these images can be realized from the estimation of network density in the gel concerned.

To a very good estimation, a good estimate of the network density  $\nu$  in a given material can be derived from the known  $G_0$  data. In the Flory model the network density is calculated from the equilibrium swelling experiments which stipulates that the network density can be approximately determined from the relation given by

$$E \approx \left[ \frac{3\rho RT}{2M_e} \right] \quad (8.8)$$

where  $E$  is the low deformation Young's modulus,  $\rho$  is rubber density, and  $M_e$  is the mean molecular weight of the polymer segment between crosslinks. Further,  $\rho = \nu M_e$  and for an affine network,  $E \approx 3G_0$  allows the above equation to be written as

$$\nu \approx \left[ \frac{2G_0}{RT} \right] \quad (8.9)$$

The relative network density  $\nu_r$  is given as

$$\nu_r = \left[ \frac{\nu}{\nu_0} \right] \quad (8.10)$$

Where  $\nu$  and  $\nu_0$  refer to the network density of DNA-DD gel and DNA gel, respectively. The variation of  $\nu_r$  with DD content is shown in Fig.8.4 which increases linearly with the DD concentration. This clearly establishes that the DDs played the role of crosslinkers in the gel network. It is pertinent to highlight the special features of the DNA-DD gel *vis a vis* those of DNA hydrogel and DNA ionogel. Table 8.1 provides a comparison of physical properties of various DNA gels and their subtle distinctions.

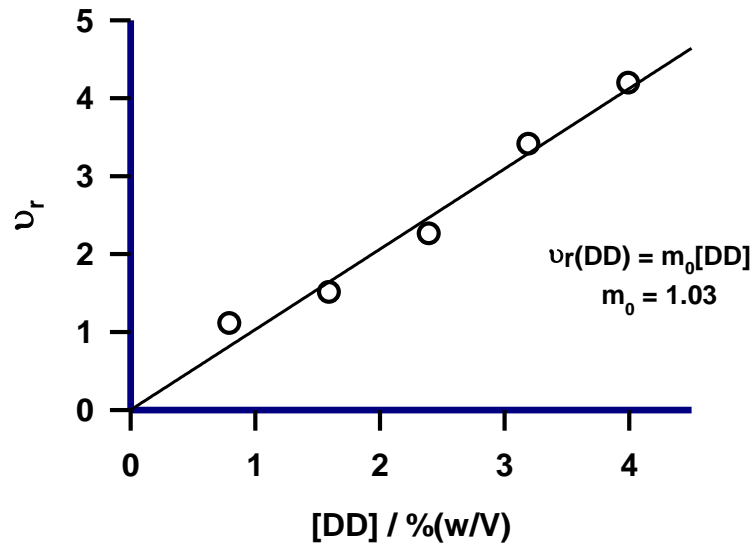


**Figure 8.4.** Relative network density of DNA-DD hydrogel with DD concentration.

**Table 8.1.** Comparison of DNA hydrogel, DNA-ionogel and DNA-DD hydrogel. Parameters compared are gelation concentration  $C_{gel}$ , gelation temperature  $T_{gel}$ , storage modulus  $G_0$ , fluorescent nature, change in gelation free energy  $\Delta G$ , viscoelastic length  $\xi_{el}$ , and relative network density  $\nu_r$ .

Parameters	Hydrogel <sup>48</sup>	ionogel <sup>7</sup>	DNA-DD gel	Speciality of DNA-DD gel
$C_{gel}$ /% (w/v)	2%	1%	1%	lower gelation conc
$T_{gel}$ / °C	34	60-65	40-50	Large gelation window
$G_0$ / Pa	20	27-70	20-80	Large gel strength window
$\xi_{el}$ /nm	59	38-45	36-58	Tunable porous gel
$\Delta G$ /kJ	-35	-33 to -78	-90 to -140	Strongly free-energy driven
$\nu_r$	1	1.35-3.5	1-4.2	Heavily crosslinked
Fluorescence	None	None	Yes	Fluorescent gel



### 8.3.3 Microbial toxicity of DDs

DDs are a new class of fluorescent dots derived from DNA and are nanomaterials with photoluminescence, biocompatible, low-cost and environment friendly properties [33]. Carbonaceous DDs are more biocompatible than other nanomaterials e.g. quantum dots since the backbone of DDs is constituted by the non-toxic element [34]. Carbon Dots (CDs) being non biotoxic, fulfill the basic requisite for bio applications such as imaging. Many research groups have evaluated the biotoxicity of CDs against various cancer cell lines and reported that the cells could withstand a very high dose of CDs for very long duration of time without any change in cell viability. Although CDs display lower toxicity than other luminescent metal nanomaterials, it is known that the toxicity of CDs is strongly dependent on the fabrication protocol [35].

Therefore, in this study, in order to determine the microbial toxicity of DDs, we evaluated the susceptibility of *Candida albicans* cells towards DDs using broth microdilution method. *Candida albicans* is an opportunistic common fungal pathogen and used in this study as a microbial model. Broth micro-dilution assay revealed that there was no change in optical density of the cells even after 48 hours even after incubating the cells to very high concentration of 8 mg/ml which implied that DDs did not affect the viability of the fungal cells (Fig. 8.5(A)). For study of the effect of DDs on growth of the fungal cells, the results were interpreted by comparing the growth of the fungal cells with the control (absence of DDs), which further revealed that there was no inhibition in growth even after incubating the cells for 48 hours up to a high concentration of 8 mg/ml (Fig. 8.5(B)).

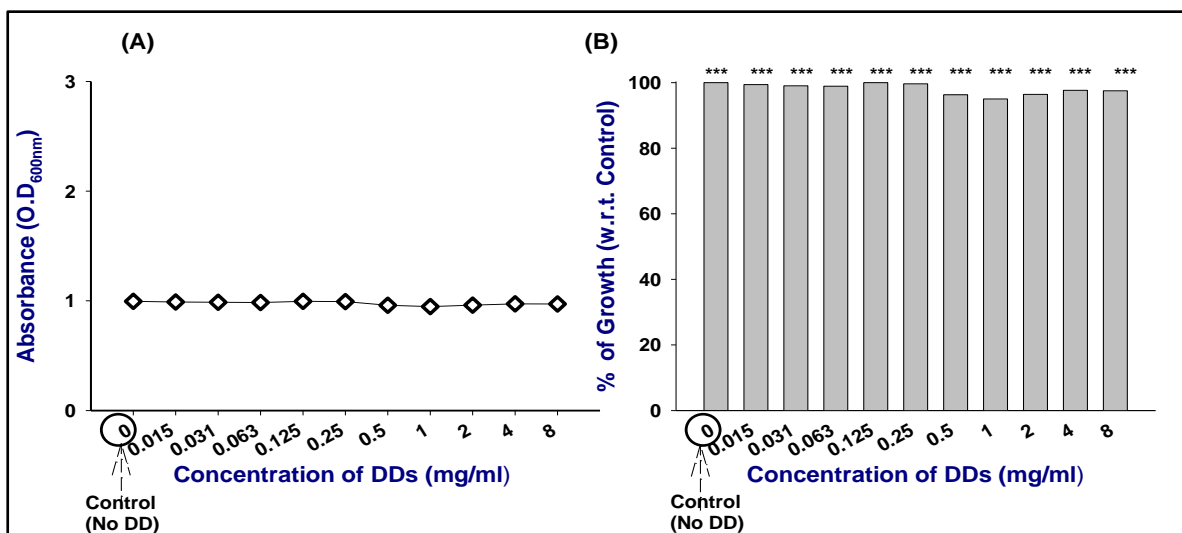


**Figure 8.5.** Effect of DDs on growth of fungal cells. (A) Determination of OD<sub>600nm</sub> by broth microdilution method for *Candida* cells grown in absence (Control) and presence of DDs respectively. The values are mean  $\pm$  SD of three independent sets of experiments. In this method, growth of the cells was evaluated both visually and by taking OD<sub>600nm</sub> in a microtitre plate reader. Growth differences were evaluated with DD-free controls following incubation of the plates for 48 hrs as described elsewhere [25,26]. (B) Percentage of growth determined by broth microdilution method for *Candida* cells grown in the absence (Control) and presence of various concentrations of DDs. The values are mean  $\pm$  SD of three independent sets of experiments. \*\*\* represents  $p < 0.0001$  with respect to control.

### 8.3.4 DD induced intracellular ROS

Nanomaterials are known to induce cytotoxicity through augmentation of intracellular ROS, which is known to exerting cytotoxic effect through induction of mitochondrial dysfunctional apoptosis especially hydroxyl radicals [36]. In this study, we measured the endogenous ROS generated due to DDs in the fungal cells, using the fluorogenic, cell permeant dye, DCFH-DA. This dye diffuses into the cells and gets deacetylated by cellular esterases to form colorless, stable dichlorofluorescein, which gets further oxidized by intracellular ROS to produce fluorescent, 2,7- dichlorofluorescein (DCF). It is thus, well understood that higher amount of intracellular ROS will lead to higher fluorescence due to increased production of DCF. However,

here it was observed that compared to the basal ROS levels in control (absence of DDs), there was no change in levels of intracellular ROS in cells incubated with 4 and 8 mg/ml DDs respectively (Fig. 8.6). The data obtained for ROS generation through fluorescence measurements was further corroborated by the results of confocal microscopy (Fig. 8.6) wherein comparable fluorescence intensity was observed within the control (absence of DDs) and *Candida* cells incubated with DDs implying similar levels of intracellular ROS (Fig. 8.6). The H<sub>2</sub>O<sub>2</sub> treated cells were used as positive control (Fig. 8.5 (a) and (b)). It is envisioned that the DDs in this study were non toxic towards the microbial cells tested, mainly because they were not able to augment generation of intracellular ROS unlike other nanomaterials. The above data suggests a promising future potential of our non-toxic DDs for further biomedical applications and in bioimaging.

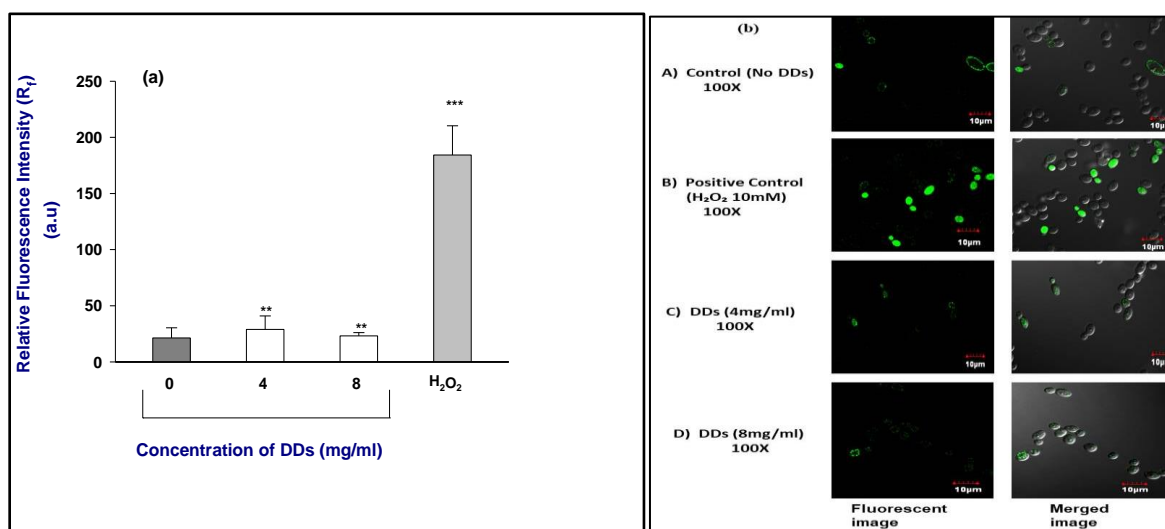


**Figure 8.6.** Assessment of intercellular ROS production. (a) Quantitative measurement of intracellular ROS in the *Candida* cells grown in absence and presence of DDs (4 and 8 mg/ml) estimated using the fluorescent dye DCFH-DA; ROS levels are measured as relative fluorescence (R<sub>f</sub>) intensity and Y axis depict the mean R<sub>f</sub> values ± the standard deviation (SD) of three sets of independent experiments; R<sub>f</sub> Intensity was calculated by subtracting the R<sub>f</sub> intensity for cells incubated without DCFH-DA (blank) from R<sub>f</sub> intensity for cells incubated with DCFH-DA [25]. \* represents  $p < 0.05$  calculated with respect to “Absence of DDs” (control), (b) Confocal images showing green fluorescence for endogenous ROS in *Candida* cells grown in the

absence (panel A) and presence of 4 mg/ml and 8 mg/ml DDs (panels B and C), respectively. Each left panel depicts the fluorescence intensity (higher fluorescence indicates higher ROS production) measured by a Confocal microscope and each right panel shows the merge for the phase-contrast micrographs and fluorescence images at magnification 100X. The obtained results were compared with control cells (Absence of DDs; panel A) and positive control (cells treated with 10 mM hydrogen peroxide, H<sub>2</sub>O<sub>2</sub>; panel D).

### **8.3.5 Cellular uptake of DDs**

For evaluating the potential of DDs in bioimaging applications, the primary prerequisites remain their biotoxicity and internalization into the cells. Uptake of DDs is important for determining their internalization within the microbial cells. As a new family of nanomaterials, DDs have been reported to be able to penetrate the plasma membrane due to their small sizes and show fluorescence inside the cells due to fluorescent properties [37]. Cellular uptake of DDs has been found to be time, dose and partially energy dependent along with the involvement of passive diffusion [38]. Red-emitting DDs exhibited incubation time dependent cytoplasmic accumulation in HeLa cells, thus confirming uptake by passive diffusion [33].

In order to be able to predict the use of DDs for bioimaging in microbial cells and other biomedical applications, the cellular uptake of DDs was quantified in terms of fluorescence intensity using spectrofluorometry after incubation with 4 mg/ml DDs for 30 mins, 1 hr, 2 hrs, 4 hrs, 8 hrs and 14 hrs. Time kinetics of cellular uptake revealed highest intracellular concentration of DDs after 30 mins incubation (Fig. 8.7) which is evident from the high fluorescence intensity due to presence of DDs inside the fungal cells. It appears that the DDs enter the cells by passive diffusion and accumulate in the cytoplasm to attain saturation, reaching the highest intracellular concentration at 30 mins (Fig. 8.7). Gradually equilibrium is attained to maintain the intracellular levels of DDs till 14 hrs (Fig. 8.7). R6G is well known fluorescent tracer dye used for real-time monitoring of cellular processes such as sub-cellular localization, biological functionality,

membrane transport processes, diffusion and kinetics [39]. R6G is known to enter *Candida cells* by passive diffusion and was used as a positive control in this study [25,26]. The uptake of 10  $\mu\text{M}$  R6G was monitored after incubation for the same time periods of 30 mins, 1 hr, 2 hrs, 4 hrs, 8 hrs and 14 hrs and it was found that the pattern of intracellular accumulation of DDs was in agreement with that of intracellular R6G accumulation.

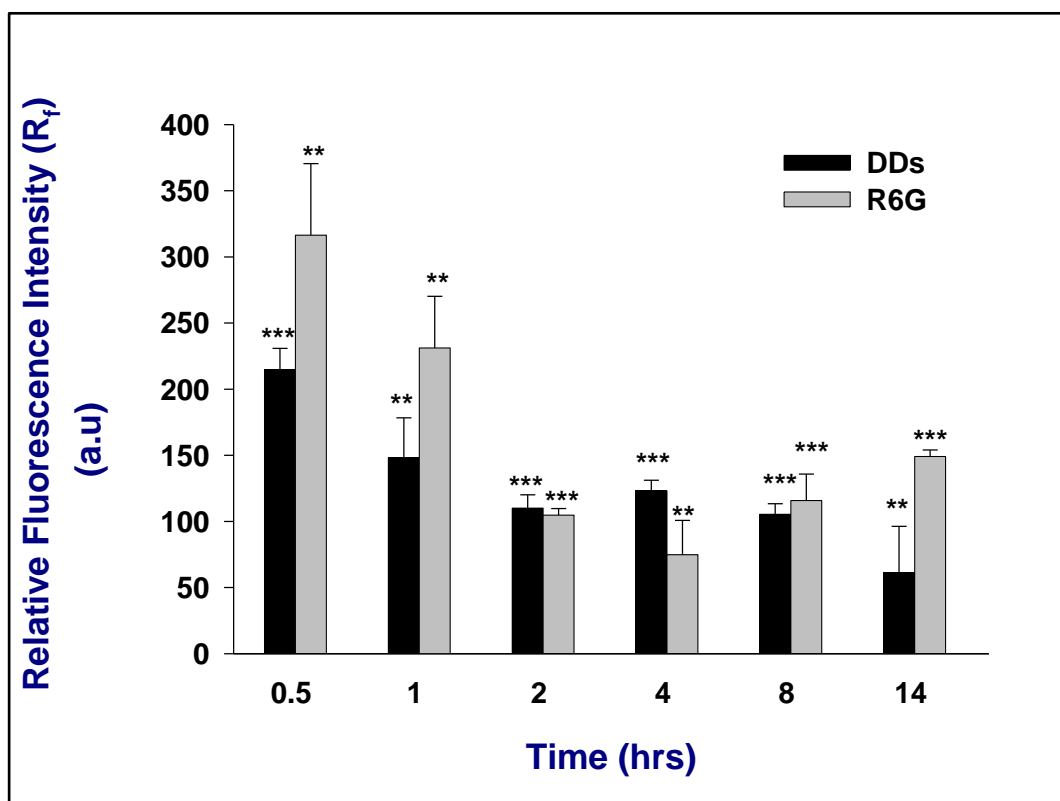


**Figure 8.7.** Quantitative time dependent cellular uptake of DDs in *Candida* cells in terms of fluorescence intensity. The *Candida* cells were incubated with 4mg/ml DDs and from this cell suspension,  $10^7$  cells were taken out at various time points viz. 30 mins, 1 hr, 2 hrs, 4 hrs, 8 hrs and 14 hrs and uptake of DDs in *Candida* cells was measured. R6G was used as positive control and the uptake of 10  $\mu\text{M}$  R6G was monitored in the fungal cells after incubation for the same time periods of 30 mins, 1 hr, 2 hrs, 4 hrs, 8 hrs and 14 hrs. Y axis depicts the mean relative fluorescence ( $R_f$ ) values  $\pm$  the standard deviation (SD) of three sets of independent experiments. Relative Fluorescence ( $R_f$ ) was calculated by subtracting the fluorescence intensity for cells incubated without DDs (blank) from fluorescence intensity for cells incubated with DDs. \*\*\* represents  $p < 0.0001$ , \*\*  $p < 0.001$  calculated with respect to “Absence of DDs” (control).

The bright blue fluorescence inside the fungal cells in the microscopy images shows the internalization of the DDs in the fungal cells after incubation with DDs (4 and 8 mg/ml) respectively for 30 mins, 1 hr and 2 hrs (Fig. 8.8). It indicated that DDs could permeate throughout the fungal cells without imposing toxicity. The uptake of the DDs appeared to be the maximum at 30 mins incubation time. No difference was observed in the intracellular uptake of DDs at concentrations of 4 mg/ml and 8 mg/ml (Fig. 8.8). R6G was used a positive control for assessing intracellular uptake. Green fluorescence inside the fungal cells indicated cellular uptake of R6G at different incubation time of 30 mins, 1 hr and 2 hrs (Fig.8.8, panel D). The cells did not show any autofluorescence as revealed from panel A in Fig.8.8, which indicated no hindrance from undesirable autofluorescence of the microbial cells. The interferences from undesirable autofluorescence of the cells significantly affect conventional fluorophores whereas this study revealed that once incorporated into the cells, the self-fluorescence of the DDs remained clearly different from the background of the medium and the cells, which is desirable for imaging applications. Thus, our results allow us to unequivocally affirm that DDs synthesized in this study have potential for bioanalytical and biomedical applications. To make DDs more appropriate for targeted cellular imaging and live imaging applications, they would require to be conjugated to molecules which will not alter the functions of DDs.

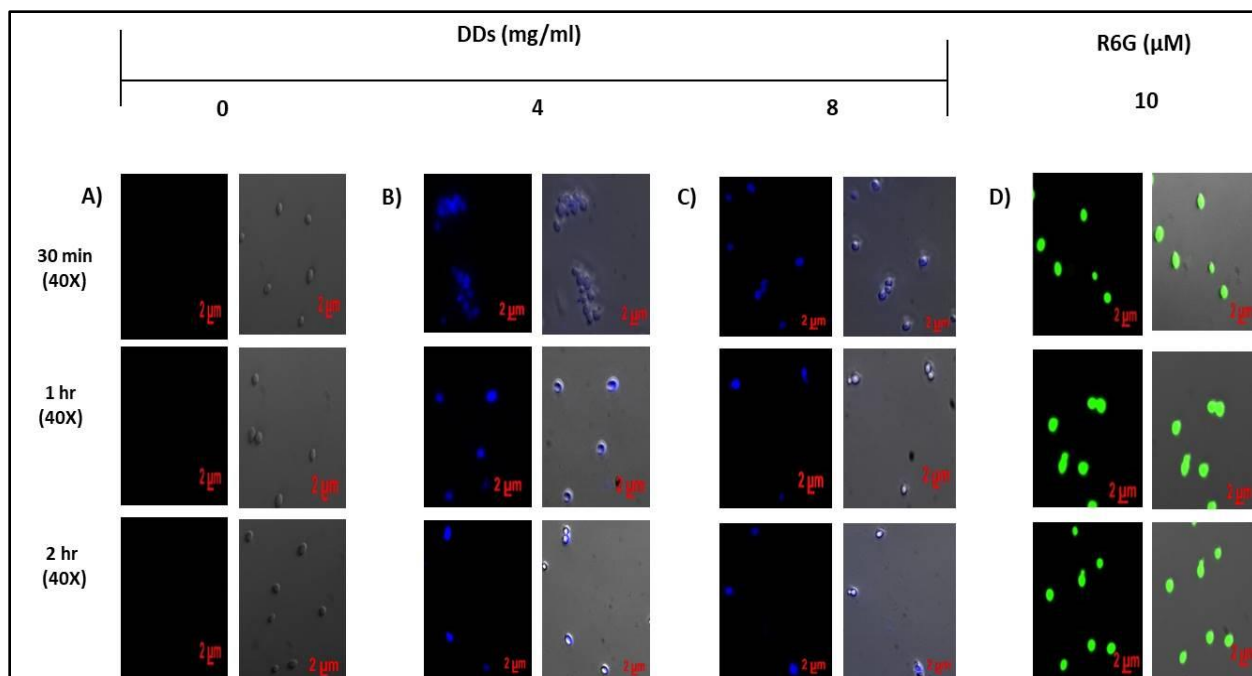


**Figure 8.8.** Fluorescence microscopy images showing cellular uptake of DDs after incubation with 4 mg/ml and 8mg/ml DDs for various time points viz. 30 mins, 1 hr, 2 hrs, 4 hrs, 8 hrs and 14 hrs. The blue fluorescence inside the fungal cells showed the internalization of the DDs. R6G was used as positive control and the uptake of 10  $\mu\text{M}$  R6G was observed as green fluorescence in the fungal cells after incubation for the same time periods of 30 mins, 1 hr, 2 hrs, 4 hrs, 8 hrs and 14 hrs.

### 8.3.6 Dopamine detection

For the electrochemical study, the sol was drop cast on the ITO plate to form a thin film at room temperature. The electrochemical response of DNA-DD hydrogel/ITO electrode was observed in 0.05 to 0.5 V potential range. The CV profile of bare ITO, and DNA-DD hydrogel /ITO electrode at 50 mV/s scan rate was investigated in order to understand the

electrochemical behavior in Zobell's solution. It was observed that the peak current of DNA-DD hydrogel/ITO electrode was more in comparison with blank ITO. This suggested the presence of thin film on the ITO surface and a reduction in electron transfer accessibility by the film

compared to ITO electrode (Fig. 8.9 (a)) [40,41]. The sole objective of this measurement was to analyze the potential ability of the electrodes towards selective detection of bioanalyte Dopamine in the presence of intereferents like, Urea (U), Citric acid (CA), L-cysteine (L-cys), alanine (Ala), Glutamine (Glu) and Glycine (Gly). The study of the electrochemical response of these electrodes for bioanalytes in the concentration range of 0.2-2.0 mM at a fixed scan rate of 50 mV/s was under taken. The observed change in anodic and cathodic peak current with varying analyte concentration determined the response of the electrode towards the bioanalyte tested. A single DNA-DD hydrogel /ITO electrode was used for the detection of the whole range of concentration of a given analyte. Distinct changes in CV profiles were observed in the case of Dopamine while no major changes were seen in the case of other tested analytes. The anodic peak current was found to increase with increasing concentration of Dopamine. Additionally, a shift of anodic peak or current towards higher potential was observed with increasing Dopamine concentration (see Fig. 8.9 (b)).

It clearly indicated increase in the oxidation ( $I_a$ ) and reduction ( $I_c$ ) current on treatment with Dopamine and thus suggested that the electro-catalytic reaction was because of the presence of Dopamine (Fig. 8.9 (c)). No change in the peak current was found for other bioanalytes even at very high concentration of 2.0 mM (data not shown). The linear regression equation for wide range of analyte is,  $I(\mu A) = 186 + 149 \times C(\text{mM})$  with  $R^2 = 0.96$ , Therefore sensitivity for the electrode was  $0.6 \mu A \mu M^{-1} \text{ cm}^{-2}$  and the detection limit was  $5 \times 10^{-3} \text{ mM}$ .



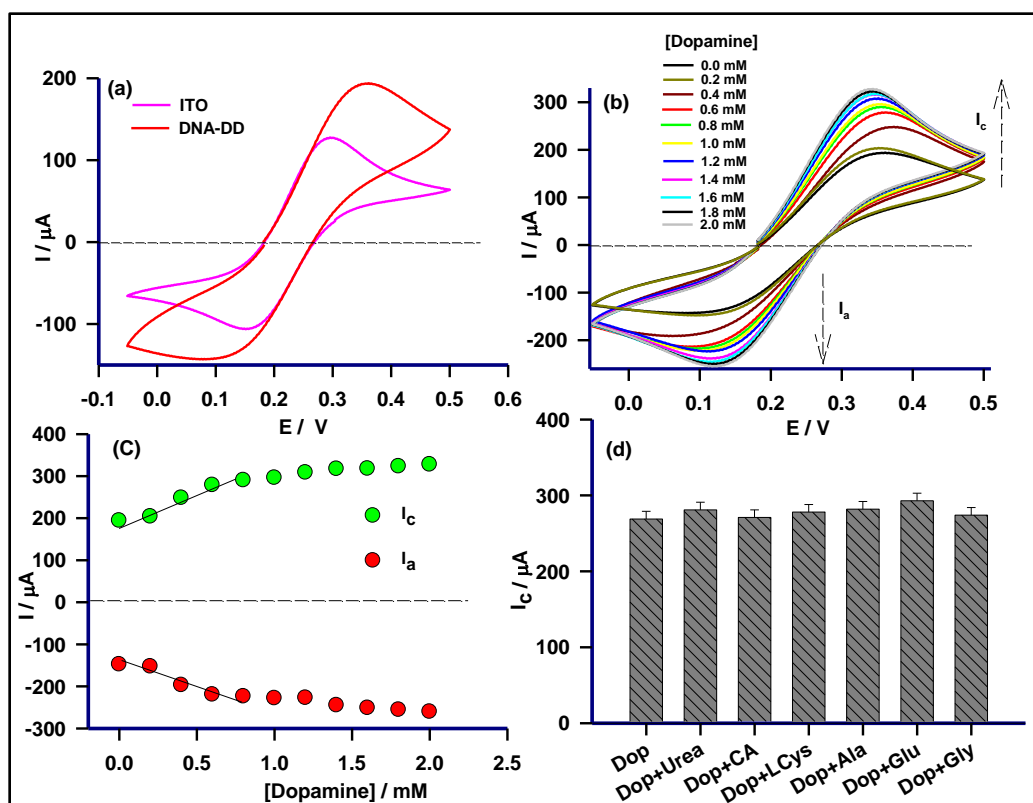


**Figure 8.9.** Response of DD based electrochemical sensor. (A) Electrochemical response of Blank ITO electrode and DND-DD hydrogel/ITO electrode without analyte, (B) Electrochemical response of DNA-DD hydrogel/ITO electrode towards Dopamine for -0.05 to 0.5 Voltage range, (C) Anodic and cathodic peak current for different Dopamine concentrations. Fitting line shown corresponds to the linear fitting of dopamine detection range, and (D) Interference histogram shows selective response for Dopamine.

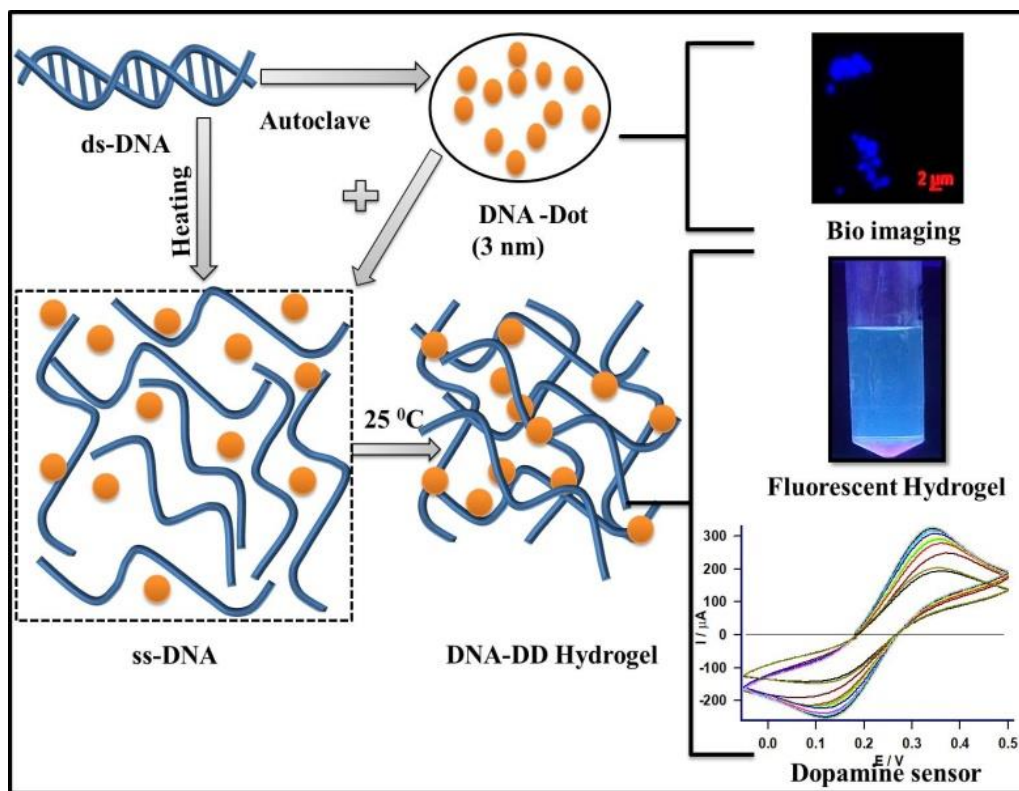
The selectivity of the electrode (Fig. 8.9 (d)) was monitored by potential interferents. The study was performed at a scan rate  $50 \text{ mV s}^{-1}$  taking 1:1 Dopamine and the normal physiological concentration of interferents viz. Urea, Citric acid, L-cysteine, Alanine, Glutamine, and Glycine. We found that this electrochemical sensor electrode was specific to Dopamine detection and did not respond to the presence of other analytes. In order to place our results in the proper perspective, a list is provided in Table 8.2 where the Figures of merit of various reported methods are compared. Our method offers a wider linear range of detection with low detection limit, in addition to the detection platform being green.

**Table 8.2.** Comparison of different electrodes used for Dopamine detection.

Sample	Linear range /mM	Detection limit /mM	Reference
AgNPs/rGO	0.01-0.8	$5.4 \times 10^{-3}$	[42]
Gold Nanoelectrode	0.001-0.1	$5.8 \times 10^{-3}$	[43]
PANI-NF/Pt	0.062-0.6.	$33.30 \times 10^{-3}$	[44]
RGO/TiO <sub>2</sub>	0.002–0.06	$6 \times 10^{-3}$	[45]
DNA-DD/ITO	0-1.0	$5 \times 10^{-3}$	Present work

### 8.1 Conclusion

In summary, combining the unique properties of DNA, we developed water soluble biocompatible DNA Dots of size 2-3 nm with potential for multifunctional applications (see Scheme 8.1 for a depiction). These DDs acted as crosslinker for the same DNA to form nanocomposite hydrogel at low DNA concentration (1 % w/v). The strength of these gels varied from 20-80 Pa and melting temperature from 40<sup>0</sup> to 50 <sup>0</sup>C tunable with dot content. The viscoelastic length of these hydrogel decreased from 58 to 36 nm which corresponds to a denser network formation with increase in DD concentration.



**Scheme 8.1.** Illustration of multifunctionality of DNA-biodots: cell imaging, fluorescent DNA gel and dopamine sensing.

These hydrogel showed blue fluorescence under UV light. Further these DDs exhibited negligible cytotoxicity and highly efficient internalization into the fungal cells. The DDs possess good PL stability and high biocompatibility; therefore, it has the potential for use as nontoxic fluorescent probe in bioimaging applications. The DNA-DD/ITO electrode displayed selective detection of dopamine, which can developed into a good sensing platform. Thus, it can be concluded that multimodality of such DNA dots based nanostructures has the versatility and potential to serve as smart systems for bioimaging, biosensing, and diagnostics applications.

## 8.2 References

- [1] Y. Zhang, J. Tu, D. Wang, H. Zhu, S. K. Maity, X. Qu, B. Bogaert, H. Pei, and H. Zhang, *Adv. Mater.* **30**, 1 (2018).
- [2] J. Kondo, Y. Tada, T. Dairaku, Y. Hattori, H. Saneyoshi, A. Ono, and Y. Tanaka, *Nat. Chem.* **9**, 956 (2017).
- [3] R. Schreiber, J. Do, E. Roller, T. Zhang, V. J. Schu"ller, P. C. Nickels, J. Feldmann, and T. Liedl, *Nat. Nanotech.* **9**, 74 (2014).
- [4] S. H. Um, J. B. Lee, N. Park, S. Y. Kwon, C. C. Umbach, and D. Luo, *Nat. Mater.* **5**, 797 (2006).
- [5] J. B. Lee, S. Peng, D. Yang, Y. H. Roh, H. Funabashi, N. Park, E. J. Rice, L. Chen, R. Long, M. Wu, and D. Luo, *Nat. Nanotechnol.* **7**, 816 (2012).
- [6] H. Qi, M. Ghodousi, Y. Du, C. Grun, H. Bae, P. Yin, and A. Khademhosseini, *Nat. Comm.* **4**, 1 (2013).
- [7] P. K. Pandey, K. Rawat, V. K. Aswal, J. Kohlbrecher, and H. B. Bohidar, *Phys. Chem. Chem. Phys.* **19**, 804 (2017).
- [8] C. X. Guo, J. Xie, W. Wang, X. Zheng, H. B. Yang, and C. Ming L, *Sci. Rep.* **3**, 1 (2013).
- [9] O. E. Semonin, J. M. Luther, S. Choi, H. Chen, J. Gao, A. J. Nozik, and M. C. Beard, *Science* (80-. ). **334**, 1530 (2011).
- [10] J. P. Clifford, G. Konstantatos, K. W. Johnston, S. Hoogland, L. Levina, and E. H.

- Sargent, *Nat. Nanotech.* **4**, 40 (2009).
- [11] Y. Ma, M. Wang, W. Li, Z. Zhang, X. Zhang, T. Tan, X. Zhang, and Z. Cui, *Nat. Comm.* **8**, 1 (2017).
- [12] L. Zhang, S. R. Jean, S. Ahmed, P. M. Aldridge, X. Li, F. Fan, E. H. Sargent, and S. O. Kelley, *Nat. Comm.* **8**, 1 (2017).
- [13] U. Resch-Genger, M. Grabolle, and S. e. al. Cavaliere-Jaricot, *Nat. Methods* **5**, 763 (2008).
- [14] C. Tzu-Heng and T. Wei-Lung, *Anal. Chem.* **89**, 11348 (2017).
- [15] X. Sun and Y. Lei, *Trends in Anal. Chem.* **89**, 183 (2017).
- [16] S. Y. Lim, W. Shen, and Z. Gao, *Chem. Soc. Rev.* **44**, 362 (2015).
- [17] J. Wang, G. Liu, K. C. Leung, R. Loffroy, P. Lu, and Y. X. J. Wáng, *Curr Pharm Des* **21**, 5401 (2015).
- [18] S. Fasbender, S. Allani, C. Wimmenauer, R.-P. Cadeddu, R. K., J. C. Fischer, B. Bulat, M. Luysberg, C. A. M. Seidel, T. Heinzl, and R. Haas, *RSC Adv.* **7**, 12208 (2017).
- [19] S. Liu, F. Shi, X. Zhao, L. Chen, and X. Su, *Biosens. Bioelectron.* **47**, 379 (2013).
- [20] D. Lakshmi, A. Bossi, M. J. Whitcombe, I. Chianella, S. A. Fowler, S. Subrahmanyam, E. V. Piletska, and S. A. Piletsky, *Anal. Chem.* **81**, 3576 (2009).
- [21] H. Tanga, P. Lina, H. L. W. Chana, and F. Yana, *Biosens. Bioelectron.* **26**, 4559 (2011).
- [22] I. Gualandi, D. Tonelli, F. Mariani, E. Scavetta, M. Marzocchi, and B. Fraboni, *Sci. Rep.*

- 1 (2016).
- [23] W. A. Fonzi and M. Y. Irwin, *Genetics* **134**, 717 (1993).
- [24] J. H. Rex, B. D. Alexander, and D. et al. Andes, *Reference Method for Broth Dilution Antifungal Susceptibility Testing of Yeasts*, 3rd ed. (Clinical and Laboratory Standards Institute (CLSI), 950 West Valley Road, Suite 2500, Wayne, Pennsylvania, USA., 2008).
- [25] T. Prasad, A. Chandra, C. K. Mukhopadhyay, and R. Prasad, *Antimicrob Agents Chemother* **50**, 3597 (2006).
- [26] T. Prasad, S. Hameed, and R. et al. Manoharlal, *FEMS Yeast Res.* **10**, 587 (2010).
- [27] S. Sanwalani, K. Rawat, M. Pal, H. B. Bohidar, and A. K. Verma, *J. Nanopart Res.* **16**, 2382 (2014).
- [28] A. L. Patterson, *Phys. Rev.* **36**, 978 (1939).
- [29] J. . Tauc, R. . Grigorovici, and A. Vancu, *Phys. Stat. Sol.* **15**, 627 (1966).
- [30] H. A. Barnes, *A Handbook of Elementary Rheology* (University of Wales, Institute of Non-Newtonian fluid Mechanics: Aberystwyth, 2000).
- [31] N. Arfin, V. K. Aswal, J. Kohlbrecher, and H. B. Bohidar, *Polymer (Guildf)*. **65**, 175 (2015).
- [32] A. Ajji and L. Choplin, *Macromolecules* **24**, 5221 (1991).
- [33] H. Ding, J. S. Wei, N. Zhong, Q. Y. Gao, and H. M. Xiong, *Langmuir* **33**, 12635 (2017).
- [34] Z. L. Wu, Z. X. Liu, and Y. H. Yuan, *J. Mater. Chem. B* **5**, 3794 (2017).

- [35] N. Vasimalai, V. V. Boas, J. Gallo, M. F. Cerqueira, M. M. Miranda, J. M. C. Fernández, L. Diéguez, B. Espiña, and B. T. F. Argüelles, *Beilstein J. Nanotechnol.* **9**, 530 (2018).
- [36] V. D. Matteis, M. Cascione, C. C. Toma, and S. Leporatti, *Nanomaterials* **8**, 1 (2018).
- [37] C. Fu, K. Qian, and A. Fu, *Mater. Sci. Eng. C Mater Biol. Appl.* **76**, 350 (2017).
- [38] N. Zhou, S. Zhu, S. Maharjan, Z. Hao, Y. Song, X. Zhao, Y. Jiang, B. Yang, and L. Lu, *RSC Adv.* **4**, 62086–62095 (2014).
- [39] S. Forster, A. E. Thumser, S. R. Hood, and N. Plant, *PLoS One* **7**, 1 (2012).
- [40] N. Joshi, K. Rawat, P. R. Solanki, and H. B. Bohidar, *Biochem. Eng. J.* **102**, 69 (2015).
- [41] N. Joshi, K. Rawat, P. R. Solanki, and H. B. Bohidar, *Sens. Bio-Sensing Res.* **5**, 105 (2015).
- [42] B. Kaur, T. Pandiyan, B. Satpati, and R. Srivastava, *Colloids Surfaces B Biointerfaces* **111**, 97 (2013).
- [43] D. Kim, E. Kang, S. Baek, S. Choo, Y. Chung, D. Lee, J. Min, and T. Kim, *Sci. Rep.* **8**, 14049 (2018).
- [44] H. N. Yu, Y. C. Pang, and J. Y. Tang, *Int. J. Electrochem. Sci.* **10**, 8353 (2015).
- [45] G. T. S. How, A. Pandikumar, H. N. Ming, and L. H. Ngee, *Sci. Rep.* **4**, (2014).

## CHAPTER-9

---

### Summary

**Abstract:** In this chapter brief summary of this thesis has been discussed.

#### 9.1 Main Summary of the thesis

In this thesis I have studied viscoelastic, dynamic and microscopic properties of DNA hydrogel, DNA ionogels and gamma irradiated DNA ionogels. We have also explored DNA-(zein) protein complex coacervation. Further we have shown the application of these ionogels as electrochemical sensor. Water soluble MoS<sub>2</sub> quantum dot was synthesized and used it to form quantum dot based nanocomposite fluorescent DNA hydrogel. We also have synthesized DNA based DNA dots and shown its multifunctional behavior. Thesis outline is as follows:

**Chapter 3:** In this chapter, we studied the self-assembly of DNA hydrogel, ionogels and gamma irradiation ionogels. The viscoelastic properties of these gels were also characterized by viscometry and rheology. We have also studied relaxation dynamics in DNA ionogels via dynamic light scattering. Modes of relaxation were also probed for the ionogels. We were able to form low concentration DNA gels in presence of ionic liquid which was an achievement in this chapter. The microscopic structures of these gels were also probed by small angle neutron scattering.

**Chapter 4:** In this chapter we have studied *in situ* formation of zein nanoparticle and DNA complex formation under certain pH condition at room temperature. Further at certain zein



concentration leads the formation of complex coacervation followed by partial charge neutralization was observed. We have also studied coacervation in (organic and inorganic) salt medium.

**Chapter 5:** In this chapter we have used [C2mim][Cl] based DNA ionogel electrode for sensing of bio analytes by electrochemical method. We found that this electrode is specific for urea sensing among all analytes used. A remarkable aspect of the study arises from the simplicity of the electrode design and non-enzymatic mode of detection that makes the approach facile and cost-effective.

**Chapter 6:** In this chapter concentration dependence of [C8mim][Cl] ionic liquid based DNA ionogels were studied and these ionogel have been used to fabricate citric acid sensor which provides a new platform for enzyme-free and sensitive detection of citric acid and for real time detection of clinical samples.

**Chapter 7:** In this chapter we have characterized water soluble MoS<sub>2</sub> quantum dots cross linked with DNA to form hydrogels. In the DNA hydrogel matrix, these QDs acted as excellent pseudo-crosslinkers that enhanced gel strength, and melting temperature of the hydrogel, regardless of the fact that the biopolymer and the QD had charge of same polarity. Here we attempt to understanding of the nature of interactions that exist between nanoparticles and polyelectrolytes of same polarity which extends the possibility to customize this new class nanocomposite materials.

**Chapter 8:** In this chapter we synthesized DNA-dots (DD) from ds-DNA and shown its multifunctional uses. These dots were incorporated in DNA solution to form fluorescent DNA hydrogel. Further these dots showed negligible toxicity and efficient internalization into the fungal cells, therefore have the potential for use as nontoxic fluorescent probe for cell imaging

applications. The dots were used for the detection of dopamine. Functional DNAs with different modifications hold promise for applications in nanotechnology and bioanalysis.

## 9.2 Ongoing Work

We have some open problems where mostly the experiments are completed. Now we have to analyze the data.

**DNA- $\beta$ -lactoglobulin ( $\beta$ -lg) complex coacervation:** In this problem I have studied the formation of DNA-  $\beta$ -lg complexes. At certain concentration of  $\beta$ -lg, there is total charge neutralization leading to complex coacervation. I have also studied these coacervates under ionic medium.

**DNA-FA hydrogel:** I have synthesized DNA-FA hydrogels and need to study the phase transition, viscoelastic properties, microscopic properties, I have performed DLS, rheology and neutron scattering etc. for better understanding for these gels

**Protein based nanodots:** I have also synthesized and characterized protein based nanodots via DLS, TEM, XRD, UV and Fluorescence studies. These nanodots have negligible toxicity. These have shown antibacterial properties and I have used them as bioimaging tool for HELA cells.

## 9.3 Open problems for future

There are various open problems which also required to study. We need to apply theoretical model for better understanding of these hydrogels and complexes formed in this thesis. I also want to explore coacervation process more deeply. DNA-nanocomposite materials may find application as solar cell, light emitting diode and in drug delivery.

## Publications

---

- (1) **Pandey, P.K.;** Rawat, K.; Aswal, V. K.; Kohlbrechere, J.; Bohidar, H. B., DNA ionogel: Structure and self-assembly, *Phys. Chem. Chem. Phys.*, **2017**, 19, 804-812
- (2) **Pandey, P.K.;** Rawat, K.; Aswal, V. K.; Kohlbrechere, J.; Bohidar, H. B., Structural hierarchy in DNA hydrogels, *J Appl Biotechnol Bioeng* **2017**, 2(4): 00038
- (3) **Pandey, P.K.;** Kaushik, P.; Rawat, K.; Aswal, V. K.; Bohidar, H. B., Solvent hydrophobicity induced complex coacervation of dsDNA and in situ formed zein nanoparticles, *Soft Matter*, **2017**, 13, 6784-6791
- (4) **Pandey, P.K.;** Rawat, K.; Aswal, V. K.; Kohlbrechere, J.; Bohidar, H. B., Imidazolium based ionic liquid induced DNA gelation at remarkably low concentration, *Colloids and Surfaces A: Physicochemical and Engineering Aspects* 538, **2018**, 184–191
- (5) **Pandey, P.K.;** Kaushik, P.; Rawat, K.; Bohidar, H. B., Effect of organic and inorganic salt environment on the complex coacervation of in situ formed protein nanoparticles and DNA, *International Journal of Biological Macromolecules*, 122, **2019**, 1290-1296
- (6) **Pandey, P.K.;** Rawat, K.; Asokan, K.; Kanjilal, D.; Bohidar, H. B., Gelation Kinetics of  $\gamma$ -radiation DNA Ionogels (*Communicated*)
- (7) **Pandey, P.K.;** Rawat, K.; Aswal, V. K.; Bohidar, H. B. DNA-MoS<sub>2</sub> Quantum dot based gel and application as schottky diode (*Under Preparation*)
- (8) **Pandey, P.K.;** Rawat, K.; Bohidar, H. B. Water soluble synthesized MoS<sub>2</sub> quantum dot as ds-DNA-MoS<sub>2</sub> Based Ascorbic Acid Sensor and the Effect of Nitrogen Ion Implantation (*Under Preparation*)
- (9) **Pandey, P.K.;** Rawat, K.; Bohidar, H. B. Biocompatible DNA ionogel Based Urea Sensor and the Effect of Nitrogen Ion Implantation (*Communicated*).
- (10) **Pandey, P.K.;** Rawat, K.; Aswal, V. K.; Bohidar, H. B. Structural dynamics of Concentration dependent 1-octyl-3-methylimidazolium chloride/ DNA gelation and its application as Citric acid sensor (*Communicated*).
- (11) **Pandey, P.K.;** Preeti.; Rawat, K.; Prasad, T.; Bohidar, H. B. Fluorescent multipurpose DNA- Dots: Luminescent DNA gels, Cell Imaging and Dopamine Detection (*Communicated*).

## Conferences, Seminars and Workshops

---

- (1) Participated in National Conference on '**Interdisciplinary Approaches in Chemical Sciences IACS -2015**' on 16<sup>th</sup> December, 2015 at Centre for interdisciplinary Research in Basic Sciences Jamia Millia Islamia, New Delhi, Jawaharlal Nehru University, New Delhi, India.
- (2) Participated in National Seminar on '**Recent Trends in nano-Bio interface**' on 18<sup>th</sup> December, 2015 at Special Centre for Nano sciences, Jawaharlal Nehru University, New Delhi, India.
- (3) Oral and Poster presentation on 'DNA gels in ionic liquid solutions: Structure and morphology', CRS-Research scholars' '**Workshop on Materials Science and Neutrons**' (RSW-2016) held at Training School Hostel, Anushaktinagar Mumbai-400094 during 3<sup>rd</sup> and 4<sup>th</sup> February 2016 organized by UGC-DAE Consortium for Scientific Research Mumbai Centre.
- (4) Participated in National seminar on '**Advances in Polymer science and Technology (POLY-2016)**' on March 9-10,2016 organized jointly by Prof. Sukumar Maiti Polymer Award Foundations & Special Centre for Nano sciences, Jawaharlal Nehru University, New Delhi, India.
- (5) Poster presentation on DNA-Ionogel in SPS March Meeting, 18-19 March 2016.
- (6) Poster Presentation in '**International Conference on Nano biotechnology**' held on February 5-6, 2018 at CIRBSC, S. Ramanujan Block, Jamia Millia Islamia, New Delhi, India.



Cite this: *Phys. Chem. Chem. Phys.*,  
2017, **19**, 804

## DNA ionogel: Structure and self-assembly†

Pankaj Kumar Pandey,<sup>a</sup> Kamla Rawat,<sup>\*bc</sup> V. K. Aswal,<sup>d</sup> J. Kohlbrecher<sup>e</sup> and  
H. B. Bohidar<sup>\*ab</sup>

DNA dissolved in ionic liquid (IL) solution (1-ethyl-3-methylimidazolium chloride, [C2mim][Cl]) showed a transition to the gel phase ([DNA]  $\geq$  1% (w/v)). The gelation time was 400 s for the 1% [IL] sample which reduced to 260 s for 5% [IL] concentration. Gelation times, obtained from the viscosity and ergodicity breaking from the dynamic structure factor data, were remarkably identical to each other. Correspondingly, the gelation temperature which was  $\sim$ 60 °C increased to 67 °C with [IL] content. The small angle neutron scattering (SANS) structure factor profile revealed the presence of the following three distinct length scales: (a) mesh size,  $\xi \approx 3 \pm 0.5$  nm for ionogels, and  $\approx 0.73 \pm 0.06$  nm, for sol; (b) cross-sectional radius of DNA strand,  $R_c \approx 1.6 \pm 0.1$  nm; and (c) the characteristic inter-cluster distance  $\approx 33 \pm 5$  nm. Physical conformation of the DNA–IL complexes remained close to the Gaussian coil definition. It was observed that without IL, in the sol phase, the system was completely ergodic and did not gel, while on addition of IL a sudden transition to the non-ergodic (arrested) gel phase occurred. This was due to the formation of an amorphous network of DNA–IL complexes preceding gelation. In summary, it is shown that the DNA ionogels can be prepared with a tunable gel strength (27–70 Pa) and gelation temperature (60–67 °C). Further, the relaxation dynamics was found to be hierarchical in IL content of the gel, revealing considerable self-organization.

Received 9th September 2016,  
Accepted 7th November 2016

DOI: 10.1039/c6cp06229f

www.rsc.org/pccp

### 1. Introduction

Natural biopolymers have been utilized for pharmaceutical applications for the last few decades due to their unique properties such as versatility, biocompatibility and bio-absorbability. Beside this, most biopolymers have good film forming ability along with better stability, which make them suitable for biomedical applications.<sup>1,2</sup> The presence of abundant functional groups on the biopolymer chains provides excellent interfacial properties, resulting in fast communication between the attached molecules for the development of biosensors.<sup>3,4</sup> Generally, the active sites of biopolymers are embedded in the core, which affects the direct binding with its receptor molecules, resulting in the hindrance of direct electron communication. However, ILs create an interface resulting in an enhanced fast electron transfer rate between the

electrolyte and the underlying electrode for sensor and biosensor applications.<sup>5,6</sup>

Nucleic acids constitute an important class of biomolecules that are a repository of genetic information. The aqueous dispersion behavior of these biopolymers is rich in soft matter phases and their self-assembly gives rise to a wide range of morphologies.<sup>7–9</sup> DNA gels have attracted much attention recently due to their potential applications as drug and gene delivery vehicles.<sup>10–12</sup> Therefore, tailoring of their physical properties is required. In order to generate a new class of intelligent biomaterials involving DNA, it is necessary to explore its dispersion behavior in IL, and other organo-solutions.

Organic salts having a melting point of less than 100 °C are called ionic liquids. These are thermally stable, non-flammable and highly conductive.<sup>13–16</sup> The ILs are found to be good stabilizers for biopolymers due to the availability of nitrogen-containing cations, such as imidazolium, and inorganic or organic anions. Ionic liquids as electrolytes or in the form of composites have been used for electrochemical based sensor applications. IL based DNA ionogels consist of two types of ILs, short and long chain {1-ethyl-3-methylimidazolium chloride [C2mim][Cl]} and {1-octyl-3-methyl imidazolium chloride [C8mim][Cl]} which are used in drug delivery and tissue engineering applications. Many reports reveal that DNA encapsulation can be used either in gene therapy or chitosan microsphere based delivery vehicles.<sup>17,18</sup> Moran *et al.* have studied the swelling and dislocation behaviour of DNA gel particles.<sup>10</sup>

<sup>a</sup> School of Physical Sciences, Jawaharlal Nehru University, New Delhi 110067, India

<sup>b</sup> Special Center for Nanosciences, Jawaharlal Nehru University, New Delhi 110067, India. E-mail: bohi0700@mail.jnu.ac.in, kamla.jnu@gmail.com; Fax: +91 11 2674 1837; Tel: +91 11 26742091

<sup>c</sup> Inter University Accelerator Centre, New Delhi 110067, India

<sup>d</sup> State Physics Division, Bhabha Atomic Research Centre, Mumbai 400085, India


<sup>e</sup> Laboratory for Neutron Scattering, Paul Scherrer Institut, Villigen, Switzerland

† Electronic supplementary information (ESI) available: The variation of relative viscosity with different temperature, gelation temperature  $T_{gel}$  as a function of gelation time  $t_{gel}$ , time dependent dynamic structure factor,  $g_1(\tau)$  intensity profile, mesh size  $\xi$ , cross sectional radius  $R_c$ , characteristic cross over lengths for different DNA–IL samples at various IL concentrations undertaken in this study. See DOI: 10.1039/c6cp06229f



Cite this: *Soft Matter*, 2017, 13, 6784

## Solvent hydrophobicity induced complex coacervation of dsDNA and *in situ* formed zein nanoparticles†

Pankaj Kumar Pandey,<sup>a</sup> Priyanka Kaushik,<sup>a</sup> Kamla Rawat,<sup>b</sup> \*<sup>bc</sup> V. K. Aswal<sup>d</sup> and H. B. Bohidar\*<sup>ab</sup>

Zein, a predominantly hydrophobic protein, was sustained as a stable dispersion in ethanol–water (80:20, % (v/v)) binary solvent at room temperature (25 °C). Addition of aqueous dsDNA solution (1% (w/v)) to the above dispersion prepared with the protein concentration of  $C_{\text{zein}} = 0.01\text{--}0.5\%$  (w/v) caused a concomitant change in ethanol content from 14–35% (v/v), which in turn generated zein nanoparticles *in situ* of size 80–120 nm increasing with water content. The subsequent associative interaction between DNA (polyanion; 2000 bps) and the positively charged zein nanoparticles, (at pH = 4) was driven by Coulombic forces, and by the solvent hydrophobicity due to the ethanol content of the binary solvent. Experimentally, two interesting regions of interaction were observed from turbidity, zeta potential, particle sizing, and viscosity data: (i) for  $C_{\text{zein}} < 0.2\%$  (w/v), zein nanoparticles of size 80 nm bind to dsDNA (primary complex) causing its condensation (apparent hydrodynamic size decreased from  $\approx 2100$  to 560 nm), and (ii) for  $0.2\% < C_{\text{zein}} < 0.5\%$  (w/v) larger nanoparticles (>80 nm) were selectively bound to primary complexes to form partially charge neutralized interpolymer soluble complexes (secondary complexes), followed by complex coacervation. During this process, there was depletion of water in the vicinity of the nucleic acid, which was replaced by hydration provided by the ethanol–water binary solvent. Equilibrium coacervate samples were probed for their microstructure by small angle neutron scattering, and for their viscoelastic properties by rheology. The interplay of solvent hydrophobicity, electrostatic interaction, and zein nanoparticle size dependent charge neutralization had a commensurate effect on this hitherto unexplored coacervation phenomenon.

Received 21st June 2017,  
Accepted 4th August 2017

DOI: 10.1039/c7sm01222e

rsc.li/soft-matter-journal

## 1. Introduction

Intermolecular associative interaction between oppositely charged macromolecules, which is mostly driven by electrostatic forces, often leads to liquid–liquid phase separation (called coacervation transition).<sup>1,2</sup> Coacervation is usually defined as the spontaneous formation of a super dense liquid phase from a homogeneous macromolecular solution of poor solvent affinity.<sup>1</sup> Typically, a homogeneous solution separates into a polymer-rich phase (called coacervate) and its supernatant.<sup>2</sup> In complex coacervation, the loss of solvation that leads to phase separation arises from the interaction of macromolecules carrying complementary net charge. The formation of such macromolecule-rich fluids is

well known in mixtures of a variety of complementary polyelectrolytes.<sup>3</sup> It may also occur from mixtures of polyelectrolytes and colloidal particles, leading to condensed phases that are associated with interesting properties. In the recent past, complex coacervation has been reported in a wide range of macromolecular systems, like poly(dimethyldiallylammonium chloride)–bovine serum albumin,<sup>4</sup> gelatin–chitosan,<sup>5</sup> gelatin–agar,<sup>6,7</sup> gelatin–gelatin,<sup>8,9</sup> DNA–gelatin<sup>10–12</sup> etc.

In addition, experiments that explored the formation of similar free-energy driven self-organized microscopic structures using nucleic acids were highly successful.<sup>13</sup> DNA being one of the polyelectrolytes having the highest linear charge density, its association with other biomolecules is of considerable interest. Binding of DNA to proteins<sup>14,15</sup> and oppositely charged spherical macroions<sup>16</sup> has revealed interesting results. Mrevlishvili and Svintradze<sup>14</sup> have reported interaction between worm-like chains of a DNA duplex with a persistence length of 50 nm, contour length of 3000 nm and width of 2 nm with collagen rod-like structures of length 300 nm and width 1.5 nm. The DNA–collagen complex was found to have overlapped hydration shells of the

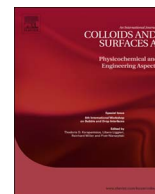
<sup>a</sup> School of Physical Sciences, Jawaharlal Nehru University, New Delhi 110067, India. E-mail: bohi0700@mail.jnu.ac.in

<sup>b</sup> Special Center for Nanosciences, Jawaharlal Nehru University, New Delhi 110067, India. E-mail: kamla.jnu@gmail.com

<sup>c</sup> Inter University Accelerator Centre, New Delhi 110067, India

<sup>d</sup> State Physics Division, Bhabha Atomic Research Centre, Mumbai 400085, India

† Electronic supplementary information (ESI) available. See DOI: 10.1039/c7sm01222e

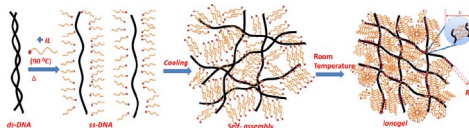


## Research Paper

## Imidazolium based ionic liquid induced DNA gelation at remarkably low concentration

Pankaj Kumar Pandey<sup>a</sup>, Kamla Rawat<sup>b,c,\*</sup>, V.K. Aswal<sup>d</sup>, J. Kohlbrecher<sup>e</sup>, H.B. Bohidar<sup>a,b,\*\*</sup><sup>a</sup> School of Physical Sciences, Jawaharlal Nehru University, New Delhi 110067, India<sup>b</sup> Special Center for Nanosciences, Jawaharlal Nehru University, New Delhi 110067, India<sup>c</sup> Inter University Accelerator Centre, New Delhi 110067, India<sup>d</sup> State Physics Division, Bhabha Atomic Research Centre, Mumbai 400085, India<sup>e</sup> Laboratory for Neutron Scattering, Paul Scherrer Institut, Villigen, Switzerland

## GRAPHICAL ABSTRACT



## ARTICLE INFO

## Keywords:

DNA  
Ionogels  
Ionic liquids  
Structure  
Gelation kinetics  
Relaxation dynamics

## ABSTRACT

DNA dissolved in 1.0% (w/v) aqueous solution of ionic liquid (IL, 1-octyl-3-methylimidazolium chloride, [C8mim][Cl]) showed gelation transition at a remarkably low concentration of [DNA]  $\approx$  0.3% (w/v) unlike in hydrogels where gelation occurs  $\geq$  2.0% (w/v). Thus, the IL induced gelation was observed at 85% lower concentration. These ionogels were probed in the 0.1%–1.0% (w/v) concentration region of DNA where the hydrogels never form. The gelation temperature  $T_{\text{gel}}$  (and gel strength  $G_0$ ,  $G_0$  is low frequency storage modulus) increased from  $T_{\text{gel}} = 52 \pm 2^\circ\text{C}$  ( $G_0 = 10 \pm 1\text{ Pa}$ ) to  $72 \pm 2^\circ\text{C}$  ( $G_0 = 40 \pm 2\text{ Pa}$ ) with increase in DNA content. The dynamic structure factor of gelling sol revealed ergodic to non-ergodic transition at the onset of gelation and the corresponding ergodicity breaking time  $\tau_{\text{EB}}$  was found to be identical to gelation time,  $t_{\text{gel}}$ . Interestingly, the characteristic parameters defining gelation transition, such as  $t_{\text{gel}}$ ,  $\tau_{\text{EB}}$  and  $T_{\text{gel}}$  revealed linear dependence with DNA content. Remarkably, the gelation (also melting) temperature could be increased by as much as  $2.4^\circ\text{C}$  when the [DNA] was raised by a mere 0.1%, which will impart considerable advantage in terms of variables, and ability to process DNA gels.

## 1. Introduction

Physical gelation of DNA in aqueous medium is an intriguing phenomenon which is much less probed, and hence, remains poorly understood. This polyanionic biopolymer exhibits excellent solubility in water due to its extremely high linear charge density. This particular attribute when combined with its biocompatibility, low cytotoxicity and easy programmability (arising from base-pairing) makes this biopolymer an excellent platform for many out of the box applications.

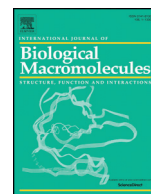
Interaction between giant bacteriophage DNA and cationic biomimetic colloidal stable particles of size 80–700 nm with moderate polydispersity and high cytotoxic against *E. Coli* could be prepared by Rosa et al. [1]. Interestingly, some nucleosome mimetic assemblies were observed at charge neutralization condition of the DNA. Kikuchi and Carmona-Ribeiro studied the DNA interaction with cationic liposomes and have concluded that this interaction was not merely electrostatic attraction between the oppositely charged DNA molecules and the liposomes [2]. They noticed liposome loses its integrity and DNA unfolds

\* Corresponding author at: Special Center for Nanosciences, Jawaharlal Nehru University, New Delhi 110067, India.

\*\* Corresponding author at: School of Physical Sciences, Jawaharlal Nehru University, New Delhi 110067, India.

E-mail addresses: [kamla.jnu@gmail.com](mailto:kamla.jnu@gmail.com) (K. Rawat), [bohi0700@mail.jnu.ac.in](mailto:bohi0700@mail.jnu.ac.in) (H.B. Bohidar).





## Effect of organic and inorganic salt environment on the complex coacervation of *in situ* formed protein nanoparticles and DNA

Pankaj Kumar Pandey<sup>a</sup>, Priyanka Kaushik<sup>b</sup>, Kamla Rawat<sup>b,c,\*</sup>, H.B. Bohidar<sup>a,b,\*\*</sup>

<sup>a</sup> School of Physical Sciences, Jawaharlal Nehru University, New Delhi 110067, India

<sup>b</sup> Special Center for Nanosciences, Jawaharlal Nehru University, New Delhi 110067, India

<sup>c</sup> School of Chemical and Life Science, Jamia Hamdard New Delhi-110062, India

### ARTICLE INFO

#### Article history:

Received 18 July 2018

Received in revised form 5 September 2018

Accepted 14 September 2018

Available online 15 September 2018

#### Keywords:

Coacervation

Protein nanoparticles

Phase separation

Charge neutralization

Crosslink density

### ABSTRACT

Complex coacervation was noticed between *in situ* formed protein (a primarily hydrophobic Zein protein with  $pI = 6.2$ ) nanoparticles (size 80–120 nm) and ds-DNA (a high charge density polyanion), in the ionic liquid (IL) solutions of 1-ethyl-3-methyl imidazolium chloride [C2mim][Cl], and 1-octyl-3-methyl imidazolium chloride [C8mim][Cl], in the studied ionic strength range of  $I = 10^{-4}$  to  $6 \times 10^{-1}$  M, which was extended to strong monovalent 1:1 electrolyte (NaCl) to explore the commonality between the organic and inorganic salt (ionic) environment on coacervation. The salt dependent coacervation profile was monitored from the measured turbidity of the interacting solution, and zeta potential, ( $\zeta$ ) and apparent hydrodynamic radius ( $R_h$ ) of interpolymer complexes, which depicted the following three discernible interaction regimes common to all the salts: (i) Region-I:  $I = 0.0001$ – $0.01$  M, primary binding, (ii) Region-II,  $I = 0.01$ – $0.1$  M, secondary binding, and (iii) Region-III,  $I = 0.1$ – $0.6$  M, saturation binding. The free-energy and the network density calculations favored preferential coacervation in [C2mim][Cl] samples. Nonetheless, commonality in the overall ionic strength dependent coacervation profiles could still be observed.

© 2018 Elsevier B.V. All rights reserved.

### 1. Introduction

Associative interaction between charge complementary polyelectrolyte-polyelectrolyte, polyelectrolyte-polyampholyte, polyelectrolyte-micelle and polyelectrolyte-colloid pairs *etc.* driven by electrostatic forces leading to liquid-liquid phase separation called coacervation has been observed [1–7]. Coacervation is usually defined as the spontaneous formation of a super dense liquid phase from a homogeneous polyelectrolyte (PE) solution of poor solvent affinity. Typically, a homogeneous solution phase separates into a polymer-rich phase (called coacervate) and its supernatant during coacervation transition. It has long been realized that surface charge density of the polyelectrolyte is an important parameter that governs the coacervation pathway [8]. In particular, study of complex coacervation between biopolymers where one is a strong polyelectrolyte (like DNA) and another a colloidal protein or protein nanoparticles is of immense importance [9,10]. Apart from the richness of this domain that resides at the interface between

soft matter and nanoscience, the coacervate material produced may be used for design of artificial organs in future. Some of the DNA based coacervates reported in the literature includes, DNA-zein [11,12], DNA-gelatin [13,14], DNA-BSA [15], and DNA-chitosan [16].

As far as the effect of ionic environment on the coacervation is concerned several studies have revealed interesting features. Dubin and coworkers [16,17] have shown that for PE-colloid coacervation, the PE ( $\xi$ ) and colloid charge density ( $\sigma_c$ ) are related to Debye-Huckel screening length ( $\kappa$ ), by  $\xi\sigma_c = \kappa$ . Perry et al. [18] studied the effect of salt type on coacervate formation using two vinyl polyelectrolytes, poly(acrylic acid sodium salt) and poly(allylamine hydrochloride), and confirmed the role of salt valence on the coacervate formation, while demonstrating the presence of significant secondary effects, which could be described by Hofmeister-like behavior. Wang et al. [19] have shown the “salt suppression” and “salt enhancement” of coacervation. In the coacervation region, the electrophoretic mobility was found to be close to zero. At higher and lower ionic strengths, soluble complexes were positive or negatively charged, respectively. Interestingly, even in coacervating systems driven by surface selective patch binding mechanism ionic strength of the solution was seen to influence the binding profile [20].

The above-mentioned literature does not answer a pertinent question: Is there any commonality between organic and inorganic salt produced ionic environment on the coacervation process? The current

\* Correspondence to: K. Rawat, School of Chemical and Life Science, Jamia Hamdard New Delhi-110062, India.

\*\* Correspondence to: H.B. Bohidar, School of Physical Sciences, Jawaharlal Nehru University, New Delhi 110067, India.

E-mail addresses: [kamlarawat@jamiahamdard.ac.in](mailto:kamlarawat@jamiahamdard.ac.in) (K. Rawat), [bohi0700@mail.jnu.ac.in](mailto:bohi0700@mail.jnu.ac.in) (H.B. Bohidar).



# Structural hierarchy in DNA hydrogels

## Abstract

Sol-gel transition in aqueous DNA solutions was probed to determine the gelation time  $t_{gel}$  and temperature  $T_{gel}$ . It was remarkable to observe that  $T_{gel}$  increased from 36 to 57°C and  $t_{gel}$  linearly decreased from 700 to 350 s with increase in DNA concentration. The hydrogels were studied by using small angle neutron scattering (SANS) ( $[DNA] \leq 3\%$  (w/v)) to determine the underlying hierarchy of length scales. From structure factor profile analysis, three distinct signatures were obtained:

- Radius of gyration  $R_g \approx 40 \pm 3$  nm, which assigned a length of 140 nm to DNA strand
- Geometry of scattering moiety defined by the value of  $\alpha \approx 2.2 \pm 0.1$  indicating Gaussian chain behavior
- Correlation length,  $\xi$  increased from 0.50 to 3.30 nm and the inter-chain spacing  $d_0$  decreased from 15.6 to 9.8 nm, with increase in DNA concentration.

Physical networks were formed for concentration,  $c^* \geq 2\%$  (w/v) and the system involved at least five identifiable length scales. A revisit has shown that hierarchical structure of DNA hydrogel owes its origin to considerable self-organization at the molecular level dependent on biopolymer concentration.

**Keywords:** DNA hydrogels, neutron scattering, guinier-regime, power-law, broad peak region, correlation length, self-assembly

Volume 2 Issue 4 - 2017

Pandey PK,<sup>1</sup> Rawat K,<sup>2,3</sup> Aswal VK,<sup>4</sup>  
Kohlbrecher J,<sup>5</sup> Bohidar HB<sup>1,2</sup>

<sup>1</sup>Department of Physical Sciences, Jawaharlal Nehru University, India

<sup>2</sup> Department of Nanosciences, Jawaharlal Nehru University, India

<sup>3</sup>Inter University Accelerator Centre, India

<sup>4</sup>Department of physics, Bhabha Atomic Research Centre, India

<sup>5</sup>Laboratory for Neutron Scattering, Switzerland

**Correspondence:** Bohidar HB, School of Physical Sciences, Jawaharlal Nehru University, New Delhi 110067, India, Fax +91 11 2674 1837, Tel +91 11 26704637,

Email bohi0700@mail.jnu.ac.in

Rawat K, Inter University Accelerator Centre, India, Fax +91 11 2674 1837, Tel +91 11 26704637, Email kamla.jnu@gmail.com

**Received:** December 28, 2016 | **Published:** March 10, 2017

**Abbreviations:** SANS, small angle neutron scattering; EGDE, ethylene glycol diglycidyl ether

## Introduction

DNA is found to be an extraordinary biopolymer because it can be used as molecular tool to construct many other objects such as nano devices, periodic arrays and genetic engineering templates. DNA plays a vital role in many biological processes like gene therapy. But due to its large extended chains it cannot be delivered directly into the cells.<sup>1</sup> DNA hydrogels are eco-friendly because these are biocompatible and biodegradable. Unlike other hydrogels, DNA hydrogel are different in terms of efficiency and strong branched cross-linking.<sup>2</sup> The benefit of it is one can achieve gelling under physiological conditions that allows for the encapsulation of drugs, proteins and mammalian cells in the sol phase instead of drug-loading step and denaturing conditions.<sup>3</sup> A strongly interactive PVA and DNA cryogel was prepared and it showed a good mechanical resistance due to its heterogeneous porous structure.<sup>4</sup> For natural DNA, formaldehyde and metal compounds such as arsenic, chromate and nickel are widely used as cross-linkers which are known carcinogens.<sup>5,6</sup> DNA-cross-linked PAA mgel could be used to release nano particles for potential drug-delivery vehicles in response to right stimulus.<sup>7</sup> DNA hydrogels reversibly respond to thermal stimulus, by switching between the gel and sol state (transition temperature) and enzymes when restriction sites are inserted into one of the building blocks.<sup>8</sup>

DNA hydrogels have a wide range of biomedical application in tissue engineering and drug-delivery system.<sup>9</sup> Lee et al inspired by silkworm and spiders gave the evidence for the formation of DNA hydrogel fiber with self-entanglement prepared in the presence of ionic liquid.<sup>10</sup> Moran et al.<sup>9</sup> prepared DNA gel particles and studied swelling, dissolution behavior and DNA release.<sup>9</sup> They made DNA gel particles in the presence surfactant CTAB and protein lysozyme, but

without using any cross-linker or organic solvents. Orakdogan et al.<sup>11</sup> showed evidence of strain hardening in both physical and chemical DNA gels.<sup>11</sup> Physical gels were prepared by physical cross-linking of DNA with heating-cooling cycle, while chemical gels were prepared by adding a cross linker like EGDE (ethylene glycol diglycidyl ether). Visco elastic properties of DNA gels and the crossover frequency for DNA in solutions that vary with concentration have been reported.<sup>12,13</sup> Liu et al.<sup>14</sup> described the relaxation time of double and single stranded DNA on the basis of viscosity measurement in an oscillatory flow and by stress relaxation measurements.<sup>14</sup> DNA hydrogel relaxation dynamics has been found to be hierarchical in concentration.<sup>15</sup> The differential shrinking of hydrogels in presence of NaBr and cationic surfactant has been reported.<sup>16</sup> Rheological behavior of DNA hydrogels indicated that storage modulus  $G'$  and loss modulus  $G''$  are frequency independent which is due to dominance of viscoelastic relaxation of the networks at lower frequencies.<sup>17</sup>

Hierarchical self-assembly in DNA gels is the primary factor which distinguishes and makes it versatile. At appropriate concentration and controlled flexibility, one-pot self-assembly of DNA gives rise to very small nanometer range tetrahedral, dedecahedra and bucky-ball size complex structures. Therefore, self-assembly of DNA allows formation of complex 3-D structures.<sup>18</sup> DNA gels exhibit universal scaled stiffening behavior that can be reproduced by a wormlike chain model keeping in mind the entropic elasticity of DNA strands.<sup>11</sup> For tissue engineering applications, due to biocompatibility and permeability of hydrogel, one can design the required three-dimensional constructions.<sup>19</sup> In spite of the availability of a large volume of literature on DNA, the micro-structural probing of their hydrogels by SANS remains poorly explored. In this report, we have comprehensively studied DNA hydrogels using SANS to develop a general understanding of hierarchical self-organization of these networks. Considering the importance of the nucleic acids in genetic engineering and pharmaceuticals, these results are of importance.